UNIVERSITY OF SOUTHAMPTON

Faculty of Engineering and Physical Sciences
School of Engineering

Numerical Investigation of Hydrogen Fuelled Internal Combustion Engines

by

Callum James Ramsay
ORCiD: 0000-0003-3262-6369

A thesis for the degree of
Doctor of Philosophy

March 2022

Abstract

Hydrogen is a clean and carbon free alternative fuel which has the potential to drastically reduce harmful emissions while maintaining or even improving the energy efficiency of internal combustion engines traditionally fuelled by fossil fuels. The focus of this thesis is to, through numerical modelling and simulation, enhance the fundamental understanding of optimal hydrogen utilisation in compression ignition (CI) engines operating with diesel-hydrogen dual-fuel combustion technologies where a high percentage of the original diesel fuel is replaced by hydrogen.

The first part of this thesis investigates high hydrogen energy share (HES) diesel-hydrogen dual-fuel combustion in a CI engine when operated with intake manifold inducted hydrogen. For this, a range of numerical simulations were carried out to investigate the performance and emissions characteristics of the engine when operating under a novel combustion strategy, currently in development by industrial collaborator Covaxe, in which the diesel injection and the majority of the hydrogen combustion occur at a constant volume. Initially, a parametric study on pure diesel operation was performed to investigate the effects of the duration and timing of the constant volume combustion phase (CVCP) on the engine's performance and emissions outputs, with comparisons to the conventional engine. The results demonstrate that the CVCP strategy is capable of yielding reduced gross indicated specific fuel consumption by up to 20% and far lower carbon based emissions. The results also found that a combination of CVCP strategy, exhaust gas recirculation (EGR) and improved fuel injection methods can counter the increased NO_x emissions somewhat, while still maintaining the improved engine performance and low carbon-based emissions. Following this, a study was performed to investigate the effects of the CVCP strategy on combustion, performance and emissions of the engine operating in diesel-hydrogen dual-fuel mode with hydrogen intake induction at up to 90% HES. The results demonstrate that the CVCP strategy can improve thermal efficiency at all HESs and load conditions with far lower carbon-based emissions. Conventional diesel-hydrogen dual-fuel engines struggle at low load high HESs due to the reduced diesel injection failing to ignite the leaner premixed charge. Through use of a CVCP thermal efficiency at low load 90% HES increased from 11% to 38% with considerably reduced hydrogen emission due to the increased temperatures and pressures allowing for the wholesale ignition of the hydrogen-air mix. It was also found that increasing the time allowed for combustion within the CVCP, by advancing the diesel injection, can lead to even further thermal efficiency gains while not negatively impacting emissions.

Direct gaseous fuel injection in internal combustion engines is a potential strategy for improving in-cylinder combustion processes and performance while reducing emissions outputs and increasing HES when compared to intake induction operation. The

second part of this thesis studied combustion in a direct hydrogen injection diesel-hydrogen dual-fuel CI engine at up to 99% HES. To facilitate this study, the gaseous sphere injection (GSI) model, which utilises the Lagrangian discrete phase model to represent the injected gas jet, is improved upon to accurately predict the high pressure hydrogen direct gas injection strategy. The improved GSI model is then validated against experimental hydrogen and methane underexpanded freestream jet studies, mixing in a direct injection hydrogen spark ignition engine and combustion in a dual direct injection diesel-methane compression ignition engine. The improved GSI model performs well across all cases examined which cover various pressure ratios, injector diameters, injection conditions and disparate gases (hydrogen and methane) while also allowing for relatively coarse meshes, with no remeshing requirement on injector parameter change, to be used when compared to those needed for fully resolved modelling of the gaseous injection process. The model is shown to be accurate, easy to implement and computationally inexpensive. The improved GSI model, coupled with computational fluid dynamics and other necessary numerical models, was applied to simulate the mixing and combustion process in a dual direct injection diesel-hydrogen dual-fuel CI engine targeting non-premixed operation. The combustion process of hydrogen in this type of engine was mapped out and compared to that of the the same engine using methane direct injection rather than hydrogen. This was followed up with a comprehensive parametric study aimed at identify how various key fuel injection and engine operational variables can be optimised to improve high hydrogen energy share (99%) performance/operation and reduce emissions at high and low load conditions. Four distinct phases of combustion were found which differ from that of pure diesel operation. Interaction of the injected gas jets with the chamber walls is discovered to be by far the most important factor in diesel-hydrogen dual direct injection operation. When combined, the likes of nozzle diameter reduction, split injection strategies, gaseous injection included angle, timing between diesel pilot and gaseous injection, start time of gaseous injection, inlet pre-heating/cooling, turbocharging and EGR were all found to be effective ways to improve performance and combustion stability/consistency while increasing hydrogen energy share and reducing NO_x emissions at both high and low load. The novel insights gained from this numerical study can be used to guide any further investigations on high HES dual direct injection diesel-hydrogen dual-fuel CI engines.

Contents

List of Figures

List of Tables

Declaration of Authorship

I declare that this thesis and the work presented in it is my own and has been generated by me as the result of my own original research.

I confirm that:

1. This work was done wholly or mainly while in candidature for a research degree at this University;
2. Where any part of this thesis has previously been submitted for a degree or any other qualification at this University or any other institution, this has been clearly stated;
3. Where I have consulted the published work of others, this is always clearly attributed;
4. Where I have quoted from the work of others, the source is always given. With the exception of such quotations, this thesis is entirely my own work;
5. I have acknowledged all main sources of help;
6. Where the thesis is based on work done by myself jointly with others, I have made clear exactly what was done by others and what I have contributed myself;
7. None of this work has been published before submission

Signed:..... Date:.....

Acknowledgements

Thanks to Dinesh for all the assistance and putting up with me for so long!

Nomenclature

$\dot{m}$	Mass flow rate	kg s^{-1}
η^*	Critical pressure ratio	
η_0	Total pressure ratio	
η_e	Exit pressure ratio	
γ	Ratio of specific heats	
θ_e	Nozzle exit cone angle	deg
θ_M	Mach disk cone angle	deg
$^\circ$CA	degrees crank angle	
A_e	Nozzle exit area	m^2
C_d	Discharge coefficient	
CO	Carbon monoxide	
CO_2	Carbon dioxide	
D_e	Nozzle exit diameter	m
D_M	Mach disk diameter	m
H_2	Hydrogen	
L_M	Mach disk length	m
L_{c-KW}	Kleinstein-Witze core length	m
L_{c-orig}	Original core length	m
L_c	Updated core length	m
NO_x	Nitrogen oxides	
P^*	Critical pressure	Pa
P_0	Total pressure	Pa

P_a	Ambient pressure	Pa
P_e	Nozzle exit pressure	Pa
R	Universal gas constant	J mol^{-1} K^{-1}
R_I	Individual gas constant	J kg^{-1} K^{-1}
T_0	Total temperature	K
T_e	Nozzle exit temperature	K
T_M	Mach disk temperature	K
V_e	Isentropic choked velocity	m s^{-1}
V_M	Mach disk velocity	m s^{-1}
ATDC	After top dead center	
BDC	Bottom dead center	
CFD	Computational fluid dynamics	
CI	Compression ignition	
CV	Constant volume	
CVCP	Constant volume combustion phase	
ECN	Engine combustion network	
EGR	Exhaust gas recirculation	
EVC	Exhaust valve close	
EVO	Exhaust valve open	
GSI	Gaseous sphere injection	
GSOI	Start of gaseous injection	
HCCI	Homogeneous charge compression ignition	
HES	Hydrogen energy share	
HL	High load	
HPDI	High pressure direct injection	
HRR	Heat release rate	J deg^{-1}
ICE	Internal combustion engine	

IMEP	Indicated mean effective pressure	Pa
IVC	Inlet valve close	
IVO	Inlet valve open	
LHV	Lower heating value	MJ kg^{-1}
LL	Low load	
LTC	Low temperature combustion	
PCCI	Premixed charge compression ignition	
PIV	Particle image velocimetry	
PLIF	Particle laser-induced fluorescence	
PSEP	Duration between pilot and gaseous injection	
RANS	Reynolds averaged Navier-Stokes	
RCCI	Reactivity controlled compression ignition	
RPM	Revolutions per minute	
SFC	Specific fuel consumption	g kWh^{-1}
SI	Spark ignition	
TDC	Top dead center	
UHC	Unburned hydrocarbon	
URANS	Unsteady Reynolds averaged Navier-Stokes	

Chapter 1

Introduction

1.1 Motivation

Renewable energy has been thrust into the spotlight in recent years due to rising global awareness of the environmental impacts of fossil fuel combustion in conjunction with growing energy demands [1]. Currently fossil fuels supply 84% of the worlds primary energy [2], as shown in Figure 1.1, with the energy sector also contributing to 76% of worldwide greenhouse gas emissions (Figure 1.2) [3]. Greenhouse gases such as carbon dioxide (CO_2) accumulate in the Earth's atmosphere and absorb radiation from the sun, insulating the planet. While greenhouse gases are essential for keeping the temperature of the planet at a livable level, their increasing accumulation due to fossil fuel usage means that too much heat is being absorbed leading to rising atmospheric temperatures, i.e. humans are the driving force in global warming [4]. Greenhouse gas emissions aren't the only problem associated with fossil fuels with the likes of harmful air-quality pollutants such as nitric oxides (NO_x), soot, unburned hydrocarbons (UHC) and carbon monoxide (CO) also being emitted through combustion and myriad geopolitical and economic issues due to locations of fossil fuel reserves and their finite nature. Many regulations and deadlines are being set for emissions reductions and the phasing out of fossil fuels. The most prominent is the Paris Agreement which saw 196 state parties commit to the long-term goal of holding the global rise in average temperature to "well below" $2^{\circ}C$ above pre-industrial revolution levels and to further pursue efforts to limit the increase to $1.5^{\circ}C$ through emissions reductions, with an overarching target of achieving a climate neutral world by the middle of the century [5]. To achieve such lofty targets a transition from fossil fuels to clean renewable fuels and energy generation methods must be made.

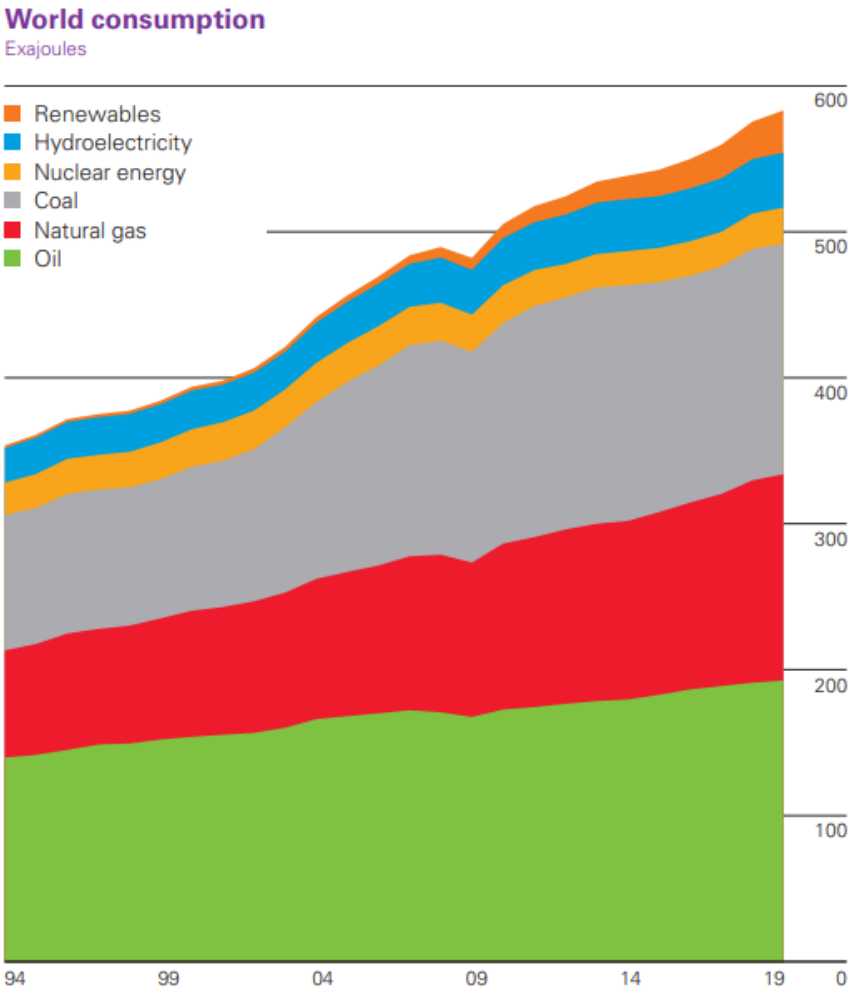

FIGURE 1.1: Breakdown of world energy consumption 1994-2019. Source: BP Statistical Review of World Energy 2020 [2].

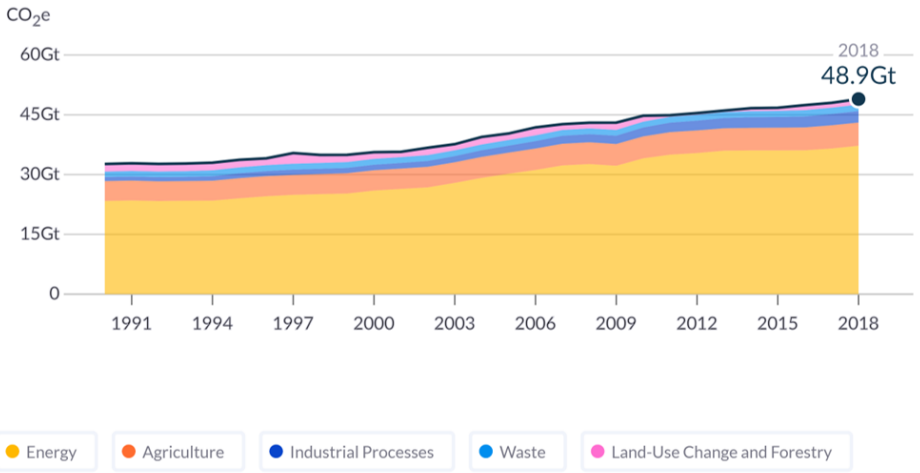

FIGURE 1.2: Breakdown of world greenhouse gas emissions 1990-2018. Source: Climate Watch [3]; CAIT dataset [6].

Hydrogen (H_2) has a promising future as both an energy carrier and fuel source. Hydrogen is a suitable alternative to fossil fuels as it is carbon free, leading to low (or zero) carbon based emissions when used as an energy source. Hydrogen also benefits from being renewable, abundant, easy to produce, not restricted to geographical formations, has many favourable combustion properties and has very high energy content by mass. However, for hydrogen to become a mainstream fuel for vehicles, power generation or industrial applications a number of problems need to be overcome. Current issues involve the needed improvement of production processes such that they are less reliant on non-renewable fuels, efficient and safe transport, advancement of storage technologies and improvement/optimisation of utilisation strategies [7].

There are two main ways in which hydrogen is currently used in vehicles, namely hydrogen fuel cell powered vehicles and hydrogen powered internal combustion engines (ICEs). Significant research and development has been carried out on hydrogen fuel cells where electrochemical reactions of hydrogen and an oxidiser are used to produce electricity which is then used to power the vehicle [8]. While fuel cell vehicles are likely the future in terms of near-zero emissions, production costs are prohibitive while also requiring very high purity hydrogen to prevent system degradation [9] and thus a bridging technology which can help improve infrastructure and drive down costs is required [10]. ICEs have the potential to achieve this goal as conversion of a conventional spark ignition (SI) or compression ignition (CI) engine to being fuelled by a gas such as hydrogen is relatively straightforwards and thus costs a fraction of a fuel cell vehicles current price of production while also not requiring as high a purity fuel [11]. Therefore, if hydrogen fuelled ICEs were to become an attractive option in terms of performance, emissions and price comparative to conventional ICEs, then any infrastructure developed would also facilitate an eventual transition to fuel cell vehicles.

CI engines fuelled by diesel play a vital role in many heavy-duty transport, power generation, agricultural and industrial applications due to the various benefits of CI engine combustion and its operating cycle. These benefits include superior torque, greater power output, higher thermal efficiency, better fuel economy and reliability when compared with SI engines [12]. Unfortunately however, diesel engines generally emit higher levels of harmful pollutant emissions such as NO_x, UHC, CO and soot. Utilisation of hydrogen in heavy duty CI engines can lead to a reduction in carbon-based emissions while maintaining or even improving performance [13, 14]. However, efficient utilisation is not a trivial task and thus improvements and optimisation of the various strategies used for hydrogen combustion in CI engines is required.

Generally utilisation of hydrogen in CI engines will require operation in a dual-fuel mode where a more reactive fuel such as diesel is used as a pilot fuel to ignite the high autoigniton temperature hydrogen fuel. The inherent complexity of dual-fuel engine design and operation in terms of both engine fuelling and combustion modes means that both experimental and numerical investigation is vital for gaining insights on the

various physical phenomena which occur such as the flow induced by fuel injection, ignition, flame propagation, heat release and formation of emissions. Computational fluid dynamic (CFD) modelling coupled with physics based modelling can be used to gain a greater understanding of macroscopic and microscopic phenomena which occur during engine operation which experimental investigation either cannot explore at all or only can with great care and difficulty. The likes of the flow field induced by fuel injection and combustion, mixture formation, the fuel ignition process, interactions of the fuel injections and flames with chamber walls and many other relevant parameters can all be investigated with relative ease. CFD also allows for operational strategies which may have otherwise been expensive or hard to implement experimentally to be explored with very little investment allowing for preliminary studies to be carried out which can guide any future experimental prototyping. Optimisation of engine operating parameters can also be carried out efficiently and at a fraction of the cost of experimentation allowing for better engine design and combustion processes which lead to improved performance and reduced pollutant emission outputs.

1.2 Aims and Objectives

The focus of this thesis is outlined as follows:

1.2.1 Aims

- To develop a CFD based modelling framework which can be applied to the study of high hydrogen energy share diesel-hydrogen dual-fuel combustion in internal combustion engines.
- To investigate novel combustion strategies for maximising hydrogen energy share during diesel-hydrogen dual-fuel combustion in internal combustion engines.
- To provide design guidelines for optimal combustion and fuel injection strategies in diesel-hydrogen dual-fuel CI engines which maximise performance and hydrogen energy share while minimising harmful pollutant emissions.

1.2.2 Objectives

- Develop a physics based gaseous direct injection model to simulate high pressure direct injection (HPDI) of gaseous fuels in internal combustion engines.
- Validate the developed gaseous direct injection model over a range of experimental conditions relevant to engine operation.

- Perform numerical simulations and evaluate a novel constant volume combustion phase strategy for high hydrogen energy share diesel-hydrogen dual-fuel CI engines.
- Perform numerical simulations and generate novel operational strategies for very high hydrogen energy share diesel-hydrogen dual direct injection CI engines.

1.3 Outline

The thesis is structured as follows: Chapter 2 gives the requisite background on hydrogen as a fuel and provides an in depth review of the literature on the various strategies used for hydrogen combustion in CI engines; Chapter 3 details the numerical and modelling approaches taken and presents the development of the modified gaseous sphere injection (GSI) discrete phase model for direct gaseous injections; Chapter 4 discusses the results of the modelling of a diesel engine and an intake induction diesel-hydrogen dual fuel engine incorporating a novel constant volume combustion phase strategy and its impact on performance and emissions; Chapter 5 details the comprehensive validation of the improved GSI model using experimental data for a range of applications including high pressure methane and hydrogen freestream jets, mixture formation in a direct injection hydrogen spark ignition engine and combustion in a diesel-natural gas dual direct injection engine; Chapter 6 presents the results of a parametric study on various injection and combustion strategies in a dual direct injection hydrogen-diesel CI engine using the previously developed discrete phase methodology and Chapter 7 summarises the thesis, provides conclusions and gives recommendations for future research directions.

1.4 Journal publications

1. C. J. Ramsay, K. K. J. Ranga Dinesh, W. Fairney, and N. Vaughan. "A Numerical Study of a Compression Ignition Engine Operating with Constant Volume Combustion Phase: Effects of Constant Volume Phase on Combustion Performance and Emissions". In: *Fuel* 280 (Nov. 15, 2020), p. 118657. ISSN: 0016-2361. DOI: 10.1016/j.fuel.2020.118657.

2. C. J. Ramsay, K. K. J. R. Dinesh, W. Fairney, and N. Vaughan. "A Numerical Study on the Effects of Constant Volume Combustion Phase on Performance and Emissions Characteristics of a Diesel-Hydrogen Dual-Fuel Engine". In: *International*

Journal of Hydrogen Energy 45.56 (Nov. 13, 2020), pp. 32598–32618. ISSN: 0360-3199. DOI: 10.1016/j.ijhydene.2020.09.021.

3. C. J. Ramsay and K. K. J. R. Dinesh. "High Pressure Direct Injection of Gaseous Fuels Using a Discrete Phase Methodology for Engine Simulations". In: *International Journal of Hydrogen Energy* (Nov. 18, 2021). ISSN: 0360-3199. DOI: 10.1016/j.ijhydene.2021.10.235.

4. C. J. Ramsay and K. K. J. Ranga Dinesh. "Numerical Investigation of Operational Strategies in a High Hydrogen Energy Share Diesel-Hydrogen Dual Direct Injection Engine" *(under preparation for submission to International Journal of Hydrogen Energy based on the results of Chapter 6)*

Chapter 2

Background and Literature Review of Hydrogen as a Fuel for Compression Ignition Internal Combustion Engines

This chapter provides the relevant background information on hydrogen as a fuel for vehicular use and reviews the current understanding and research trends for diesel-hydrogen dual-fuel combustion in compression ignition engines.

2.1 Hydrogen life cycle

The life cycle of hydrogen as a fuel can mostly be broken down into 4 key steps steps: production, storage, distribution and utilisation (Figure 2.1).

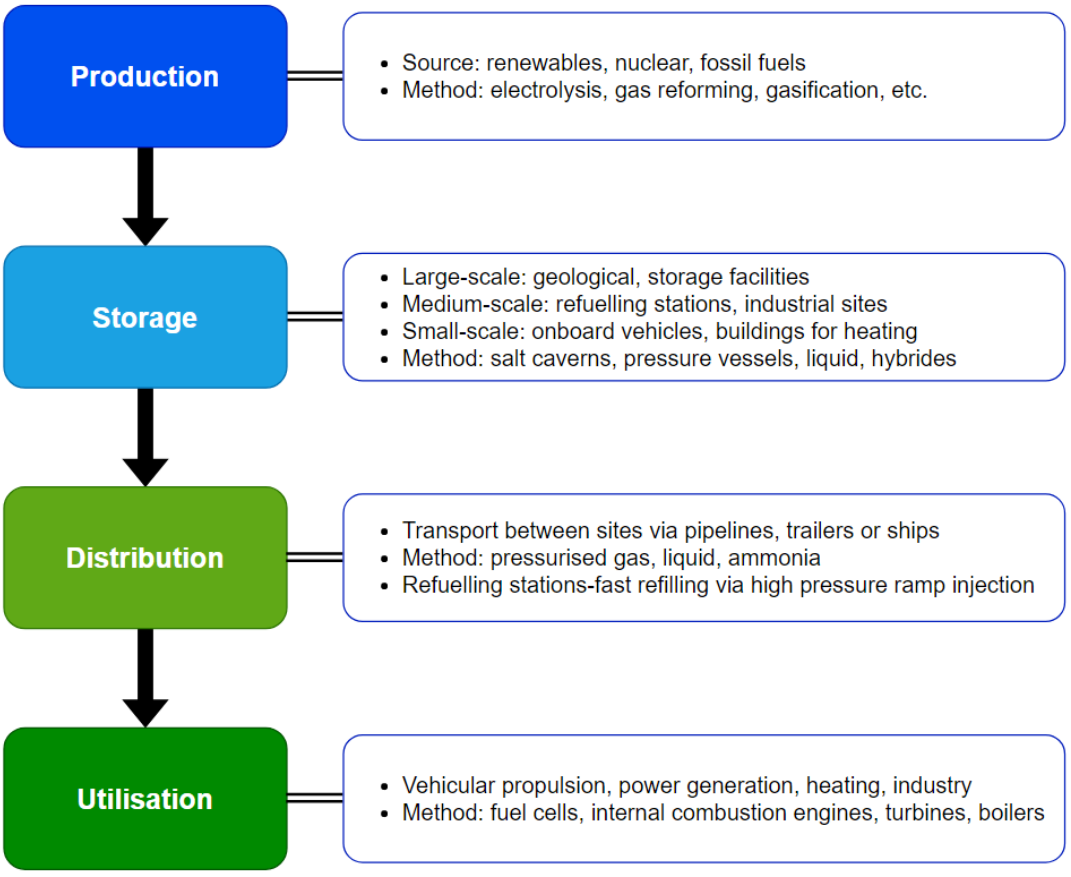

FIGURE 2.1: Hydrogen life cycle.

There are a number of ways in which hydrogen can be produced such as gas reforming, gasification, thermolysis, photoelectrochemical, electrolysis, etc. [18]. The end goal is to have all hydrogen produced by clean methods such as electrolysis using a renewable energy source, e.g. wind or solar [19–21], but currently the vast majority is produced using fossil fuels [18, 22] which works counter to the decarbonisation efforts which a transition to hydrogen is aiming for. Efficiency of renewable production processes need to be improved such that costs and production rates can rival and eventually beat those of fossil fuel based methods.

Storage, be that at large scale sites, at the filling station or onboard vehicles is another major hurdle in the hydrogen life cycle because of its low volumetric energy density, i.e. the amount of space required to store sufficient amounts is much higher than other fuels. This is a particularly difficult problem to solve in vehicles where range and space are major concerns and while this is somewhat offset by hydrogen's high gravimetric energy density it is still one of the major issues standing in the way of a transition to hydrogen. Figure 2.2 compares hydrogen's energy density with various other typical fuels. For the most part hydrogen storage onboard vehicles is limited to high pressure storage tanks at either 35 MPa or 70 MPa to allow for reasonable vehicle operating

range. Due to safety and weight concerns the tanks are generally made with strong composites reinforced with a metal (type III) or plastic liner (type IV) to avoid hydrogen embrittlement or are completely made out of composites (type V) [23, 24]. The tanks, however, are expensive while also taking up a large amount of space and the cost and safety concerns involved with compressing the hydrogen remain problematic. Other onboard storage methods such as cryogenic liquid or storage in chemical/metal hydrides are being developed but due to costs, low energy storage densities and/or safety concerns these technologies are currently outclassed by the more mature and simplistic high pressure storage tanks [25]. In terms of large scale and on-site hydrogen storage compression is still generally required albeit at a lower pressure as space isn't as big a concern and thus the likes of geological locations such as salt caverns or large pressure vessels tend to take precedence [26].

Transport of hydrogen from production sites to storage facilities and then to refuelling stations suffers from similar issues due to the low volumetric energy density and thus it proves difficult to move substantial amounts, by energy, in a cost effective manner. For the most part pressurised steel tube trailers are used for short distance transport, steel pipelines at lower pressure than trailers can service all distances given the necessary infrastructure is developed and liquid cryogenic transport using ships for long ranges and trailers for short-medium can also be used [27]. However, while liquid storage/-transport offers the greatest volumetric energy density, the costs involved in cooling the hydrogen to around the required 20 K is energy intensive and currently not financially feasible for most applications [28]. Steel is used as a storage medium for transport due to its relatively low cost and resistance to hydrogen embrittlement. [29].

Another area of active research which may help solve some of the production, storage and transport issues is hydrogen storage in ammonia [30]. Ammonia has a much higher volumetric energy density than hydrogen and can be stored at much lower pressures in liquid form as ammonia boils at 240 K; 220 K higher than hydrogen's boiling temperature. It can then either be utilised directly or decomposed into hydrogen depending on the use case. Ammonia also benefits from having a well developed infrastructure in terms of production, transport and storage due to its wide spread use as a fertilizer and doesn't produce carbon monoxide during decomposition to hydrogen [31]. Given the processes used during decomposition can be improved and made more efficient to drive down costs ammonia has the potential to aid in the development of a working hydrogen infrastructure.

Refuelling high pressure storage tanks onboard vehicles also offers some problems due to safety concerns which generally stem from needing to keep filling times to a level close to that of a standard diesel or gasoline vehicle. Current regulations and targets set by safety and standards agencies state that tank gas temperatures must always be above 233 K and below 358 K and take roughly 180 s to reach a state of charge greater than 95% [32]. This requires a good understanding of the effect that the buoyant impinging

hydrogen jet and compression process has on tank temperature distributions as well as the heat transfer through the tank walls - further research is still required in this area [23]. The decompression and cooling process which occurs when fuel is used may also lead to the temperatures falling below the lower limit and thus also needs to be investigated [33]. While improvement and optimisation of the refuelling process is required, the building of more refuelling stations themselves is likely a larger issue as they are a key component of the infrastructure required for a working hydrogen economy.

Clearly a well implemented fuelling network which accounts for the previously discussed factors needs to be developed but this will only be achieved if costs are reduced and hydrogen adoption increases [18].

Utilisation is the final step in hydrogen's life cycle and is one of the main ways in which hydrogen adoption may be increased. If understanding and implementation of utilisation strategies improves then so will pollution reduction and performance leading to a higher likelihood of adoption as the value of the technology increases. As discussed in Section 1.1 hydrogen for vehicular use is generally employed in fuel cells which use electrochemical reactions or through combustion in internal combustion engines with the latter being the focus of this thesis.

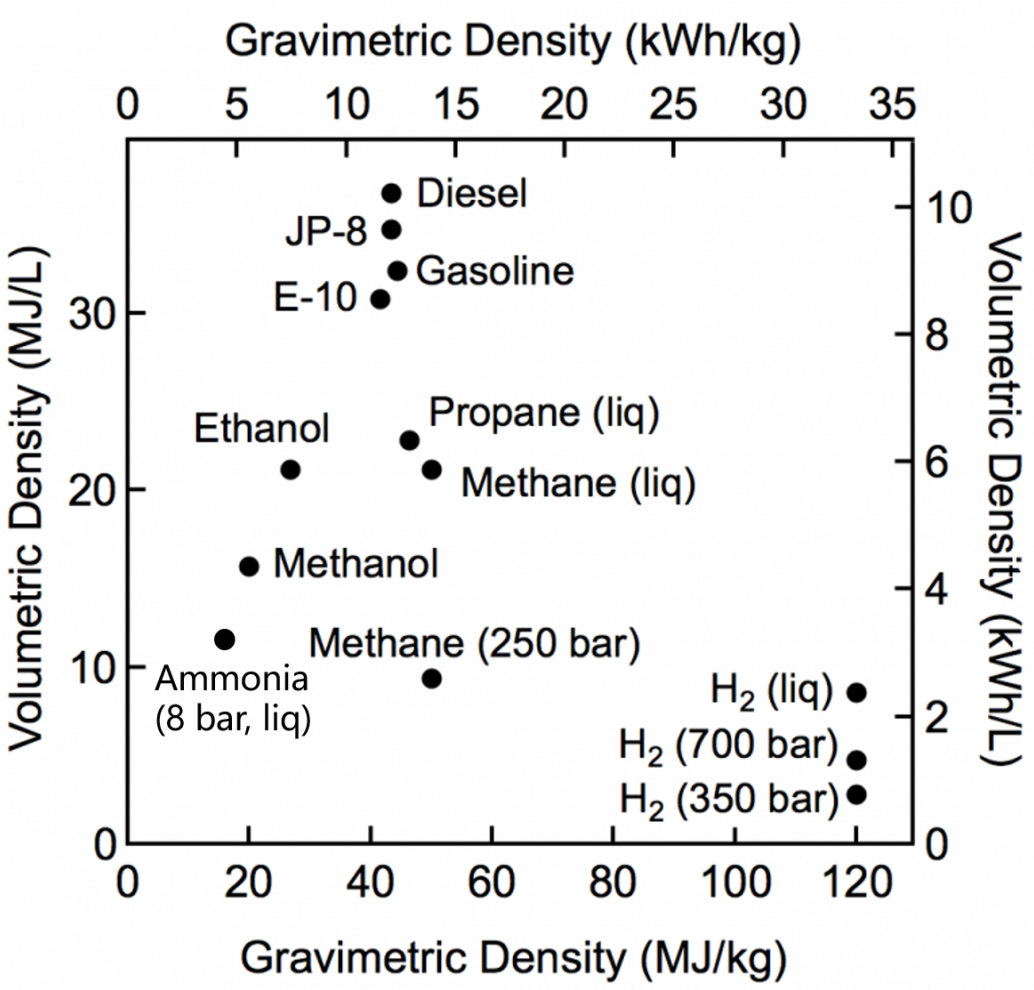

FIGURE 2.2: Comparison of volumetric and gravimetric density for various fuels. Source: US Department of Energy [34]

2.2 Hydrogen fuel properties

TABLE 2.1: Properties of hydrogen, methane, gasoline, diesel, n-heptane and ammonia [12, 35–42] (diesel and gasoline are generally blended fuels so properties will vary from those listed).

Properties	Hydrogen	Methane	Gasoline	Diesel	n-Heptane	Ammonia
Chemical formula	H_2	CH_4	C_nH_2n	C_nH_{2n}	nC_7H_{16}	NH_3
Molecular weight (g/mol)	2.016	16.043	107	170	100.16	17.031
Density(kg/m^3)	0.08	0.65	750	840	692	0.73
Mass diffusivity in air (cm^2/s)	0.61	0.16	-	-	-	0.23
Flammability limits in air (vol%)	4-75	5-15	1-7.6	0.7-7.5	1.05-6.7	15-28
Burning velocity (m/s)	2.65-3.25	0.37-0.43	0.45	0.3	0.2-0.6	0.07
Quenching distance (mm)	0.61	2.00	2.00	-	-	8.95
Autoignition temperature (K)	858	813	523	483	479	930
Minimum ignition energy (mJ)	0.02	0.28	0.24	0.24	0.24	8
Adiabatic flame temperature (K)	2390	2226	2275	2275	2275	2080
Stochiometric air/fuel ratio by mass	34.3	17.2	14.5	14.5	15.1	6.1
Lower heating value (MJ/kg)	120	50	43.4	42.6	44.6	18.6

Hydrogen's properties are much different compared to other typical engine fuels such as diesel, gasoline and methane. Table 2.1 shows the differences for most relevant combustion and physical properties for hydrogen and other conventional fuels.

Hydrogen has a very low density due to its small molecular weight, which as noted previously means that even though its energy density by mass (lower heating value of 120 MJ/kg) is much higher than most fuels its energy density by volume, even at high pressures, is also much lower than most (Figure 2.2). Hydrogen's high gravimetric energy density does however mean that the time taken to supply an engine with a given quantity of hydrogen fuel energy during operation is somewhat comparable to the likes of methane.

Hydrogen has a remarkably wide flammability limit which means very lean mixtures with fuel-air equivalence ratios as low as 0.1 and as high as 7.1 will burn which should allow for hydrogen usage at many engine operating points without loss of performance. The lower flammability limit of hydrogen is particularly useful when targeting low NO_x emissions in premixed hydrogen-air operation as use of a lean fuel-air mix is possible without impacting performance, given an adequate ignition source, and can help to control temperatures. In non-premixed combustion modes the high mass diffusivity and wide flammability limit lead to high rates of heat release due to the high rate of mixing of fuel with oxidiser and less mixing being required in general for combustion to occur. The burning velocity of hydrogen is also much higher than other conventional fuels ($\approx$ 6-10 times greater) which leads to a much more rapid combustion rate during premixed combustion and also likely contributes to the higher rates of

combustion during non-premixed/stratified operation. In partially premixed combustion modes where the injection event increases turbulence in the chamber the laminar flame speed will also increase and enhance the combustion rate further. The lower quenching distance of hydrogen also allows both non-premixed and premixed flames to burn closer to chamber walls without extinguishing which will increase combustion efficiency in wall bounded flows such as those in an engines combustion chamber.

The minimum ignition energy of hydrogen is greater than 10 times less than the likes of gasoline and methane meaning much leaner mixtures can be used in premixed operation. Similarly, pilot diesel ignited direct injection hydrogen engines targeting non-premixed operation should benefit from the low minimum ignition energy as a smaller volume pilot injection should be sufficient for ignition, compared to methane for example, leading to potentially greater hydrogen substitution rates. A low minimum ignition energy means that hot spots within the chamber are more likely to cause premature combustion or flashback/backfire in premixed operation and is one of the major issues which needs to be addressed for intake manifold/port inducted dual-fuel or early compression stroke direct injection operation. These issues are largely avoided when late direct hydrogen injections are used.

The high autoignition temperature of hydrogen means combustion in dual-fuel CI engines can generally only be achieved by use of another low autoignition fuel such as diesel as an ignition source [13]. Compared to methane, hydrogen's higher autoignition temperature could lead to difficulties with fully igniting the non-premixed jet if a reduced pilot diesel injection doesn't provide sufficient energy for ignition during dual direct injection operation. Or may simply offset any gains in hydrogen substitution level which minimum ignition energy indicates is possible. Similar problems may be apparent in premixed operation where a reduced pilot injection may struggle to cause flame propagation and then also be unable to cause autoignition of any of the surrounding mixture which can sometimes aid in the onset of full mixture ignition.

For the most part the literature [43, 44] shows that at engine relevant conditions (higher pressures) reactivity of hydrogen is largely controlled by the pressure dependant reaction

$$H_2O_2(+M) \leftrightarrow OH + OH(+M), \tag{2.1}$$

while ignition delay is heavily influenced by the reaction of hydrogen with HO_2

$$H_2 + HO_2 \leftrightarrow H_2O_2. \tag{2.2}$$

Most other fuels show a similar link between ignition delay and their reaction with HO_2.

2.3 Diesel-hydrogen dual-fuel compression ignition engines

The principle operation of a dual-fuel engine is based on using two different types of fuel: the first is used as an ignition source and the second one a source of energy [13, 45, 46]. This two fuel system is required due to the high autoignition temperature of hydrogen (and other gaseous fuels such as methane/natural gas) and thus a lower autoignition temperature pilot fuel is required. It should be noted that single gaseous fuel solutions using SI or glow plugs have been researched extensively but they generally require lower compression ratios, and thus power outputs, to reduce the likelihood of unstable combustion [47–49]. The present study focuses on dual-fuel combustion concepts in CI engines using pilot diesel injections to ignite either a well-mixed hydrogen-air charge which is generated through intake induction of the hydrogen fuel leading to premixed combustion or a hydrogen jet which is generated through HPDI of the hydrogen fuel into the combustion chamber close to top dead center (TDC) leading to mostly non-premixed combustion.

2.3.1 Engine combustion process

Understanding the combustion process is essential for improving engine performance and reducing pollutant outputs. Figure 2.3 compares the two dual-fuel CI engine operational modes with pure diesel operation.

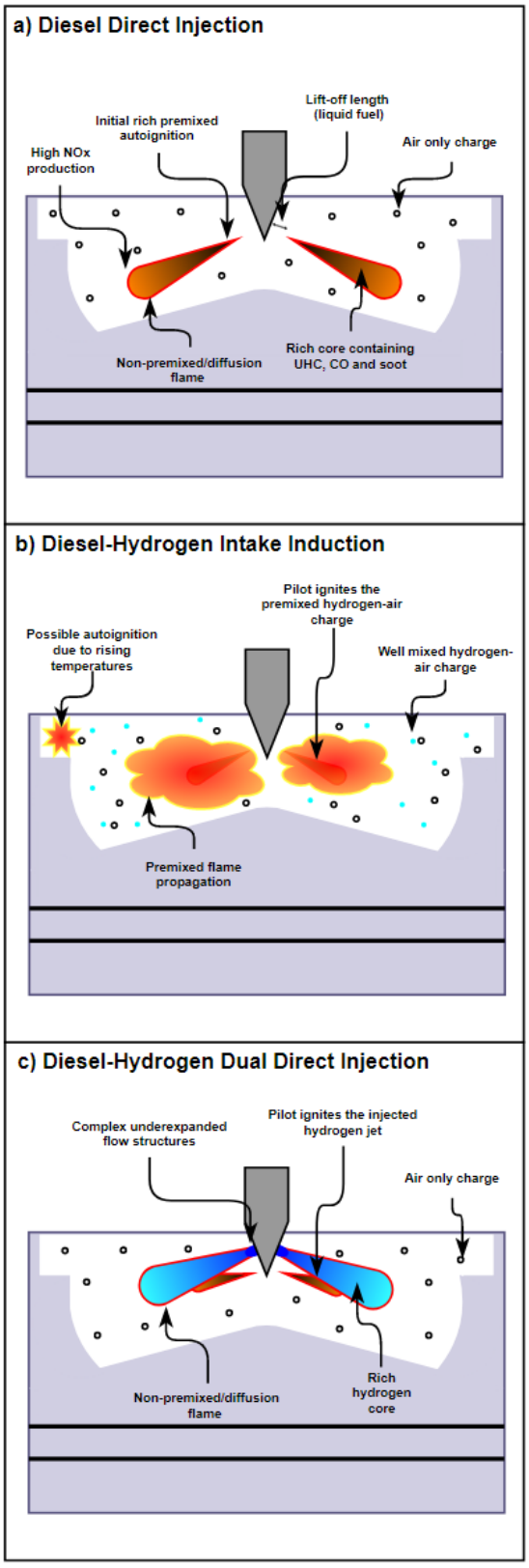

FIGURE 2.3: Schematic representation of the combustion processes in a) diesel direct injection, b) diesel-hydrogen intake induction and c) diesel-hydrogen dual direct injection operational modes.

2.3.1.1 Diesel single-fuel - non-premixed combustion

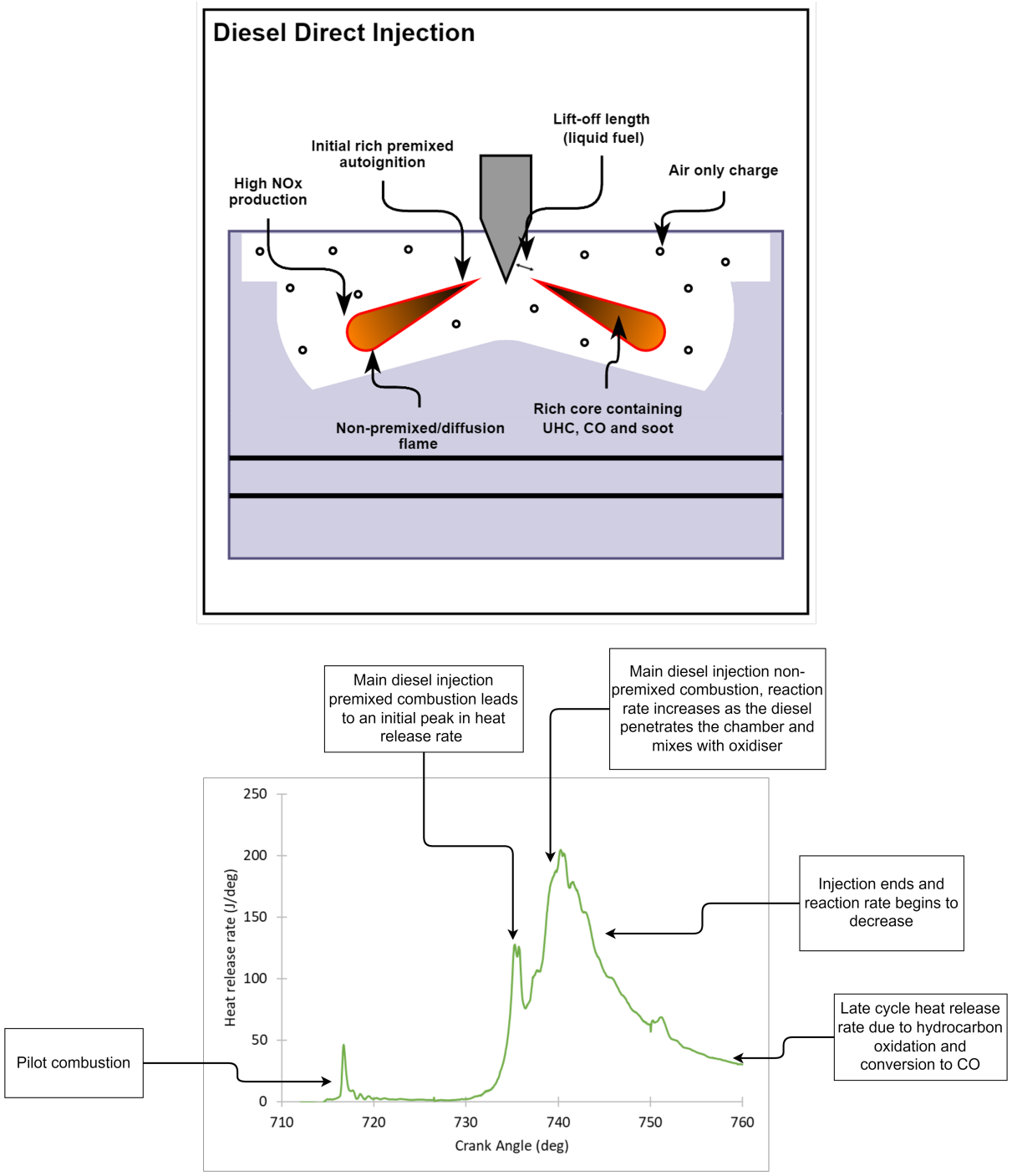

FIGURE 2.4: Example combustion process in a conventional diesel compression ignition engine (720°CA is TDC).

The non-premixed combustion process of diesel in a compression ignition engine is well understood, Figure 2.4 depicts some of the key processes. Many factors impact the diesel combustion process, including but not limited to: in-cylinder temperature, pressure and oxygen levels as well as spray parameters such as injection pressure, timing,

duration, injected fuel temperature, injector geometry (hole diameter, barrel length-/width, number of injectors, orientation, etc.) and engine geometry can also play a large role due to the liquid spray droplets, vapourised gas jet and flames interaction with the chamber walls [12].

Liquid diesel fuel is generally injected into the combustion chamber at a high velocity through a small nozzle close to TDC which causes atomisation of the fuel into small droplets which penetrate the chamber [50]. These droplets then gain heat from the warmer bulk gases and once surpassing a given temperature threshold vapourise and mix with the surrounding air. Diesel continues to mix with the hot compressed air until the compression process raises in-cylinder temperatures to a level above the autoignition temperature of the fuel. The ignition delay period (time between start of injection and ignition) ends at this point and the premixed diesel-air charge which has formed ignites and begins to rapidly combust. This process leads to a large spike in heat release and in-cylinder pressure which raises in-cylinder temperatures further. This is then followed by the non-premixed combustion phase where combustion rate is now controlled by the rate at which fuel and oxidiser can mix and is indicated by a fall off from the peak heat release rate (HRR) achieved during the premixed combustion phase to a moderate level. Often a secondary smaller peak in heat release rate is observed as the diesel injection continues and promotes further mixing of fuel and oxidiser. Finally the late-cycle combustion phase begins and is signalled by the end of the diesel injection and thus heat release rate falls off to a low level for the remainder of the power stroke until exhaust valve open (EVO). During this phase oxygen in the excess air which was not involved in the earlier combustion aids in the oxidation of carbon monoxide and remaining unburned hydrocarbons. Throughout the entire process combustion occurs across a wide range of fuel lean and fuel rich conditions leading to varying levels of combustion efficiency [12].

CO and UHC emissions are the result of incomplete combustion which tends to occur during fuel rich combustion. Initial production of *CO* and UHC occurs during the early rich premixed combustion close to the injector during diesel operation [51]. Diffusion of the rich premixed combustion products into the non-premixed flame allows for their conversion to CO_2. However, quenching of the flame at chamber walls tends to lead to an accumulation of the incomplete combustion products along the relatively cool walls. After the injection finishes, excess air in the chamber oxidises UHC and CO throughout the power stroke until EVO but if mixing isn't sufficient and high carbon areas form without enough oxidiser *CO* and UHC emissions will increase. Higher chamber temperatures tend to reduce these carbon emissions due to a speed up in the combustion rate and thus faster completion of the full transition of hydrocarbons to CO_2 but high temperatures generally come at the cost of greater NO_x emissions [52]. UHCs can also be absorbed by lubricating oils or get caught in crevices causing increased emission [53].

Soot emissions are due to locally rich carbon areas where excess air is not present to oxidise UHCs and temperatures are generally lower due to a lack of, or poor, combustion leading to increased soot formation rates and growth [12]. Soot inception generally begins in the rich core of the jet due to the initial rich premixed combustion which occurs close to the injector. The small particles which are initially produced grow as they stay within the high carbon jet core leading to much larger particles at the head of the jet [54]. Soot levels are controlled through their diffusion (and UHCs) into the non-premixed flame and proceeding oxidation. At the end of a cycle the highest concentration soot areas tend to be close to the injector due to the rich premixed combustion and also along the piston bowl walls due to quenching of the flame and thus reduction in soot oxidation and pooling of UHCs [55].

NO_x emissions are generally higher than in SI engines due to the higher in-cylinder temperatures and increased oxidiser levels which occur in CI engines [12]. Load in an SI engine is controlled by intake reduction (less oxidiser) which often further decreases due to fuel displacement, whereas CI engines control load via turbocharging (more oxidiser) and quantity of fuel injected. This leads to an increase in excess air which is essential for NO_x production as clearly oxygen is required. SI engines also generally operate at lean fuel-air equivalence ratios which reduces temperatures, whereas during diesel operation combustion often occurs at much less lean conditions. Diffusion flames generally occur at high temperatures and thus are ideal for NO_x production due to the thermal Zeldovich mechanism [56]. Combustion in the high temperature non-premixed diffusion flame takes place at close to stoichiometric fuel/air ratio which is ideal for NO_x formation (production greatest at roughly 0.9 equivalence ratio) [39]. Any attempt to reduce NO_x emissions generally involves reducing temperatures but this is often met with an increase in carbon emissions and performance reductions, or lower control over combustion, so trade offs need to be made [57].

2.3.1.2 Diesel-hydrogen dual-fuel with hydrogen intake manifold induction - hybrid non-premixed and premixed combustion

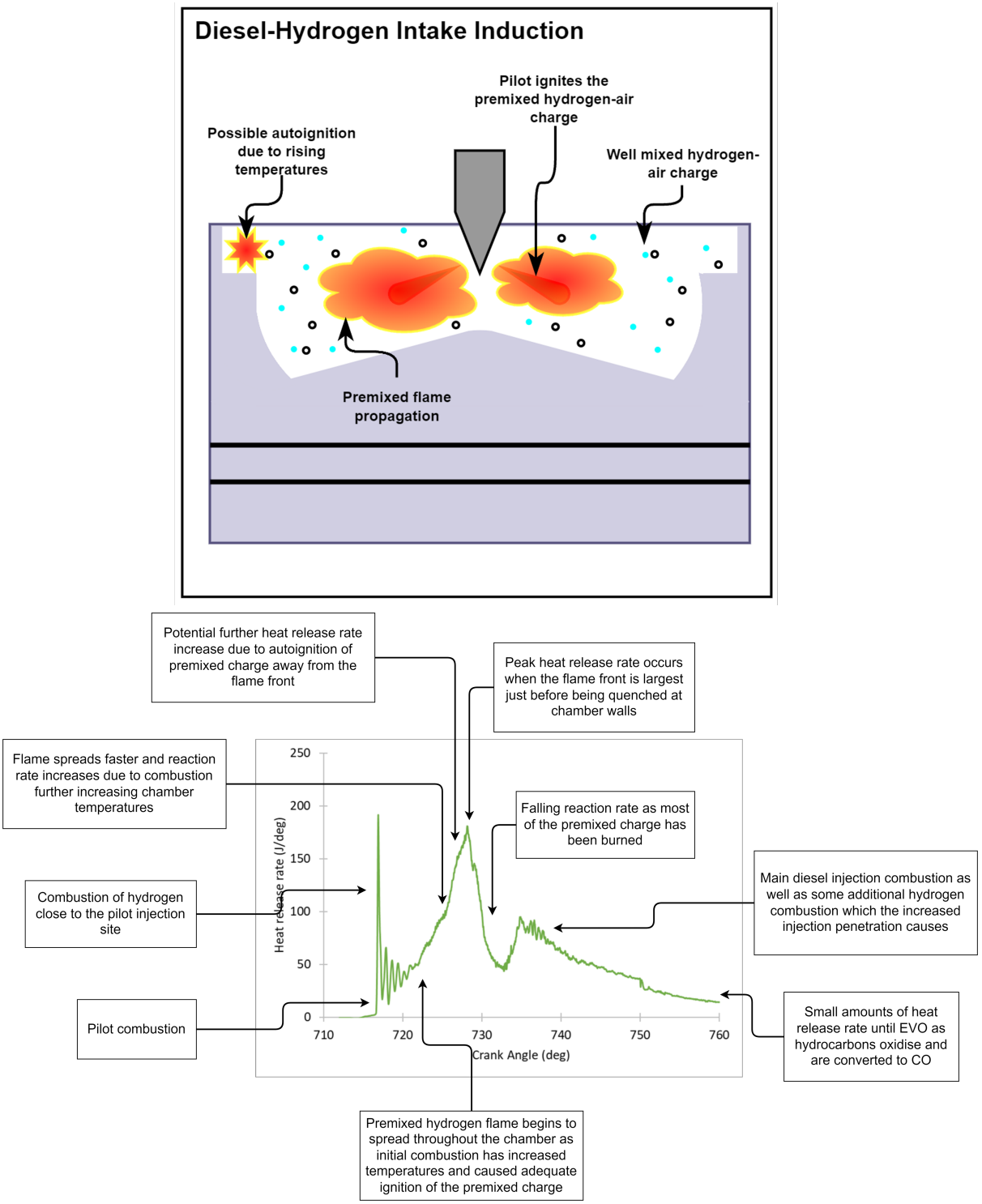

FIGURE 2.5: Example combustion process in a dual-fuel compression ignition engine with intake manifold hydrogen induction and diesel pilot (720°CA is TDC).

Figure 2.5 provides an overview of the ignition and combustion process in an intake induction diesel-hydrogen dual-fuel engine. The pilot diesel combustion in an intake inducted hydrogen-diesel dual-fuel engine tends to follow a similar process to the conventional engine with some key differences. The total volume of the diesel pilot is reduced comparative to pure diesel operation which normally causes a reduction in penetration which can lead to a longer ignition delay. This is compounded by the reduction in oxidiser concentration, resulting from air displacement by the hydrogen injected during intake, leading to further ignition delay increase. These factors however, are often counteracted by the very low minimum ignition energy of hydrogen which becomes entrained in the diesel jet as it penetrates the chamber leading to a speed up in the initial rate of combustion when the pilot first ignites [58]. The hydrogen which is entrained in the jet also causes a higher peak heat release rate in the pilots premixed combustion phase as both the diesel and small amounts of hydrogen surrounding the injection site combust. Both of these behaviours are enhanced as equivalence ratio of the hydrogen-air mix increases [59]. As the diesel combustion continues into the non-premixed combustion phase the rising temperatures due to the pilot combustion begins the ignition of a sufficient amount of the hydrogen-air mix causing a premixed flame to spread from the injection site towards the peripheries of the chamber. Due to hydrogen's high burning velocity the flame spreading is rapid and leads to a second peak in heat release rate. At this point, depending on the likes of combustion efficiency and equivalence ratio, the increased chamber temperatures due to combustion can start the autoignition of parts of the hydrogen-air mix away from the flame front leading to an even higher HRR peak [58, 60] (can be called knocking, but is referred to as "wholesale ignition" in this thesis). Finally, the majority of the premixed hydrogen-air charge is burned and the premixed flame reaches the chamber walls and quenches leading to a fast fall off in heat release rate. Since hydrogen also doesn't have a long chemical breakdown pathway there is generally far less heat release in the late power stroke when compared to pure diesel operation as oxidation of hydrocarbons and CO is limited to the diesel pilot region.

2.3.1.3 Diesel-hydrogen dual-fuel with high pressure direct injection of hydrogen - non-premixed combustion

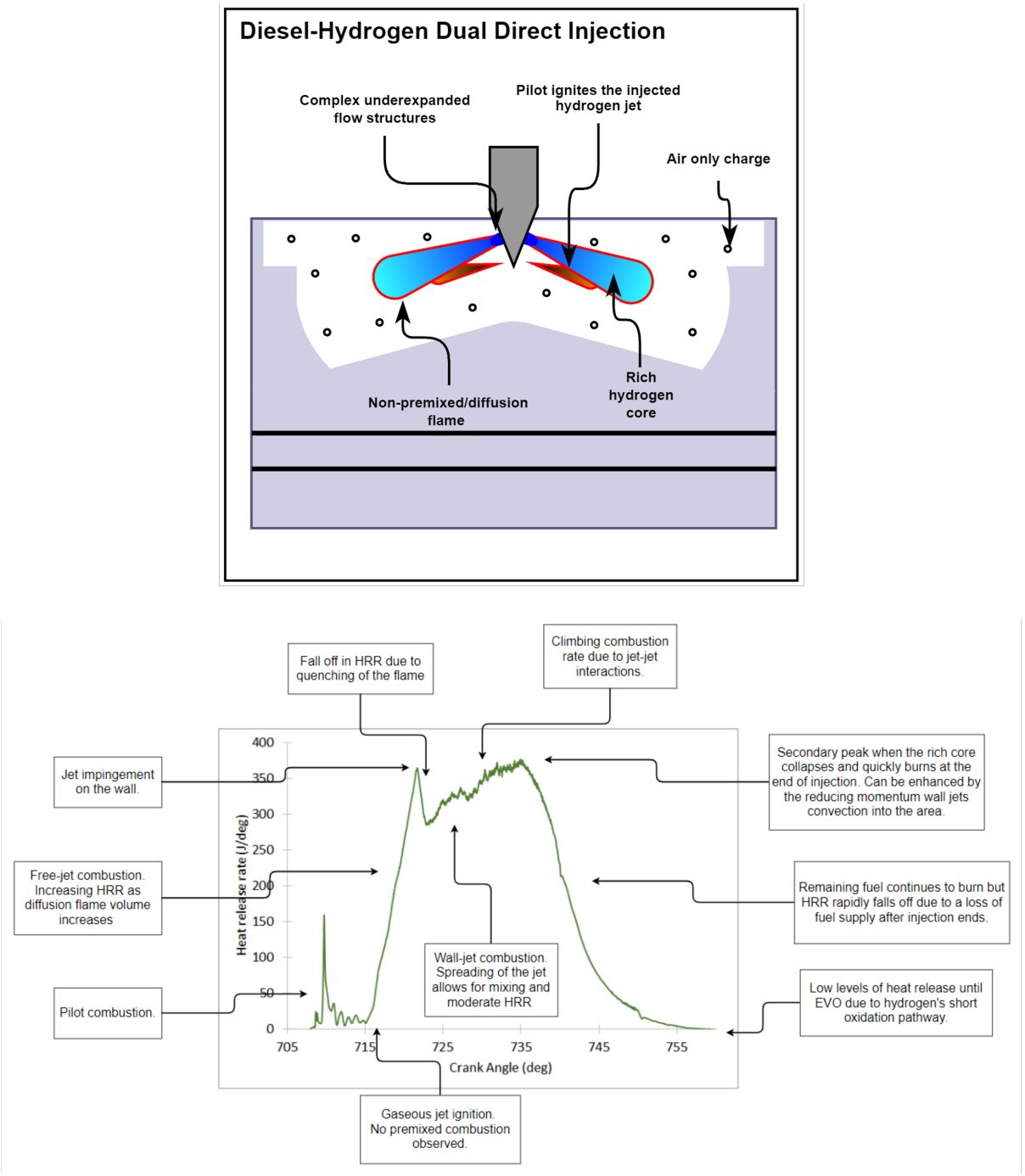

FIGURE 2.6: Example combustion process in a dual direct injection hydrogen-diesel dual-fuel compression ignition engine (720°CA is TDC).

Studies on dual direct injection diesel-hydrogen engines aiming for non-premixed combustion are scarce so the processes at work are not fully mapped out. However, using the work of this thesis, Chapter 6, and the few recent studies which are available in the

literature [61, 62] the general combustion process is broken down in Figure 2.6. Much like single fuel diesel combustion no other fuels are present in the chamber when the pilot diesel ignition occurs so the only difference between the two is the reduced injection volume and thus potential increase in ignition delay. Generally the diesel injection will have ended when the gaseous injection begins but there will still be small amounts of heat release. The diesel combustion will have created a high temperature region in the vicinity of the injected hydrogen jets trajectory and the hot combustion products should act as an ignition source and begin the combustion of the gaseous jet. The ignition delay phase of the gaseous injection will be short due to hydrogen's low minimum ignition energy combined with the underexpanded flow structures which form close to the injector limiting air entrainment. This means the levels of premixed combustion which occur should also be small given the pilot diesel injection managed to increase local temperatures adequately. Therefore, in a dual direct injection engine a greater amount of the heat release will be dominated by non-premixed combustion compared to even single fuel diesel combustion. Non-premixed free jet combustion occurs as the hydrogen jet penetrates the chamber, propagating the non-premixed flame which surrounds the rich core of the jet, and is limited by the rate at which penetration and thus mixing of fuel and oxidiser occurs as well as the rate of diffusion of fuel away from the rich core and into the high temperature flame. A peak in HRR will be present just before impingement of the jet on the chamber wall. The peak HRR value is determined by the maximum volume of the non-premixed flame, which for hydrogen will be large due to its wide flammability limits. Upon the jets contact with the wall part of the non-premixed flame is quenched leading to a reduction in flame volume from the peak achieved prior to impact causing HRR to fall off as fuel begins to accumulate in the piston bowl. This begins the wall jet combustion phase in which the impinging jets momentum will push the fuel in all directions along the piston wall; up towards the chamber roof/liner, into the piston bowl and back towards the injectors and laterally towards other sectors of the chamber. The flame will begin to propagate in these directions as hydrogen mixes with oxidiser leading to a levelling off in HRR at a moderate level. At this point interaction with other jets in multi-hole arrangements is possible and will lead to a slow down in the lateral spreading and potentially reaction rate as the jets collide, followed by their momentum combining and aiding the spreading of the flame back towards the injector region, enhancing the combustion rate as mixing increases. Finally, the gaseous injection will end, leading to the fast burning of the remaining fuel along the trajectory of the injection as the rich core deteriorates and eventually collapses. The reducing momentum of the jets traversing the walls can also lead to their convection into the same region, further increasing the combustion rate. This is followed by a rapid fall off in heat release rate to minimal levels until EVO as hydrogen has a short and fast breakdown pathway and there is relatively little UHC/CO oxidation occurring as the pilot injection was small.

2.3.2 Engine fueling requirements

From a fuel delivery perspective the two main requirements of an injection system are [63]:

1. To reliably deliver the correct amount of fuel within a given cycles operating window, forming the desired mixture, e.g. between inlet valve open (IVO) and inlet valve close (IVC) in intake induction or within a given number of crank angles around TDC during non-premixed HPDI.
2. Be affordable with a reasonable operating lifetime.

Due to the high pressure required, the injection process generally leads to choked flow through the nozzle and the development of underexpanded gas jets. The following analysis assumes isentropic choked flow of an ideal gas through a straight or converging nozzle where mass flow rate, $\dot{m}_{theory}$, can be calculated using

$$\dot{m}_{theory} = A_e P_0 \sqrt{\frac{\gamma}{T_0 R_I}} \left(\frac{\gamma + 1}{2} \right)^{\frac{\gamma+1}{2(1-\gamma)}}, \tag{2.3}$$

where A_e is the area of the nozzle exit, P_0 is the pressure upstream of the nozzle, T_0 is the temperature upstream of the nozzle, γ is the ratio of specific heats of the injected gas and R_I is the individual gas constant of the injected gas.

It's also worth noting that real-world injection durations will be somewhat longer than those calculated due to the various loses in the injector which reduce mass flow rate as well as injector opening and closing transients, but for the purposes of this analysis the theoretical value should be sufficient. Underexpanded gas jets are described in more detail in Section 3.5.2.

The injection window for a given engine is inversely proportional to engine speed which becomes increasingly more important as RPM or load (more fuel needed) increases. Figure 2.7 compares some example injection durations at differing engine speeds. Clearly engine speed is a much bigger factor during HPDI where in the most extreme case of a 20°CA window, injection duration reduces from 6.7 ms at 500 RPM to 1.3 ms at 2500 RPM.

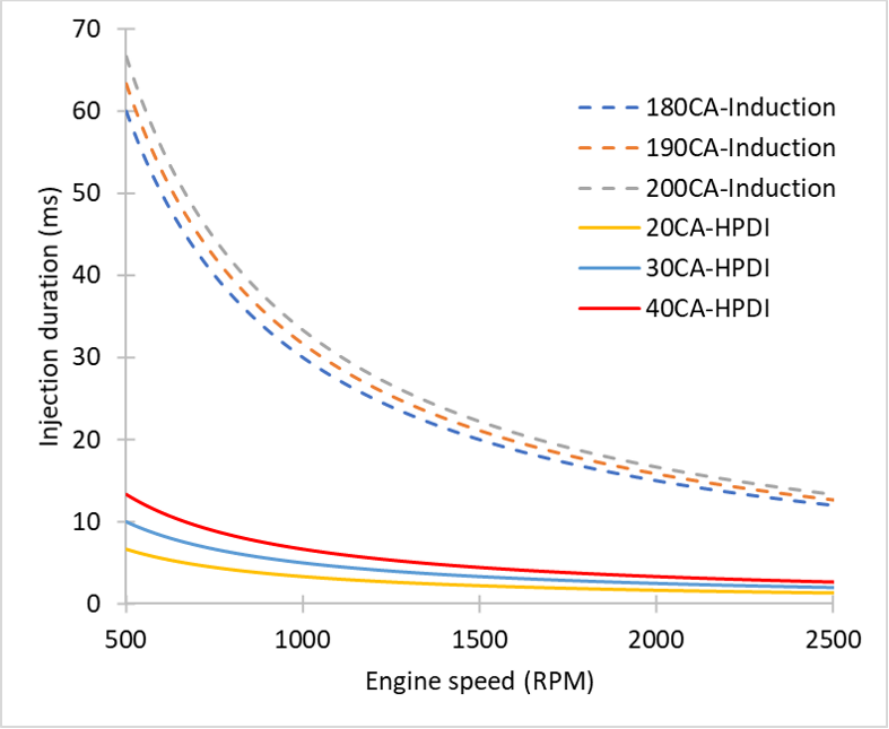

FIGURE 2.7: Example injection duration windows at typical heavy duty compression ignition engine speed ranges for intake induction and HPDI operation.

This short window is of particular importance when dealing with gaseous fuels such as methane and especially hydrogen as their densities are much lower compared to liquid fuels like gasoline and diesel. This means that larger injector orifices compared to liquid fuel injectors, high injection pressures and likely increased injection durations are required to deliver the requisite mass of fuel within the injection window. These requirements lead to a number of issues such as increased energy usage for an additional compressor to allow for the high gas pressures at injection, insufficient time for injecting the desired fuel mass, sealing/delivery issues and a lack of the lubricating effects which liquid fuels offer [63].

While hydrogen's low density means that mass flow rate is lower than the likes of methane its high energy content by mass means that at equivalent injection conditions hydrogen's energy flow rate is only roughly 13% less than methane's. This makes it easier than it may initially seem to supply an adequate quantity of hydrogen by energy in a given injection window. Figure 2.8 a) compares the mass flow rate and b) required injection duration to deliver 1250 J of hydrogen fuel energy over injection pressures and nozzle diameters expected for HPDI operation using a constant injection temperature of 300 K. Delivery of 1250 J (10.04 mg) of hydrogen is chosen as it matches the amount of fuel (by energy) required per injector in the HPDI engine studies carried out in Chapters 5 and 6 which is also a fairly large engine and thus represents a case which should be "difficult" to adequately supply. Mass flow rate scales proportionally with injection pressure and with the square of the nozzle exit diameter. Figure 2.8 b) clearly

shows that given a large enough nozzle diameter is used that injection pressures of 10-50 MPa are more than adequate to meet the previously referenced worst-case scenario of a 1.3 ms injection duration (2500 RPM and 20°CA injection window). As CI engines will often operate at in-cylinder pressures around 10-20 MPa, injection pressures of at minimum 20 MPa and ideally 40+ MPa should be targeted to ensure choked flow and smooth metering which indicates injector diameters of 0.5-0.8 mm should be adequate.

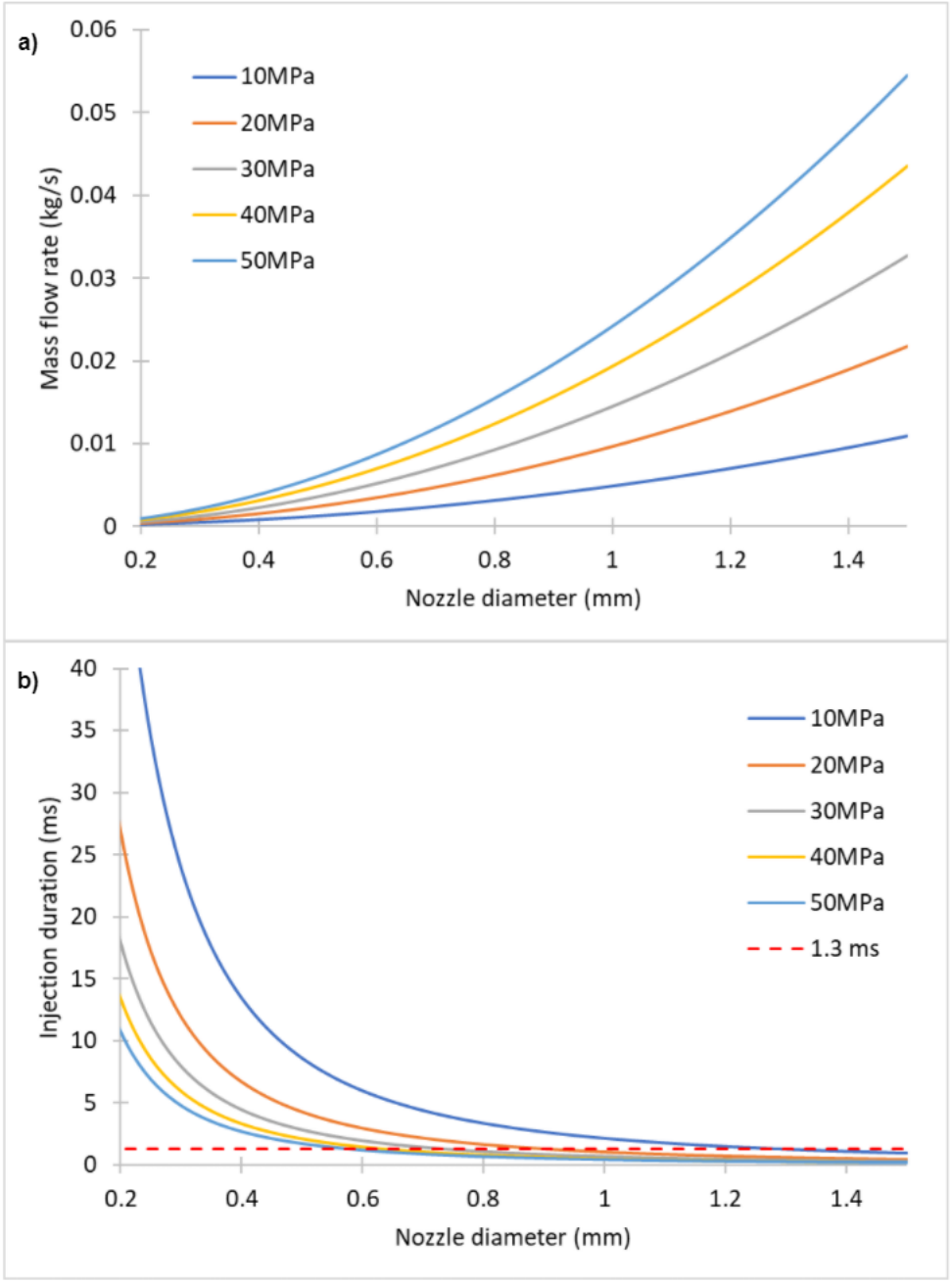

FIGURE 2.8: Comparisons of varying injection pressure and nozzle diameter on a) theoretical isentropic choked mass flow rate and b) injection duration required to supply 1250 J (10.04 mg) of hydrogen.

Cost of a gaseous fuel injection system will generally be greater than that of a conventional diesel injection system due to various manufacturing requirements, e.g. tight tolerances required to avoid leakage, difficulties in delivering precise fuel quantities, the possibility of requiring both liquid and gaseous injectors, as well as the technology's lesser maturity and thus less well developed manufacturing process and general design [64]. However, compared to fuel cells the cost is much reduced while not requiring extremely pure hydrogen during usage [10, 65].

2.3.3 Engine operational characteristics

A large number of experimental and numerical investigations have looked into the various issues relevant to the design and operation of diesel-hydrogen dual-fuel engines. Some of the key issues addressed in the literature include diesel-hydrogen dual-fuel combustion efficiency and performance [13, 58, 66–68], exhaust emission analysis [69–72], different engine geometries and engine conditions [73, 74] and hydrogen gas injection strategies [14, 62, 67, 75].

2.3.3.1 Hydrogen intake manifold induction

The findings in the literature indicate a reduction in soot, UHC, CO and CO_2 emissions comparative to the pure diesel operation as hydrogen energy share (HES) increases due to the inherent reduction in carbon within the chamber [58, 69]. At medium-high loads HES increase was shown to speed up the rate of combustion significantly and potentially lead to knocking/extreme pressure rise rates as well as a retardation of the start of combustion when compared to pure diesel operation but given the correct conditions can lead to increases in performance [13, 68, 73]. Although utilising hydrogen in CI engines demonstrated significant benefits to the performance and carbon-based emissions, several issues still pose significant challenges to operate the engine at higher HESs. For example, recent investigations [59, 76] reported that engine performance generally deteriorates at low load (LL) operating conditions once a certain HES threshold is met due to poor ignition of the hydrogen-air mix by the reduced diesel injection and leaner hydrogen-air mixture relative to higher load conditions. This issue can cause increases to UHC, soot and unburned hydrogen emissions. The LL problem requires more attention as only two studies have focused on addressing the issue by using high rates of exhaust gas recirculation (EGR) and diesel fuel injection optimisation [59, 76]. The literature also reported higher NO_x levels at high HESs for medium-high engine loads due to the higher burning temperature and chamber wide combustion of the well-mixed hydrogen fuel which can both combust via spreading of the premixed flame but also due to autoignition as temperatures rise all of which leads to high pressure rise

rates and limits the HES which can be used [58, 70, 71, 77, 78]. Nevertheless, several studies have addressed the increased NO_x problem at high and medium loads via low temperature combustion (LTC) strategies [79] such as EGR [72], combinations of reductions in compression ratio and water injections [80] and use of the likes of homogeneous charge compression ignition (HCCI) [81], premixed charge compression ignition (PCCI) [72] and reactivity controlled compression ignition (RCCI) [82]. While LTC is clearly beneficial to NO_x emissions the likes of EGR, water injection and compression ratio reduction can lead to reduced performance and increases to soot and UHC emissions and HCCI/RCCI/PCCI struggle with controlling combustion, and therefore performance and emissions, due to the reliance on auto-ignition timing and this can be especially problematic as load and engine speed are varied [13, 73, 83]. Backfire is also a major problem when dealing with intake induction as the inlet valve is open during fuel injection and hydrogen's low minimum ignition energy makes it susceptible to pre-ignition or explosion [84, 85]. Hot spots within the combustion chamber or intake system can lead to pockets of explosion or pre-ignition and the flame can spread back through the intake port, manifold and injection system causing major damage to the engine. Similarly, pre-ignition or explosion/knocking during the compression stroke due to hot spots or too high a mixture temperature within the combustion chamber can lead to unstable operation and engine damage. These pre-ignition and knocking problems are exacerbated as equivalence ratio of the hydrogen-air mix increases which generally means there is a limit to the possible hydrogen substitution levels at medium-high loads. Clearly problems exist across all loads when operating intake induction diesel-hydrogen dual fuel engines and strategies aimed at achieving reliable operation at high HESs are required for the advancement of the technology.

2.3.3.2 Hydrogen high pressure direct injection

A promising solution for a number of the issues involved with intake inducted hydrogen combustion is to instead directly inject the gaseous fuel into the combustion chamber. High pressure direct injection of gaseous fuels allows for flexible engine operation as the likes of injector orientation, injector geometry, injection duration, injection pressure, injection timing, number of injections and ignition timing can be optimised to improve engine performance, reduce harmful emissions and increase the amount of liquid fuel which can be substituted out for gaseous fuel during dual-fuel operation. Backfire is also not an issue due to all fuel injections occurring after the inlet valve has closed, injectors can be orientated in such a way to avoid hot spots within the chamber to reduce the likelihood of pre-ignition/knocking and no oxidiser need be replaced during intake thus a high power density is maintained. Some of the biggest problems facing this method are the need to fit new injectors which can handle the high pressures

and velocities of the injected gases while also using materials which won't rapidly degrade to allow for commercial uses and the need to maintain these high injection pressures across a reasonable vehicle operating range (either an additional compressor is required or onboard high pressure gaseous storage tanks can only be depleted until they drop below the pressure required for injection) [14, 63, 86, 87]. Current research is also generally lacking with regards to investigation of practical engine setups which utilise pilot ignited non-premixed hydrogen direct injection, so the knowledge base needs to be expanded such that operation can be better understood and optimised.

The majority of the hydrogen HPDI investigations have been in SI [75, 88–91], glow plug [92–95] or HCCI [14, 96–99] type engines so there lies many unknowns with regards to utilisation in dual-fuel CI engines aiming for a non-premixed mode of combustion [14]. Hydrogen HPDI aiming for non-premixed combustion modes have only recently begun to gain traction. Rottengruber et al. [100] aimed for non-premixed combustion similar to diesel operation and investigated pure hydrogen direct injection in a compression ignition engine, however, inlet pre-heating to 343 K was required to allow for reasonable autoignition delay timings which led to a reduction in performance. Similarly, Gomes Antunes et al. [101] also investigated a pure hydrogen direct injection CI engine and required pre-heating to 353 K for reasonable ignition delay. While this mode of operation may be reasonable the required high in-cylinder temperatures and reduction to intake air density are likely to both increase NO_x emissions and reduce performance. With regard to dual-fuel engines, there are only two studies found in the literature directly addressing pilot ignited non-premixed direct injection hydrogen operation which are recent CFD studies carried out by Babayev et al. [62] and Frankl et al. [61]. Section 2.3.4.2 discusses their findings. For the most part pilot ignited non-premixed HPDI studies have utilised methane/natural gas rather than hydrogen with the likes of injection pressure [102, 103], relative angle between injections [104], nozzle diameter [105, 106], relative injection timings/strategies [105–109], etc. all being investigated. None of these parameters have currently been explored in dual-direct injection diesel-hydrogen CI engine operation and due to hydrogen's disparate fuel properties conclusions cannot be drawn from the studies on methane/natural-gas.

Gaining a deeper understanding of the mixing process and the impact of various injection strategies and injector properties on HPDI of gaseous fuels is essential for improving the combustion and emissions characteristics of gaseous fuelled engines. While clearly further experimental studies are required, numerical studies are just as, if not more, important for the advancement of understanding the phenomena involved in the mixing and combustion process and should facilitate the better design and optimisation of gaseous fuelled engines.

2.3.4 Application of CFD modelling to diesel-hydrogen dual-fuel compression ignition engines

Reacting engine simulations are inherently complex due to the need to account for combustion, heat transfer, turbulence, piston movement, complex geometries, fuel injection events, multiphase flow and various other factors. Introduction of multiple fuels and combustion modes only further increases complexity.

The general CFD modelling approaches previously used for the study of diesel-hydrogen CI engines are discussed including the insights gained from CFD and the challenges involved with modelling dual-fuel CI engine combustion.

2.3.4.1 Hydrogen intake manifold induction

Lilik et al. [110] studied up to 15% hydrogen substitution rates and found that the increasing HO_2 levels can lead to an increased conversion of NO to NO_2 . Maghbouli et al. [111] investigated localised knocking behaviour and found that increasing hydrogen substitution to 5% of the intake charge by volume caused high pressure rise rates, upon onset of combustion by the pilot, originating in the center of the piston bowl and above the crown but not close to the cylinder walls. Li et al. [112] researched a high speed 4000 RPM CI engine and found that increasing HES lead to an increasingly intense high temperature zone in the center of the cylinder where both fuels were burning as well as increasing performance and NO_x emission, however, these effects reduced as engine load was lowered. Similar results with regards to engine temperature were found by Chintala et al. [113] who also noted a similar NO_x formation rate increase. Yousefi et al. [114] compared pilot ignited hydrogen, natural gas and methanol premixed operation at varying equivalence ratios with hydrogen being found to have the best performance and lowest emissions under lean conditions compared to the other two fuels but relatively worse characteristics at richer conditions. Sharma et al. [78] investigated compression ratio influence and found that compression ratios below 14.5 lead to poor operation due to the pilot not igniting the premixed charge adequately while maximum possible substitution rate without knocking/pre-ignition decreased from 45% HES at 14.5 compression ratio to 20% at 19.5. Combustion chamber geometry influence was studied by Jyothi and Reddy [74] who found that use of a re-entrant combustion chamber can reduce UHC, CO, soot and NO_x emissions due to an increase of turbulence in the piston bowl which enhances both the hydrogen and diesel combustion. Various other authors have applied computational modelling to the study of intake induction hydrogen-diesel dual fuel operation [85, 115–118].

As evidenced by the number of studies, intake induction is for the most part much easier to study computationally than HPDI as the hydrogen-air mixture can be assumed to be homogeneous and thus no gaseous injection event need be simulated. Difficulties

with modelling are generally confined to the multiple combustion modes and multiple fuels present. Differentiating between non-premixed diesel and premixed hydrogen combustion as well as the various ignition phenomena involved and needing to model multiple fuels adds significant complexity. Many combustion models cannot accommodate these factors and those that can often still require further improvement thus care needs to be taken when implementing the combustion modelling approach [119, 120].

2.3.4.2 High pressure hydrogen direct injection

HPDI modelling can still suffer from all the same issues which intake induction modelling does, e.g. multiple fuels and multiple combustion modes if a premixed/partially premixed hydrogen charge is targeted (early compression stroke injection or late pilot ignition), with the added difficulty of adequately simulating the underexpanded jet which forms as a result of the gaseous injection event. Generally a very fine mesh is required at the injector (< 1 mm nozzle diameters requiring multiple cells across) and in the jet region (shock structures) to adequately resolve an underexpanded jet along with normally also needing to mesh a reasonable distance upstream of the nozzle (injector barrel and fuel tank/holding area) to ensure the correct flow develops. The computational expense involved normally makes the modelling of HPDI infeasible in engine studies and at the very least makes the normal optimisation and parametric studies which are carried out in the likes of diesel engines (injector orientation/geometry etc.) much more difficult as a full remeshing is required with any small parameter change. As a result very few HPDI dual-fuel engine combustion modelling studies have been carried out.

While the literature is sparse recently some authors have carried out CFD simulations for dual direct injection diesel-hydrogen dual-fuel operation targeting non-premixed combustion. Babayev et al. [62] validated a CFD model and compared the combustion characteristics of pilot ignited direct injection hydrogen non-premixed combustion to pure diesel operation in a CI engine. Distinct combustion phases (similar to those explained in Section 2.3.1.3) were found which differ somewhat from the standard diesel combustion process. Frankl et al. [61] also validated a CFD model and compared the combustion process of hydrogen with ammonia. Again a similar combustion process with minimal premixing and a non-premixed flame surrounding the rich hydrogen core is noted, however, less jet-jet interaction is observed due to what appears to be a much shorter injection event and flat/square piston bowl which doesn't allow for the same type of movement of the jet along the walls as was observed in the engine studied by Babayev et al. [62]. Convection of pilot combustion products, by the gaseous jet, into the piston bowl is also noted. To this authors knowledge no other CFD studies

on this form of dual-fuel diesel-hydrogen CI engine combustion are present in the literature, this, combined with the complete lack of experimental investigation previously discussed presents a clear gap in knowledge.

It's obvious that further study on the subject is required and one way to ensure this is to increase accessibility by reducing computational expense and complexity of the setup. Both of the previous CFD studies referenced used a refined injector which needed to begin upstream of the start of the injector nozzle and would likely have not been computationally feasible without use of automatic mesh refinement in key regions. If any injector geometry or orientation change is desired they will have to modify the geometry and carry out a full remeshing. The injector meshing requirement is solved in diesel engines by utilising the Lagrangian discrete phase model which represents the liquid injection as a particle phase separate from the Eulerian bulk phase. The Lagrangian phase is coupled with the main flow solution and can originate from any point in the domain without requiring the very fine meshes which a direct Eulerian approach would require. Section 3.5 details some of the modelling approaches which have been applied to deal with underexpanded gas jets and proposes improvements to a discrete phase methodology for gaseous injections in engine simulations which should allow for accurate, easy to implement and computationally efficient simulation of direct injection gaseous fuelled engines.

Chapter 3

Numerical Modelling and Simulation

This chapter provides a comprehensive breakdown of the CFD modelling framework employed in the research of internal combustion engines carried out in this thesis. The chapter discusses the governing equations required to describe turbulent reacting flow along with turbulence, combustion, fuel chemistry, fuel injection and dynamic mesh modelling details. A detailed model development section for the improved high pressure direct injection gaseous sphere injection model which is later validated in Chapter 5 and applied in Chapter 6 is also provided. This is followed by descriptions of the flow solver, numerical discretisation schemes and initial/boundary conditions applied to the various problem sets investigated in this work which uses the commercial CFD software ANSYS Fluent 19.1.

3.1 Governing equations

Turbulent flows can be described by a number of fundamental laws allowing for them to be expressed as governing differential equations which can then be solved, or and modelled, using computational fluid dynamics. The governing equations required to fully describe the flow of a fluid is dependant on the specific problem. For the multi-species reactive flows studied in this thesis conservation of mass, momentum, energy and species mass along with an equation of state is required. The conservative compressible form of the governing equations is used in the following sections.

In the following descriptions $i = j = k = 1, 2, 3$ where 1, 2 and 3 denote the x, y and z directions respectively.

3.1.1 Conservation of mass

The continuity equation, or conservation of mass, for a compressible fluid is given by:

$$\frac{\partial \rho}{\partial t} + \frac{\partial \rho u_j}{\partial x_j} = S_m, \tag{3.1}$$

where ρ is the density of the fluid, t is time, u_j is a component of the velocity vector, x_j is a component of the position vector and S_m is the source term for mass added to the continuous phase by the dispersed phase (e.g. vapourising liquid droplets).

3.1.2 Conservation of momentum

Derived from Newtons 2^{nd} law, conservation of momentum is given by:

$$\frac{\partial \rho u_i}{\partial t} + \frac{\partial \rho u_i u_j}{\partial x_j} = -\frac{\partial P}{\partial x_i} + \frac{\partial \tau_{ij}}{\partial x_j} + \rho B_i + F_i \tag{3.2}$$

where u_i is a component of the velocity vector, x_i is a component of the position vector, P denotes the pressure, B_i is a component of the body forces, F_i is a component of the external body forces acting on the flow accounting for interactions with the dispersed phase and τ_{ij} is the viscous stress tensor which, for Newtonian fluids, can be expressed by:

$$\tau_{ij} = \mu \left(\frac{\partial u_j}{\partial x_i} + \frac{\partial u_i}{\partial x_j} - \frac{2}{3} \delta_{ij} \frac{\partial u_k}{\partial x_k} \right), \tag{3.3}$$

where μ is the dynamic viscosity and δ_{ij} is the Kronecker delta defined by:

$$\delta_{ij} = \begin{cases} 0 & \text{if } i \neq j, \\ 1 & \text{if } i = j. \end{cases} \tag{3.4}$$

3.1.3 Conservation of energy

Derived from the 1^{st} law of thermodynamics, conservation of energy can be expressed as:

$$\frac{\partial \rho H}{\partial t} + \frac{\partial \rho u_j H}{\partial x_j} = \frac{\partial}{\partial x_j} \left(\frac{k_{eff}}{C_p} \frac{\partial H}{\partial x_j} \right) + S_h, \tag{3.5}$$

where H is the total enthalpy, k_{eff} is the effective conductivity, C_p is the specific heat capacity of the fluid, S_h is the source term accounting for any further heat losses.

This is one of the many ways in which energy conservation can be expressed, other common forms include expressions in terms of specific energy, internal energy and temperature.

3.1.4 Conservation of species mass

The species transport equation, or conservation of species mass, for species n is given by:

$$\frac{\partial \rho Y_n}{\partial t} + \frac{\partial \rho u_i Y_n}{\partial x_j} = -\frac{\partial J_n}{\partial x_j} + R_n + S_n \tag{3.6}$$

where Y_n is the mass fraction of species n, J_n is the diffusion flux of species n, R_n the net rate of production of species n by chemical reaction and S_n is the rate of creation of species n by the discrete phase and any other sources. This equation is solved $N-1$ times where N is the total number of chemical species.

For the turbulent flows studied in this thesis diffusion flux is computed using

$$J_n = -\left(\rho D_{n,m} + \frac{\mu_t}{S_{c_t}}\right)\frac{\partial Y_n}{\partial x_i} - \frac{D_{T,n}}{T}\frac{\partial T}{\partial x_i} \tag{3.7}$$

where $D_{n,m}$ is the mass diffusion coefficient for species n, μ_t the turbulent viscosity, S_{c_t} the turbulent Schmidt number and $D_{T,n}$ the thermal diffusion coefficient. A constant $S_{c_t} = 0.7$ is used as for the most part turbulent diffusion will be much greater than laminar diffusion in engine simulations. It's worth noting that hydrogen has a much lower Schmidt number than the likes of oxygen and nitrogen so multi-component diffusion or tuning of the Schmidt number may be worthwhile to improve prediction when hydrogen is present in the simulations. However, this is left to future work as the gains have been shown to be relatively minor compared to the computational cost involved with a full multi-component diffusion approach and changing Schmidt number will impact the other fuels present in dual-fuel combustion simulations [121].

3.1.5 Equation of state

An equation of state links pressure, temperature and density by assuming the fluid is always at thermodynamic equilibrium within a given infinitesimal volume i.e. any changes to thermodynamic properties within a fluid element occur instantly, with no time needed to adjust. A number of unknown variables are present in the conservation of mass, momentum and energy equations including the thermodynamic properties

listed thus an equation of state is required to calculate said variables. Equations of state also link together continuity and momentum equations with the energy equation.

In this thesis the ideal gas law is used due to its simplicity and applicability to a wide range of flow conditions, and is given by

$$PV = n_m RT \tag{3.8}$$

where V is the volume of the gas, n_m is the number of moles of gas and T is the temperature. The compressible form of the equation is used in this thesis and since a pressure based solver is used it's often more logical to express the ideal gas law as follows:

$$\rho = \frac{P_{abs}}{\frac{R}{M_w}T}, \tag{3.9}$$

P_{abs} is the absolute pressure, R is the universal gas constant and M_w is the molecular weight.

It should be noted that an equation of state is not required when using the non-premixed diesel unsteady flamelet combustion model described in Section 3.3.3 and used during Section 4.3.

3.1.6 Scalar transport equation

All governing equations can be expressed in a generic form. The general scalar transport equation for a scalar variable, ϕ, is given by:

$$\underbrace{\frac{\partial \rho\phi}{\partial t}}_{Transient\ term} + \underbrace{\frac{\partial \rho u_j \phi}{\partial x_j}}_{Convection\ term} = \underbrace{\frac{\partial}{\partial x_j}\left(\Gamma \frac{\partial \phi}{\partial x_j}\right)}_{Diffusion\ term} + \underbrace{S_\phi}_{Source\ term} \tag{3.10}$$

where Γ is the diffusion coefficient. The transient term determines the rate of increase of ϕ in the fluid element, the convective term accounts for the net rate of the transport of ϕ out of the fluid element due to the velocity field, the diffusion term gives the rate of increase in ϕ due to diffusion and the source term accounts for any additional sources or sinks that can cause the creation or destruction of ϕ.

Additional scalar transport equations are required when dealing with the likes of turbulence, combustion, pollutant modelling, etc.

3.2 Turbulence

One of the major difficulties with modelling any practical flow is turbulence. Turbulence is apparent in most real world flows and refers to the unsteady chaotic fluctuation of flow properties. This causes many issues with modelling as if every tiny variation needs to be accounted for computational costs will be extremely high, and in most cases direct computation is infeasible.

Turbulence can be characterised by the Reynolds number:

$$\frac{U_c L_c}{\nu} \tag{3.11}$$

where U_c and L_c are the characteristic velocity and length scales of the flow and ν the kinematic viscosity. If the Reynolds number exceeds a certain critical value the fluctuations in the flow become larger and the flow transitions from a laminar to turbulent flow. Once a flow fully transitions to turbulence it is intrinsically unsteady under all conditions and all flow properties vary both chaotically and randomly. Other properties of turbulent flow include: eddies of wide ranging length scales, always 3-dimensional (3D), enhanced mixing, highly dissipative, energy cascades from larger to smaller eddies, large eddies are anisotropic while small eddies are isotropic, etc.

3.2.1 Reynolds-averaged Navier-Stokes

As a result of the difficulty in describing and simulating such complex flows, vast amounts of research has been dedicated to the development of techniques which can be used to make the problem of turbulence more tractable. One such approach is Reynolds averaging. Reynolds averaging splits the velocity field into two components, the mean velocity field, $\overline{u}$, and a fluctuating component u'. The same is also done for all other scalars. Substituting these variables into the governing equations while taking the time average provides the Reynolds-averaged Navier-Stokes (RANS) equations:

Mass:

$$\frac{\partial \rho}{\partial t} + \frac{\partial \rho \overline{u}_j}{\partial x_j} = S_m, \tag{3.12}$$

Momentum:

$$\frac{\partial \rho \overline{u}_i}{\partial t} + \frac{\partial \rho \overline{u_i u_j}}{\partial x_j} = -\frac{\partial \overline{P}}{\partial x_i} + \frac{\partial}{\partial x_j}\left(\mu\left(\frac{\partial \overline{u}_j}{\partial x_i} + \frac{\partial \overline{u}_i}{\partial x_j} - \frac{2}{3}\delta_{ij}\frac{\partial \overline{u}_k}{\partial x_k}\right)\right) - \frac{\partial \rho \overline{u_i' u_j'}}{\partial x_j} + \rho B_i + F_i. \tag{3.13}$$

Energy:

$$\frac{\partial \rho \overline{H}}{\partial t} + \frac{\partial \rho \overline{u}_j \overline{H}}{\partial x_j} = \frac{\partial}{\partial x_j}\left(\frac{k_{eff}}{C_p}\frac{\partial \overline{H}}{\partial x_j}\right) + S_h, \tag{3.14}$$

Species:

$$\frac{\partial \rho \overline{Y}_n}{\partial t} + \frac{\partial \rho \overline{u}_i \overline{Y}_n}{\partial x_j} = -\frac{\partial J_n}{\partial x_j} + R_n + S_n \tag{3.15}$$

The equations are now in terms of the time averaged flow properties, but since we are dealing with compressible flows we also need to assume these are the Favre averaged RANS equations. Another issue is the final term on the right-hand side of the momentum equation, namely the Reynolds stress $\rho\overline{u_i' u_j'}$, which is a non-linear term accounting for convective acceleration in the flow and must be modelled to completely remove all fluctuating velocity components from the RANS equations.

3.2.2 Realizable k-epsilon model

In this project the realizable k-ϵ model [122] is used to close the RANS equations due to its suitability for flows involving recirculation and good prediction of spreading and penetration in jets. Realizable k-ϵ is well validated over a wide range of flows [122] and varies from the standard k-ϵ model by using an altered turbulent viscosity, μ_t, formulation and a different equation for the turbulence dissipation rate which is derived from an exact transport equation for the mean-square vorticity fluctuation.

The realizable k-ϵ model uses the Boussinesq hypothesis to express the Reynolds stresses as a function of the mean flow velocity gradients such that

$$-\rho\overline{u_i' u_j'} = \mu_t\left(\frac{\partial \overline{u}_i}{\partial x_j} + \frac{\partial \overline{u}_j}{\partial x_i}\right) - \frac{2}{3}\left(\rho k + \mu_t \frac{\partial \overline{u}_k}{\partial x_k}\right)\delta_{ij}. \tag{3.16}$$

Realizable k-ϵ then solves additional transport equations for the turbulence kinetic energy, k, and turbulence dissipation rate, ϵ:

$$\frac{\partial \rho k}{\partial t} + \frac{\partial\left(\rho k \overline{u}_j\right)}{\partial x_j} = \frac{\partial}{\partial x_j}\left(\left(\mu + \frac{\mu_t}{\sigma_k}\right)\frac{\partial k}{\partial x_j}\right) + G_k + G_b - \rho\epsilon - Y_M + S_k, \tag{3.17}$$

$$\frac{\partial \rho \epsilon}{\partial t} + \frac{\partial\left(\rho \epsilon \overline{u}_j\right)}{\partial x_j} = \frac{\partial}{\partial x_j}\left(\left(\mu + \frac{\mu_t}{\sigma_\epsilon}\right)\frac{\partial \epsilon}{\partial x_j}\right) + \rho_1 C_1 S\epsilon - \rho C_2 \frac{\epsilon^2}{k + \sqrt{\nu\epsilon}} + C_{1\epsilon}\frac{\epsilon}{k} C_{3\epsilon} G_b + S_\epsilon, \tag{3.18}$$

where G_k describes the generation of k due to mean velocity gradients, G_b the generation due to buoyancy, Y_M accounts for compressibility's affect on dissipation rate due to fluctuating dilation, C_2 and $C_{1\epsilon}$ are constants, σ_k and σ_ϵ represent the turbulent Prandtl numbers of k and ϵ respectively, S_k and S_ϵ represent any further sources or sinks and

$$C_1 = max\left[0.43, \frac{\frac{k}{\epsilon}\sqrt{2S_{ij}S_{ij}}}{\frac{k}{\epsilon}\sqrt{2S_{ij}S_{ij}}+5}\right], \quad \text{for} \quad S_{ij} = \frac{1}{2}\left(\frac{\partial u_j}{\partial x_i} + \frac{\partial u_i}{\partial x_j}\right). \tag{3.19}$$

Model constants have been tested over many flows and due to their wide applicability the current analysis takes them to be:

$$C_{1\epsilon} = 1.44,\ C_2 = 1.9,\ \sigma_k = 1,\ \sigma_\epsilon = 1.2. \tag{3.20}$$

This leaves the eddy-viscosity term:

$$\mu_t = \rho C_\mu \frac{k^2}{\epsilon} \tag{3.21}$$

where

$$C_\mu = \frac{1}{A_0 + A_S\frac{kU*}{\epsilon}} \tag{3.22}$$

for

$$U^* = \sqrt{S_{ij}S_{ij} + \tilde{\Omega}_{ij}\tilde{\Omega}_{ij}} \tag{3.23}$$

and

$$\tilde{\Omega}_{ij} = \Omega_{ij} - 2\epsilon ijk\omega_k, \tag{3.24}$$

$$\Omega_{ij} = \overline{\Omega}_{ij} - \epsilon ijk\omega_k. \tag{3.25}$$

Ω_{ij} is the rate of rotation tensor in a moving reference frame, $\overline{\Omega}_{ij}$ denotes the mean of this and ω_k is the angular velocity, while A_0 and A_S are constants given by:

$$A_0 = 4.04,\ A_s = \sqrt{6}\cos(\phi), \tag{3.26}$$

where

$$\phi = \frac{1}{3}\cos^{-1}\left(\frac{\sqrt{6}S_{ij}S_{jk}S_{ki}}{\left(S_{ij}S_{ij}\right)^{\frac{3}{2}}}\right). \tag{3.27}$$

Standard wall functions [123] are employed for near-wall treatment which is formulated with a y^* limiter to ensure the value doesn't fall below 11.225 meaning results won't deteriorate if grid refinement is too high. In general, the wall bounded engine

simulations will always have $y^* > 11.225$ so any inaccuracies due to the forcing of the log-law shouldn't be of concern.

3.3 Combustion modelling

Accurate combustion modelling is one of the key components in effective engine simulation. Combustion in a given system is governed by both the rate of chemical reaction and the rate of mixing. The rate of mixing is generally enhanced by the many length scales of turbulent flow which means their contribution cannot be ignored. As previously noted this thesis employs a RANS based turbulence model which inserts a turbulent viscosity to model the Reynolds stress and enhance mixing when removing the smaller scales of the flow. The major advantage of this procedure is the ability to adequately resolve the remaining larger length scales of the flow with a much coarser mesh than would be required in the likes of direct numerical simulation (DNS) which has to resolve the smallest scales. To put this into perspective, in engine simulations the minimum length scale without turbulent viscosity will generally be in the range of 0.01 to 0.001 mm, but with turbulent viscosity this increases to between 0.1 and 1 mm [124]. However, often times compromises still need to be made with regard to mesh resolution in RANS simulations due to computational constraints which can lead to increasing error resulting from sub-grid effects, i.e. effect of the length scales which weren't captured by the under-resolved mesh on mixing. Therefore one of two approaches can be taken to adequately account for mixing's impact on combustion, a) resolve all/most of the RANS scales with a fairly fine mesh, or b) model the sub-grid terms and use a relatively coarse mesh.

In this work the simulations carried out in Chapter 4 use option b) and explicitly model the turbulence chemistry interaction (TCI), whereas in the engine combustion validation carried out in Chapter 5 and the proceeding simulations based on this validated setup in Chapter 6 option a) is employed and solely relies on the adequate resolution of the RANS scales to compute the mixing. All of the approaches taken incorporate detailed Arrhenius chemical kinetics.

3.3.1 Finite-rate formulation

The net source of species n due to chemical reaction is computed using the Arrhenius rates such that

$$R_n = M_{w,n} \sum_{r=1}^{N_R} \hat{R}_{n,r} \tag{3.28}$$

where $M_{w,n}$ is the molecular weight of species n, N_R is the total number of reactions, r is a given reaction and $\hat{R}_{n,r}$ is the Arrhenius molar rate of creation or destruction of species n during reaction r which for a reversible reaction is given by

$$\hat{R}_{n,r} = \Gamma_p \left(v''_{n,r} - v'_{n,r}\right) \left(k_{f,r} \prod_{j=1}^{N} \left[C_{j,r}\right]^{\eta'_{j,r}} - k_{b,r} \prod_{j=1}^{N} \left[C_{j,r}\right]^{v''_{j,r}} \right) \tag{3.29}$$

where Γ_p represent the net effect of third bodies on reaction rate, $v''_{n,r}$ is the stoichiometric coefficient for product n during reaction r, $v'_{n,r}$ is the stoichiometric coefficient for reactant n during reaction r, $k_{f,r}$ is the forward rate constant for reaction r, $k_{fb,r}$ is the backward rate constant for reaction r, N the number of chemical species, $C_{j,r}$ is the molar concentration of species j during reaction r and $\eta'_{j,r}$ is the rate exponent for reactant species j during reaction r.

The forward rate constant is computed using the Arrhenius expression

$$k_{f,r} = A_r T^{\beta_r} e^{\frac{E_r}{RT}}, \tag{3.30}$$

and the backward rate

$$k_{b,r} = \frac{k_{f,r}}{K_r}, \tag{3.31}$$

where A_r is the pre-exponential factor, β_r is the temperature exponent, E_r is the activation energy and R is the universal gas constant and K_r is the equilibrium constant for reaction r. Sometimes it's also necessary to include a backwards rate which differs from Equation (3.31) where

$$k_{b,r} = A_{b,r} T^{\beta_{b,r}} e^{\frac{-E_{b,r}}{RT}}, \tag{3.32}$$

where $A_{b,r}$ is the backward reaction pre-exponential factor, $\beta_{b,r}$ is the backward reaction temperature exponent and $E_{b,r}$ is the backward reaction activation energy for the reaction.

All values relevant to the combustion problem set are input via Chemkin mechanism and thermodynamic database. Further discussion on the specific mechanisms used in this thesis are carried out in Section 3.3.4.

Chemical kinetic mechanisms contain a broad range of time scales which makes the computation of reaction rates difficult as a set of non-linear, stiff coupled ordinary differential equations (ODEs) are formed. The timescales involved in combustion are generally much smaller than those of the flow itself thus difficulties arise with regards to computation. In this work, operator splitting is applied in which first the flow is paused and the reaction rates of the combustion system are computed using the flow quantities calculated in the previous time step (pressure, temperature and species mass fractions), followed by the combustion system being paused and the flow computed using the updated species mass fractions from the combustion calculations and so on. This is termed a well-mixed model as it assumes that flow conditions don't change during the combustion calculation.

Arrhenius rates are integrated numerically using the Chemkin-CFD solver in combination with Fluent's in situ adaptive tabulation (ISAT) algorithm [125]. The Chemkin-CFD solver directly integrates the reactions rates of an initial unreacted state over a given time step, this process is time consuming however. Therefore using ISAT, the computed reaction rate and specific flow conditions are then mapped to the ISAT table allowing for the retrieval of more and more reaction rates without need for direct computation as the solution progresses, leading to a significant speed up in simulation time.

As noted previously this formulation is sufficient for the computation of a reacting flow given adequate mesh resolution as the detailed chemical kinetics should accurately predict the combustion given the initial conditions provided by the flow solution are correct, i.e. as long as the sub-grid effects are minimal. This methodology is then applied in the engine simulations carried out in Chapters 5 and 6.

3.3.2 Eddy-dissipation concept model

To reduce computational cost of the initial studies carried out in Chapter 4 coarser meshses were used. As a result sub-grid effects are not minimal and thus additional turbulence chemistry interaction modelling is required.

The eddy-dissipation concept (EDC) model [126] is used to model the turbulence chemistry interaction in the simulations concerning intake inducted diesel-hydrogen dual-fuel combustion carried out in Section 4.4. The EDC model allows for detailed chemical kinetic mechanisms to be coupled with the flow by dividing the fluid into a non-reacting part and reacting part termed the fine-scales. The fine scale length fraction, ξ^*, is given by

$$\xi^* = 2.1377 \left(\frac{\nu\epsilon}{k^2}\right)^{\frac{1}{4}} \tag{3.33}$$

where ν is the kinematic viscosity. The time scale of the reaction, τ^* is taken to be

$$\tau^* = 0.4082 \left(\frac{\nu}{\epsilon}\right)^{\frac{1}{2}} \tag{3.34}$$

Reactions then proceed over the time scale τ^* using Equation (3.29), and the same solution procedure as the finite-rate formulation using operator splitting, Chemkin-CFD solver and ISAT follows. The reaction rate for a species n is then modelled as:

$$R_n = \frac{\rho(\xi^*)^2}{\tau^* \left[1 - (\xi^*)^2\right]} \left(Y_n^* - Y_n\right). \tag{3.35}$$

where Y_n^* is the fine-scale species mass fraction after reacting over τ^*.

3.3.3 Diesel unsteady flamelet non-premixed combustion model

When only diesel and a single mode of combustion is present in the pure diesel engine study carried out in Section 4.3, the fuel and air is mixed and burned simultaneously hence representing a non-premixed combustion mode.

The diesel unsteady flamelet model (a modification of the representative interactive flamelet model) [127, 128] computes the combustion in mixture fraction space where the mixture fraction, f, is defined as

$$f = \frac{Z_n - Z_{n,ox}}{Z_{n,fuel} - Z_{n,ox}}, \tag{3.36}$$

where Z_n denotes the elemental mass fraction of an element n, ox denotes the value at the oxidiser stream and $fuel$ denotes the value at the fuel stream inlet.

Rather than calculating $N - 1$ equations for each individual species using Equation (3.6), species concentrations are taken from the predicted mixture fraction field. This involves the solution of the scalar transport equations for the Favre mean mixture fraction, $\overline{f}$, given by

$$\frac{\partial\left(\rho\overline{f}\right)}{\partial t}+\frac{\partial\left(\rho u_j\overline{f}\right)}{\partial x_j}=\frac{\partial}{\partial x_j}\left(\left(\frac{\mu_l+\mu_t}{\sigma_t}\right)\frac{\partial\overline{f}}{\partial x_j}\right)+S_f \tag{3.37}$$

and the Favre mean mixture fraction variance $\overline{f'^2}$, given by

$$\frac{\partial\left(\rho\overline{f'^2}\right)}{\partial t}+\frac{\partial\left(\rho u_j\overline{f'^2}\right)}{\partial x_j}=\frac{\partial}{\partial x_j}\left(\left(\frac{\mu_l+\mu_t}{\sigma_t}\right)\frac{\partial\overline{f'^2}}{\partial x_j}\right)+C_g\mu_t\left(\frac{\partial\overline{f}}{\partial x_j}\right)^2-C_d\rho\frac{\epsilon}{k}\overline{f'^2} \tag{3.38}$$

where μ_l is the laminar viscosity, μ_t is the turbulent viscosity, S_f is the source term due to the transfer of mass from the discrete phase, C_g and C_d are constants.

The diesel unsteady laminar flamelet model uses a finite amount of 1D laminar flamelets to calculate the chemistry. Computational costs of the diesel unsteady flamelet model are much reduced due to this reduction of the chemical kinetics to 1D when compared to the other methods discussed. A separate flamelet solver is used to calculate flamelet properties simultaneously with the flow. Operator splitting is used whereby first the flamelet equations are solved using the flow properties producing a probability density function (PDF) table which is then used by the flow solver to advance the flow to the new time step.

In the generation of the 1D flamelets, N equations are solved for the species mass fraction given by

$$\rho\frac{\partial Y_n}{\partial x}=\frac{1}{2}\rho\chi\frac{\partial^2 Y_n}{\partial f^2}+S_{nr}, \tag{3.39}$$

and one for temperature

$$\rho\frac{\partial T}{\partial x}=\frac{1}{2}\rho\chi\frac{\partial^2 T}{\partial f^2}-\frac{1}{c_p}\sum_n H_n S_n+\frac{1}{2c_p}\rho\chi\left[\frac{\partial c_p}{\partial f}+\sum_n c_{p,n}\frac{\partial Y_n}{\partial f}\right]\frac{\partial T}{\partial f}+\frac{1}{c_p}\frac{\partial P}{\partial t}, \tag{3.40}$$

where $c_{p,n}$ is the specific heat of species n, c_p the mixture average specific heat, S_{nr} is the reaction rate of species n, H_n is the specific enthalpy of species n and P is the volume average pressure. The scalar dissipation, χ, is modelled using

$$\chi=\frac{a_s}{4\pi}\frac{3\left(\sqrt{\frac{\rho_\infty}{\rho}}+1\right)^2}{2\sqrt{\frac{\rho_\infty}{\rho}}+1}\exp\left(-2\left[erfc^{-1}\left(2f\right)\right]^2\right) \tag{3.41}$$

where ρ_∞ is the oxidiser stream density and $erfc^{-1}$ is the inverse complementary error function. The characteristics strain rate, a_s, is given by

$$a_s = \frac{v}{2d}, \tag{3.42}$$

where v is the relative speed of the fuel and oxidiser and d is the distance between the streams.

The PDF table is used to link turbulence and chemistry models, i.e. explicitly model the TCI. The PDF predicts the temporal fluctuations of the species mixture fraction, f, in the turbulent flow which can then be used to calculate the Favre averaged values which are dependent on mixture fraction. The β function is used to represent the PDF, $p(f)$, using the following 'assumed shape':

$$p(f) = \frac{f^{\alpha-1}(1-f)^{\beta-1}}{\int f^{\alpha-1}(1-f)^{\beta-1}\mathrm{d}f}, \tag{3.43}$$

where

$$\alpha = \overline{f}\left(\frac{\overline{f}(1-\overline{f})}{\overline{f}'^2} - 1\right), \tag{3.44}$$

and

$$\beta = (1-\overline{f})\left(\frac{\overline{f}(1-\overline{z})}{\overline{f}'^2} - 1\right). \tag{3.45}$$

Clearly the PDF function is only dependant on the Favre mean mixture fraction and variance thus once these values are processed for all points in the flow field, the assumed shape of the PDF is found. From this, the averaged values of species mass fraction, temperature and density required for turbulence modelling can be calculated by inserting the assumed PDF values into the mean time-averaged fluid density

$$\frac{1}{\rho} = \int_0^1 \frac{p(f)}{\rho(f)}\mathrm{d}f, \tag{3.46}$$

and the density-weighted mean species mass fractions and temperatures follow from

$$\phi_n = \int_0^1 p(f)\phi_n(f)\mathrm{d}f. \tag{3.47}$$

3.3.4 Chemical kinetic mechanisms

In this study a number of problem sets with differing fuels are addressed so each require their own oxidation mechanism,.

Throughout this thesis diesel fuel chemistry is represented by the reduced n-heptane mechanism developed by Nordin [129] containing 40 species and 165 reactions. It is reasonable to use n-heptane as a surrogate for diesel as it shares many similar fuel qualities (Table 2.1) while also allowing for efficient computation due to its relatively short breakdown pathway. The mechanism developed by Nordin (often called the Chalmers mechanism) has been used and validated extensively due to its accuracy and compact nature [124, 130, 131].

Hydrogen is represented by the detailed hydrogen oxidation mechanism developed by Kéromnès et al. [43] consisting of 15 species and 48 reactions. This mechanism is well validated and applicable to both the premixed and non-premixed modes of hydrogen combustion used during this thesis. A comprehensive review on recent hydrogen combustion mechanisms determined that the Kéromnès et al. mechanism performed best across a wide range of tests out of the 19 mechanisms investigated [44].

Compressed natural gas (CNG) combustion is represented by the detailed methane combustion mechanism GRI mech 3.0 developed by Smith et al. [132] consisting of 53 species and 325 reactions. Methane is used as a surrogate as the makeup of CNG generally contains 80-90% methane and thus combustion qualities will be very similar.

Mechanisms are then combined for their required use case and unneeded duplicate species/reactions removed, Table 3.1 details each study and the mechanism employed. We note that the diesel-methane study uses the detailed hydrogen mechanism also as it was used as a validation case for the final chapter on diesel-hydrogen combustion and thus was required anyway. All mechanisms were tested/checked in Chemkin to ensure no mistakes were made during alteration and that the combination of the mechanisms didn't change combustion behaviours. This is a common strategy when multiple fuels are required and specialised mechanisms are not available and has been shown to give good results [61, 133].

TABLE 3.1: Chemical kinetic mechanisms used throughout thesis.

Study	Chapter/section	Mechanism
CVCP 1 (diesel)	Section 4.3	Nordin [129]
CVCP 2 (diesel-hydrogen)	Section 4.4	Nordin + Kéromnès et al. [43]
GSI validation (diesel-CNG)	Section 5.4	Nordin + Kéromnès et al. + GRI mech 3.0 [132]
GSI parametric (diesel-CNG-hydrogen)	Chapter 6	Nordin + Kéromnès et al. + GRI mech 3.0

3.3.5 Pollutant modelling

Pollutant modelling can be carried out directly within the combustion model if the chemical mechanism includes the required species and reactions or additional transport equations can be solved to predict pollutant emissions. In this study separate NO_x and soot models are employed and additional transport equations are solved due to the reduced computational cost involved while still providing reasonable results.

NO_x emissions are calculated using the following transport equation for the NO_x mass fraction, $\overline{Y}_{NO_x}$, accounting for thermal [56] and prompt [134] mechanisms

$$\frac{\partial \rho \overline{Y}_{NO_x}}{\partial t} + \frac{\partial \rho \overline{u}_j \overline{Y}_{NO_x}}{\partial x_j} = \frac{\partial}{\partial x_j}\left(\rho D \frac{\partial \overline{Y}_{NO_x}}{\partial x_j}\right) + S_{NO_x} \tag{3.48}$$

where D is the effective diffusion coefficient, S_{NO_x} is the source term for an additional thermal or prompt NO_x development.

Soot emissions are calculated using the Moss-Brookes soot model [135] using acetlyene as the inception species. Two additional transport equation are solved for the soot mass fraction, $\overline{Y}_{soot}$, given by

$$\frac{\partial \rho \overline{Y}_{soot}}{\partial t} + \frac{\partial \rho \overline{u}_j \overline{Y}_{soot}}{\partial x_j} = \frac{\partial}{\partial x_j}\left(\frac{\mu_t}{\sigma_{soot}} \frac{\partial \overline{Y}_{soot}}{\partial x_j}\right) + \frac{\mathrm{d}M}{\mathrm{d}t} \tag{3.49}$$

and normalised radical nuclei concentration, $\overline{b^*}_{nuc}$, given by

$$\frac{\partial \rho \overline{b^*}_{nuc}}{\partial t} + \frac{\partial \rho \overline{u}_j \overline{b^*}_{nuc}}{\partial x_j} = \frac{\partial}{\partial x_j}\left(\frac{\mu_t}{\sigma_{nuc}} \frac{\partial \overline{b^*}_{nuc}}{\partial x_j}\right) + \frac{1}{N^*_{norm}} \frac{\mathrm{d}N^*}{\mathrm{d}t}, \tag{3.50}$$

where σ_{soot} is the turbulent Prandtl number for soot transport, M is the soot mass concentration, σ_{nuc} is the turbulent Prandtl number for radical nuclei transport, N^* is the soot particle number density and N^*_{norm} is 10^{15} particles.

3.3.6 Heat release rate

Throughout this thesis heat release rate is used to gain insights into the combustion processes. Apparent heat release rate is calculated by using the simulated rate of change of cylinder pressure and volume assuming a uniform temperature for the chamber by the equation [12]

$$\frac{\mathrm{d}Q_n}{\mathrm{d}\theta} = \frac{\gamma}{\gamma - 1} P \frac{\mathrm{d}V}{\mathrm{d}\theta} + \frac{1}{\gamma - 1} V \frac{\mathrm{d}P}{\mathrm{d}\theta}, \tag{3.51}$$

where the left-hand side represents the apparent net rate of heat release which is the difference between the apparent gross heat release rate (due to combustion) and the rate of heat transfer out of the system through the chamber walls plus the fuel fuel vapourisation process, θ is the crank angle degree, γ is the ratio of specific heat of the mixture, P is the in-cylinder pressure and V is the cylinder volume. The ratio of specific heats (γ) is taken to be a constant equal to 1.3 (rough average between γ during combustion and at the end of the power stroke) which the literature has shown to give good results considering the simplicity [136]. While it's true that using an instantaneous value of γ, based on charge composition and temperature, or direct calculation from reaction rates could improve the heat release rate calculation the literature shows that it's largely unnecessary, especially since heat release rate is for the most part used as a qualitative comparison tool [12, 136, 137]. The terms heat release rate and apparent heat release rate are used interchangeably throughout this thesis.

3.3.7 Exhaust gas recirculation

EGR is implemented by replacing a percentage of the intake air with exhaust gases. This is achieved by changing the oxidiser stream composition in the flamelet when using the diesel unsteady flamelet model or simply the initialised gas composition when using species transport. A form of cooled EGR is assumed when required so initial

temperature is unchanged allowing for easier comparison of results. Relations for the exhaust gas stream composition are deduced from [12] such that

$$CH_y + \left(1 + \frac{y}{4}\right)(O_2 + 3.773N_2) \longrightarrow CO_2 + \frac{y}{2}H_2O + 3.773\left(1 + \frac{y}{4}\right)N_2, \tag{3.52}$$

where y is the ratio of hydrogen to carbon in the fuel.

Note that since Faghani et al. [109] provide experimental measurements for gas composition and charge temperature that these are used instead for the validation carried out in Section 5.4.

3.4 Finite volume method and sliding/dynamic mesh modelling

In this work finite volume method, combined with numerical methods, is used to solve the previously described transport equations by discretising the computational domain into a finite set of control volumes, i.e. creating a mesh. In this way the scalar transport equation (3.10) in integral form can be expressed as

$$\frac{\mathrm{d}}{\mathrm{d}t}\int_V \rho\phi \mathrm{d}V + \int_{\mathrm{d}V} \rho\phi(\mathbf{u})\mathrm{d}\mathbf{A} = \int_{\mathrm{d}V} \Gamma\nabla\phi \mathrm{d}\mathbf{A} + \int_V S_\phi \mathrm{d}V \tag{3.53}$$

where $\mathbf{u}$ is the flow velocity vector, ∂V represents the boundary of a control volume V and $\mathbf{A}$ is the face area vector. This allows for the partial differential equations to be discretised into a system of algebraic equations which can then be solved numerically and thus predict the flow field.

In engine simulations the movement of the piston, and valves when required, needs to be modelled. A sliding mesh is a special case of dynamic mesh motion which allows for separate zones of the mesh to move relative to each other while a full dynamic mesh allows for the boundaries of a zone to move relative to other boundaries of the same zone. A sliding mesh is much simpler and efficient type of dynamic meshing as cells retain their original volume and shape as they need not be deformed to prescribe motion. As a result, the majority of this work utilises sliding mesh motion which is prescribed via layering and smoothing with the one exception being the full spark ignition engine geometry studied in Chapter 5 which uses both sliding mesh motion and deforming mesh motion with remeshing to allow for valve movement.

When mesh motion is required Equation (3.53) becomes

$$\frac{\mathrm{d}}{\mathrm{d}t}\int_V \rho\phi \mathrm{d}V + \int_{\mathrm{d}V} \rho\phi(\mathbf{u}-\mathbf{u_g})\mathrm{d}\mathbf{A} = \int_{\mathrm{d}V} \Gamma\nabla\phi \mathrm{d}\mathbf{A} + \int_V S_\phi \mathrm{d}V \tag{3.54}$$

where $\mathbf{u_g}$ is the velocity vector of the moving mesh.

Ratio-based layering is employed which adds or removes layers of hex cells adjacent to the desired moving boundary based on the height of the layer adjacent to the moving surface once a threshold value is exceeded. A variable layering height is also implemented to allow for coarsening of the mesh towards EVO and reduce computational cost in the engine simulations carried out in Chapters 5 and 6. The UDF for its implementation is provided in Appendix A. Spring-based and Laplacian smoothing are used to adjust the mesh of the zone to ensure connectivity and number of nodes are maintained during mesh movement while keeping element quality high.

3.5 Gaseous sphere injection model development

Development of the improved gaseous sphere injection (GSI) model is presented.

3.5.1 Review of direct gaseous injection modelling

Gaining a deeper understanding of the mixing process and the impact of various injection strategies and injector properties on HPDI of gaseous fuels is essential for improving the combustion and emissions characteristics of gaseous fuelled engines. While a fair amount of experimental research has been carried out there is a lack of numerical studies on the full engine mixing and combustion process by comparison [45, 86, 138, 139]. Numerical studies are required to properly understand the mixing and combustion process to facilitate the better design and optimisation of direct injection gaseous fuelled engines.

Particularly, HPDI of gaseous fuel into a combustion chamber will lead to the occurrence of highly compressible flow structures in the form of an underexpanded gas jet, see Figure 3.1. Much modelling work has been carried out on underexpanded gas jets with the majority requiring a very fine mesh at the injector nozzle and in the near-nozzle region of the jet to properly resolve the flow [140–143]. This, however, is not fully scalable for efficient parametric investigation of engine operating points as any changes to injector orientation or design would require a full remeshing of the combustion chamber and nozzle, while the very fine mesh required also leads to much higher computational expense than is generally feasible during an engine simulation. As a result, a number of authors have proposed physics based theoretical and numerical models which can be used to circumvent fully resolving the nozzle/near-nozzle

region while still maintaining jet characteristics at a given distance downstream of the complicated flow regime in the near-nozzle region.

This type of approach first began with the finding that the behaviour of an underexpanded jet may be treated as a usual compressible perfectly expanded jet once far enough downstream of the near nozzle shock region given a characteristic length is found which can scale all variable [144, 145]. Early models used an approach which set an "equivalent/pseudo/notional/fictional nozzle" downstream of the near-nozzle region, based solely on the real nozzles exit conditions and physical hypotheses, eliminating the need to model the complex turbulent structures prior to the equivalent nozzle, see Figure 3.2. Examples include the pseudo-diameter approaches of Birch et al. [146, 147], the sonic jet approach of Ewan and Moodie [148], the Mach disk approach of Harstad and Bellan [149], the adiabatic expansion approach of Yüceil and Ötügen [150] and a number of others [144, 151–153]. In the review of underexpanded jets by Franquet et al. [145] it was noted that while it is true that the actual jet may be approximated accurately by the equivalent nozzle approaches there exists discrepancies between the results of each of the proposed models and thus further analysis is required to determine which offers the best predictions. A number of other models have been proposed and directly integrated with CFD codes. Ra et al. [154] used a hybrid combination of a theoretical model to describe the near-nozzle region and CFD to describe the remainder of the underexpanded jet with good agreement for freestream results. A phenomenological model was created by Andreassi et al. [155, 156] to describe the near-nozzle region without need for a fine mesh, and good validation was found for both freestream and impinging jets. Other models have also been suggested [157–160]. While good validation of the mentioned models is achieved, in most cases mesh adaption will likely be required as injection parameters vary or other difficulties in implementation are present. Hessel et al. [161] proposed the gaseous sphere injection model which modifies the previously developed Lagrangian liquid spray model for use with high pressure gaseous injections on coarse meshes. A number of studies have used the GSI modelling approach with reasonable agreement for jet characteristics and mixing at engine relevant conditions using coarse grids [133, 161–168]. Particularly, four separate authors have carried out successful combustion modelling for HPDI of natural gas; both Choi et al [164] and Wang et al. [167] in pure natural gas spark ignition engines and both Zoldak et al. [133] and Liu et al. [168] in natural gas-diesel dual fuel compression ignition engines. Due to the ease of implementation, relative familiarity, no remeshing/fine grid constraints and extensive capabilities due to the basis of the GSI model being that of the mature strongly developed discrete phase liquid injection model this approach is a promising one.

The objective of this work is to further improve the original GSI model with a focus on improving the core length estimation which determines the transition from the Lagrangian particles of the GSI model to the Eulerian bulk gas. The original GSI model

opts to set a core length which is only dependant on injector diameter and also alters turbulence quantities in the jet region to improve penetration. This paper aims to provide a novel approach to better estimate the core length and avoids changing turbulence parameters within the jet region. The validation study of the improved model is carried out in Chapter 5 for a range of applications covering underexpanded natural gas and hydrogen freestream jets, mixture formation in a hydrogen direct injection engine and combustion in a natural gas-diesel dual direct injection compression ignition engine. The proposed novel modification will help apply the GSI model with greater accuracy and easier implementation to the prediction of HPDI of gaseous fuels, such as hydrogen and natural gas, enabling better design and optimisation of injection strategies for improved mixing and efficient combustion.

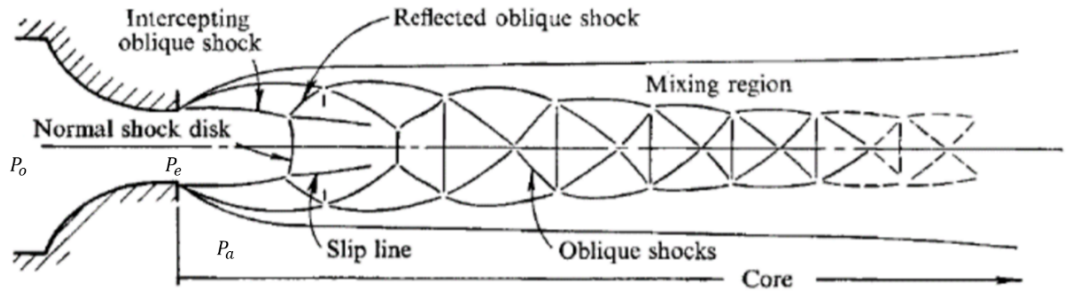

FIGURE 3.1: Highly underexpanded gas jet structure. Source: Donaldson and Snedeker [169].

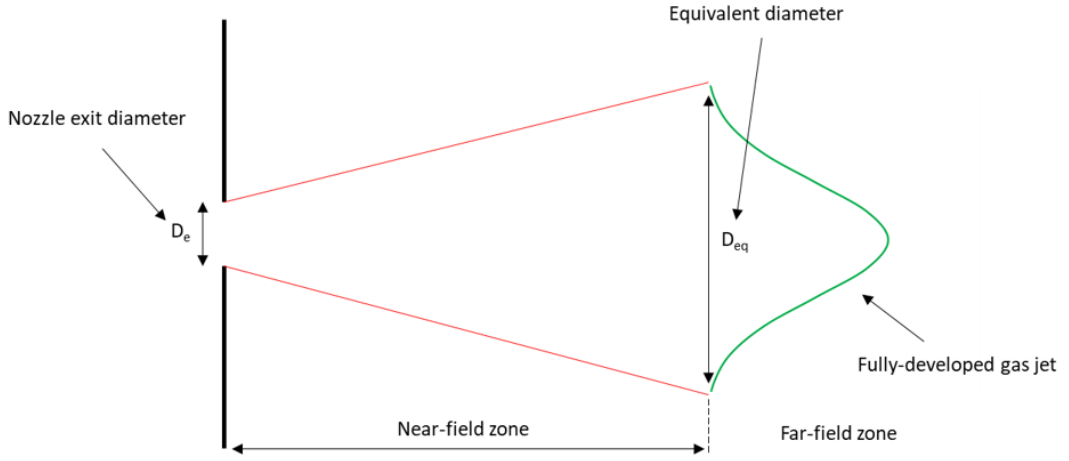

FIGURE 3.2: Schematic of the equivalent-source approach.

3.5.2 Underexpanded gas jets

Before describing underexpanded gas jets further we make the distinction between the total pressure ratio, η_0, nozzle pressure ratio, η_e, and the critical pressure ratio, η^*. Total

pressure ratio is given by

$$\eta_0 = \frac{P_0}{P_a}, \tag{3.55}$$

where P_0 is the total pressure and P_a is the ambient pressure. Nozzle pressure ratio (NPR) is given by

$$\eta_e = \frac{P_e}{P_a}, \tag{3.56}$$

where P_e is nozzle exit pressure. The critical pressure ratio is given by

$$\eta^* = \frac{P^*}{P_0}, \tag{3.57}$$

where P^* is the critical nozzle exit pressure.

Total pressure ratio refers to source pressure divided by ambient pressure, i.e. pressure at the compressor or gas storage tank upstream of the nozzle divided by chamber pressure downstream of the nozzle. Nozzle pressure ratio refers to pressure at the nozzle exit divided by ambient pressure downstream of the nozzle. While critical pressure ratio refers to the nozzle exit pressure at which choked flow will first occur divided by the total pressure.

In isentropic choked flow of a perfect gas through a converging/straight nozzle, nozzle exit pressure can be calculated using the ratio of specific heat of the injected gas, γ, along with the total pressure such that

$$P_e = P_0 \left(\frac{2}{\gamma + 1} \right)^{\frac{\gamma}{\gamma - 1}}. \tag{3.58}$$

Isentropic choked mass flow rate, $\dot{m}_{theory}$, of an ideal gas can be calculated using

$$\dot{m}_{theory} = A_e P_0 \sqrt{\frac{\gamma}{T_0 R_I}} \left(\frac{\gamma + 1}{2} \right)^{\frac{\gamma+1}{2(1-\gamma)}}, \tag{3.59}$$

where A_e is the area of the nozzle exit, T_0 is the temperature upstream of the nozzle and R_I is the individual gas constant of the injected gas.

However, in the real-world flow is not isentropic and thus other factors can cause losses within the nozzle and so a discharge coefficient, C_d, must also be accounted for. Most

commonly discharge coefficient is expressed as the ratio of the actual mass flow rate, $\dot{m}_{actual}$, over the theoretical isentropic mass flow rate such that

$$C_d = \frac{\dot{m}_{actual}}{\dot{m}_{theory}}. \tag{3.60}$$

Typically discharge coefficients are in the region of 0.6-0.9 [63, 139, 170, 171] [21,56–58] but values of 0.1 and lower have been observed in the literature [172].

During gaseous injection if nozzle exit pressure equals the critical pressure then the flow will be choked. Any further increases of the total pressure cannot cause the velocity of the gas travelling through the nozzle to increase further, however, mass flow rate through the nozzle will continue to increase as total pressure increases causing rapid expansion of the gas once it exits the nozzle, i.e., the gas jet is underexpanded. The rapid expansion of the gas upon exiting the nozzle causes the flow to accelerate, becoming supersonic, and producing expansion waves which reflect at the flow boundaries creating a complex shock structure. At NPRs greater than roughly 2 the jet will be highly underexpanded and the core structure will contain a barrel-shaped shock and normal shock termed the Mach disk at its leading edge just downstream of the nozzle exit. Downstream of the Mach disk oblique shocks will continue to propagate extending the core region. At NPRs less than 2, but still at exit pressures greater than the critical pressure, a moderately underexpanded jet will form with a core region made up of oblique shocks. In both cases a small mixing layer will form around the compressible core region however no mixing of ambient gas and injected gas will occur within the core shock structures. As the jet travels further downstream this core region will begin to diminish due to momentum decay and the mixing layer surrounding it will grow until the core regions eventual collapse where full mixing of the injected and ambient gases will begin. After a transition region the jet will achieve self-similarity and thus can be termed fully developed.

3.5.3 Gaseous sphere injection model

The basis of the GSI model is rooted in the findings of Ouellette [173] and Ouellette and Hill [174] which state that momentum injection rate of the gas must be reproduced if mixing rate of the gas is to be reproduced. This is backed up by the findings of the various other equivalent nozzle approaches.

As noted previously, simulating flow through the nozzle and the proceeding shock structures is computationally expensive. The GSI model aims to simplify this and allow for simulations to be carried out on coarse grids by adapting the Lagrangian liquid spray model for gaseous injections. The main difference between the liquid and

gaseous injection models is when the transition from the discrete Lagrangian droplet phase to the continuous Eulerian bulk phase occurs. In liquid injection droplets will vapourise and transition to the bulk phase over a period of time once they have been heated to a given vapourisation temperature. In gaseous injection droplets will instead transition instantaneously once they have travelled a given distance from the injector nozzle defined by the length of the previously described jet core region. Energy exchange only occurs at the moment of transition and thus gaseous droplets stay at the same temperature they were injected at. Breakup, collision and droplet deformation, which play a pivotal role in liquid injections, are also neglected as surface tension is a property which only occurs at a liquid's interface. Injected gaseous droplets are essentially treated as "pseudo-liquids" until transition but will have all the correct properties of the intended gaseous fuel when transferred to the bulk phase. Momentum exchange is coupled between the discrete and continuous phase throughout. Upon transition all mass, energy and momentum of the droplet are handed over to the cell in which it transitioned producing a gas jet which is free to mix with the surrounding bulk gases.

Using the core length to determine transition of the spheres should be a reasonable approach as in a real underexpanded jet the ambient gases are not able to enter and mix with the injected gases in the jet core. This in turn means combustion of an underexpanded jet should be largely limited to the far-field zone as the fuel needs to mix with oxidiser for ignition/combustion to take place. Some optical experiments in the literature have backed up this assumption with the likes of Ishibashi and Tsuru [175] showing the natural gas flame being unable to traverse the near-field region directly following the nozzle exit during or after injection. Admittedly some combustion could take place in the transition region between the near and far-field and also in the mixing layer surrounding the jet core, however, the amount of mixing occurring in either region will be hard to quantify, yet further focus on this area could be a direction for future improvements to the model, e.g. something analogous to the liquid core length used in the KHRT breakup model for liquid injections where child droplets are shed from the core.

3.5.3.1 Original GSI model

Core length in the original GSI model was estimated using the findings of a study by Witze on air injection into air [176]. Witze defines the jet core as an inviscid region near the nozzle and through theoretical derivation, based on an incompressible form of Warren's axisymmetric jet theory [177], finds the core length, L_{c-orig}, to be

$$L_{c-orig} = 6.25 D_e, \tag{3.61}$$

where D_e is the nozzle exit diameter. Having an accurate core length estimation is vital for the success of the GSI model as it greatly influences jet penetration, with longer core

lengths leading to greater penetration. The original GSI model [161] was implemented in KIVA-3V CFD software and went on to alter the turbulence length scales, turbulence kinetic energy and turbulence kinetic energy dissipation rates in cells within the jet core and fully developed region, citing the tendency for the RNG k-ϵ model to overpredict gas jet diffusion and therefore underpredict penetration. While the turbulent round/-plane jet anomaly is well known and may be the crux of the issue it may also indicate some other underlying issues with the model as there are turbulence models which are fairly well suited to dealing with the issue such as the realizable k-ϵ model.

Helldorff and Micklow [178] examined a modified implementation of the GSI model in KIVA-3V and identified that part of the issue is likely the result of incorrect momentum coupling of the gas and droplet phase in KIVA-3V and shows good agreement with experimental data for subsonic jets without need for turbulence correction given the momentum coupling is adjusted. KIVA-3V stores the flow velocity field at cell vertices while all other properties are stored at cell centres, leading to a slight offset in momentum compared to mass placement in the mesh when transition occurs. The issue is exacerbated due to the velocity at each vertex being derived from the momentum equation leading to a single vertex greatly overpredicting velocity with the remainder underpredicting. The problem is more apparent in the GSI model compared to normal liquid injections due to a large number of parcels transitioning simultaneously in close proximity to one another at the end of the core length. In the current study the GSI model was implemented in ANSYS Fluent CFD software which uses a co-located scheme where the velocity field is stored at cell centres along with all other variables and thus should not suffer from the same issues.

3.5.3.2 Core length review

The core length derivation is another issue as pressure ratio is not factored in. Pressure ratio however, determines the makeup of the entire jet core [145] and thus its length is strongly dependant on the pressure ratio. If core length is underpredicted not only will penetration likely be underpredicted but full mixing of the injected fuel and oxidiser will take place too early leading to an earlier than desired onset of combustion.

The review of Franquet et al. [145] showed there is a clear correlation across a number of cases for supersonic core length increase as total pressure ratio increases. The supersonic core can extend further than the actual jet core but is nonetheless indicative of an increasing core length. Many other authors have noted the increase of pressure ratio leading to an increase in core length and Witze himself in an earlier paper [152] noted that jet core length can be estimated by the compressible free jet theory of Kleinstein [151] and stated

$$L_{c-KW} = 9.46 \left(\frac{\rho_e}{\rho_a} \right)^{\frac{1}{2}}, \tag{3.62}$$

where L_{c-KW} is the Kleinstein-Witze core length, ρ_e is the injected gas density at nozzle exit and ρ_a the density of the ambient gas downstream of the nozzle. Witze reviewed several experimental studies on underexpanded air jets and found the core length estimate fit well when compared to jet centerline velocity decay. A number of other studies have noted that the Kleinstein-Witze correlation can accurately predict jet centerline velocity decay [148, 179–182] indicating the core length estimation is likely reasonable. The following review of core lengths focusses on recent studies using choked convergent or straight nozzles with circular exit geometries at total pressure ratios which are most likely to be applicable at engine relevant conditions. An attempt is made to be consistent about where the core ends as the definition varies in the literature. Where reported the value at which centerline pressure/density ceases to fluctuate is taken or, if not available, mass fraction contours are used ($Y_i < 1$). Experimental and both RANS and large eddy simulation (LES) based CFD works are presented.

TABLE 3.2: Summary of core length review (*denotes when mass fraction contours were required).

Reference	Type of study	Jet composition	Total pressure ratio (η_0)	Core length normalised by nozzle exit diameter
Banholzer et al. [142]	Exp & CFD-RANS	Methane	5.0	15.0*
			10.0	20.7
			15.0	26.5
			20.0	28.0
			25.0	30.6
André et al. [183]	Exp	Air	2.14	8.0
			2.27	8.5
			2.97	11.0
			3.67	11.7
Li et al. [184]	CFD-LES	Nitrogen	5.6	11.0
		Hydrogen	5.6	18.0
Vuorinen et al. [141]	CFD-LES	Methane	4.5	8.9
			6.5	10.1
			8.5	11.0
			10.5	11.6
		Nitrogen	4.5	8.0
			6.5	11.7
			8.5	12.2
			10.5	13.8
Bonelli et al. [185]	CFD-RANS	Hydrogen	6.5	16.0
Traxinger et al. [143]	CFD-RANS	n-Hexane	8.5	48.0*
				79.0*
				124.0*

While not exhaustive, the review gives a clear indication of the importance of accounting for pressure ratio when estimating core length. As can be seen in Table 3.2 and Figure 3.3 a) an increase in pressure ratio leads to an increase in core length in all gases examined. There is however, clearly a wide variance in the reported core length values. This can be attributed to the differing experimental/setup conditions along with the difficulties associated with accurately modelling, and or measuring, the characteristics of the jet core. There is also not a clear indication of how exactly differing gases affect core length. From the two authors which examine multiple gases, Vuorinen et al. [141] showed that nitrogen, the denser gas, has slightly greater core lengths than methane, whereas, Li et al. [184] showed a considerable increase in core length for hydrogen (less

dense) compared to nitrogen. As a result, the proposed improved core length will simply depend on pressure ratio as the relationship between differing gases still appears to be unclear. A clear correlation between jet core length, L_c, and total pressure ratio is found and a new core length estimation of

$$L_c = 5D_e\sqrt{\eta_0} \tag{3.63}$$

is proposed. Figure 3.3 compares the core length prediction of Equation (3.63) with that of the original GSI model, Equation (3.61), and the Kleinstein-Witze correlation, Equation (3.62), for hydrogen and methane assuming they are ideal gases and nozzle exit temperature is equal to ambient temperature. The original GSI model prediction is only adequate for very low pressure ratios and is likely only truly applicable for subsonic jets. For a very low density gas such as hydrogen the Kleinstein-Witze correlation proves to be a poor indicator of core length. This is somewhat to be expected as most of the studies for which it is based dealt with higher density air jets. The correlation is much better when applied to methane (quite similar density to air) and fits remarkably well with the plotted data. The proposed improved core length estimation of Equation 3.63 gives almost exactly the same trend as the Kleinstein-Witze methane case and fits equally well with the data without the need to account for the variable density of the gases. Furthermore, the high pressure ratio cases studied in Traxinger et al. [143] of supercritical n-hexane fit very well with the core length estimate, Figure 3.3 b), indicating applicability over the full range of possible pressure ratios and fuel densities which will be present in HPDI engine operation.

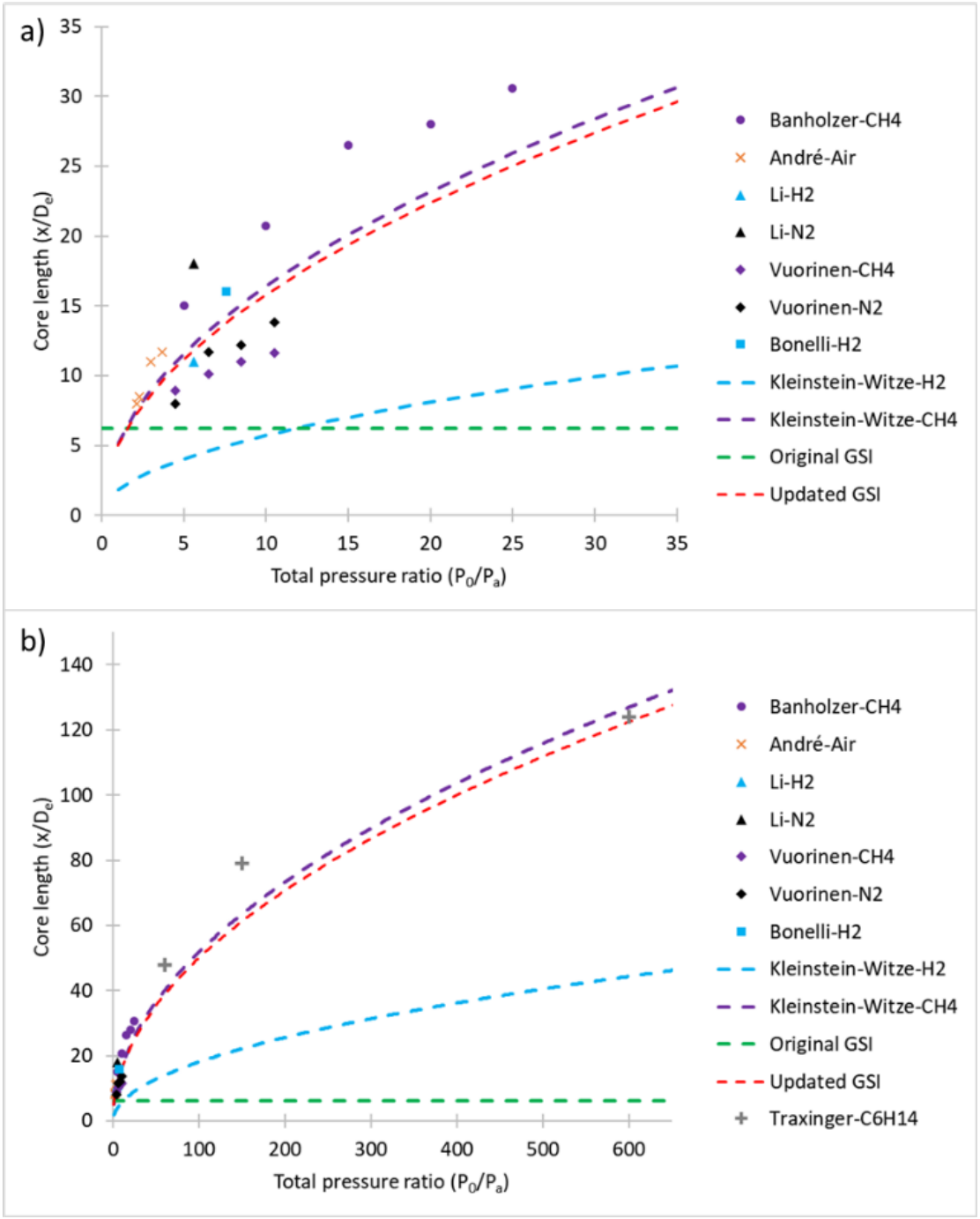

FIGURE 3.3: Core length review summary. Core length normalised by nozzle exit diameter plotted vs. total pressure ratio, a) low to moderate pressure ratios, b) high pressure ratios.

We find that there is a general lack of studies dedicated to characterising core length with Banholzer et al. [142] being the only recent study found which specifically focusses on it. Further research into identifying the various factors which may affect the core length value such as pressure ratio, differing gases, discharge coefficient, nozzle geometries, cross flows, combustion, etc. must be carried out. We also not that the vast majority of the studies in the literature focus on the near-field underexpanded flow

structures, in particular the mach disk, but lack validation and study of the macroscopic structures in the far-field and in the transition region where the compressible core collapses.

In terms of modelling, core length is calculated at each iteration in the simulations and thus will account for changes due to pressure ratio decrease when compression and combustion are present. When a particle's distance from the injector exceeds the core length it will entirely transition to the bulk phase, transferring all its mass, momentum and energy to the cell in which it resides. It should be noted that one of the main assumptions of the GSI model is that combustion in the mixing layer is negligible. Using a variable core length increases the reliance on this assumption but it should still be reasonable as very high pressure ratios will only be present in cases where gas is injected much earlier than TDC, e.g. spark ignition or some form of homogeneous compression ignition, and thus combustion would not be taking place during injection anyway. Further improvements to the model should address this assumption however.

3.5.3.3 Injection and particle properties

As we are not modelling the actual underexpansion process in which the injected gas quickly expands to reach ambient pressure once exiting the nozzle, another method must be applied to properly define the jet properties. Currently the GSI model relies on experimental data to set cone angle. While using experimental data to determine jet width and cone angle is likely the best course of action, said data is rarely available so a theoretical derivation is better suited. The original implementation of the GSI model [161] simply used the real nozzle exit diameter with a cone angle measured from images of the jet but as noted this isn't practical. Whitesides et al. [162] and Wang et al. [167] used the pseudo-Mach disk assumption [173] to set gas and injector properties. The pseudo-Mach disk assumption assumes the nozzle is choked and isentropic expansion of the gas occurs at nozzle exit. Mass flow rate and velocity at the Mach disk is assumed to be equivalent to nozzle exit conditions and injected gas density is assumed to be equal to the density at chamber conditions, then the equivalent injection diameter can be calculated as mass flow rate at the injector is equivalent to that at the Mach disk. In a real underexpanded jet the expansion process at nozzle exit leads to a rapid acceleration of the jet. Velocity on the centerline within the jet core will fluctuate at values about Mach 1 while the surrounding core is supersonic, this is then followed by rapid decay once the core region ends. The acceleration of the jet caused by the expansion means that setting an initial jet velocity of Mach 1 may lead to underprediction in jet penetration rate.

The derivation of Yüceil et al. [150], which assumes adiabatic expansion of the injected gas to chamber pressure, is used instead as it provides a way to estimate jet velocity, V_M, temperature, T_M, and diameter, D_M, at the Mach disk leading edge which is then

used to set initial injection conditions. Assuming an ideal gas and choked converging/straight nozzle

velocity is given by

$$V_M = V_e \left(1 + \frac{\eta_e - 1}{\gamma \eta_e}\right), \tag{3.64}$$

temperature by

$$T_M = T_e \left(1 + \frac{\gamma - 1}{2}\left(1 - \left(\frac{V_M}{V_e}\right)^2\right)\right), \tag{3.65}$$

and diameter by

$$D_M = \sqrt{\eta_e \frac{T_M}{T_e}\frac{V_e}{V_M}}, \tag{3.66}$$

where V_e is the isentropic nozzle exit velocity and T_e is the temperature of the gas at nozzle exit. Pressure ratio can vary and therefore so can the above values, however, for simplicity an expected average value of η_e is taken on a case by case basis.

Whitesides et al. [162] and Wang et al. [167] also assumed the leading edge of the Mach disk barrel was at the injector nozzle, but the length of the Mach disk increases with pressure ratio so this assumption will become increasingly more inaccurate as pressure ratios increase. Mach disk length is well studied, and a number of authors have proposed estimates [186–189]. The detailed review of Franquet et al. [145] on the topic comes to the conclusion that the best estimate for Mach disk length, L_M, for a converging nozzle was provided by Crist et al. [187] which uses the assumption that pressure behind the Mach disk is equivalent to chamber pressure to find

$$L_M = C_x D_e \sqrt{\eta_0}, \tag{3.67}$$

where $C_x = 0.645$ is a constant. More recent works are in agreement with Crist and have shown only small variations of the constant C_x [63, 148, 190, 191]. This estimate is then used when determining the position of the injector in the computational domain (also factored into core length computation) with an assumed average value of η_0.

Half jet cone angle, θ_e, is sensitive to a number of factors and there exist many discrepancies in the literature both in how to go about measuring spreading and the difficulties in doing so as well as the results themselves. This means that it will be difficult to adequately define a method for setting cone angle so tuning will likely be necessary. The half jet cone angle which is input in Fluent, θ_M, defined at the Mach disk leading edge, will generally be different to θ_e as depending on the pressure ratio, the initial expansion may be much more or less rapid than the proceeding spreading and can be estimated

using

$$\theta_M = \arctan\left(\frac{L_c \tan(\theta_e) - \frac{D_M - D_e}{2}}{L_c - L_M}\right) = \arctan\left(\frac{\tan(\theta_e) - \frac{D_M - D_e}{2L_c}}{0.871}\right). \tag{3.68}$$

Again, an average value of η_0 is used to determine L_c. For consistency, in the remainder of this study a commonly reported value in the literature of $\theta_e = 12°$ [63, 138, 139] is used, this value is also in line with those used in previous implementations of the GSI model [161, 162].

In the GSI model the density and diameter assigned to the injected droplets is only relevant to the particle force balance equation as the modelling of breakup, collision, coalescence, etc. is not required. Fluent struggles to properly model particle drag when droplet density is less than 10 times greater than the fluid density, as is normally the case in gaseous injections. It makes sense to use a pseudo-density as particle density has no impact on the actual mass delivered at the end of the core length, only on the amount of drag the particle experiences throughout its trajectory and therefore final velocity at the end of the core. The particle force balance can be written as

$$\frac{\mathrm{d}\overline{u}_p}{\mathrm{d}t} = \frac{18\mu C_D R_e}{24\rho_p d_p^2}(\overline{u} - \overline{u}_p) \tag{3.69}$$

where $\overline{u}_p$ is the particle velocity, $\overline{u}$ the fluid phase velocity, μ is the molecular viscosity of the fluid, ρ is the fluid density, ρ_p is the particle density, d_p is the particle diameter, R_e is the relative Reynolds number defined as

$$R_e = \frac{\rho d_p \left|\overline{u}_p - \overline{u}\right|}{\mu}, \tag{3.70}$$

and C_D is the drag coefficient for a spherical particle which is set equal to 0.424 as R_e is assumed to be large.

Small amounts of momentum shedding will occur as the core region penetrates the chamber which leads to the eventual collapse of the core. Using the assumption that velocity of the jet at the end of core should be roughly equal to velocity at the nozzle exit [151, 152], the average rate of velocity decay throughout the core can be estimated by

$$\frac{\mathrm{d}\overline{u}_p}{\mathrm{d}t}(x = L_c) = \frac{(V_M - C_d V_e)(V_M + C_d V_e)}{2L_c}, \tag{3.71}$$

where nozzle discharge has been accounted for and is assumed to apply only to the exit velocity. Then using Equations (3.69) and (3.71) with $\overline{u} << \overline{u}_p$ it follows that the particle density required to achieve a reasonable velocity at the end of the core can be

approximated by

$$\rho_p = \rho \left(\frac{0.159 L_c \left(V_M + C_d V_e \right)}{d_p \left(V_M - C_d V_e \right)} \right) \tag{3.72}$$

Particle density is then adjusted at each time step both initially and throughout a given particles trajectory and a constant (arbitrary) particle diameter of 5e - 6 is used.

3.5.4 Improvements to the GSI model

The proposed improved model will forgo the alterations of the turbulence model in the core and jet region. Instead an improved core length estimation using Equation (3.63), along with the use of the previously described theoretical derivations to define injector and particle properties are implemented. Both the variable core length and various Mach disk quantities used in this study have not been previously applied to the GSI model. Figure 3.4 shows a schematic representation of the updated GSI model and Appendix A provides the UDF source code used to implement the model in ANSYS Fluent.

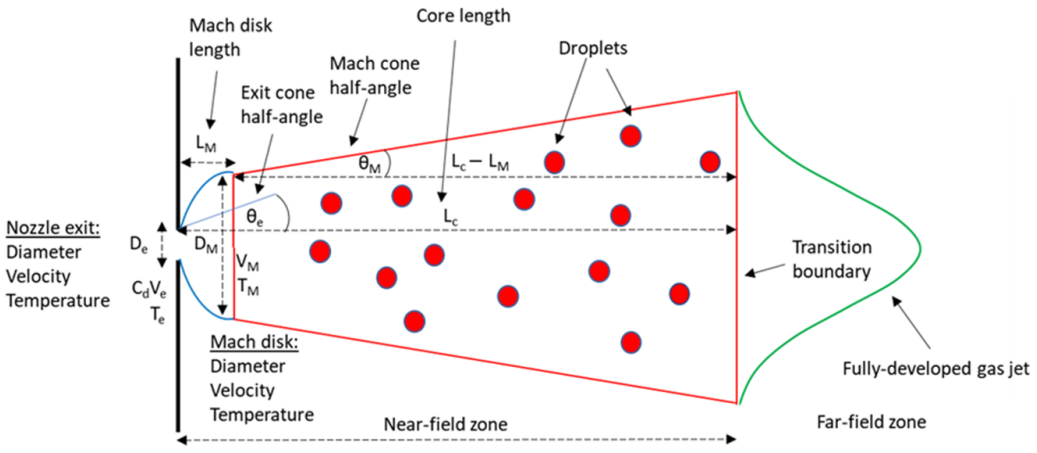

FIGURE 3.4: Schematic of the modified GSI model.

3.6 Liquid injection discrete phase modelling

The general coupled solution procedure during a given time step for both the GSI model and the liquid injection discrete phase model is shown in Figure 3.5 and can be broken down into the following steps:

1. At the beginning of a given time step the flow field is calculated prior to the discrete phase.

2. Particle trajectories are then calculated for each discrete phase injection.
3. The continuous phase is then recalculated accounting for the exchange of mass, momentum and energy with the discrete phase, as determined by the previous particle calculation.
4. Again recalculate the particle trajectory using the updated flow field calculation.
5. Repeat steps 3 and 4 until convergence when both the continuous and discrete phases stop changing then continue onto the next time step.

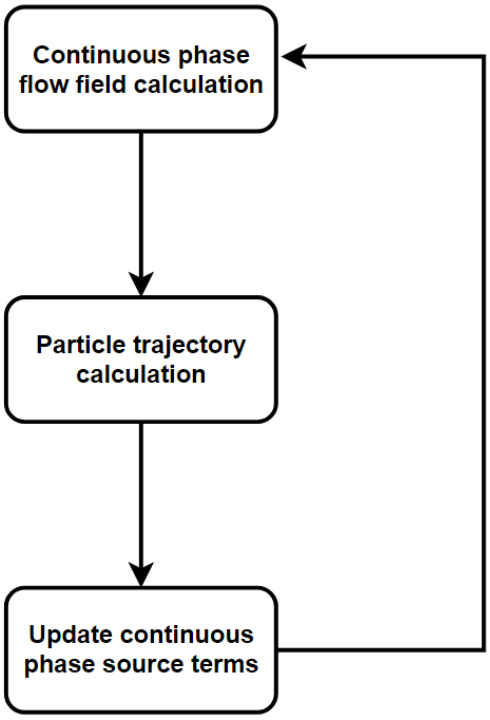

FIGURE 3.5: Coupled discrete phase solution procedure.

Modelling of liquid injections differs from the GSI model in some key areas:

- Droplet properties represent the actual liquid properties of the injected fuel.
- Transition from the discrete phase to the continuous phase is governed by the vapourisation/boiling temperature of the injected liquid and occurs over a given time period rather than being instant. This also means that heat exchange between the droplet and continuous phase needs to be applied. That is to say the laws obeyed by the liquid droplets are a) inert heating, b) vapourisation and c) boiling.
- Liquid physics such as atomisation, breakup, coalescence and collision need to be modelled as well as a drag law which accounts for deformation of the droplets.

- Interaction of liquid droplets with chamber walls needs to be modelled.

Inert heating is applied when a given droplet is below the specified vapourisation temperature of the injected liquid; vapourisation occurs when the vapourisation temperature is exceed but boiling temperature of the liquid is not and boiling starts when the boiling temperature is exceeded.

A plain orifice atomiser model combined with Kelvin-Helmholtz Rayleigh-Taylor (KHRT) primary and secondary breakup [50] is applied to deal with atomisation and breakup. Stochastic collision model[192], dynamic-drag model [193] and an impingement/splashing wall-film model at the chamber boundaries [194, 195] are applied to account for the various remaining phenomena involved in liquid fuel injections. In both types of discrete phase injections, an automated tracking scheme which changes between a high order runge-kutta and low order analytical scheme is used to track particles, grouped into parcels, as they traverse the continuous phase and the discrete random walk (DRW) stochastic tracking model [196] predicts turbulent dispersion of particles.

3.7 Boundary conditions

In most of the engine simulations the domain is decomposed into a sector due to the symmetry of the injectors to reduce computational costs. As a result periodic boundary conditions are set at the side faces of the sectors. Constant temperature boundary conditions (which assume the engine has already been run for a number of cycles) are applied to deal with heat transfer at the gas-solid boundaries. Using the constant temperature condition means that the wall need not be meshed and is a reasonable assumption due to the relatively small time scales involved. Wall functions are used to deal with near-wall interactions unless stated otherwise, as well as the previously noted wall-film model when liquid droplet impingement occurs.

In terms of inflow and outflow boundary conditions, in all of the sector engine simulations (and freestream studies) sources from the discrete phase model are the only inflow of matter. Mass flow rate profiles are prescribed and provided in the relevant sections. In the optical spark ignition full engine mixture formation simulations the gas exchange process is modelled using pressure inlet and outlet boundary conditions which are prescribed by experimentally measured profiles and provided in the specific section as well as the mass flow rate profiles for the discrete phase injection.

3.8 Solver and numerical setup

All numerical simulations were carried out using three-dimensional unsteady Reynolds Averaged Navier-Stokes (URANS) approach. Simulations were performed on the University of Southampton IRIDIS 4 high performance computing cluster by employing commercial CFD software ANSYS Fluent 19.1.

Fluent's pressure based solver is employed to solve the conservation equations using finite volume method. A co-located scheme stores computed variables at cell centers and utilises the Rhie-Chow algorithm [197] to stop checker-boarding. Pressure Implicit with Splitting of Operators (PISO) pressure-velocity coupling algorithm [198] with neighbour and skewness correction is used to reformat the continuity equation and obtain a pressure field. Second order upwind schemes are used for the spatial discretisation. Least squares cell-based method is used to compute gradients. First-order implicit time-stepping is employed to maintain accuracy and stability due to variable time step profiles generally being used in engine simulations during fuel injection and combustion. Convergence criteria are set to converge at residuals of 1e-3 apart from energy and post-processed scalars which are set to 1e-6. In all cases injected mass is also monitored to ensure the correct intended mass is delivered. Max iterations per time step are set to 50 with up to 10 post-time step iterations. Figure 3.6 Table 3.3 outlines and summarises of numerical methods employed.

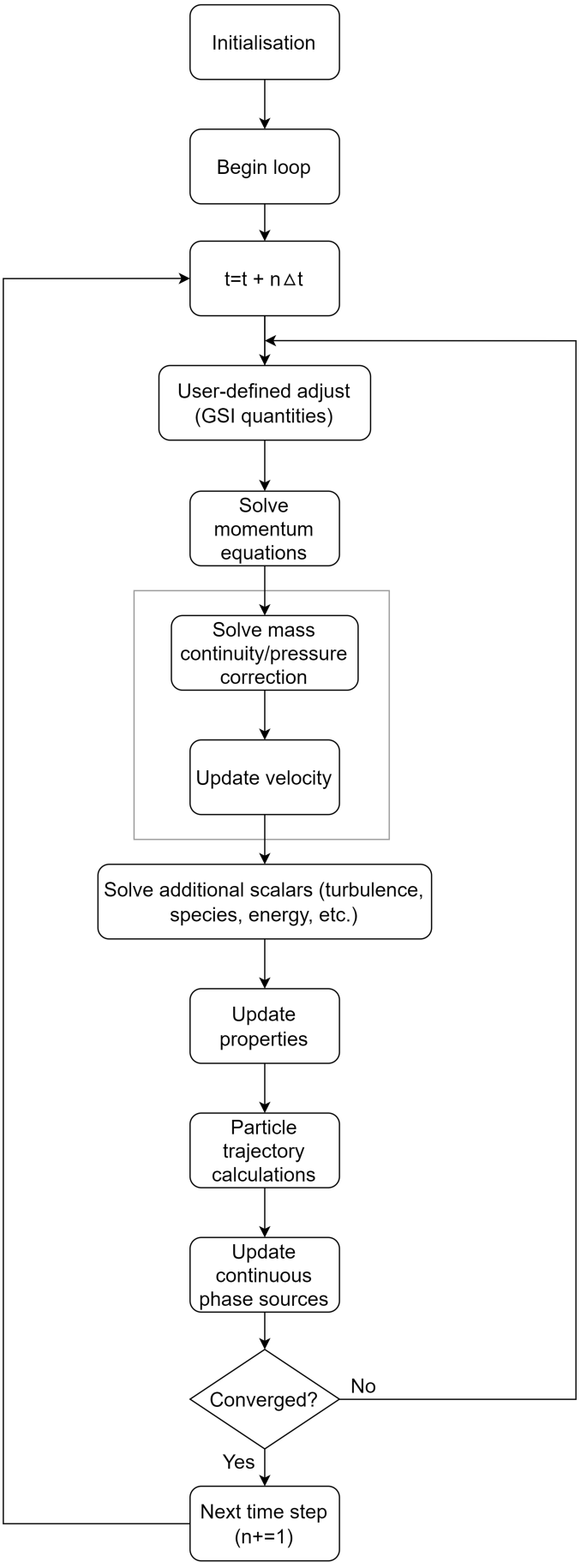

FIGURE 3.6: Fluent pressure-based segregated solver solution procedure.

TABLE 3.3: Summary of numerical methods employed during simulations.

Description	Parameter	Method/model/value	Applicable chapters/sections
Solver	General	Pressure-based	All
Pressure-velocity coupling	Flux type	Rhie-Chow	All
	Scheme	PISO	All
	Skewness correction	1	All
	Neighbour correction	1	All
Spatial discretisation	Gradient	Least squares cell based	All
	Density	Second order upwind	All
	Momentum	Second order upwind	All
	Energy	Second order upwind	All
	κ	Second order upwind	All
	ϵ	Second order upwind	All
	Mean mixture fraction	Second order upwind	4.3
	Mixture fraction variance	Second order upwind	4.3
	Species ($N-1$ equations)	Second order upwind	4.4, 5, 6
	Pollutant NO_x	Second order upwind	4, 5.4, 6
	Pollutant soot mass	Second order upwind	4, 5.4, 6
	Pollutant soot nuclei	Second order upwind	4, 5.4, 6
Temporal discretisation	Time	First order implicit	All

Chapter 4

Numerical Modelling of an Intake Induction Diesel-Hydrogen Dual-Fuel Engine Operating with a Novel Constant Volume Combustion Phase Strategy

4.1 Background

As noted in Section 2.3.3.1, low load combustion and performance characteristics greatly deteriorate as hydrogen energy share is increased during intake induction diesel-hydrogen dual-fuel operation. This is due to a reduced pilot not providing enough energy to allow for ignition of the lean premixed charge and also due to the pilots reduced penetration not creating a large enough ignition kernel. Penetration is important as the pilot will entrain hydrogen along its trajectory and the greater the penetration the more hydrogen combustion which will occur in the vicinity of the diesel injection and thus increase the likelihood of flame spreading. A secondary factor is the reduced temperatures also not allowing for any autoignition of the hydrogen-air mix, which while not ideal, can often aid with increasing combustion efficiency. The current literature is lacking in studies focused on solving these LL issues with the only investigation focussed on the topic coming from Dimitriou et al. [59, 76] who found that high levels of EGR and pilot injection optimisation were the best strategies for high HES performance improvements. In this chapter we propose to apply a novel constant volume combustion phase (CVCP) strategy which aims to enhance the pilot injections combustion efficiency along with in-cylinder temperature increase to address the LL high HES ignition problem.

One of the major operating points of conventional internal combustion engines is the piston dwelling near TDC which increases the time allowed for combustion. Further increasing this dwell time has the potential to improve the quality of combustion and therefore increase performance while simultaneously reducing pollutant emissions such as *CO*, soot and UHC. In theory the most efficient cycle for a given internal combustion engine is the ideal Otto cycle [12, 199]. While many combustion strategies aim to achieve the efficiency levels of the Otto cycle, none in practice are able largely due to the lack of combustion occurring at a constant volume. Diesel engines in particular are largely designed with the constant pressure combustion cycle in mind so there is potential to improve performance by incorporating a constant volume combustion phase. Conventional internal combustion engines use simple crank-slider mechanisms to convert linear work to rotational torque which means that the piston can only move between TDC and bottom dead centre (BDC) at a frequency proportional to engine speed. Combustion however occurs over a fixed period and is largely unaffected by engine speed. This means that any combustion occurring before TDC incurs negative work and combustion occurring during the expansion does not reach its maximum thermal potential due to reductions in pressure and temperature since combustion is not occurring at a constant volume. Reducing crank rotational velocity greatly, or ideally completely, at TDC while increasing velocity during the expansion and or compression stroke to maintain average engine speed is one such practical way to allow for a greater amount of combustion to occur at a constant volume.

A number of authors have shown the advantages of increasing piston dwell time near TDC [200–205]. Chen et al. [200] controlled piston trajectories and rotational velocity with an electric motor/generator leading to an 11% increase in work output compared to conventional operation when piston velocity was slowed at TDC. Dorić et al. [201] modelled a SI engine which combined variable compression ratio and engine displacement to give increased amounts of constant volume combustion due to slower piston movement at TDC and BDC, leading to increased performance. Variable compression ratio engines are promising in this regard as they can be adjusted based on operating conditions of the cycle [202]. Zhang et al. [203] modelled a free piston engine with asymmetric piston trajectories and showed a reduction in NO_x, *CO* and UHC emissions and improvements to performance by increasing piston dwell time near TDC. The same group also showed the applicability of HCCI and hydrogen combustion when using similar piston trajectories [204, 205].

Use of a full constant volume combustion phase has the potential to increase CI engine performance and substantially reduce *CO*, UHC and soot emissions. A CVCP allows for the ignition delay phase, premixed charge combustion phase and a large part of the mixing controlled combustion phase to all occur at top-dead centre [206]. This leads to a high quality complete combustion of the fuel-air mix, and allows for the full combustion pressure which is built at TDC to drive the piston, unlike in a conventional CI

engine where a significant amount of combustion is still occurring during the power stroke and any combustion which happened during the compression stroke will have incurred negative work penalties [199, 207]. The constant volume combustion strategy should benefit both modes of diesel-hydrogen dual-fuel combustion (HPDI and intake induction) for similar reasons. Particularly, this strategy should be able to tackle the aforementioned poor combustion/ignition problem of low load intake inducted hydrogen operation due to improved pilot combustion and higher in-cylinder temperatures being maintained for an extended time which will aid in the ignition/flame spreading within the premixed hydrogen and oxidiser. For HPDI of hydrogen the benefits will likely be less pronounced but should still allow for improved performance and a reduction in carbon emissions (explored in Chapter 6). Figure 4.1 shows a comparison of pressure-volume diagrams for an Otto cycle, a conventional diesel engine cycle and the proposed CVCP cycle, where the integration of pressure with respect to volume between BDC of the expansion stroke and BDC of the intake stroke gives the net-work output (area between the curves).

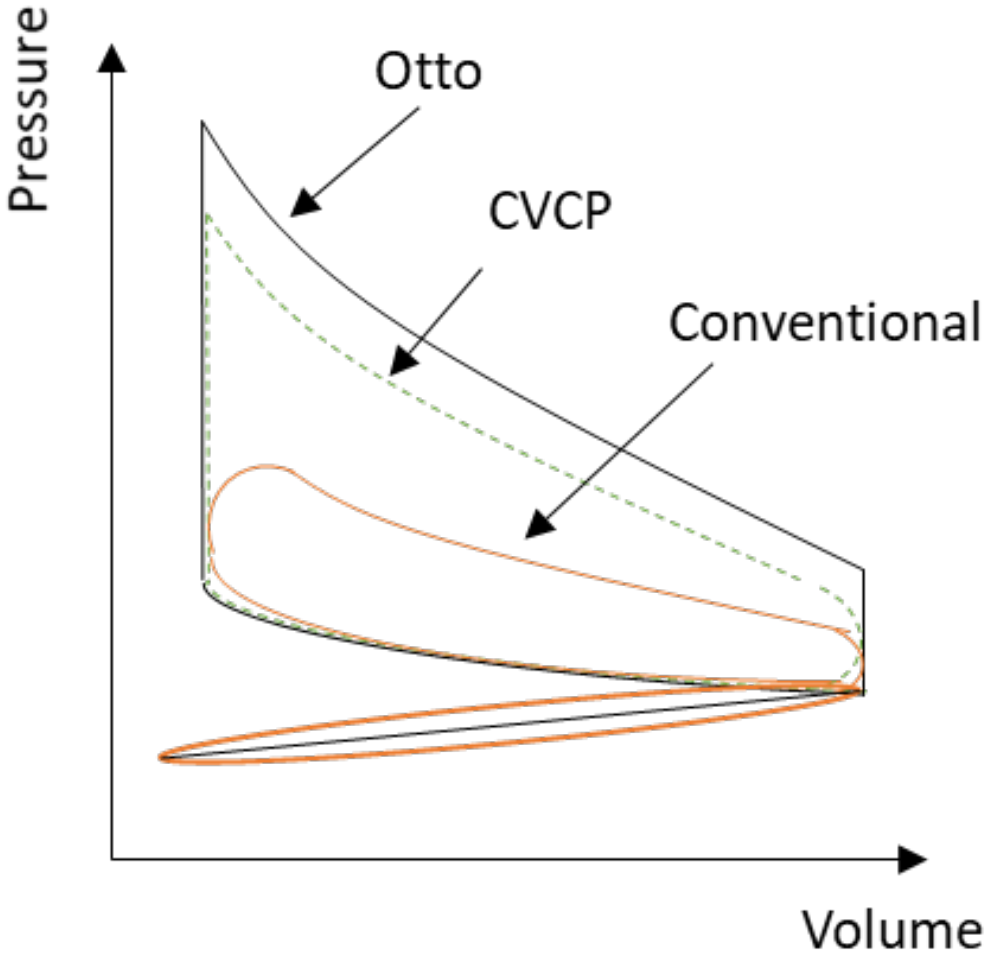

FIGURE 4.1: Pressure-volume diagram for ideal Otto, CVCP and conventional engine cycles

Our industrial partner Covaxe are developing an opposed piston axial engine configuration which operates with a constant volume combustion phase [208]. As seen in Figure 4.2, the initial design of the engine consists of opposed pistons which drive two cams mounted directly on the main drive shaft. The pistons meet at TDC where fuel is injected and combustion takes place. The cams are profiled so as to hold the pistons together at TDC for the duration of fuel injection until combustion is virtually completed. The engine is designed to run under the CVCP cycle and aims to improve thermal efficiency due to higher in-cylinder pressures and temperatures while reducing carbon-based emissions due to a higher quality of combustion compared to the conventional cycle.

Working with Covaxe two studies are carried out in this chapter. The first, Section 4.3, addresses pure diesel operation and is focussed on the impacts of varying the start time and duration of the CVCP. The second, Section 4.4, applies the findings of the

initial study and extends the modelling framework to an investigation on the effects of a CVCP on intake inducted diesel-hydrogen dual-fuel operation at low and high load for increasing hydrogen energy shares with a specific focus on improving low load performance.

In this study we take a simplified approach whereby a 4-stroke single piston engine is modelled using a piston lift profile which holds the piston at TDC during fuel injection and combustion. This decision was made due to the current lack of experimental data available to validate an accurate geometry. The simplified approach will still provide results of significance with regards to emissions and performance trends which should roughly carryover to the real engine. The key findings of the present studies will be considered for the optimisation CVCP periods in the CVCP opposed piston engine currently being developed by Covaxe.

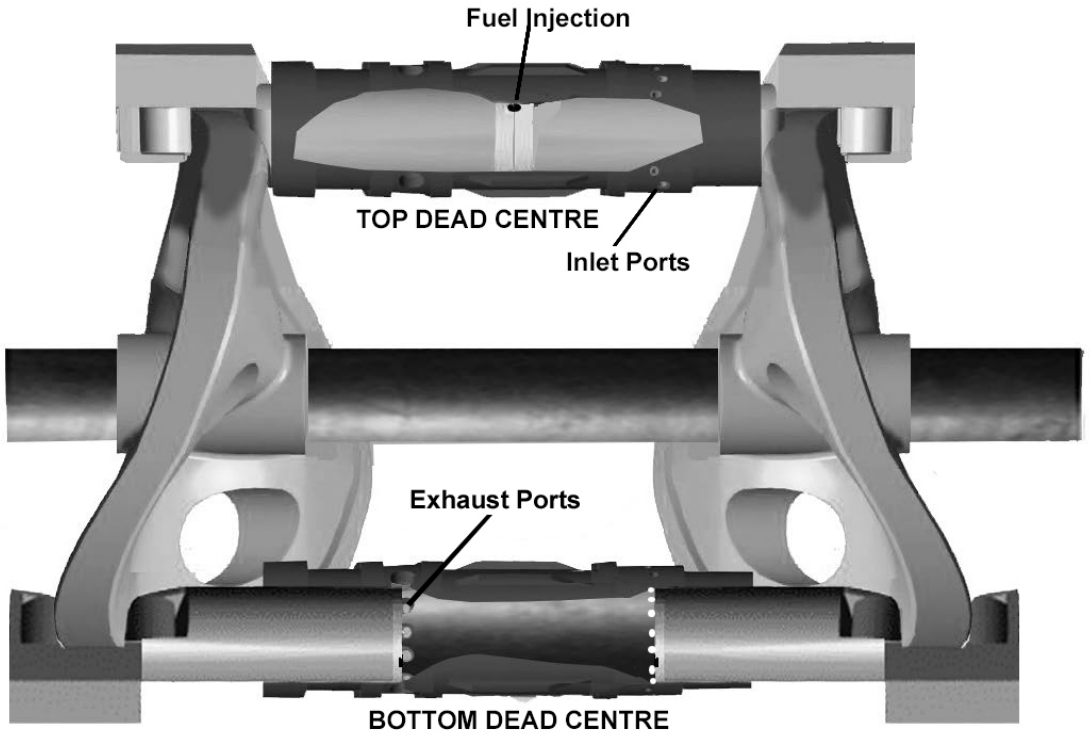

FIGURE 4.2: Schematic of the opposed piston CVCP CI engine configuration being developed by Covaxe

4.2 Numerical setup

Validation is carried out using the four-stroke turbocharged diesel-hydrogen dual-fuel CI engine experimentally studied by Tsujimura et al. [58]. The simulations are validated using data for engine geometry, in-cylinder pressure, heat release rate, injected fuel mass, injection timings and initial charge compositions. For continuity the same

engine is used in Section 4.3 and 4.4. This engine specification shares a number of similarities with the prototype CVCP engine described in Section 4.1. Table 4.1 provides engine specifications for the reference engine at low and high load conditions.

TABLE 4.1: Engine specifications for the experimental reference engine at low and high load [58].

Description	**Low load**	**High load**
Bore (mm)	115	115
Stroke (mm)	125	125
Compression ratio	17.5	17.5
Initial absolute pressure (bar)	1.1	1.6
Injector holes in full cylinder	7	7
Engine speed (RPM)	1500	1500
Pilot signal start of injection (°CA)	713.1	710.1
Pilot diesel injection volume (mm^3)	1.0	1.2
Main signal start of injection (°CA)	724.1	726.1
Main diesel injection volume (mm^3)	22-2.2	76-21
Hydrogen energy share (%)	0-90	0-73
Total fuel energy (J)	821	2756
IMEP (MPa)	0.3	0.9

A 51.43° geometry representing $1/7^{th}$ of the full combustion chamber was created with SOLIDWORKS and then meshed using ANSYS Workbench (Figure 4.3). Meshing a sector allows for a large reduction in computational costs and is possible due to the symmetry of the 7 injector holes in the combustion chamber as well as the IVC mixture in CI engines generally being fairly homogeneous. Periodic boundary conditions are set at the side faces of the cylinder to represent the symmetry. The mesh is refined in the piston bowl region and inflation layers are added to the piston walls. A mostly hex mesh is used to reduce numerical diffusion and increase computational efficiency. Due to movement of the piston, a rigid dynamic sliding mesh is used to model compression and power strokes. Constant temperature boundary conditions are set such that the chamber top wall and piston walls are at 600 K and 650 K respectively while the remainder, excluding the periodic side faces, are set to 500 K.

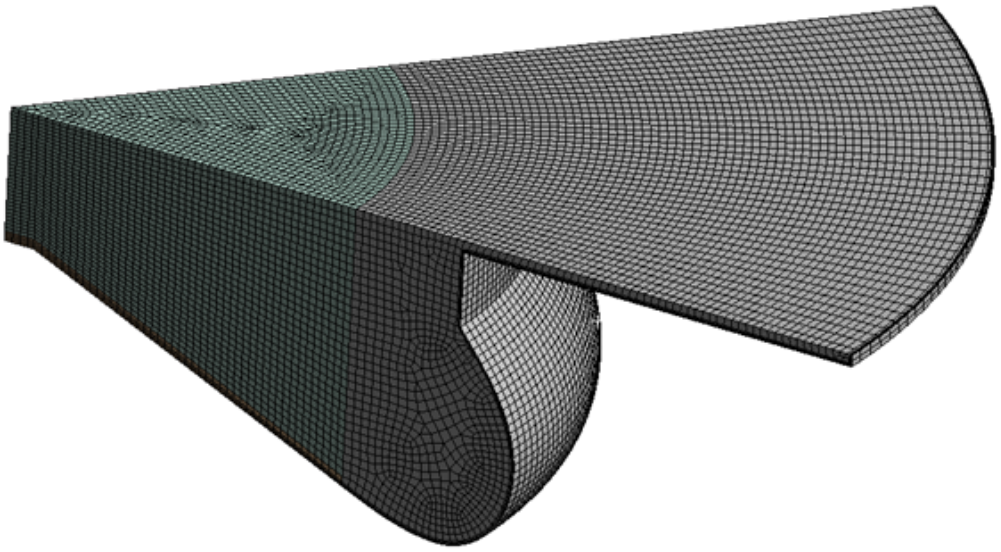

FIGURE 4.3: Medium density mesh at TDC-CVCP.

The major differences between the modelling approaches taken for the pure diesel operation studied in Section 4.3 and the diesel-hydrogen intake induction simulations carried out in Section 4.4 are as follows:

- Combustion model - Diesel unsteady flamelet for the pure diesel case vs. EDC for the dual-fuel case.
- Chemical mechanism - Nordin reduced n-heptane mechanism [129] vs. Nordin reduced n-heptane mechanism [129] + Kéromnès et al. detailed hydrogen mechanism [43].
- Mesh density - Medium density was adequate in the diesel study but the Fine mesh was required for dual-fuel.
- Initialisation - Initial gas composition is used as a vector for the introduction of hydrogen fuel in the dual-fuel case to avoid extra injection and gas exchange modelling as the well mixed fuel-oxidiser assumption is sufficient.

Further details about the full modelling setup can be found in Chapter 3.

4.3 Effects of constant volume combustion phase on operational characteristics of a pure diesel fuelled compression ignition engine

A preliminary study on pure diesel CI engine operation is carried out to asses the benefits of a constant volume combustion phase in a conventional engine setup and the learnings applied to dual-fuel operation in Section 4.4.

In this work the effect of start time and duration of CVCP at low and high loads is investigated. Simulations of both conventional and CVCP cycles are carried out and combustion characteristics, efficiency and emissions are compared. Section 4.3.2 focuses on the effects of CVCP start time; Section 4.3.3 investigates the effects of CVCP duration and Section 4.3.4 examines further emission reduction strategies.

Figure 4.4 a) shows the schematic of the conventional "Base" test cases where fuel injection occurs when the piston is near TDC and then combustion with normal reciprocating motion, while Figure 4.4 b) shows the schematic of CVCP test cases where fuel injection and combustion occur at TDC. Figure 4.5 shows an example of the piston profiles used in the test cases. In this investigation the convention that 720 degrees crank angle (°CA) refers to TDC at the end of the compression stroke is followed.

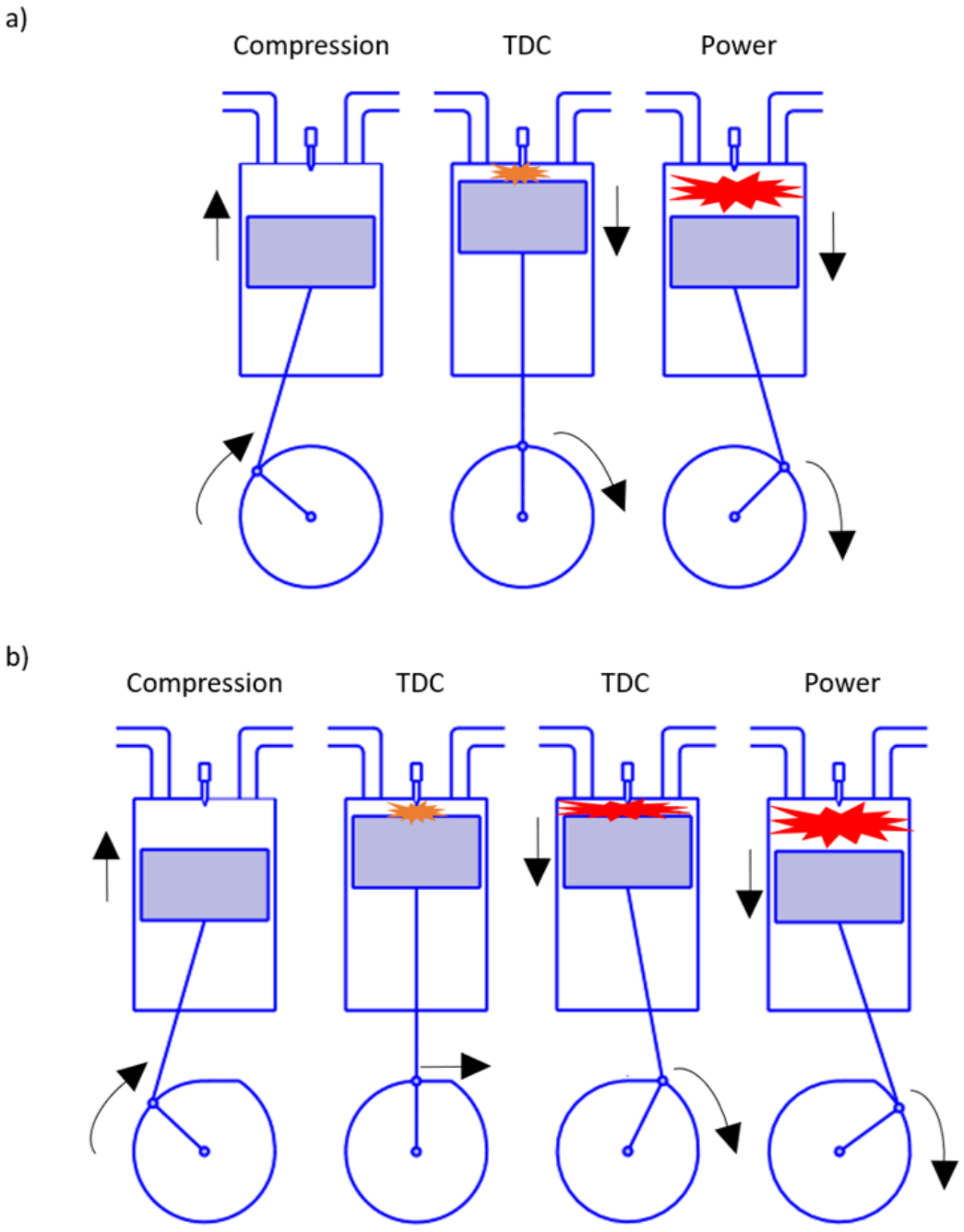

FIGURE 4.4: (a) Schematic of the conventional Base test case, (b) Schematic of CVCP test cases.

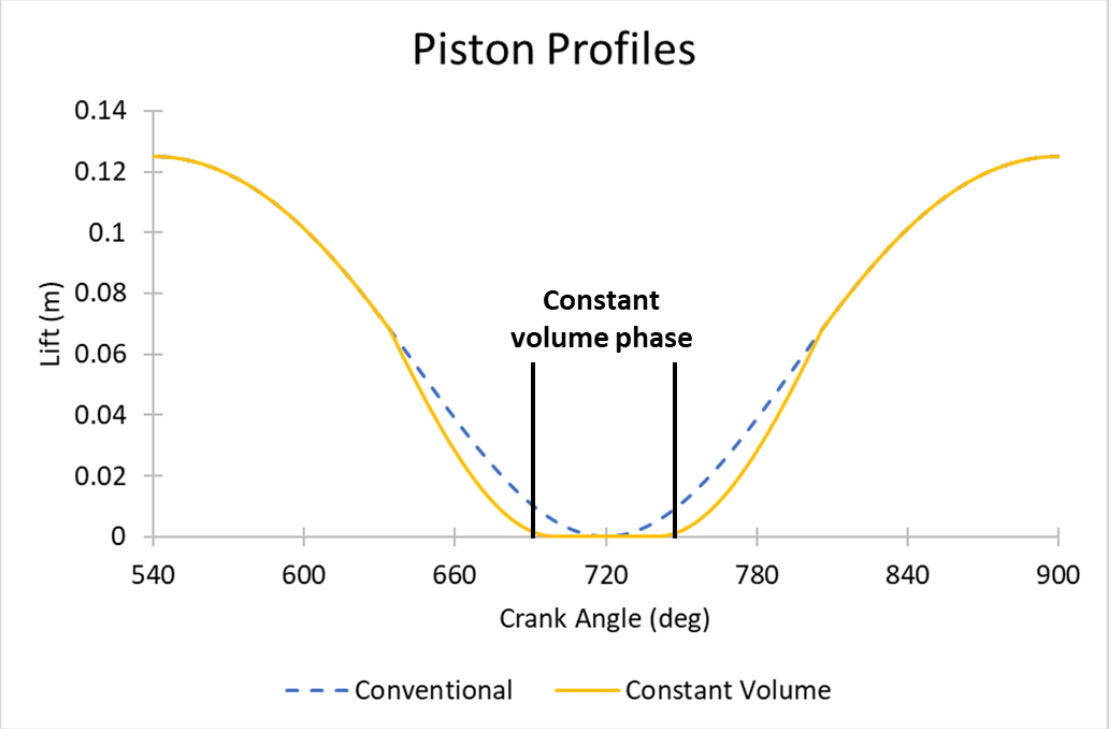

FIGURE 4.5: Example piston profiles used in the conventional and constant volume test cases.

4.3.1 Validation and mesh sensitivity analysis

Results using 3 different mesh resolutions were compared with experimental conventional engine data in order to select a mesh for the study. Mesh densities were varied by changing minimum element size and maximum face size to ensure the solution is mesh independent and accurate. Table 4.2 details the number of elements in each mesh at IVC.

TABLE 4.2: Mesh densities for validation and mesh sensitivity analysis

Mesh density	Elements	Run time
Coarse	443868	≈7h
Medium	746063	≈13h
Fine	1177867	≈19h

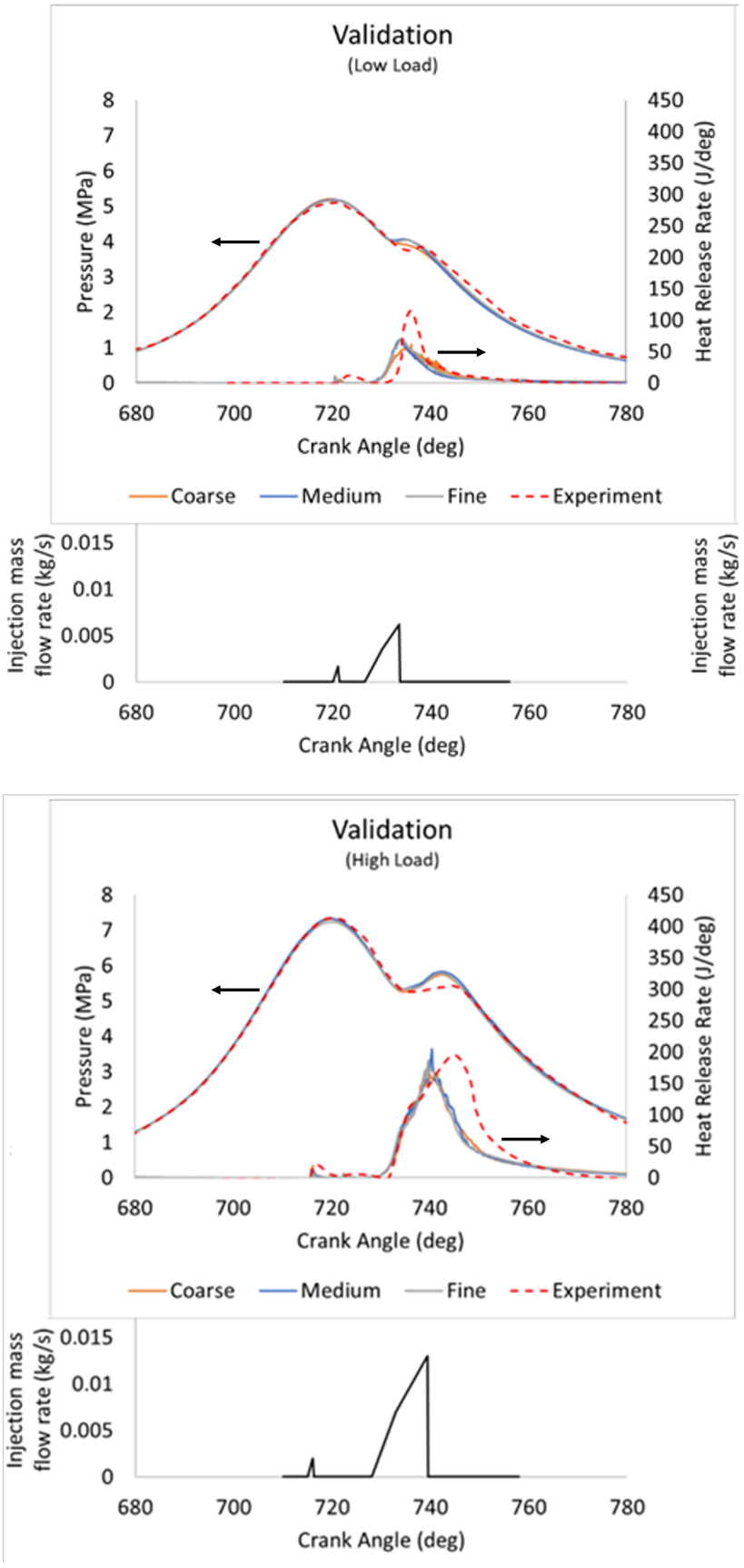

FIGURE 4.6: Pressure and HRR validation for the high and low load simulations against the experimental reference [58].

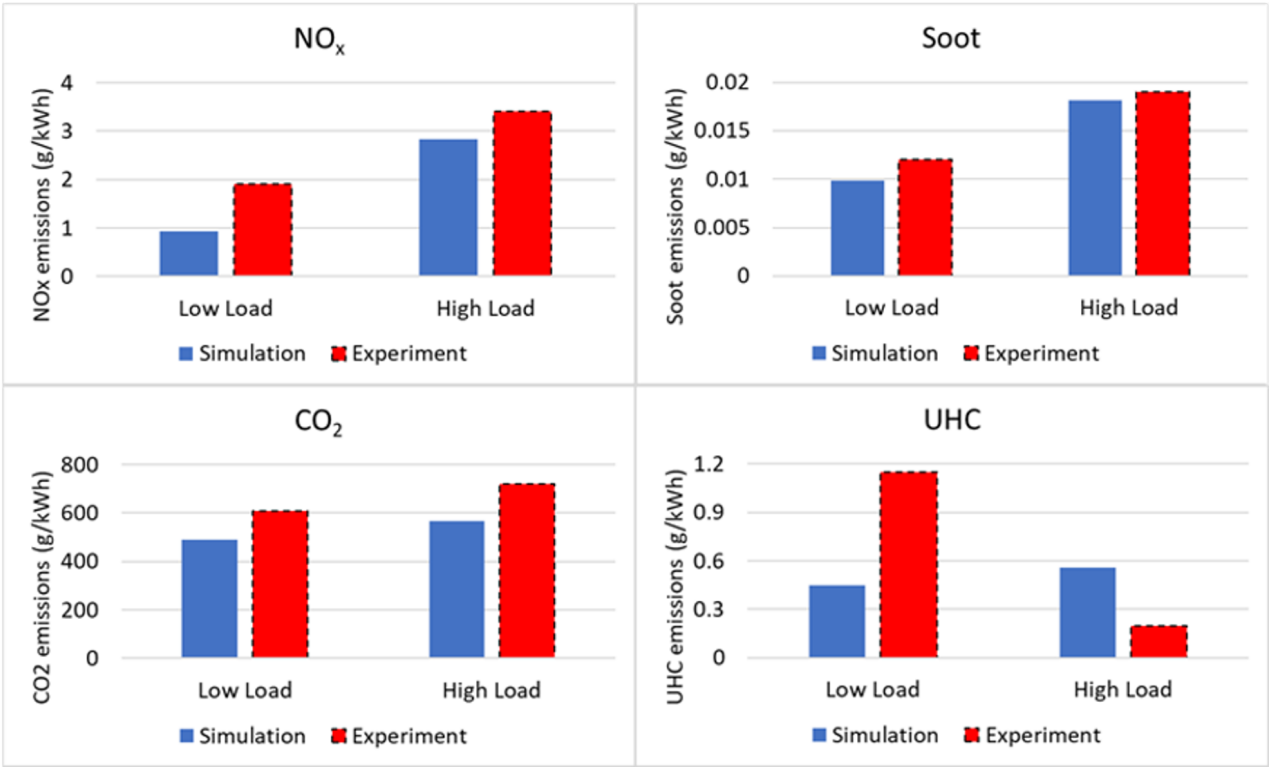

FIGURE 4.7: Soot, NO_x, CO_2 and UHC emissions validation for the high and low load simulations against the experimental reference [58].

Figure 4.6 shows the comparison of pressure and heat release rate HRR between the experimental reference [58] and three mesh densities. Each mesh does a reasonable job at capturing the pressure and HRR profiles, with pre-combustion pressure, ignition delay and initial heat release rate all being represented accurately. The coarse mesh underpredicts peak HRR and combustion pressure at low load and is discarded. Medium and fine meshes do a better job at capturing HRR but still slightly underpredict at both loads while peak combustion pressure is also somewhat overpredicted. Both meshes capture trends well, with the fine mesh showing only minor improvements over the medium mesh. Results are deemed adequately mesh independent and the medium mesh was used during the remainder of the simulations due to reduced computational cost.

Figure 4.7 compares the emissions predictions at EVO in the simulations with those of the exhaust gases in the reference engine. Soot, NO_x and CO_2 trends between low and high load are represented well with all increasing as load increases. Values are somewhat underpredicted however, which can partly be attributed to scaling the results with gross indicated work output and taking values at EVO rather than from exhaust gases due to limitations of the simulations. Discrepancies arise in the UHC plot. It is much more difficult to capture accurate UHC values due to the many intermediate combustion products involved as noted by Kim et al. [90] and a more detailed reaction mechanism is likely required. The earlier heat release of the low load main diesel

injection observed in the simulations is another contributing factor as well as the use of n-heptane as a surrogate for diesel. Consideration of the likes of UHCs in the initial composition of gases at IVC may also be required to reproduce the experimental results more accurately.

4.3.2 Varying CVCP start time

The start time of the CVCP in a cycle can have an impact on performance and emissions. To evaluate the effect of CVCP start time, three different CVCP start crank angles are tested, namely: 40cv700, 40cv710 and 40cv720 which refer to cases with a CVCP duration of 40 degrees (°) and start times of 700°CA, 710°CA and 720°CA respectively. Injection timings are also altered to line up with the start of a given CVCP. These tests are then compared with the conventional engine results denoted as Base. Table 4.3 details the test cases.

TABLE 4.3: CVCP start time test cases. All at high load with 40° CVCP duration.

Description	**Base**	**40cv700**	**40cv710**	**40cv720**
CVCP period (°CA)	-	700-740	710-750	720-760
Injection period (°CA)	714-739	700-725	710-735	720-745

4.3.2.1 Combustion Characteristics

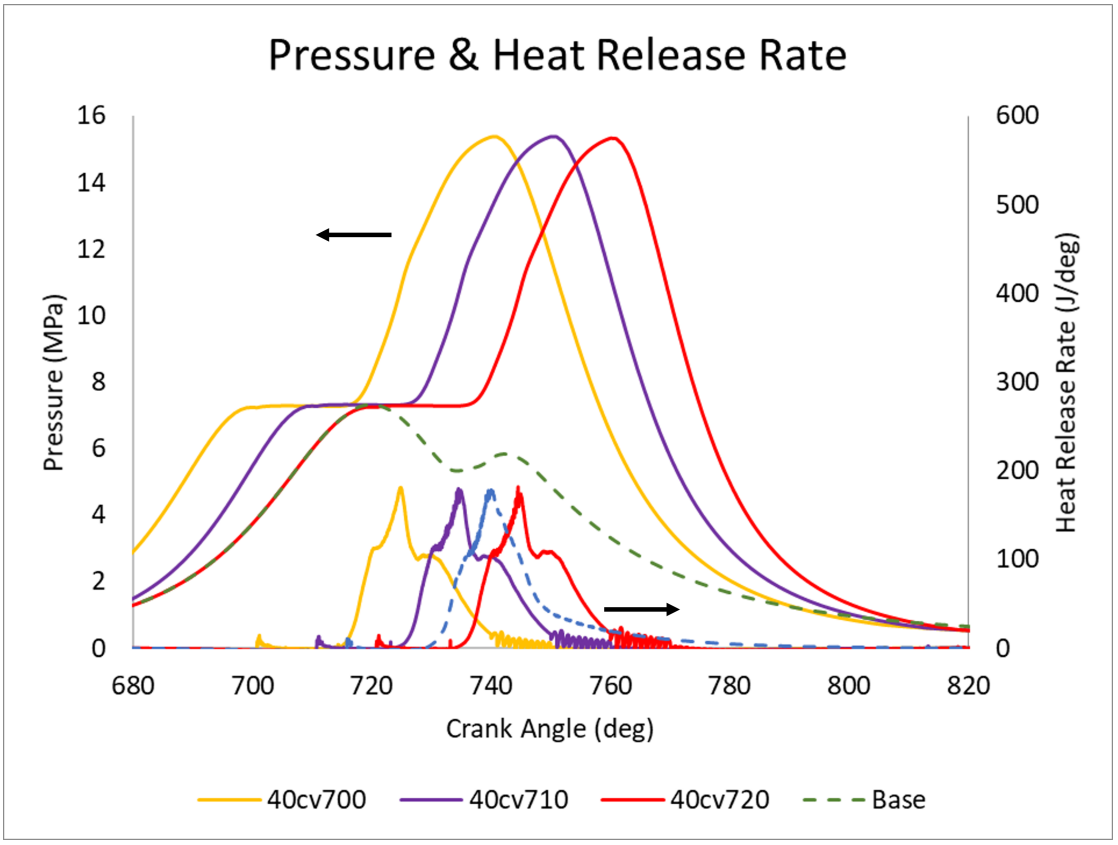

FIGURE 4.8: Pressure and HRR-CVCP start time.

Figure 4.8 shows the in-cylinder pressure and HRR curves at high load for the 3 CVCP cases and the conventional Base case. All cases show an initial ignition delay phase of roughly 1° with little to no difference between any of the cases due to temperature and pressure being largely the same at start of injection in all cases. All cases show similar premixed-charge combustion phases due to the time for mixing being almost identical, there is however slightly higher peaks in HRR with a faster fall off for the CVCP cases. The early increase in heat release is expected due to the higher pressures and temperatures leading to improved combustion. The faster fall off is due both to there being less fuel/oxidiser availability as more has been burned and the reduced piston motion leading to poorer mixing of newly injected fuel and oxidiser compared to the conventional engine. This poorer mixing results both from a decrease in charge motion but also due to the injection being incident at the same part of the piston bowl wall leading to a greater accumulation of fuel which is too rich to combust straight-away. The major difference in HRR between CVCP and conventional cases appears during the non-premixed combustion phase, where a secondary peak in HRR occurs. This secondary peak is partly due to the accumulating fuel in the piston bowl beginning to combust but is also due to the increased temperature and pressure allowing for a higher quantity of the fuel to combust. The higher temperatures increase the amount

of UHC oxidation which can occur and also increases the rate of vapourisation of the liquid fuel leading to an increase in the mixing rate of fuel and oxidiser. There is also another uptick in HRR in the CVCP cases which is not present in the conventional case when the piston begins to move after being held at TDC. This is due to the displacement of fuel which has not had a chance to mix properly with oxidiser, a mechanism which is also somewhat enhanced by the faster piston acceleration away from TDC, evidenced by the HRR being highest at this point in 40cv720 i.e. the case with the fastest piston movement after TDC. This is then followed by the late combustion phase where minimal amounts of combustion occur with the conventional engine showing slightly higher amounts of HRR as the piston approaches EVO due to there being more unburned fuel remaining in the cylinder. It should be noted that 40cv700 has the fastest approach to TDC with 40cv710 being slower and 40cv720 slower still (same as conventional) while the opposite is true for movement away from TDC after the CVCP.

The main combustion event in the conventional engine occurs sometime after TDC due to the engines operation not being fully optimised with regards to pure diesel operation and performance [58, 59] which is a factor in the reduced levels of HRR. Peak pressure in the conventional engine is observed to be 7.32 MPa while as expected the CVCP cases show much higher peak pressures of around 15.3 MPa. The higher pressures are the result of the piston being held at TDC and therefore all of the combustion energy is built up until the CVCP ends and the piston is released. Higher pressures are then observed for the majority of the expansion stroke until around 50° after each CVCP ends. There is very little difference between pressure rise rate, peak pressure and HRR when comparing the 3 CVCP cases. The only major differences between the 3 cases is the offsetting of each pistons approach to TDC causing pressure to rise prior to the conventional TDC in the two early start times, fuel injection and therefore combustion being offset from one another successively by 10 degrees and the slightly faster piston acceleration away from TDC the later the CVCP ends.

One of the issues that these graphs highlight is two instances of "wasted time" at TDC in all CVCP cases. First is the time between pilot and main injections being too spaced out. This leads to the pressure being largely stagnant for the first 20° of the CVCPs- either the pilot should be removed, and the main injection substituted in its place or the dwell time between pilot and main injection should be reduced. Utilising the full CVCP is important as work is not generated until the expansion begins and if expansion could start for example 10° earlier work output would also increase. The second instance of "wasted time" is the levelling off in pressure rise rate observed towards the latter stages of the non-premixed combustion phases. It could be more beneficial to end the CVCP earlier when the pressure rise rate begins to reduce as this would not impact performance greatly and could lead to an increase if the longer expansion stroke increases work output more than the further constant volume combustion would. This

approach would likely lower NO_x significantly due to high temperatures being maintained for a shorter time period. While not investigated in this study, it should also be noted that RPM will alter how much of the CVCP is fully utilised. At lower RPMs wasted time would increase and at higher RPMs reduce as actual time spent at TDC changes while rate of combustion generally does not.

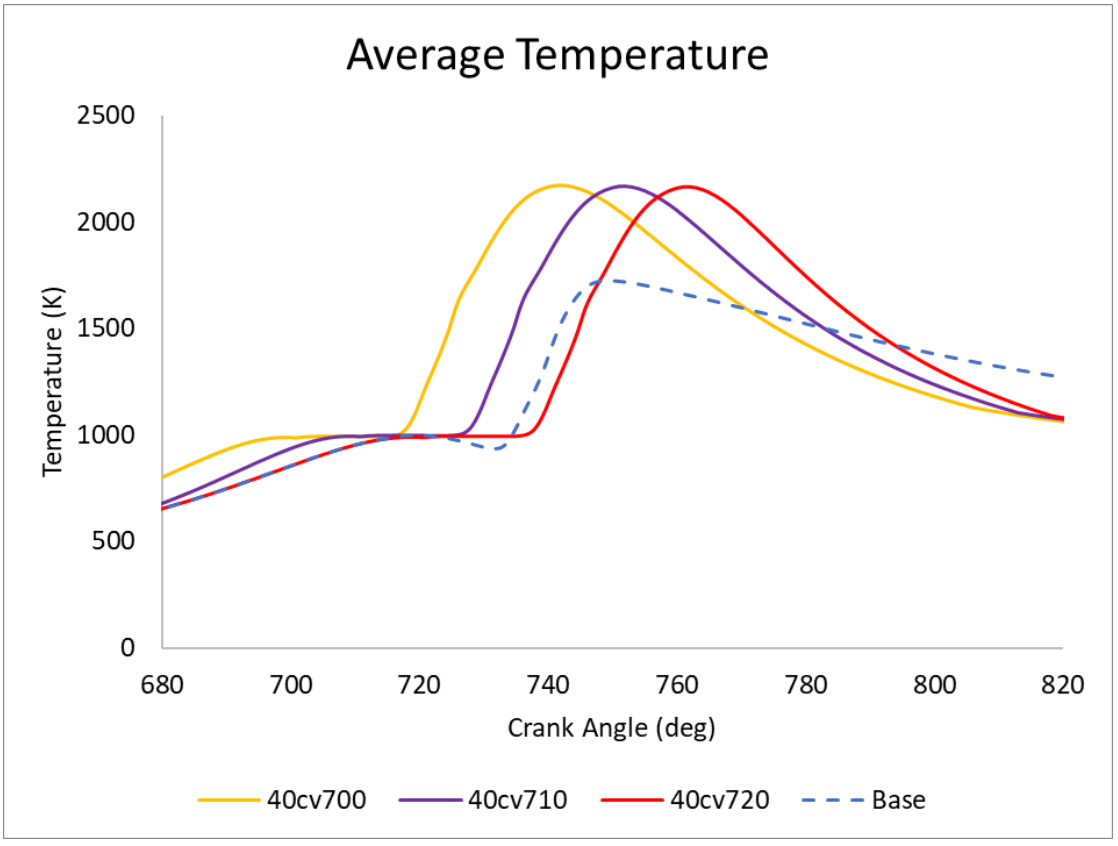

FIGURE 4.9: Average temperature-CVCP start time.

Figure 4.9 shows average in-cylinder temperatures for each case. Average in-cylinder temperatures are for the most part higher for all CVCP cases when compared to the conventional case, with the conventional case only having slightly higher temperature during the late power stroke. Average in-cylinder temperatures in the CVCP cases increase until the end of the CVCP due to the build-up of pressure and heat released by the combustion, but fall off more rapidly once the piston begins to move again, whereas the conventional case peaks during fuel injection and temperatures fall off more steadily. The rapid fall off in temperature is due to higher amounts of heat loss to the walls, faster piston movement away from TDC and reduced amounts of excess fuel/oxidiser left for combustion when compared to the conventional case. Peak in-cylinder temperatures are about 50 K higher in the CVCP cases compared to the Base case (roughly 2720 K vs. 2670 K). Similar maximum temperatures are reached during/just after the main fuel injection in the CVCP cases due to the build-up of energy but lower maximum temperatures are observed in the conventional engine due to the

lower pressure, chamber expansion and reduced amounts of premixed combustion. Comparing the CVCP cases, temperatures are generally higher for longer when earlier CVCP start times are used, owing to fuel injection and therefore combustion occurring earlier. This is somewhat counteracted by the faster piston movement in the later CVCP start times but average in-cylinder temperatures at EVO are essentially equal and roughly 150 K lower than that of the conventional engine.

4.3.2.2 Emissions

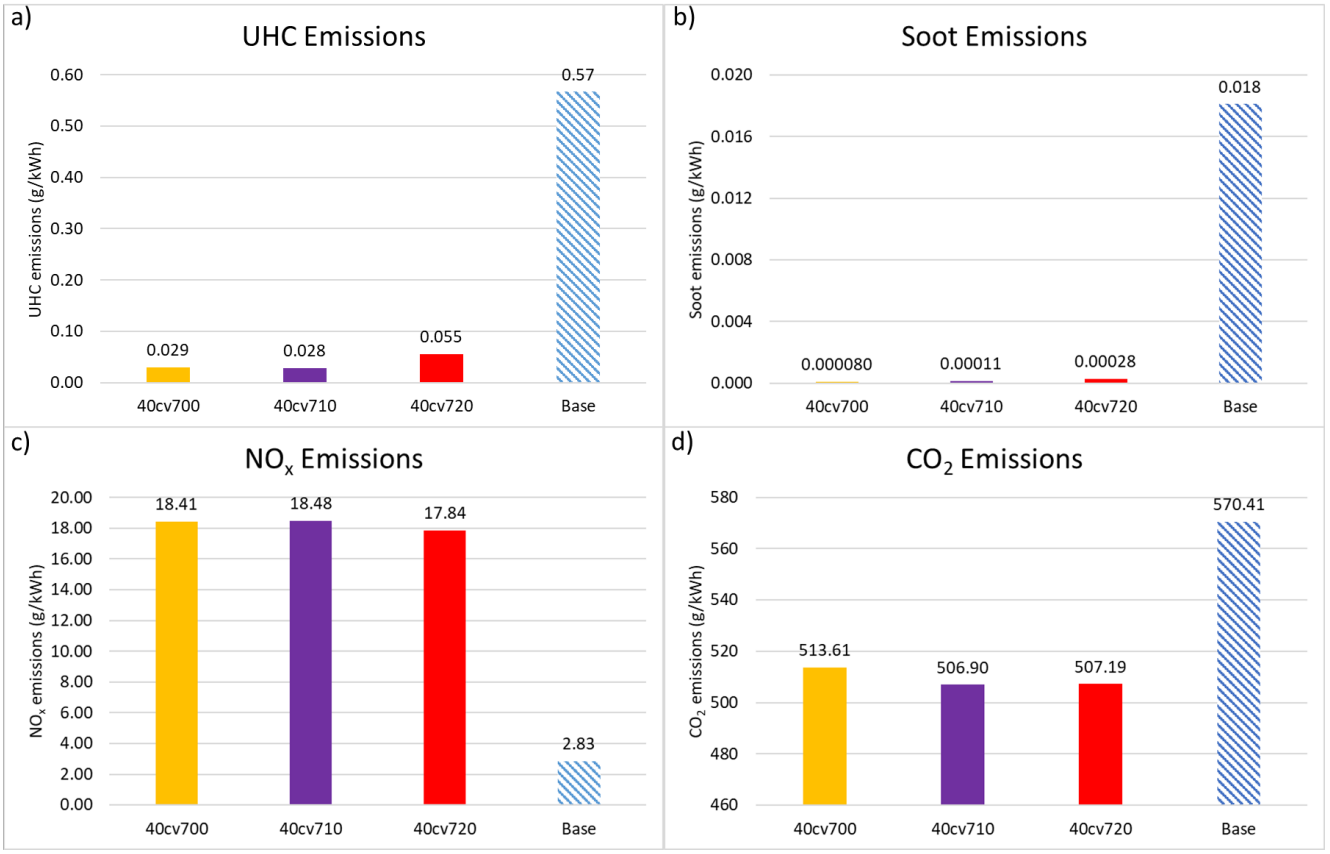

FIGURE 4.10: Emissions levels at EVO for (a) UHC, (b) Soot and (c) NO_x and (d) CO_2- CVCP start time.

UHC emissions are a good indicator for the quality of combustion which occurred as the lower the value the more complete the combustion and the more fuel which was utilised. A number of factors can cause high UHC emissions including poor mixing of fuel and oxidiser, low temperatures, fuel getting caught in small crevices and fuel mixing with lubricating oil [12, 209]. Figure 4.10 a) shows UHC emissions reduce dramatically with implementation of the CVCP indicating a much more efficient conversion of fuel to work. This is a result of large amounts of complete combustion occurring at a constant volume and the higher temperatures and pressures being ideal for high combustion efficiencies. For similar reasons this also leads to increased levels of *CO*

oxidation and thus CO emission also reduces at a similar rate. The reduced mixing caused by the stationary piston is clearly outweighed by the improved thermodynamic conditions. The 40cv720 case shows the highest UHC values out of the 3 CVCP cases which is likely due to the shorter amount of time allowed for slower reactions to occur before EVO and slightly reduced mixing due to the slower compression stroke. Clearly a CVCP can give significantly reduced UHC emissions, indicative of significantly more efficient conversion of fuel into work.

Soot emissions are sensitive to many factors, with the main cause of high soot production being areas of locally rich carbon and low temperatures [210, 211]. Figure 4.10 b) shows the CVCP cases produce low soot levels which are orders of magnitude smaller than the conventional setup. The low soot levels in the CVCP cases are due to the higher temperatures and high levels of combustion efficiency during the CVCP leading to fewer rich distributions of carbon in the cylinder as a large quantity of the injected fuel has gone through quality, complete, combustion while also providing high enough temperatures for good soot oxidation rates. Fast movement of the piston after the CVCP ends also promotes the oxidisation of soot and thus reduces its formation further. The highest soot levels out of all CVCP cases is that of the late CVCP start time and is the result of the increased UHC levels leading to comparatively more locally rich carbon distributions where soot can form than the early CVCP start times. The faster fall off in temperature due to the shortened expansion also contributes.

NO_x emission is sensitive to in-cylinder temperatures due to the thermal Zeldovich mechanism [56] with thermal NO_x production rate doubling with every 90 K increase above 2200 K but falling to much lower rates when temperatures are below 1800 K [39]. As expected, the prolonged higher temperatures associated with the CVCP strategy lead to a significant increase in NO_x emission, as shown in Figure 4.10 c). NO_x emissions are shown to be 6 times higher than the conventional case and are therefore clearly one of the limiting factors when implementing a CVCP cycle and optimisation is required to reduce their level. The later CVCP starts lead to a small reduction in NO_x due to the faster temperature fall off and fuel injection closer to EVO.

Similar to UHC, high levels of CO_2 are generally an indicator that the fuel has undergone complete combustion as a larger quantity of CO in the chamber has been oxidised. While CVCP cases tend to have increased CO_2 emissions in terms of mass output per cycle, Figure 4.10 d) clearly shows that the specific output of CO_2 is highest in the conventional case. This is a result of the increase in performance/efficiency attributed to the CVCP outweighing the increased CO_2 output per cycle leading to a small reduction comparative to the conventional engine.

4.3.2.3 Performance

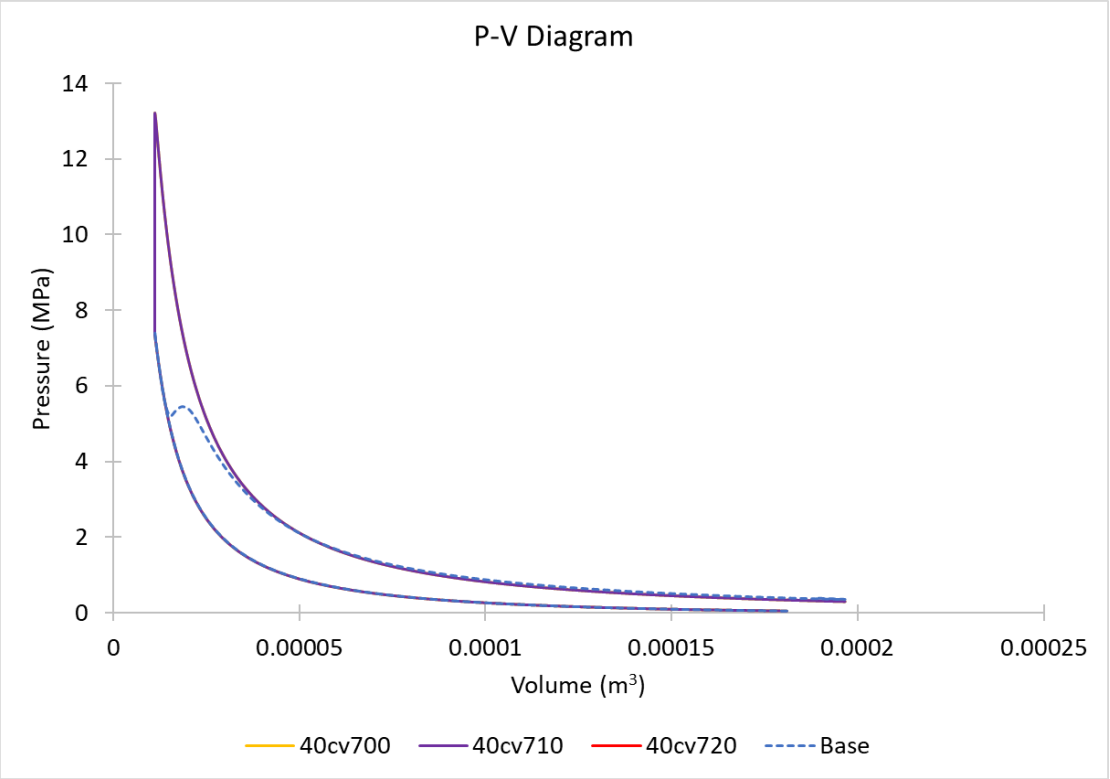

FIGURE 4.11: P-V diagrams - CVCP start time.

Gross indicated performance characteristics are calculated and any further mention of performance refers to gross indicated performance. Trapezoidal rule [212] is used to integrate and find the area between P-V curves (Figure 4.11) for each case, providing the work output. From this power, indicated mean effective pressure (IMEP) and thermal efficiency were calculated. All performance characteristics are linearly linked and therefore only thermal efficiency is presented in Figure 4.12.

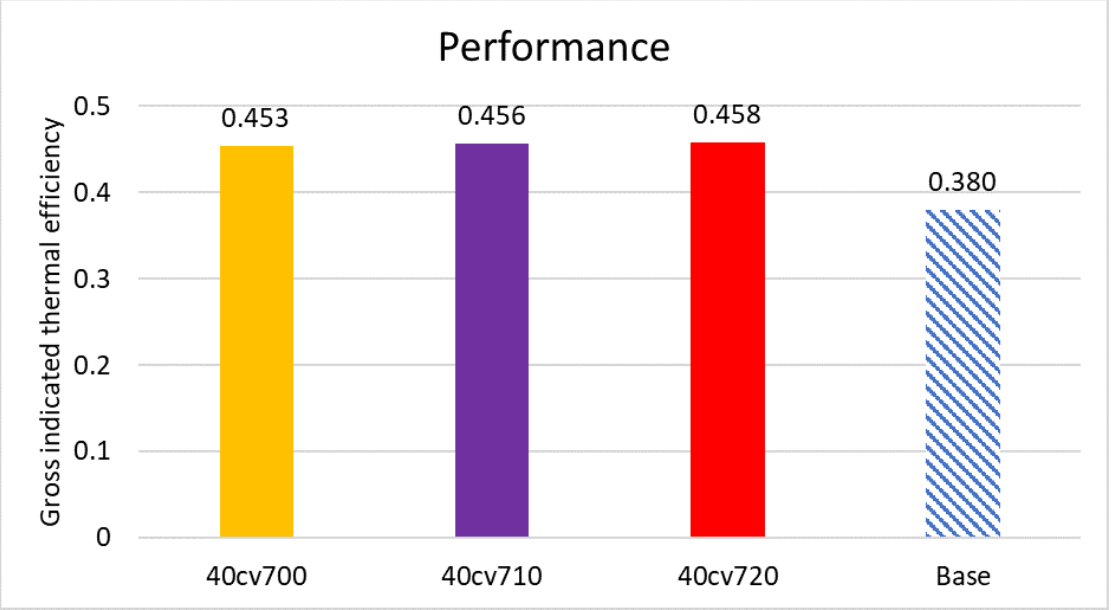

FIGURE 4.12: Performance characteristics for thermal efficiency-CVCP start time.

The CVCP leads to increases to thermal efficiencies by 7-8% compared to the conventional engine-a reduction of specific fuel consumption (SFC) by over 20%. The increase in performance is caused by factors including: increased fuel utilisation, higher in-cylinder pressures and temperatures being built to drive the piston and increased amounts of combustion occurring at these conditions. The reduced expansion stroke caused by later CVCP start times appears to be largely balanced out by the longer compression stroke and increased piston speed when moving away from TDC enhancing mixing and therefore promoting combustion, leading to very similar thermal efficiencies between the CVCP cases.

There is room for improvement in terms of performance increases due to the previously mentioned "wasted time" during the CVCP phases. This can be achieved through injection profile optimisation and or reduction of the CVCP duration to eliminate the constant pressure region and fall off in pressure rise rate. Sections 4.3.3 and 4.3.4 explore these options.

4.3.3 Varying CVCP duration

Three different CVCP durations are tested, namely: 20° (CV20), 30° (CV30) and 40° (CV40) and are compared to the conventional "Base2" test case. In all cases dwell time between pilot and main injection has been reduced to address the "wasted time" at TDC discussed in the previous section. All CVCP start at 720°CA to allow for easier comparison to the conventional test case and low load cases are introduced to gauge the effectiveness of the CVCP cycle across multiple engine loads. Table 4.4 outlines the cases.

TABLE 4.4: Simulated test cases for CVCP duration at low and high load. All with CVCP start time of 720°CA.

Case	**Base2**	**CV20**	**CV30**	**CV40**	**Base2**	**CV20**	**CV30**	**CV40**
Load	Low	Low	Low	Low	High	High	High	High
Constant volume period (°CA)	-	720-740	720-750	720-760	-	720-740	720-750	720-760
Constant volume duration (°)	0	20	30	40	0	20	30	40
Injection period (°CA)	720-736	720-736	720-736	720-736	720-740	720-740	720-740	720-740
Mass of fuel injected (kg)	1.93e-5	1.93e-5	1.93e-5	1.93e-5	6.49e-5	6.49e-5	6.49e-5	6.49e-5

4.3.3.1 Combustion characteristics

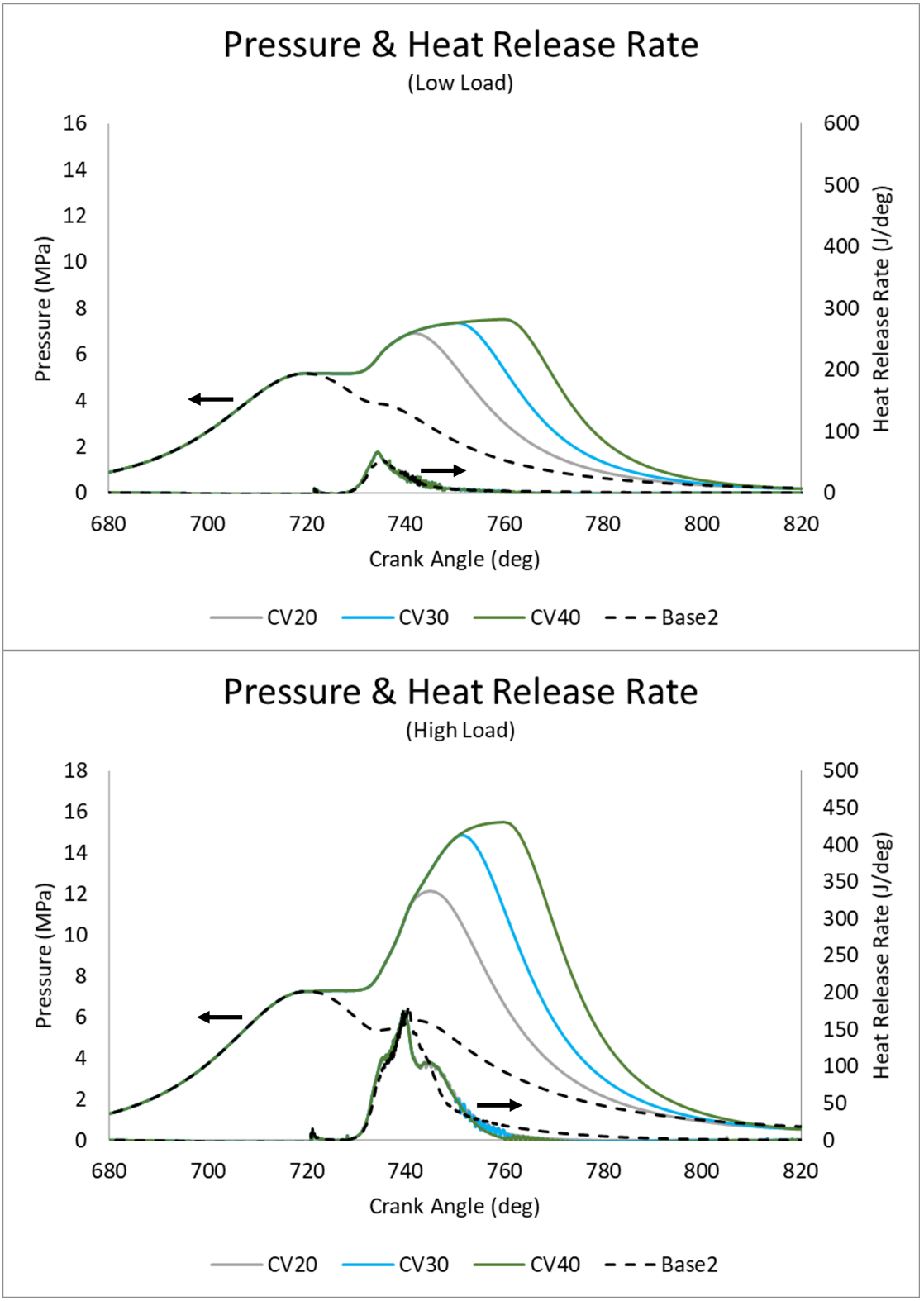

FIGURE 4.13: Pressure and HRR at low and high load-CVCP duration.

Figure 4.13 shows the in-cylinder pressure and HRR for the 3 CVCP durations and conventional engine test cases at low and high loads. All cases at a given load condition show very similar ignition delay timings with no considerable differences between each other. High load CVCP cases exhibit the same HRR trends as the previous section with slightly increased initial peak, a faster fall off from peak, a secondary peak and an uptick upon piston release compared to the conventional engine. HRR at low load shows a large increase in premixed-charge HRR for CVCP operation, but no secondary peak due to the reduced injection volume. HRR also exhibits the upticks when the piston is released from TDC similar to the high load (HL) cases.

At high load peak pressure in the conventional engine is observed to be 7.25 MPa while the CVCP cases show peak pressures of 12.15 MPa, 14.86 MPa and 15.51 MPa for CV20, CV30 and CV40 respectively. At low load peak pressure in the conventional engine is predicted to be 5.18 MPa, while CV20, CV30 and CV40 have peak pressures of 6.92 MPa, 7.37 MPa and 7.52 MPa respectively. The higher pressures are the result of much of the combustion occurring at a constant volume while the piston is being held at TDC and the reduction in pressure as CVCP duration decreases is simply due to there being less time for pressure to build and more fuel still needing to undergo complete combustion. Higher pressures are then observed for much of the expansion strokes until around 50° after each CVCP ends.

"Wasted time" at TDC is still present in all cases with the dwell time between pilot and main injection not being adequately reduced (difficult to reduce further while still comparing fairly to the conventional engine). However, at high load and low load the CV20 cases adequately eliminate the part of the CVCP where pressure rise rate begins to fall off. As do the CV30 cases to a lesser extent but there is still a reduction in pressure rise rate especially at low load where the drop off is far more apparent and will impact engine performance. The lower duration CVCP cases should also benefit from having longer expansion strokes, and therefore time to output work, which will alleviate the loss of potential complete combustion and increased peak pressure which a longer CVCP would have given.

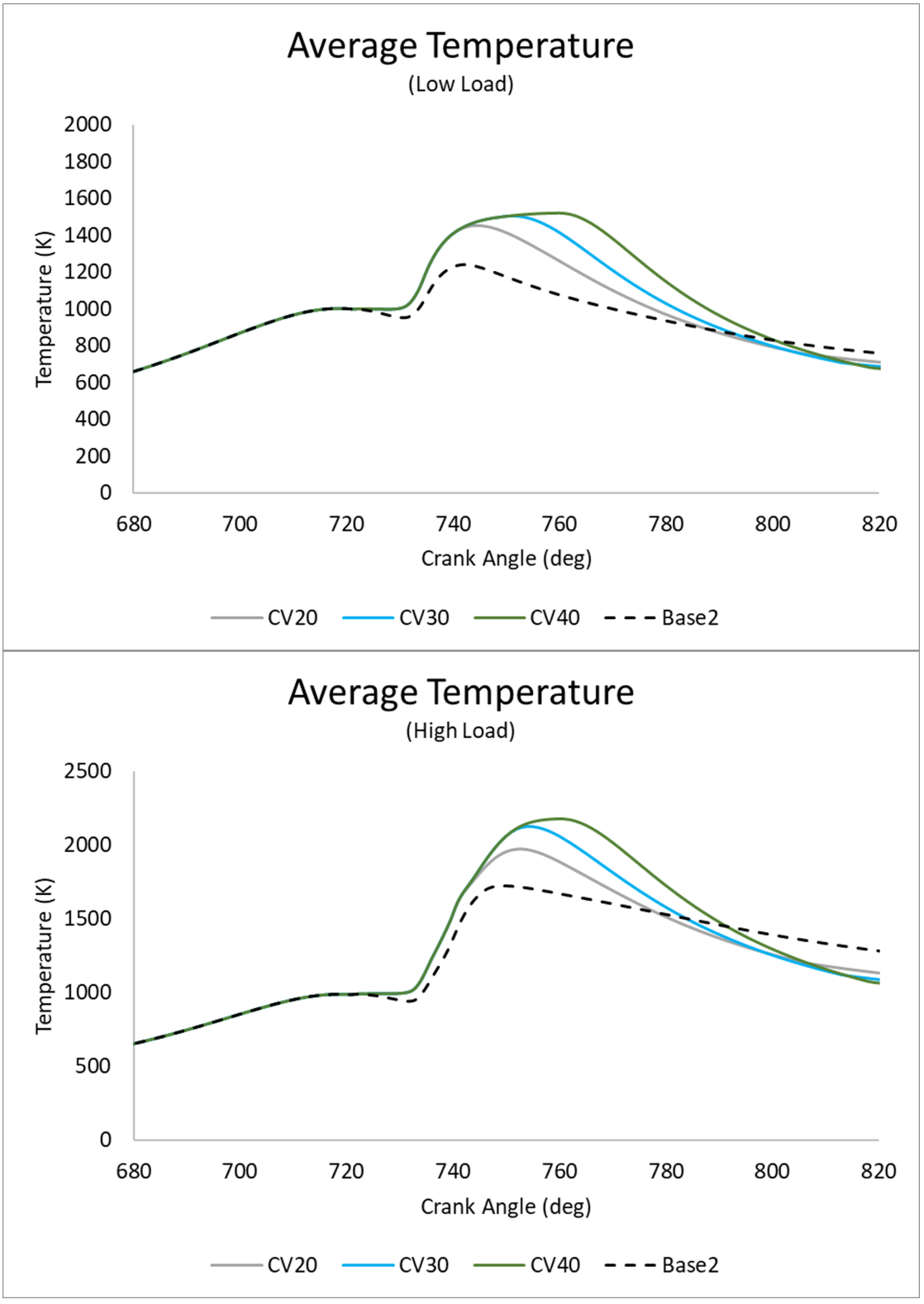

FIGURE 4.14: Average temperature at low and high load-CVCP duration.

Figure 4.14 shows the average in-cylinder temperature at high and low loads. Average temperatures show similar trends across both load conditions. Higher temperatures

over a prolonged duration are observed in the longer CVCP test cases due to there being more time for pressure and temperature to build and be maintained. Once released from TDC each CVCP case falls off more quickly than the conventional cases with the rate of fall off increasing the longer the piston was held at TDC due to increased heat transfer to the walls, lesser amounts of fuel being available for combustion and faster piston movement away from TDC. In the late expansion stroke all CVCP cases have lower temperatures than their corresponding conventional case and the longest duration CVCP cases have the lowest temperatures at EVO. Peak temperatures at low load are all within 5 K due to heat transfer counteracting the build-up of temperature once HRR slows down. At high load each successive increase in CVCP duration (0-40°) leads to an increase in peak temperature of roughly 30 K.

4.3.3.2 Emissions

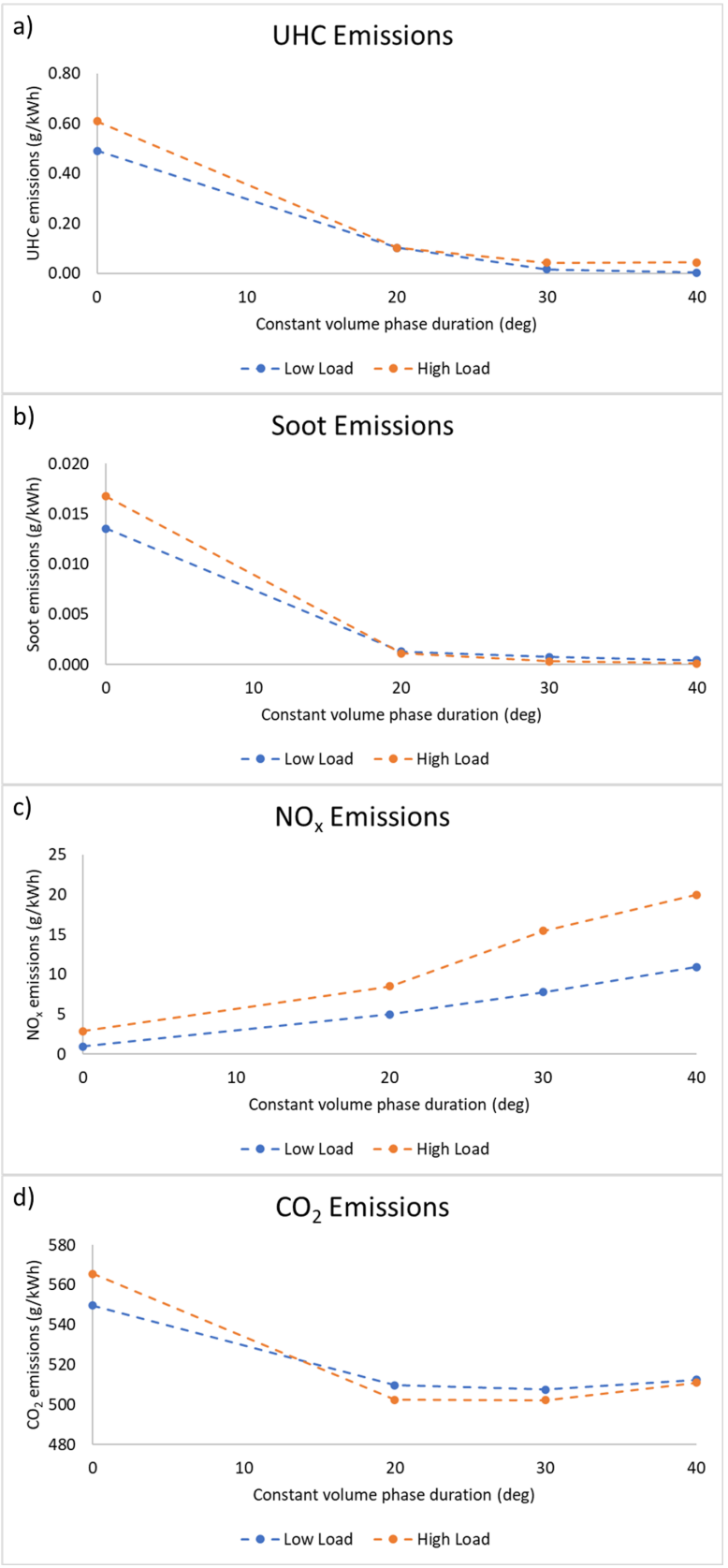

FIGURE 4.15: a) UHC, (b) soot, (c) NO_x and (d) CO_2 emissions at low and high load-CVCP duration (0° represents Base2).

UHC emissions, Figure 4.15 a), significantly reduce as CVCP duration is increased at both load conditions, but the amount of reduction levels out after CV20. The trends indicate that the longer CVCP duration leads to higher levels of quality complete combustion of the fuel-air mix. The benefits falling off at both loads are linked to the reduction in pressure rise rate and therefore performance/specific output. Most of the fuel which could go through complete combustion already has and the remainder is not mixed well with oxidiser and the longer the piston is held at TDC the more likely it is to accumulate.

For similar reasons there is an initial significant reduction in soot between conventional and CV20 but much less of a reduction between CV20 and CV40 at both loads, Figure 4.15 b). The reduced amounts of UHC and higher temperatures greatly contribute to the reduction in soot. The accumulation of UHC which can occur as the piston dwells near TDC may also contribute to the slowdown in soot reduction at longer CVCP durations as this can lead to locally rich high carbon areas in which soot can form. However, the levels of soot observed are still much lower than the conventional case soot levels across all CVCP cases at both loads indicating that even a poorly optimised setup lowers carbon-based emissions considerably. The levelling off is also somewhat due to performance reducing slightly at higher CVCP durations due to reduction in expansion work and therefore specific output is impacted.

Figure 4.15 c) shows that NO_x emissions increase with increasing CVCP duration at both load conditions due to the higher temperatures present for extended periods as duration increases. However, the increase between the conventional case and CV20 is manageable and further optimisation of fuel injections, CVCP duration and potentially the implementation of EGR or LTC technologies for example could bring this value down further while still maintaining the varied benefits of CVCP operation. When CVCP duration is increased beyond 20° significant increases to NO_x are observed and a trade-off between performance, UHC, soot and NO_x emissions will need to be made.

CO_2 emissions, Figure 4.15 d), reduce compared to the conventional case at all CVCP durations and loads but show a small increase between CV30 and CV40. In general the per cycle CO_2 emissions increase for CVCP cases compared to the conventional cases due to the more complete combustion and therefore conversion of fuel to CO_2 but the much improved performance leads to a reduction in specific output. Comparing the CVCP cases the reduced performance and increased CO oxidation at the longer durations leads to an increased specific output at CV40 and again we observe the general levelling off in reduction after CV20. As with all other carbon-based emissions CO_2 levels are still lower than the conventional case at all CVCP durations.

4.3.3.3 Performance

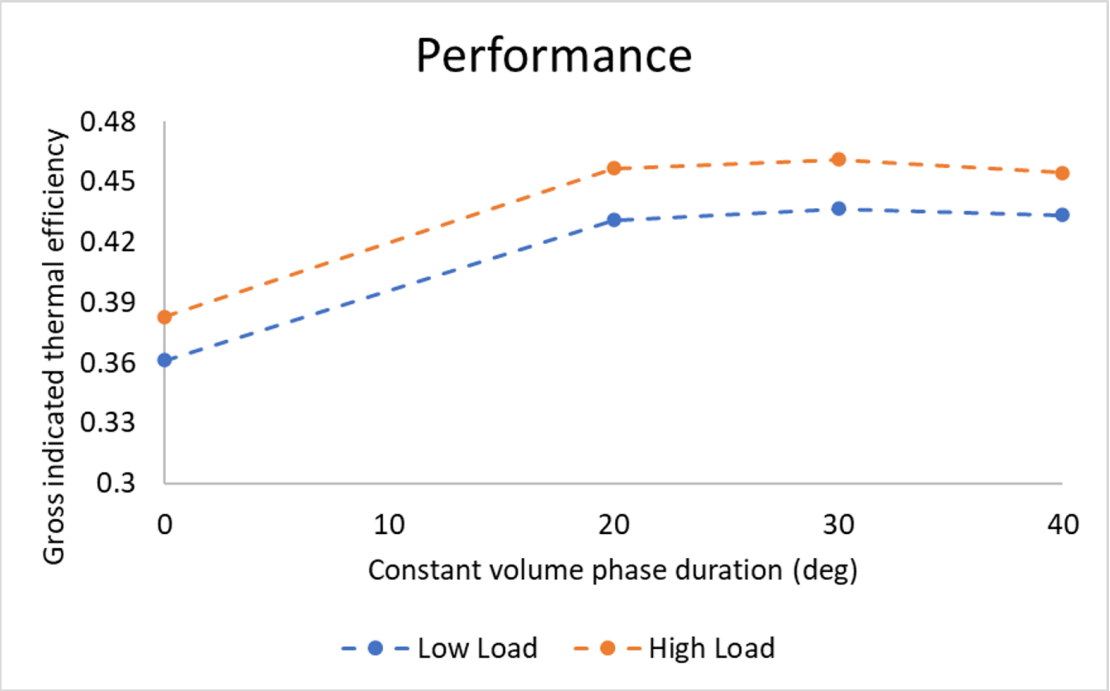

FIGURE 4.16: Performance characteristics at low and high load-CVCP duration.

Thermal efficiency at high and low load is presented in Figure 4.16 and a significant increase of 7-8% is observed between conventional and CVCP cases. As expected due to the "wasted time" and reduced expansion stroke there is a considerable levelling off in performance after CV20 with CV40 even reducing compared to CV30. CV20 shows the greatest relative increase due to the reduction in "wasted time" at TDC and therefore the elimination of the pressure rise rate fall off which is present at other durations. Pressure rise rate fall off is essentially an indicator for the beginning of diminishing returns for CVCP duration increase in terms of performance. While for the most part there is a greater amount of complete combustion and higher peak pressures occurring at longer CVCP durations the reduction in potential work output by shortening the expansion stroke unnecessarily begins to outweigh the combustion benefits, evidenced by the performance decrease between CV30 and CV40.

4.3.3.4 Contour analysis

Figure 4.17 shows contours of UHC at 740°CA which represents a crank angle both very close to end of injection and before the end of the CVCP in all cases (contour will be the same in CV20, CV30 and CV40) and therefore highlights the difference between fuel injection in the conventional and CVCP engines. There is clearly a wider distribution of fuel in the conventional case with the fuel spray impinging at the top edge

of the piston bowl and causing a flow which pushes the mixture both towards the top face/liner of the cylinder as well as along the piston bowl wall and towards the bowl centre. Whereas in the CVCP cases the fuel spray is incident lower, much more towards the piston bowl, and while a similar pattern emerges in that some of the fuel reflects upwards, the majority moves along the piston bowl wall and towards the centre of the bowl. With that said, even with the reduced level of mixing involved in the CVCP cases, the UHC concentrations are much lower compared to the conventional case due to the improved combustion quality and therefore generally reduced levels of UHC.

Contours of temperature, NO_x , soot and fuel-air equivalence ratio are depicted for high load at 760°CA in Figure 4.17. 760°CA is chosen due to it being the end of the longest CVCP phase (CV40). Areas of high NO_x production are shown to occur at areas of high temperature, which correspond to the main combustion sites where the fuel spray was aimed. Temperature contours show that combustion is much more spread out and of a lower temperature in the conventional case whereas as CVCP duration increases combustion becomes much more focussed on the centre of the piston bowl and temperature increases. This is clearly reflected by the increased NO_x levels in these areas. The main areas of initial soot production are near to the injector where temperatures are lower and there is increased mixing in the wake of the injection as well as in the piston bowl on the edge of the main combustion site. These areas of early soot formation correspond to zones of rich fuel-air equivalence ratio where the diffusion flame cannot contact, i.e. flame quenches at piston bowl walls while fuel accumulates and close to the injector where there is a zone above the rich flammability limit and no flame. Fuel rich areas are much more focussed around the piston bowl area in the CVCP cases due to this being the area where the injection is directed at TDC (piston does not move during injection in any CVCP case). However even with the areas being the focus of the entire fuel injection they are much leaner than the corresponding conventional case due to the higher quality of combustion leading to far reduced levels of UHCs. The high combustion quality in the CVCP cases means that soot has hardly developed comparative to the conventional case.

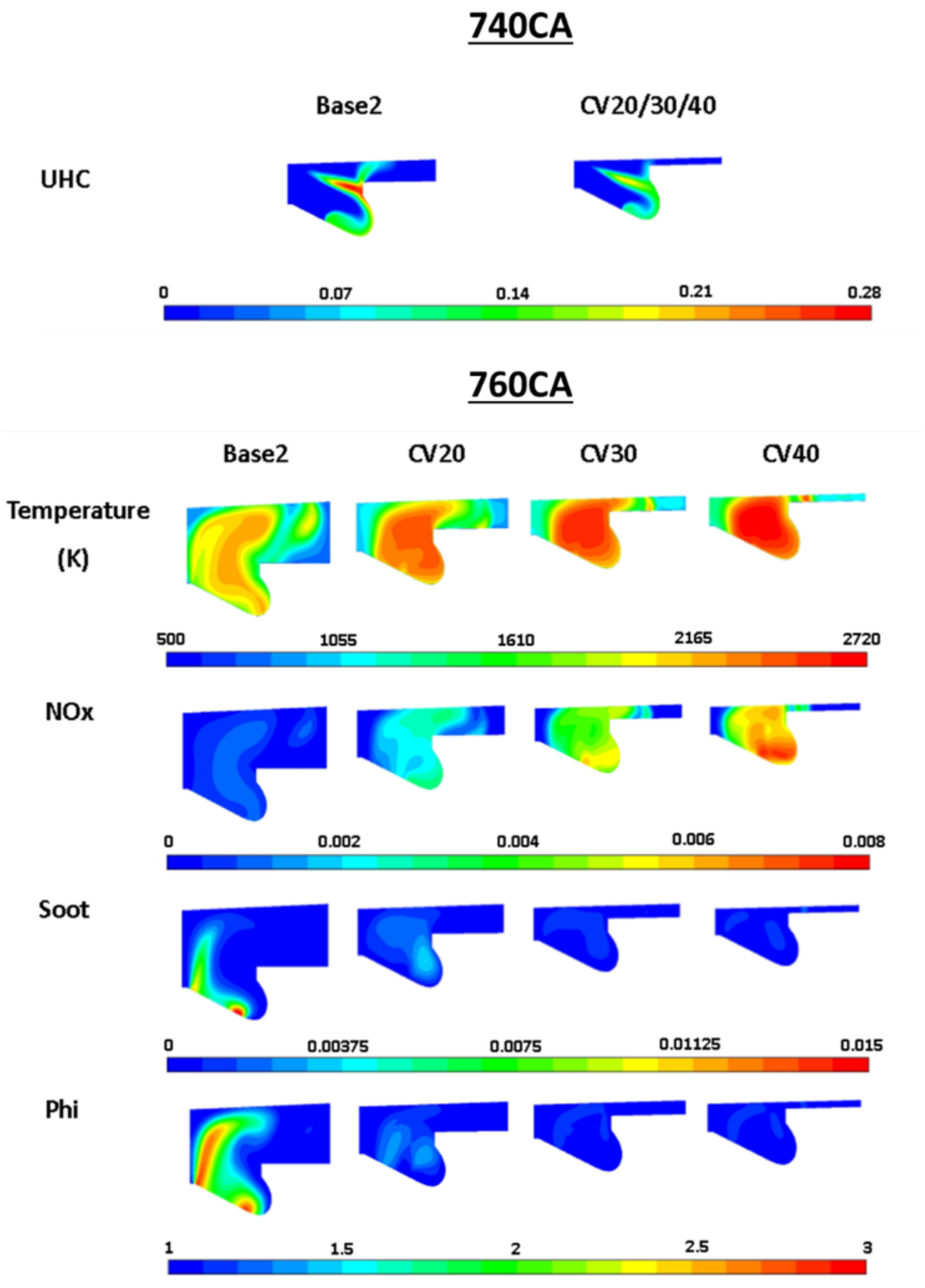

FIGURE 4.17: Contours of UHC at 740°CA and temperature, NO_x, soot and fuel air equivalence ratio at 760°CA for the high load cases-CVCP duration.

4.3.4 NO_x reduction study

As noted in the previous sections several improvements can be made to the engine operation which should lead to a reduction in NO_x levels and potentially further improve performance of the CVCP strategy. The two avenues explored in this section are EGR and injection profile optimisation. EGR is introduced as this is an effective method for NO_x reduction which when implemented correctly can have minimal impact on engine performance and other emissions outputs [213]. Three different fuel injection profiles are tested to examine the effects of injection rate and the reduction of the "wasted time" at the start of the CVCP periods. Finally, a "best" case is tested which combines the most successful EGR and fuel injection profile cases. Each case in this section utilises a 20° CVCP starting at 720°CA as this constant volume phase duration receives many of the benefits of the strategy while not increasing NO_x as severely as the longer durations. Table 4.5 outlines the cases.

TABLE 4.5: Simulated test cases for NO_x reduction. CVCP start time 720°CA and duration 20deg.

	EGR			**Fuel Injection**			**Best Case**
Case	0%	15%	25%	Small Dwell	No Pilot	Increased Duration	Small Dwell & 15% EGR
Pilot Injection Period (°CA)	720-722				-	-	720-722
Main Injection Period (°CA)	728-739			725-736	720-732	720-739	725-736
Mass of fuel injected (kg)	6.49e-5						

4.3.4.1 EGR

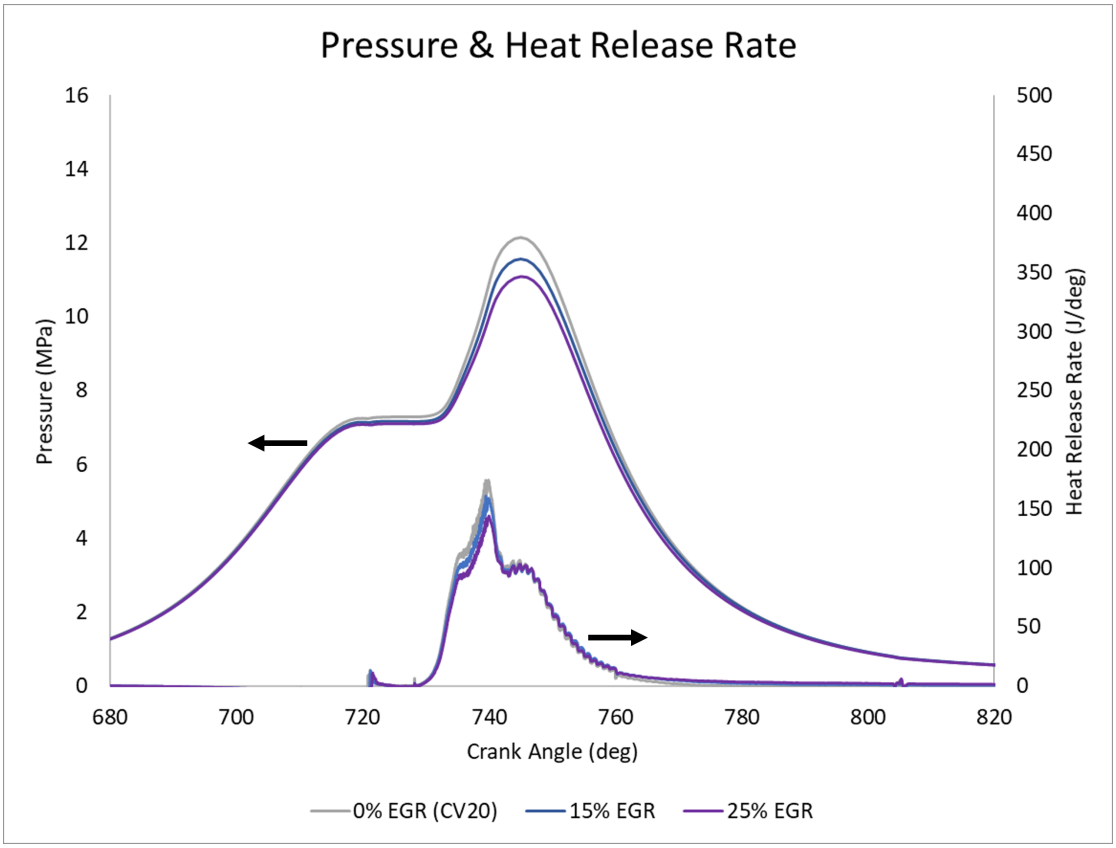

FIGURE 4.18: Pressure and HRR for NO_x reduction using EGR.

A cooled form of EGR is used which assumes exhaust gas recirculation does not change initial in-cylinder temperatures and intake air is replaced by exhaust gases which are made up of CO_2, H_2O and N_2. Figure 4.18 shows the in-cylinder pressure and HRR for 0%, 15% and 25% EGR rates. Increasing the amount of EGR leads to a reduction in peak pressure by 0.58 MPa and 1.06 MPa for 15% and 25% EGR respectively. Pressure rise rate is also reduced as well as peak and total heat release. This is largely the result of a reduction in oxidiser, but dissociation of CO_2 and H_2O during combustion and the higher heat capacity of the exhaust gases causing them to act as a heat sink also contributes to the lowering of both combustion rate and rise in temperature.

Figure 4.20 shows emission levels at EVO for each test case. The addition of EGR reduces the in-cylinder temperatures and thus there is a considerable reduction in NO_x for the 15% and even more-so 25% EGR rates. However, increasing the rate of EGR also leads to the increase of UHC, soot and CO_2 emissions, Figure 4.20 a), b), d). For CO_2 this is largely due to the recycling of CO_2 from the previous cycle. For UHC and soot several factors cause the increase. Oxidiser reduction means the amount of fuel rich zones in which soot formation can occur increases as the overall fuel-air equivalence ratio in the chamber increases and also reduces the amount of soot oxidation that is possible.

The reduction also means there is less oxidiser for fuel to undergo complete combustion with and therefore hydrocarbons are left unburned and more CO is observed due to less oxidation leading to CO_2. The increase in UHC also further promotes soot production as there are more locally carbon rich areas. Generally lower in-cylinder temperatures due to the aforementioned dilution, chemical and thermal effects of EGR also promote soot production and UHC increases. Nevertheless, the significant reduction in NO_x when operating under a CVCP strategy is a promising finding.

Figure 4.21 shows the thermal efficiencies for each test case. Performance decreases slightly at the low EGR rate but somewhat more significantly at the higher rate. This performance decrease is expected as Figure 4.18 shows both pressure at the end of the CVCP period and total heat release are lower as EGR rate increases, thus leading to a lower work output and therefore performance. The finding is also backed up by the increased UHC level, i.e. wasted fuel energy. EGR essentially slows down the rate and total amount of combustion to the benefit of NO_x emissions, but to the determinant of performance, and thus the two must be balanced.

4.3.4.2 Injection profile

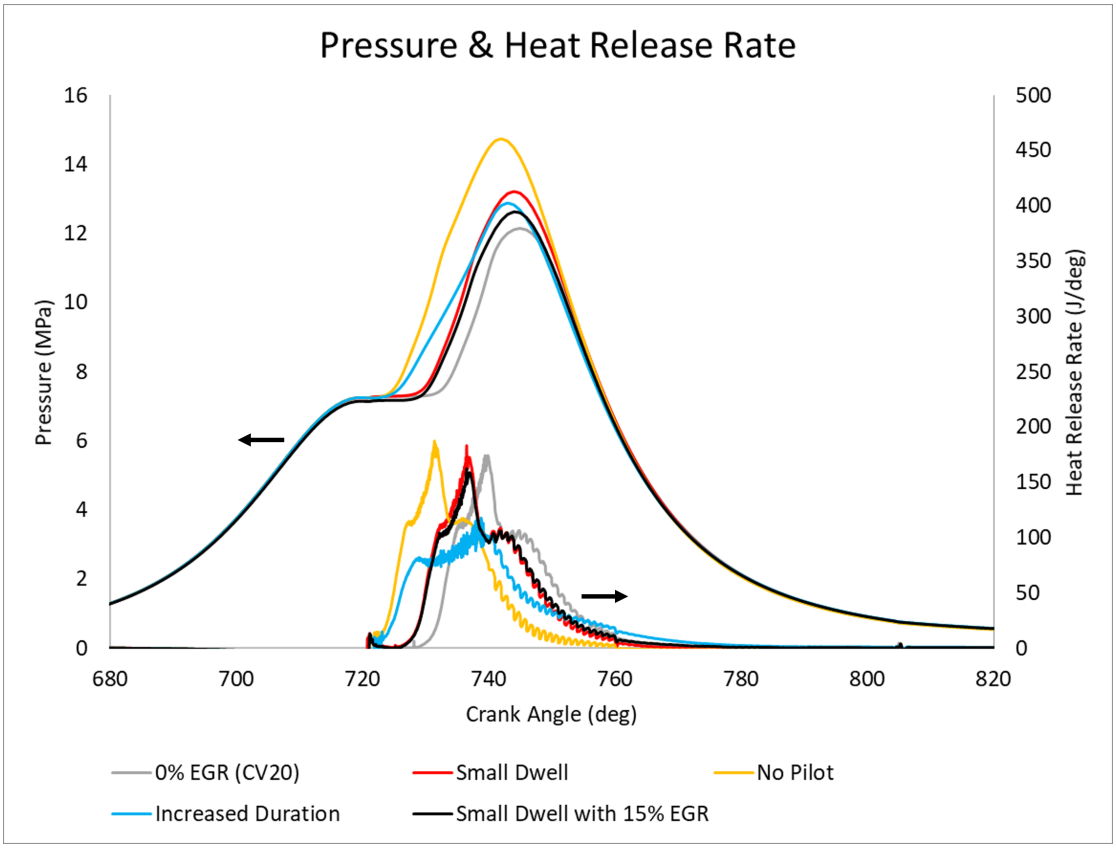

FIGURE 4.19: Pressure and HRR for NO_x reduction using varied injection profiles.

The "wasted time" during the CVCP is addressed by testing 3 new injection profiles. This issue stems from some of the time spent at a constant volume not being used for combustion and therefore either unnecessarily increasing NO_x or and reducing the potential performance gains. The 3 injection profile cases are: Small Dwell which uses a reduced dwell time between pilot and main injection; No Pilot which combines main and pilot injections and moves the main injection to the start of the CVCP phase; and Increased Duration which uses a single long injection with reduced injection rate. Figure 4.19 shows the in-cylinder pressure and HRR for the fuel injection profiles.

No Pilot leads to the greatest increase in peak pressure and has the fastest peak pressure rise rate. This is due to there being a greater amount of time for combustion to occur at a constant volume (fuel injection finishes earliest out of all cases), the increased volume of fuel in the main injection and the increased amount of premixed charge combustion owing to there not being a pilot injection (longer main injection ignition delay). While this does increase performance, Figure 4.21, and decrease UHC/soot emissions, Figure 4.20a), b), the large increase in NO_x, Figure 4.20c), due to in-cylinder temperature increases associated with the higher pressures and longer ignition delay likely means this is not a feasible injection strategy.

Increased duration leads to a higher peak pressure than CV20 due to the increased time allowed for fuel to combust at a constant volume. Large amounts of combustion occur in the premixed charge combustion phase due to the lack of pilot injection, but peak pressure rise rate is lower due to the much slower injection rate and slower release of fuel for combustion in the mixing-controlled combustion phase. This injection strategy also has the lowest amount of heat release during the early expansion after the piston is released from TDC which means pressure falls faster and less work is output compared to CV20. Increased fuel injection duration is a reasonable way to maintain NO_x levels while attaining a higher peak pressure due to the temperature rise being slower throughout the CVCP. However, this strategy incurs increases to soot and UHC emissions due to the poorer mixing of the fuel injection leading to zones of high carbon concentrations in the chamber which, when combined with the lower in-cylinder temperatures, leads to UHC and soot formation. Further optimisation of this strategy is required but the pressure increasing while NO_x is maintained means the strategy has potential given better implementation.

Small Dwell achieves the second highest peak pressure while the pilot injection means the peak pressure rise rate is slightly slower than that of the No Pilot test case. The advancement of the main injection allows for a greater amount of combustion to occur in the CVCP when compared to CV20 which in turn leads to the higher pressure, performance and decreased UHC. NO_x does however increase by a small amount due to the increased temperature, a result of the reduced benefit of a pilot with a smaller dwell time between injections. Small Dwell is likely the best of the injection profiles due to

the improvements to performance and carbon-based emission outputs, however, none of the current injection profiles assist adequately with NO_x reduction.

4.3.4.3 Combining "best" EGR and injection profile cases

Finally, a combination of the "best" EGR and injection case was carried out to obtain an end result. Small Dwell with 15% EGR was chosen due to the benefits of both strategies outlined previously. Positive results were found with a small peak pressure increase (Figure 4.19) observed compared to CV20. The EGR addition reduces the overall combustion rate when compared to the normal Small Dwell case but performance is only slightly reduced. NO_x emissions are much reduced compared to CV20 and even slightly lower than the conventional case. UHC emissions are higher than CV20 but half that of the conventional case while soot emissions climb a small amount but are still much less than in the conventional case. All in all, this strategy would appear to be feasible with NO_x emissions comparable to the conventional engine but much lower soot/UHC emissions and improved performance.

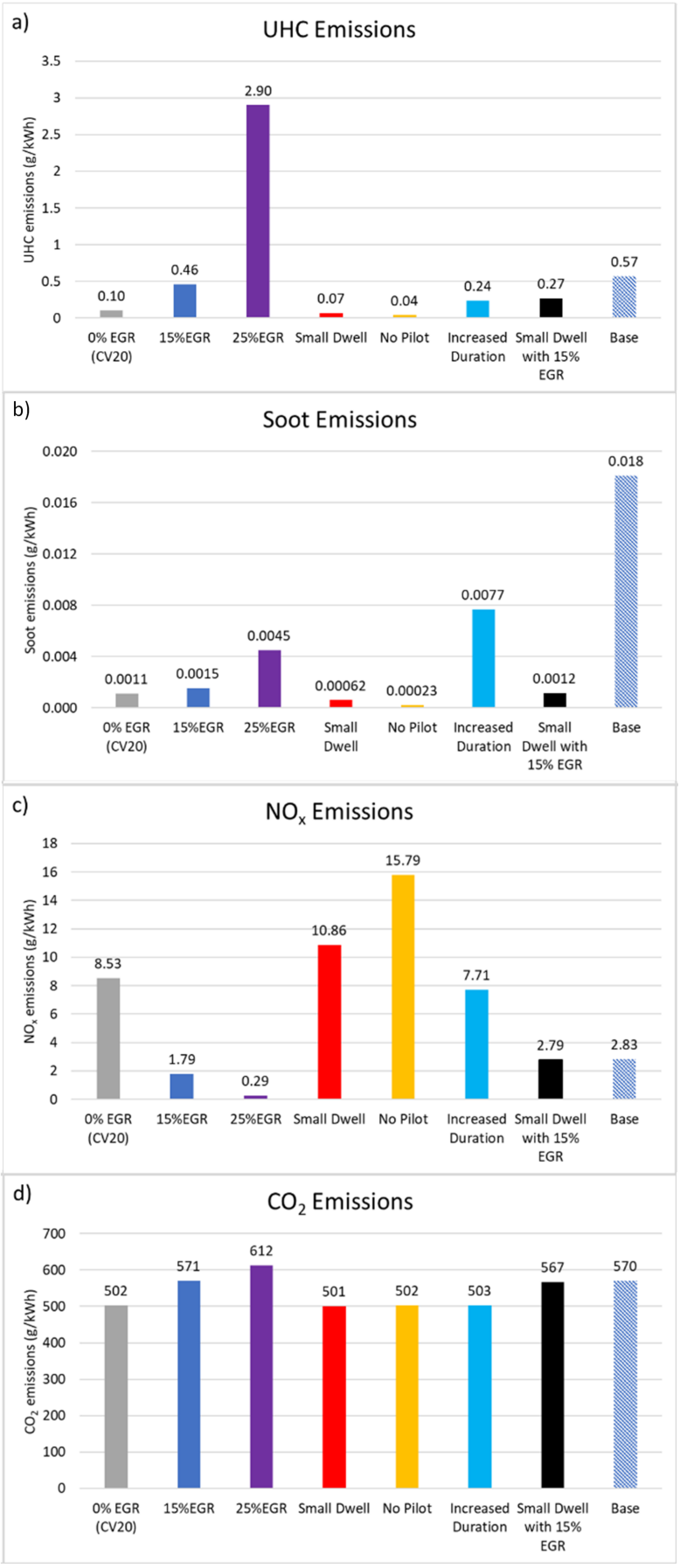

FIGURE 4.20: Emissions levels at EVO for a) UHC, b) soot, c) NO_x and d) CO_2-NO_x reduction.

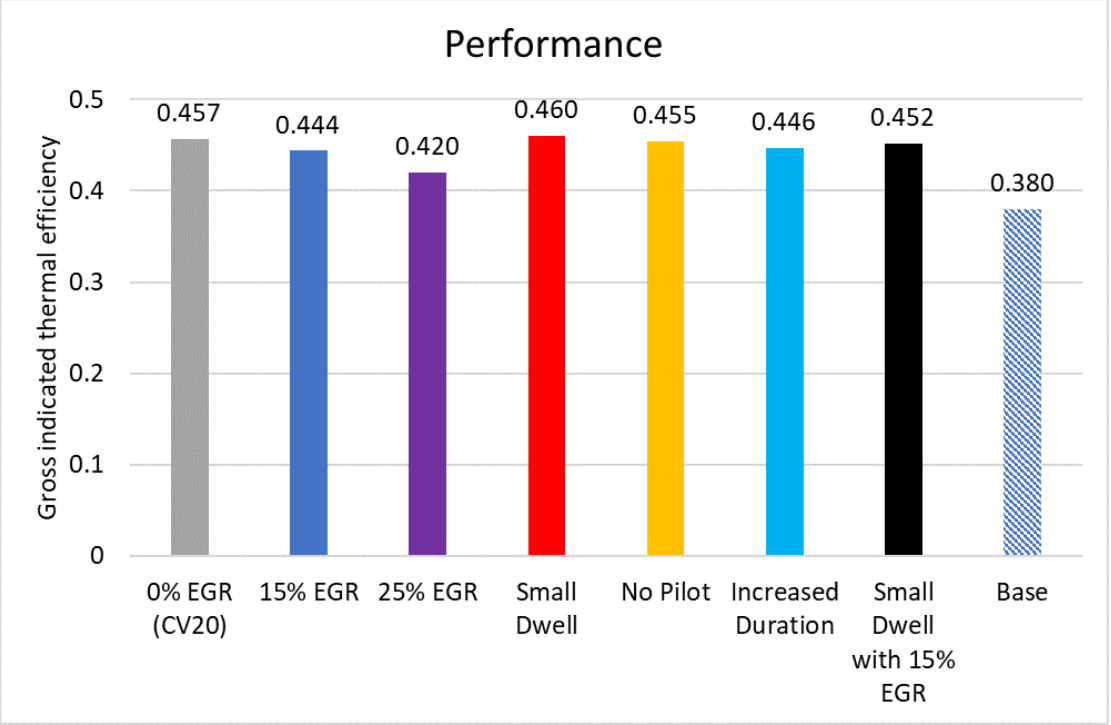

FIGURE 4.21: Performance characteristics for thermal efficiency-NO_x reduction.

4.3.5 Summary

A comprehensive numerical modelling study has been carried out to assess the benefits of a constant volume combustion phase (CVCP) being implemented in a compression ignition engine with focus on performance/efficiency and emissions. The CFD modelling framework has been validated with experimental data from a conventional turbocharged compression ignition engine.

The study examined the effects of CVCP start time, CVCP duration, EGR addition and injection strategies demonstrating that a properly optimised CVCP engine has many benefits, in terms of pollutant emissions and performance, compared to conventional engine operation.

Key findings and conclusions are as follows:

1. The CVCP strategy was shown to increase thermal efficiency by up to 8%, representing a reduction in specific fuel consumption of up to 20% compared to conventional engine operation.

2. The CVCP strategy leads to a large reduction in carbon-based emissions with soot and UHC values often being an order of magnitude smaller compared to conventional engine operation.

3. The CVCP strategy incurs a large increase to NO_x compared to conventional engine operation, however this can be negated by the introduction of low levels of EGR and in combination with the correct injection strategy does not sacrifice the benefits listed above.

4. The CVCP strategy leads to higher peak in-cylinder pressures and temperatures compared to conventional engine operation with greater amounts of heat release during the non-premixed charge combustion phase.

5. CVCP start time has very little impact on emissions and performance allowing for flexibility in engine balancing later in the design process.

6. Increasing CVCP duration beyond a certain point (CV20 in this study) leads to large increases in NO_x emissions and diminishing returns in terms of performance and carbon-based emissions reductions due to pressure rise rate fall-off and wasted time spent at TDC when work output could have begun if the piston was released earlier.

7. EGR rates as low as 15% are shown to greatly reduce NO_x emissions and when combined with improved injection strategies which reduce the amount of wasted time during the CVCP, such as decreasing dwell time between pilot and main diesel injections, can maintain the improvement in performance and reduction in carbon based emissions.

The key findings of the present numerical study on CVCP start time, CVCP duration, EGR addition and diesel fuel injection strategy will be considered in the optimisation of the CVCP opposed piston engine currently being developed by the Covaxe Group [208].

4.4 Effects of constant volume combustion phase on operational characteristics of an intake inducted diesel-hydrogen dual-fuel compression ignition engine

In this section the effect of the implementation of a CVCP is investigated at both low and high loads in a dual-fuel compression ignition engine setup which utilises intake inducted hydrogen with a diesel pilot injection as an ignition source. Simulations of both conventional and CVCP cycles are carried out and combustion characteristics, efficiency and emissions are compared. Section 4.4.2 focuses on the effects of CVCP operation on a diesel-hydrogen dual-fuel engine at low and high load. Section 4.4.3 addresses the LL performance issues at high hydrogen substitution levels through fuel injection improvements and CVCP implementation.

Figure 4.22 a) shows the schematic of the conventional test cases where diesel injection occurs when the piston is near TDC and then combustion with normal reciprocating motion, while Figure 4.22 shows the schematic of a CVCP test cases where diesel injection and the majority of combustion occur at TDC. Figure 4.22 also shows the corresponding piston profiles used in the analysis and a valve timing diagram which highlights important parts of the engine cycle.

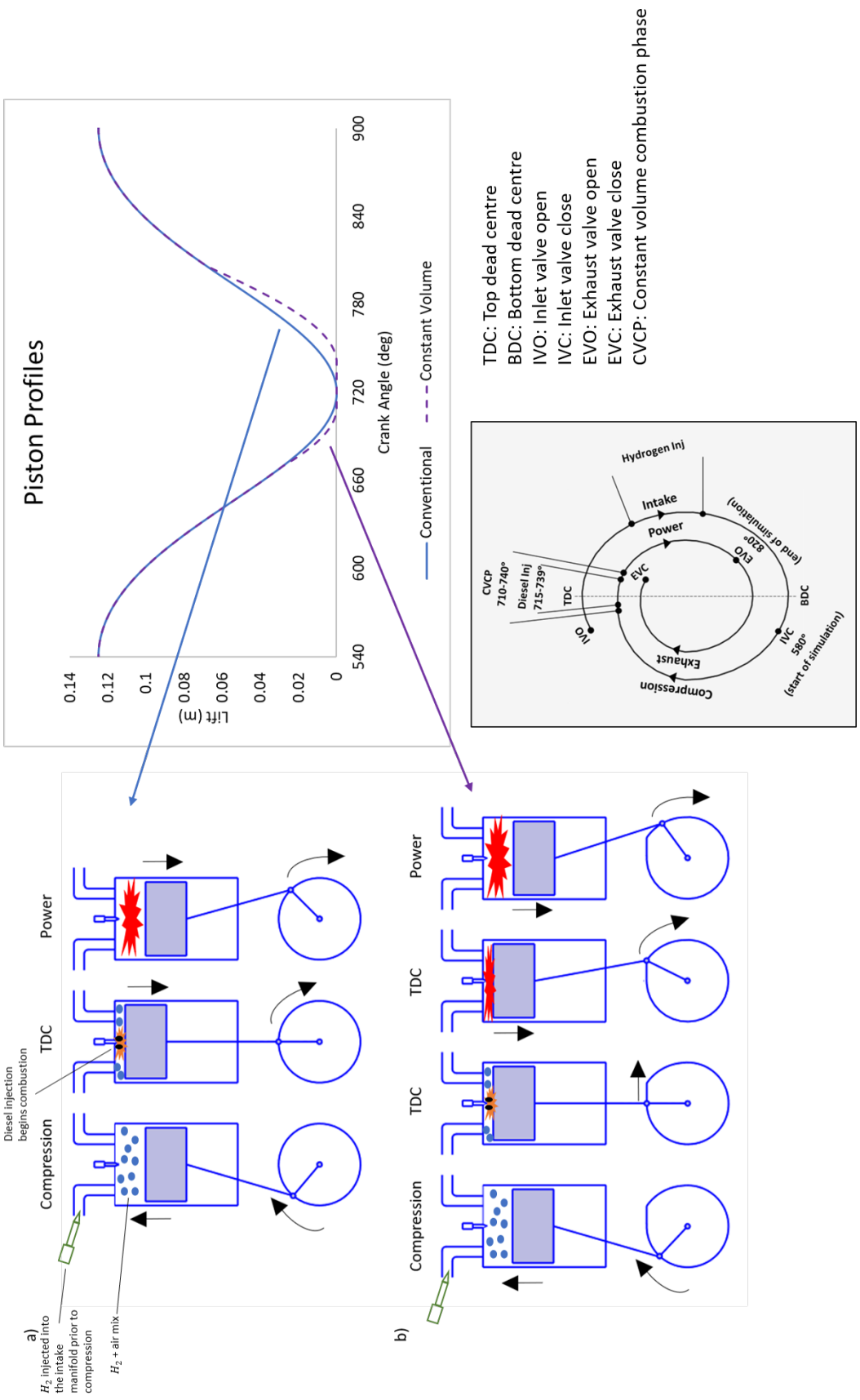

FIGURE 4.22: Schematic of a) conventional test cases, b) CVCP test cases, with the piston profiles used in the simulations and valve timing diagram.

4.4.1 Validation and mesh sensitivity analysis

Validation of the present numerical results including a mesh sensitivity analysis is carried out to ensure CFD results are accurate in comparison to experimental data for the reference engine [58], and independent of mesh resolution. Mesh densities were varied by changing minimum element size and maximum face size. Table 4.6 details the number of elements in each mesh at IVC and Figure 4.3 shows the medium density mesh/geometry.

TABLE 4.6: Mesh densities for validation and mesh sensitivity analysis.

Mesh density	**Elements**	**Run time**
Coarse	443868	≈11h
Medium	746063	≈18h
Fine	1104985	≈25h
Very Fine	1448346	≈38h

Figures 4.23 and 4.24 show the comparison of pressure and heat release rate (HRR) between the experimental reference and the coarse and fine mesh densities for 0%, 24%, 57% and 73% HES at high load. All mesh densities do a reasonable job at capturing the pressure and HRR profiles, with pre-combustion pressure, ignition delay, HRR and combustion pressure trends all being represented accurately at each HES apart from the 57% HES coarse simulation which does not accurately capture diesel pilot ignition of the premixed charge. In all mesh densities as HES increases the initial amounts of hydrogen which combusts at the same time as the diesel pilot are overpredicted which also leads to slightly higher than expected peak combustion pressures in the 57% and 73% cases. This is likely due to the reduced chemical mechanism implemented and could potentially be remedied by using a more detailed mechanism or one better adapted for dual-fuel combustion. While the medium mesh does a better job at capturing the early hydrogen combustion in the 57% case, power stroke pressure is generally overpredicted similar to those shown in the coarse mesh cases. The fine mesh better predicts the power stroke pressure and HRR timings and further mesh refinement did not offer any meaningful improvement to results. Therefore the fine mesh is chosen for the remainder of the simulations as it is adequately mesh independent and offers good agreement with experimental data.

Figures 4.25 and 4.26 compare emissions predictions at EVO in the simulations to those measured in the exhaust gases of the experimental engine. It should be noted that scaling of results with gross indicated work output and taking values at EVO rather than exhaust gases due to limitation of the simulations will have impacted values. H_2 emission trends are captured well with levels increasing up to 57% HES before decreasing

at 73%. The trending down of soot emissions with HES increase is captured reasonably but levels are overpredicted at low HES meaning the relative decrease is too great but still adequate for the current study. NO_x and CO_2 emissions are underpredicted slightly but the correct trends are captured for the most part. Some discrepancies arise in the UHC predictions. Predicted UHC values decrease rapidly with increasing HES indicating that they are too heavily affected by the reduction of injected diesel whereas the lower injection penetration/mixing appears to outweigh this reduction in the experiments. It is much more difficult to capture accurate UHC values due to the many intermediate combustion products involved, as noted by Kim et al. [90], and a more detailed reaction mechanism is likely required for accurate prediction. Consideration of UHCs in the initial species composition at IVC may also be required to reproduce experimental results which would also likely improve soot emission trends. Generally, CFD results reasonably well predict in-cylinder combustion characteristics such as pressure, HRR and exhaust emissions as observed in the experiments for each of the diesel-hydrogen dual-fuel test cases. This suggests that the numerical framework employed in this work is sufficient to perform a detailed parametric study about the effects of CVCP strategy on combustion performance and emissions of a diesel-hydrogen dual-fuel engine with respect to hydrogen concentration at differing engine operating conditions.

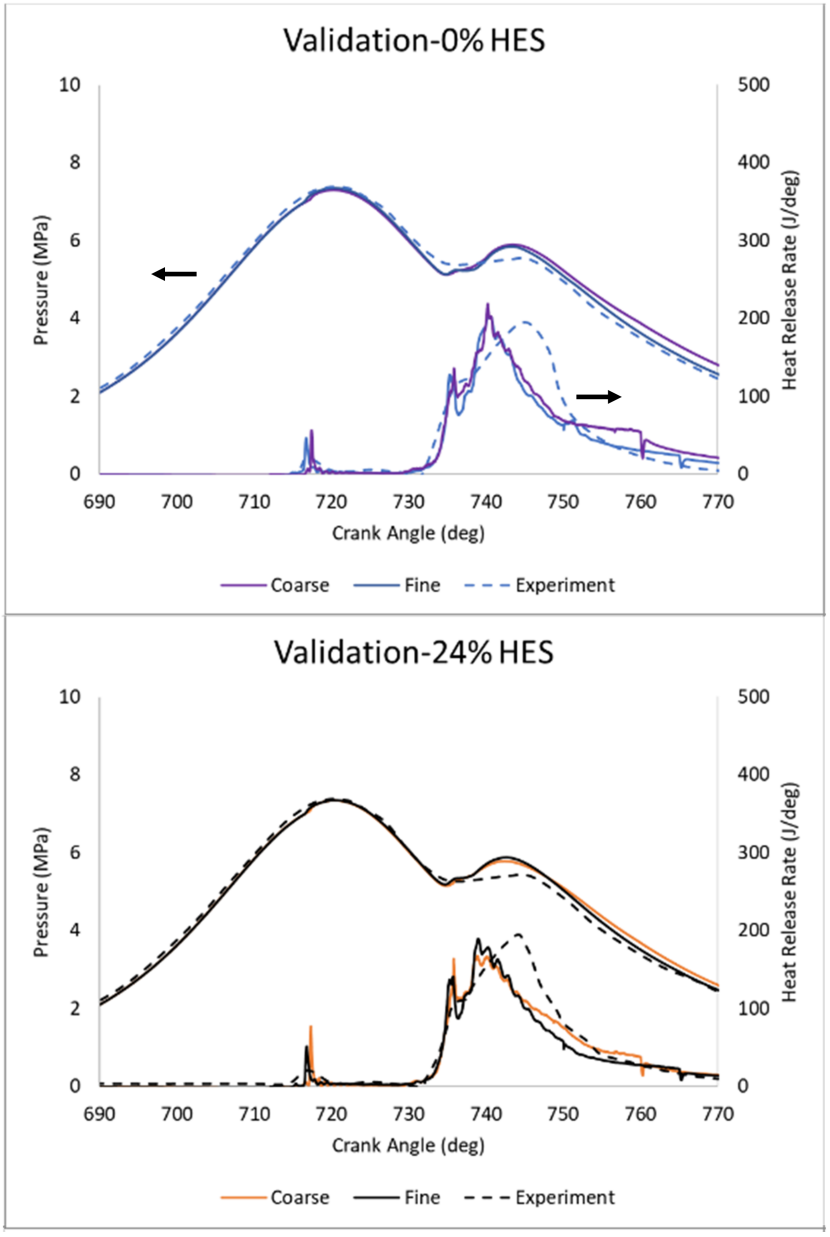

FIGURE 4.23: Pressure and heat release rate Validation for the simulations at 0% and 24% HES against the experimental reference [58]

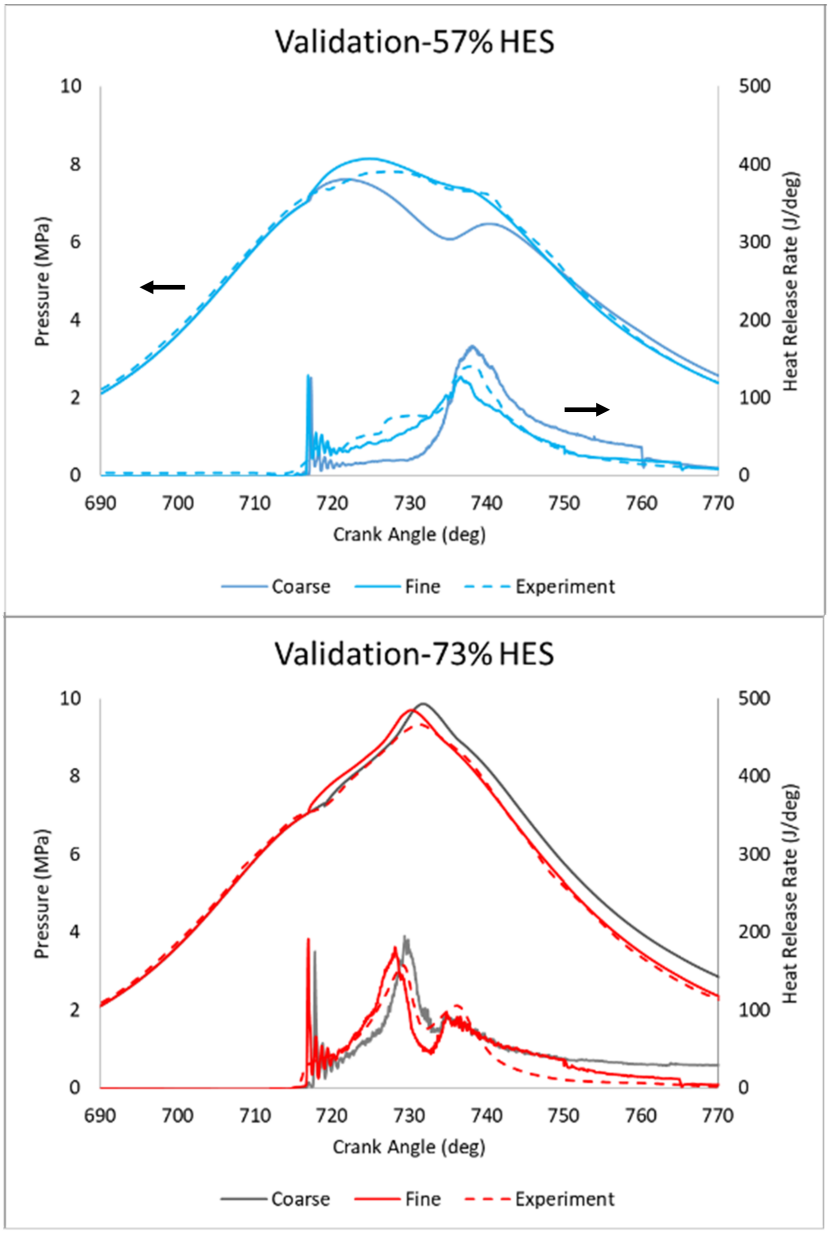

FIGURE 4.24: Pressure and heat release rate Validation for the simulations at 57% and 73% HES against the experimental reference [58]

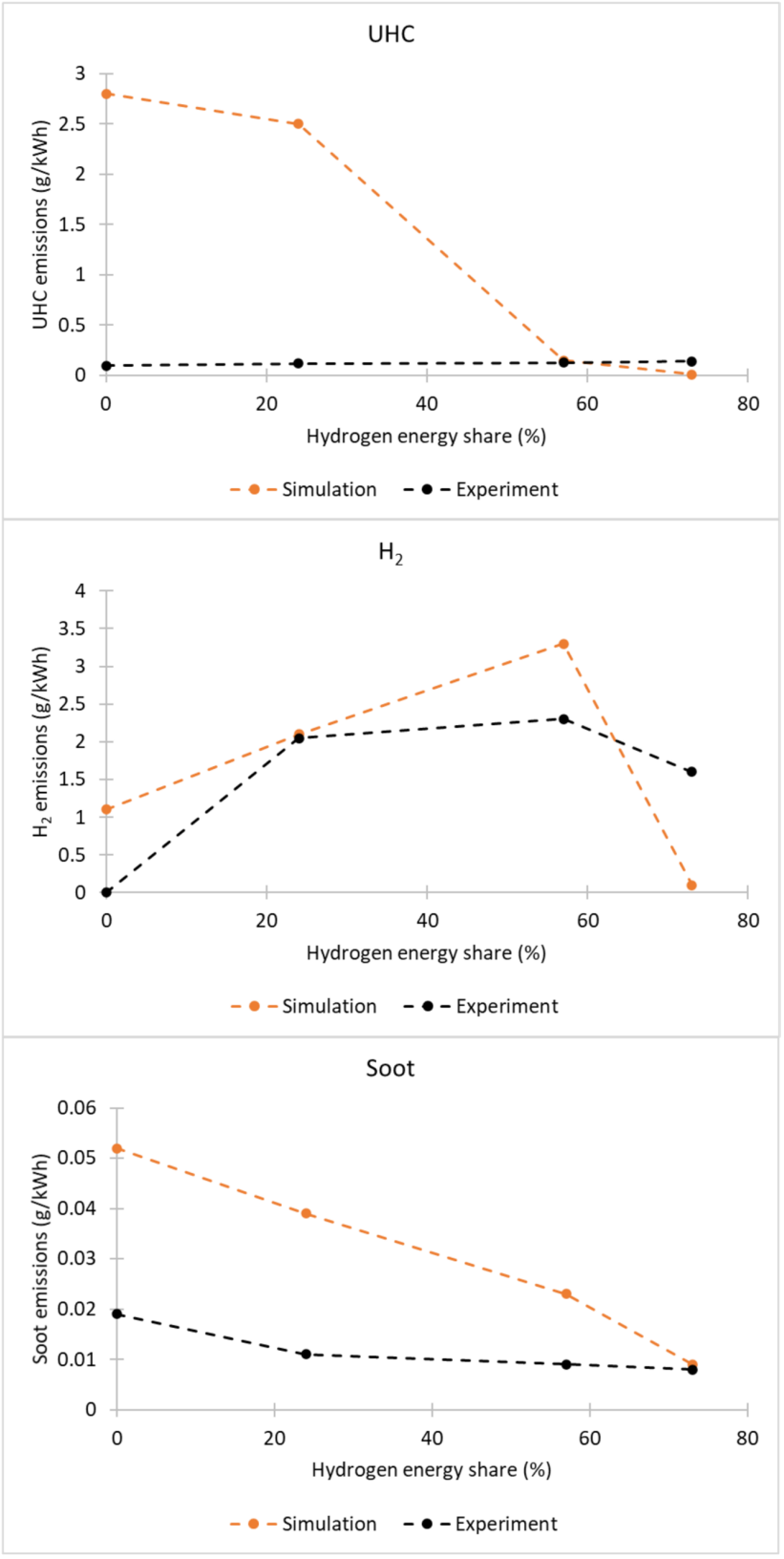

FIGURE 4.25: Validation for the simulations at 0%, 24%, 57% and 73% HES against the experimental reference [58] for UHC, H_2 and soot emissions at high load using the fine mesh.

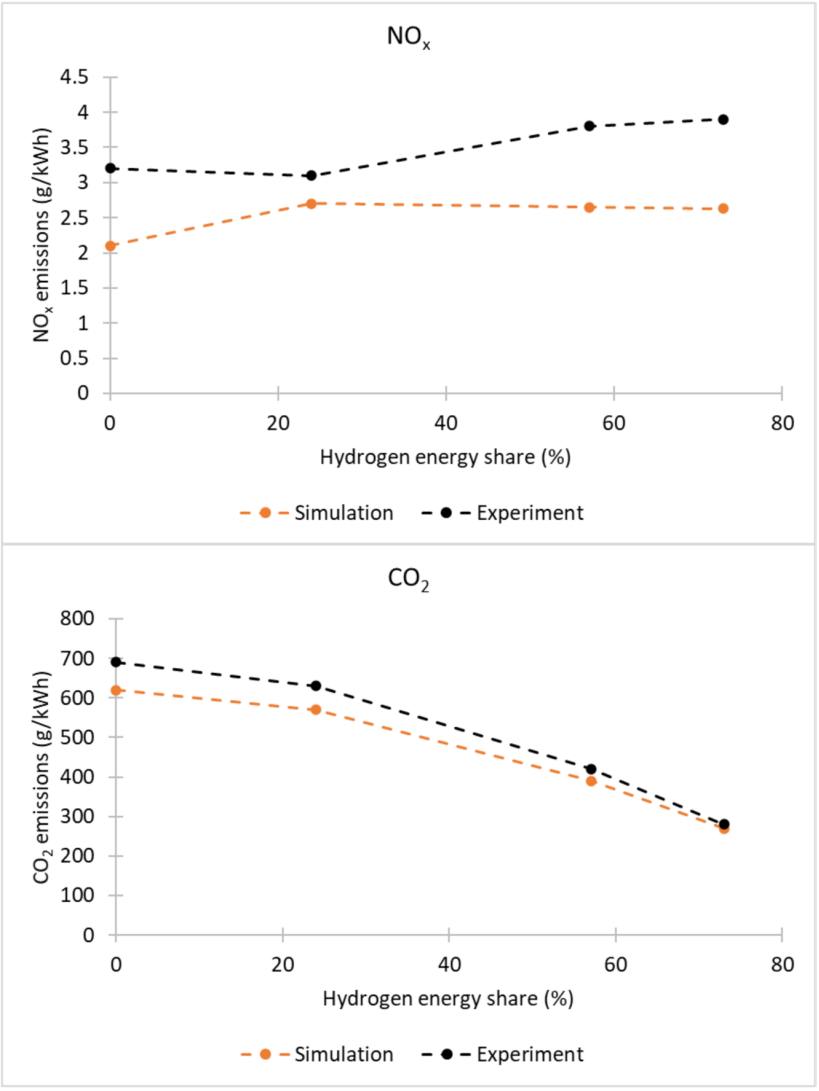

FIGURE 4.26: Validation for the simulations at 0%, 24%, 57% and 73% HES against the experimental reference [58] for NO_x and CO_2 emissions at high load using the fine mesh.

4.4.2 CVCP operation at increasing hydrogen energy share

The effect of the CVCP is investigated for 4 HESs at LL and HL conditions; 0%, 24%, 57% and 73% at HL and 0%, 57%, 73% and 90% at LL. The fuel-air equivalence ratio of the hydrogen-air mixes at HL are 0, 0.09, 0.21 and 0.27 for 0%, 24%, 57% and 73% HESs respectively and at LL 0, 0.12, 0.15 and 0.19 for 0%, 57%, 73% and 90% HESs respectively. The HL cases are selected as these align with those tested in the experimental paper. At LL, the experimental paper states 57% HES was deemed the limit as any further increase caused unacceptable decreases to performance [58]. However, we considered two additional cases at LL with 73% and 90% HES to examine the effectiveness of the CVCP on improving LL performance at high HESs. For all cases, a CVCP duration of 30° is implemented spanning from 710°CA to 740°CA. This CVCP period

is selected as it coincides with the diesel injection and the study carried out in the previous section indicated that a 30° duration should be sufficient for raising in-cylinder temperatures to the level needed for hydrogen autoignition.

4.4.2.1 Combustion characteristics

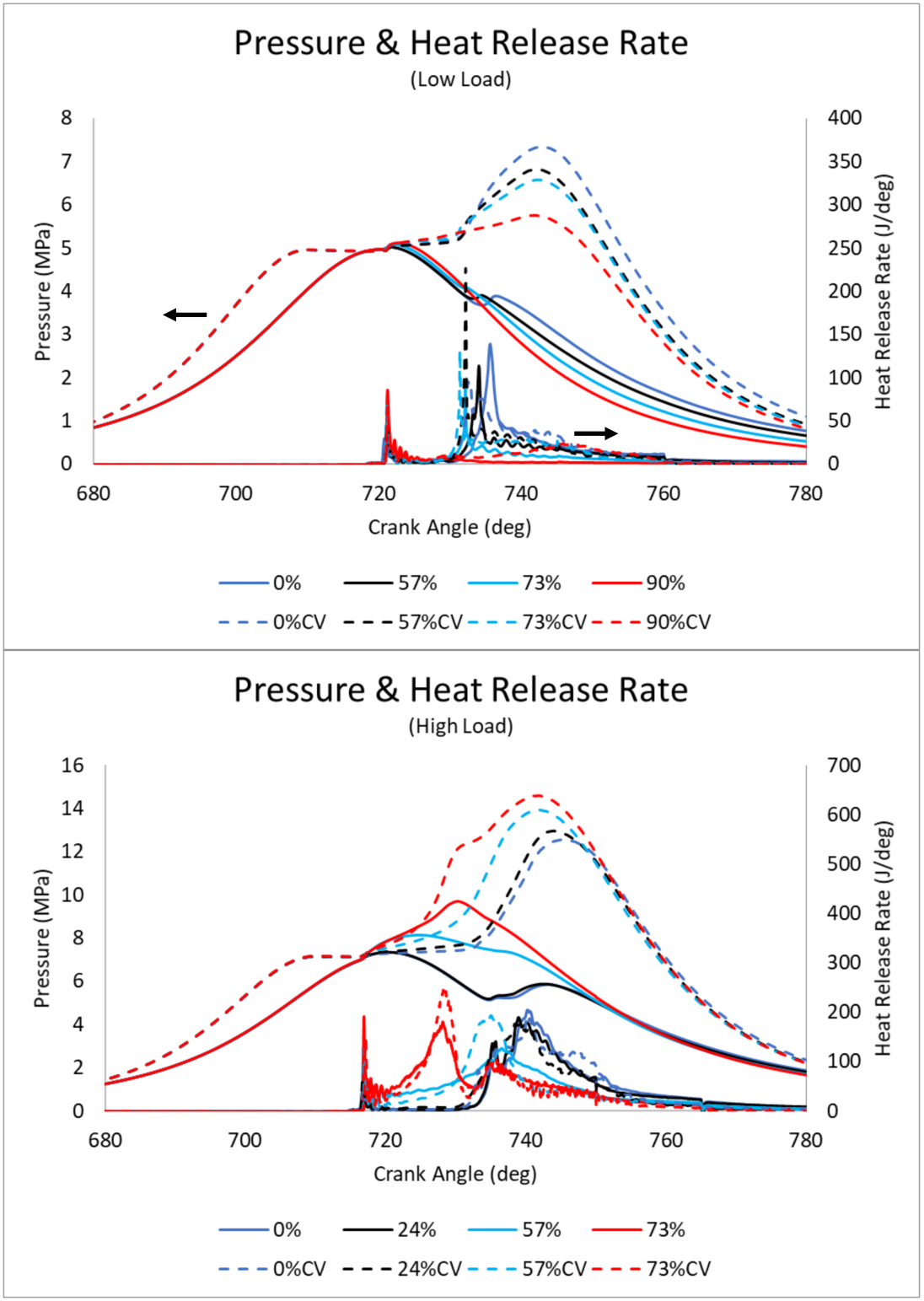

FIGURE 4.27: Pressure and HRR at low and high load for increasing levels of HES - CVCP-dual fuel

Figure 4.27 shows in-cylinder pressure and HRR curves at low and high load for the CVCP and conventional test cases. All cases at a given load condition have similar ignition delay timings with higher HES cases generally showing a small increase due to oxidiser substitution. CVCP does not have a considerable effect on ignition delay timing as thermodynamic conditions are much the same. Initial pilot injection HRR increases with HES increase due to small amounts of hydrogen becoming entrained in the diesel jet and combusting at this stage as well as the slightly longer ignition delay allowing for increased mixing of diesel, oxidiser and hydrogen.

At LL the pilot injection does not adequately ignite the premixed hydrogen-air charge in any test case. This is the result of a number of factors including: poor pilot injection penetration, small temperature increase in the cylinder due to only small injection volume and a fairly lean hydrogen-air mix even at high HESs due to there being less fuel needed at LL. It is also observed that main injection heat release generally starts earlier as HES increases, which is likely a result of the increased temperatures caused by the initial increased HRR. In the conventional engine the main injections also struggle to ignite the hydrogen-air mix at LL, for the same reasons as the pilot, with the total amounts of heat release becoming progressively lower as HES increases. In the 90% case there is almost no ignition of the premixed charge and at 57% and 73% most of the heat release occurs around the same time as the diesel injection heat release indicating that the flame front does not properly spread and only hydrogen near to the injection site is combusting. With the introduction of the CVCP the 57%CV and 73%CV cases show higher peak HRRs and an extended phase of heat release after the initial peak indicating flame spreading in the hydrogen-air mix throughout the combustion chamber. This is the result of temperatures and pressures being built up allowing for much more of the cylinder to reach hydrogen's autoignition temperature. Pockets of autoignition occur and increase temperatures further which help to begin the flame spreading. The higher temperatures both means the flame can spread faster and be maintained without extinguishing. However, while there is some improvement to HRR in the 90%CV case clearly the main injections reduced quantity was not adequate to cause full ignition of the premixed-charge and further optimisation is still required. Each LL hydrogen case could benefit from a longer combustion period at TDC to allow for more temperature to build-up (achieved by increasing CVCP duration or advancing injections) prior to the end of the CVCP as afterwards in-cylinder temperatures drop and the flame extinguishes before it can spread through the entire hydrogen-air mix. The highest amounts of heat release are observed in the pure diesel cases, in particular the 0%CV case where the higher temperatures and pressures caused by the holding of the pistons at TDC promote a higher quality of combustion.

At HL the pilot injection adequately ignites the hydrogen-air mix in all cases apart from the 24% and 24%CV cases where the relatively leaner mix means that the flammability limits are not met so flame propagation can't occur. The 24% cases show very similar

HRR trends to those of the 0% hydrogen cases, with slightly earlier peak HRRs and faster fall offs. At 73% HES the CVCP and conventional cases show similar trends. There are two clear peaks (after initial pilot combustion), the first is due to the fast burning of the majority of the hydrogen as the high fuel-air equivalence ratio and temperatures leads to a high flame speed and the second is when the main diesel injection occurs and combusts causing its own heat release with small amounts of remaining hydrogen combustion. The much increased rate towards the first peak also indicates wholesale ignition of the mix where autoigntion is also occuring as the flame spreads due to the rising temperatures. In the 57% cases there is one peak and this occurs at the same time as the main diesel injection. The lower fuel-air equivalence ratio of the hydrogen-air mix means flame spreading occurs at a reduced rate. As a result, no autoignition occurs and the mixture has not had a chance to entirely combust prior to the diesel injection and thus the injection enhances the remaining premixed charge combustion. The 73% CVCP case does however exhibit similar behaviour to the 73% cases in that the climb towards peak HRR accelerates in the latter stages indicating some autoignition in the mixture. In general at 57% and 73% HES the introduction of a CVCP leads to a slower initial ramp up to peak HRR but this is followed by a somewhat higher peak and faster fall off. The initially slower HRR is due to the reduced mixing of the diesel injection which is caused by the stationary piston (reduced turbulence and injection always targeted in the same area) meaning less hydrogen is entrained, slowing the initial flame spreading. The subsequent higher peak HRR is caused by a larger amount of the combustion chamber being at a high enough temperature for hydrogen autoignition due to the build-up of temperature, and is also somewhat enhanced by the reduced distance needed for the flame to travel due to the minimum combustion chamber volume being maintained. Increased levels of hydrogen utilisation also likely play a part. The faster fall off in HRR is largely due to the higher fuel utilisation and therefore less fuel/oxidiser availability.

CVCP cases have a slightly faster piston approach to TDC which leads to pre-combustion pressure peaking 10° earlier. Peak pressures are higher in the CVCP cases compared to conventional, and all occur at the end of the CVCP, a result of the piston being held at TDC and therefore all the combustion energy is built up until the piston is released. Higher pressures are observed for most of the expansion stroke until around 50deg after the end of the CVCP in most cases.

At LL the initial amounts of high HRR observed in the high HES cases means that peak pressure increases slightly in the conventional engine as HES increases. However, the pilot not igniting the hydrogen-air mix and subsequently the main injection also struggling to ignite the mix leads to lower pressures in the power stroke as HES increases which will greatly impact engine performance. The addition of a CVCP leads to promising increases in combustion of hydrogen, especially for 57%CV and 73%CV,

where pressures increase reasonably. 90%CV shows more combustion than the corresponding conventional case leading to a small rise in pressure during the CVCP, but optimisation is clearly required for further improvement to hydrogen utilisation.

At HL increasing HES leads to increases to peak pressure and peak pressure rise rate. The low HES cases follow similar trends to the pure diesel cases only with slightly increased pressures. At 57% and 73% HESs the conventional engine cases both initially have higher pressure rise rates than the corresponding CVCP cases but are overtaken once the combustion chamber temperatures in the CVCPs catch up and exceeds them, leading to rapid hydrogen combustion. At 57% and 73% HES peak pressure occurs in the conventional engine prior to the main diesel injection which causes secondary smaller peaks. After the initial HRR peak the pressure rise in 73%CV levels off and increases at a slower rate up until the end of the CVCP, whereas for 57%CV the increase is much slower and picks up towards the middle of the CVCP before also levelling off.

Generally pre-ignition is caused by hot spots within the combustion chamber which lead to early hydrogen ignition. Since simplified constant temperature boundary conditions are used at the walls for computational efficiency as well as only running a single cycle these hot spots do not exist in the simulations and the chamber temperatures prior to diesel injection do not reach a high enough temperature for hydrogen autoignition and thus knocking is not observed. Knocking was not experienced in the experimental reference paper at the studied hydrogen energy shares either and thus these assumptions are reasonable. It could also be argued that the increased pressure rise rates associated with the CVCP may cause undue engine noise, however, in the realistic CVCP engine the amounts of fuel and timings of injection will be adjusted to allow for the same increased efficiency without excessive pressure rise rates due to a reduction in required fuel per cycle. It should also be noted that in most cases HRR trends are fairly similar to the conventional engine and there are no extreme/-sudden rises which would indicate abnormal combustion. An analysis more focused on cycle-cycle variation, wall temperatures and the potential for knocking under CVCP operation is required for a more complete view of engine operation.

The pressure curves indicate several instances of “wasted time” at TDC in the CVCP cases. Utilising the full CVCP is important as work is not generated until the expansion begins and if expansion could start earlier work output would also increase. The first instance is the time between the start of the CVCP and the start of combustion. Injection timings are not properly optimised and all CVCP cases would likely benefit from an advancement of the injection timing to allow for the full phase to be utilised. This would be most beneficial at LL high HESs where allowing for temperatures to build for longer should also increase the likelihood of full ignition of the hydrogen-air mixes. The second instance is the time between pilot and main injections in cases where the pilot does not ignite the premixed charge. This leads to a stagnation in pressure which could be alleviated by advancing the main injection, combining the pilot and main

or increasing pilot injection volume such that hydrogen-air combustion begins earlier. The third instance is the levelling off in pressure rise rate observed most obviously in the 73%CV case. At this HES it would be more beneficial to end the CVCP directly after the peak in HRR attributed to the hydrogen-air premixed charge combustion (just prior to main diesel injection) for maximum work output. Ending the CVCP earlier in this instance would also reduce NO_x emissions as there would not be any needless temperature build-up.

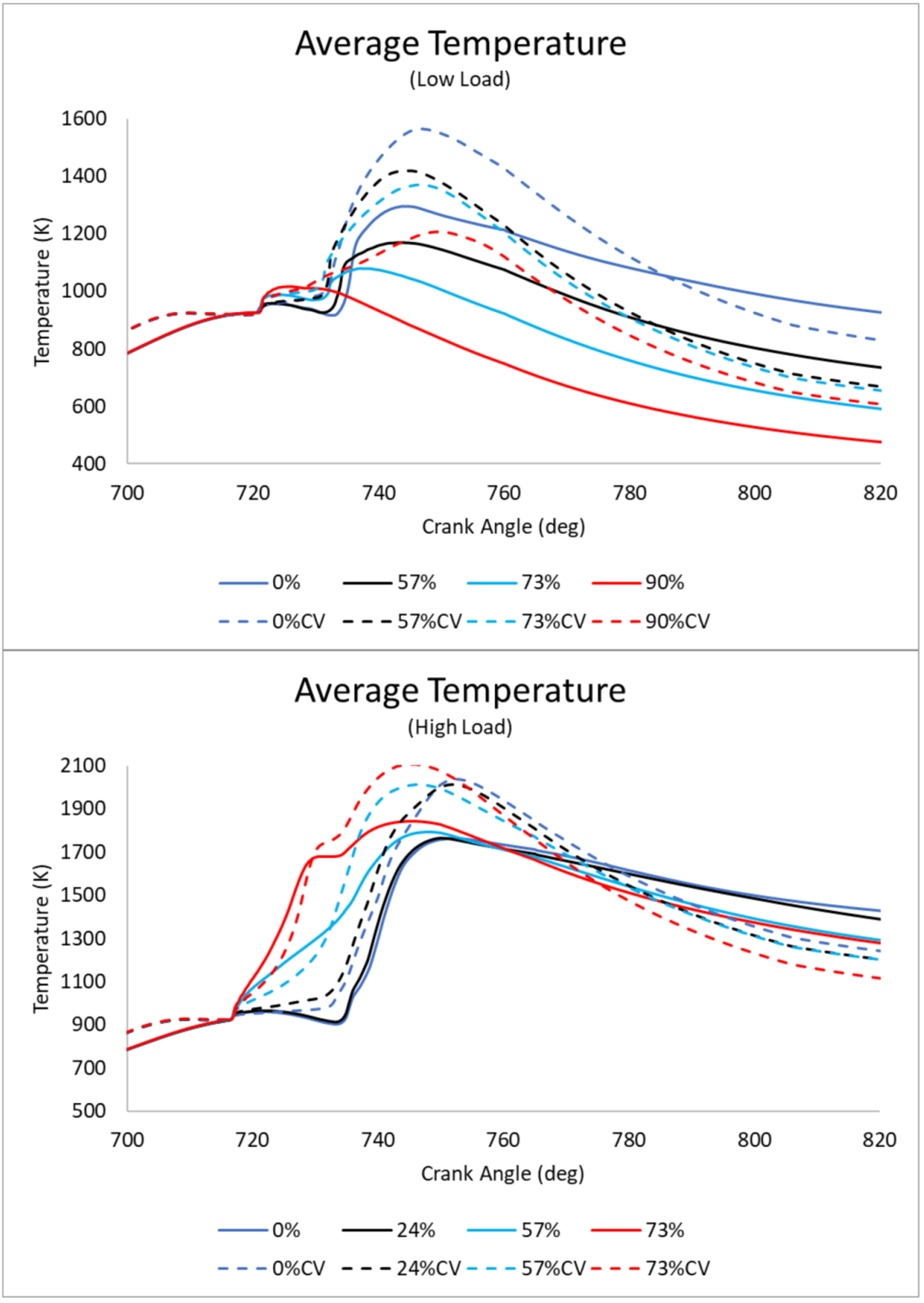

FIGURE 4.28: Average in-cylinder temperature at low and high load for increasing levels of HES - CVCP dual-fuel

Figure 4.28 shows the average in-cylinder temperatures for each case. As expected, average in-cylinder temperatures are mostly higher for all CVCP cases when compared to

their conventional counterparts, with the conventional cases only having higher temperatures in the late power stroke. Average in-cylinder temperatures in the CVCP cases increase until the end of the CVCP due to the build-up of pressure and heat released by the combustion, but fall off more rapidly once the piston begins to move again, whereas the conventional cases peak during combustion of the main diesel injection and fall off more steadily. The rapid fall off in temperature in CVCP cases is due to higher amounts of heat loss to the walls, faster piston movement away from TDC and reduced amounts of excess fuel/oxidiser left for combustion when compared to the conventional cases. At LL average in-cylinder temperatures mostly decrease as HES increases due to the reducing quality/amount of combustion occurring. Whereas at HL the opposite trend is true and temperatures mostly increase with increasing HES, they do however decrease with HES increase in the late power stroke due to the chamber wide combustion causing greater amounts of heat loss to the walls. Peak temperatures also tend to occur earlier as HES increases at both load conditions.

4.4.2.2 Emissions

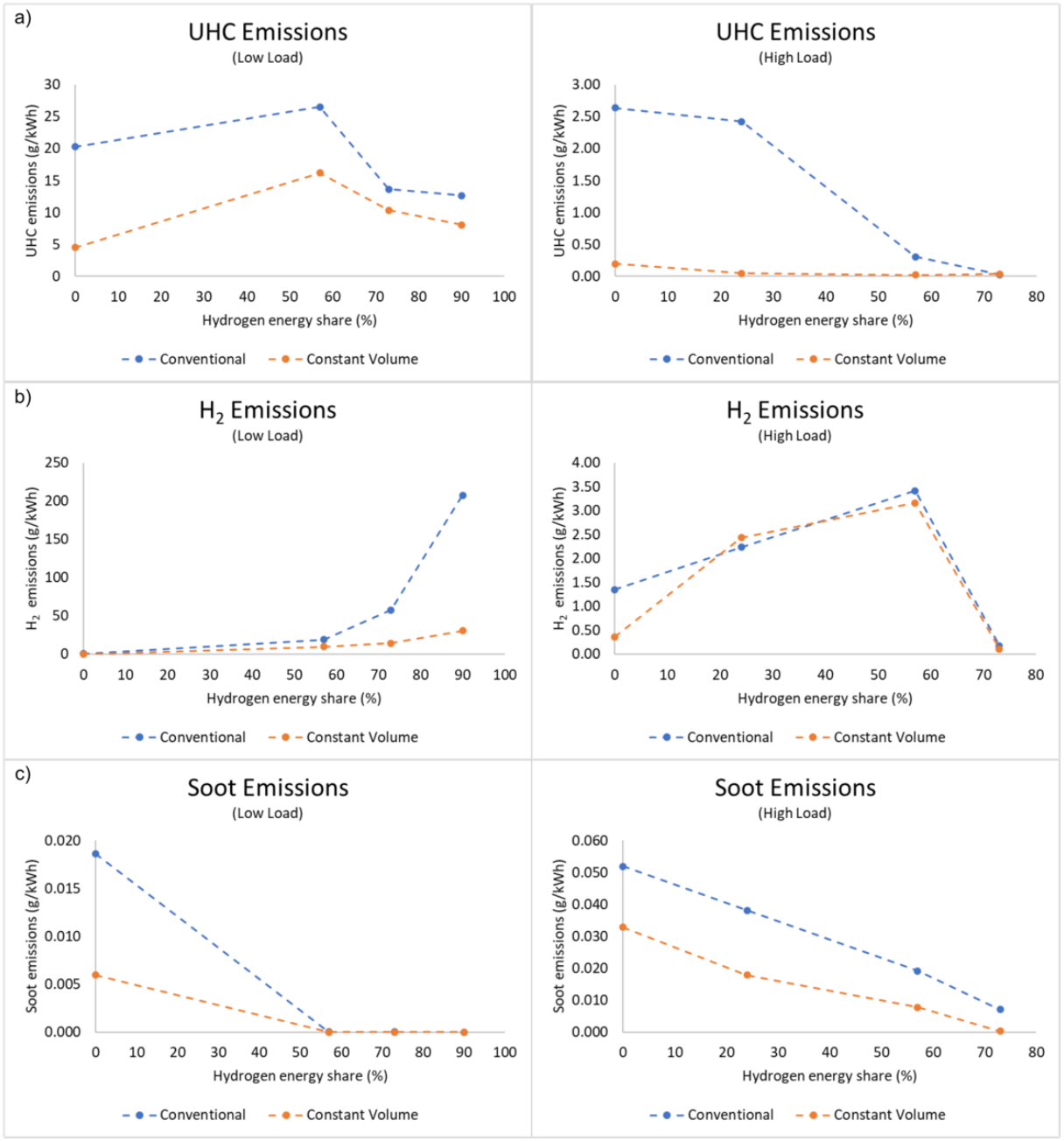

FIGURE 4.29: Emissions levels at EVO for a) UHC, b) H_2 and c) soot for increasing levels of HES - CVCP dual-fuel

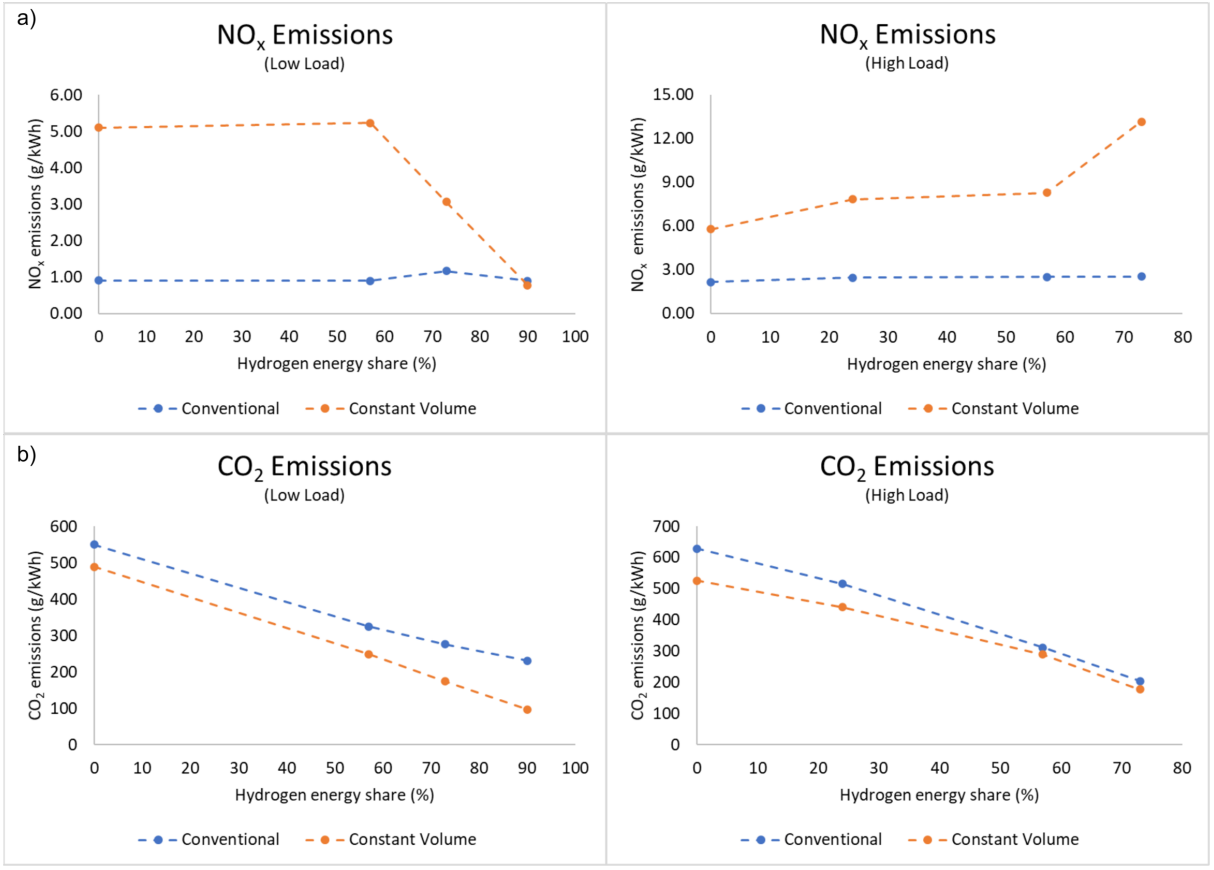

FIGURE 4.30: Emissions levels at EVO for a) NO_x and b) CO_2 for increasing levels of HES - CVCP dual-fuel

UHC emissions are a good indicator for the quality of combustion which the diesel went through as the lower the value the more complete the combustion and more diesel which was utilised. A number of factors can cause high UHC emissions including poor mixing of fuel and oxidiser, low temperatures, fuel getting caught in small crevices and fuel mixing with lubricating oil [12, 209]. Figure 4.29 a) shows UHC emissions reduce dramatically with implementation of the CVCP at both load conditions indicating a much more efficient conversion of fuel to work. This is a result of large amounts of complete combustion occurring at a constant volume and the higher temperatures and pressures being ideal for high diesel combustion efficiencies. The reduced mixing caused by the stationary piston is clearly outweighed by the improved thermodynamic conditions. A reduction is also generally observed as HES increases due to a reduction in hydrocarbons entering the chamber. LL goes against this trend somewhat due to the reduction in performance leading to increased specific output.

H_2 emissions are also a good indicator of combustion quality and can be largely correlated with how well the diesel injection ignited the hydrogen-air mixture. At LL there is a clear and unacceptable increase in hydrogen emissions as HES increases in the conventional engine, Figure 4.29 b). This is a result of the deterioration of performance

and general lack of combustion occurring when the injected diesel does not adequately ignite the mixture. The CVCP helps to alleviate the issue to an extent but still emits a large amount of hydrogen in the 90% case. Hydrogen emission at HL is much lower with the lowest emissions being that of the 73% cases due to high combustion quality as the flame manages to spread throughout the entire chamber (evidence by the two peaks present in the HRR graphs). CVCP does not meaningfully impact hydrogen emissions at HL because the diesel injection is adequate without need for the increased temperatures offered by the CVCP.

Soot emissions are sensitive to many factors, with the main cause of high soot production being areas of locally rich carbon and low temperatures [12, 211]. Figure 4.29 c) shows the CVCP cases produce lower soot levels than the conventional setup. The low soot levels are due to the higher temperatures and high levels of combustion efficiency during the CVCP leading to very few rich distributions of carbon in the cylinder, as a large quantity of the injected diesel has gone through quality complete combustion. Reducing the amount of carbon injected into the cylinder also reduces soot levels due to there being a smaller chance for carbon rich distributions to occur so higher HESs improve emissions at both loads.

NO_x emission is sensitive to in-cylinder temperatures due to the thermal Zeldovich mechanism [56] with thermal NO_x production rate doubling with every 90K increase above 2200 K but falling to much lower rates when temperatures are below 1800K [39]. As expected the prolonged higher temperatures associated with the CVCP strategy lead to a significant increase in NO_x emission, as shown in Figure 4.30 a). This increase is present at both loads and therefore is clearly one of the limiting factors when implementing a CVCP cycle and optimisation is required to reduce their level. NO_x emissions are shown to generally increase at higher HESs at HL due to the higher burning temperature of hydrogen and chamber wide increase in temperature due to premixed flame propagation and autoigniton, but specific output is somewhat offset by the corresponding performance increase. At LL NO_x decreases at higher HESs but this is due to the reduction in combustion which will lead to poor performance.

High levels of CO_2 are also an indicator that the diesel has undergone complete combustion as a larger quantity of CO in the chamber has been oxidised. While CVCP cases have higher CO_2 levels on a per cycle basis, the increased performance leads to a lower specific output, as shown in Figure 4.30 b). HES increase also leads to lower CO_2 emissions as there is less carbon being injected into the chamber and a reduction of air intake, which contains CO_2, due to hydrogen substitution will also contribute a small amount.

4.4.2.3 Performance

Gross indicated performance characteristics are calculated and any further mention of performance, thermal efficiency, power and work refer to gross indicated values. Trapezoidal rule [212] is used to integrate and find the area between P-V curves for each case, providing the work and from this power and thermal efficiency were calculated. All gross indicated performance characteristics are linearly linked and therefore only thermal efficiency and cumulative heat release are presented in Figures 4.31 and 4.32 .

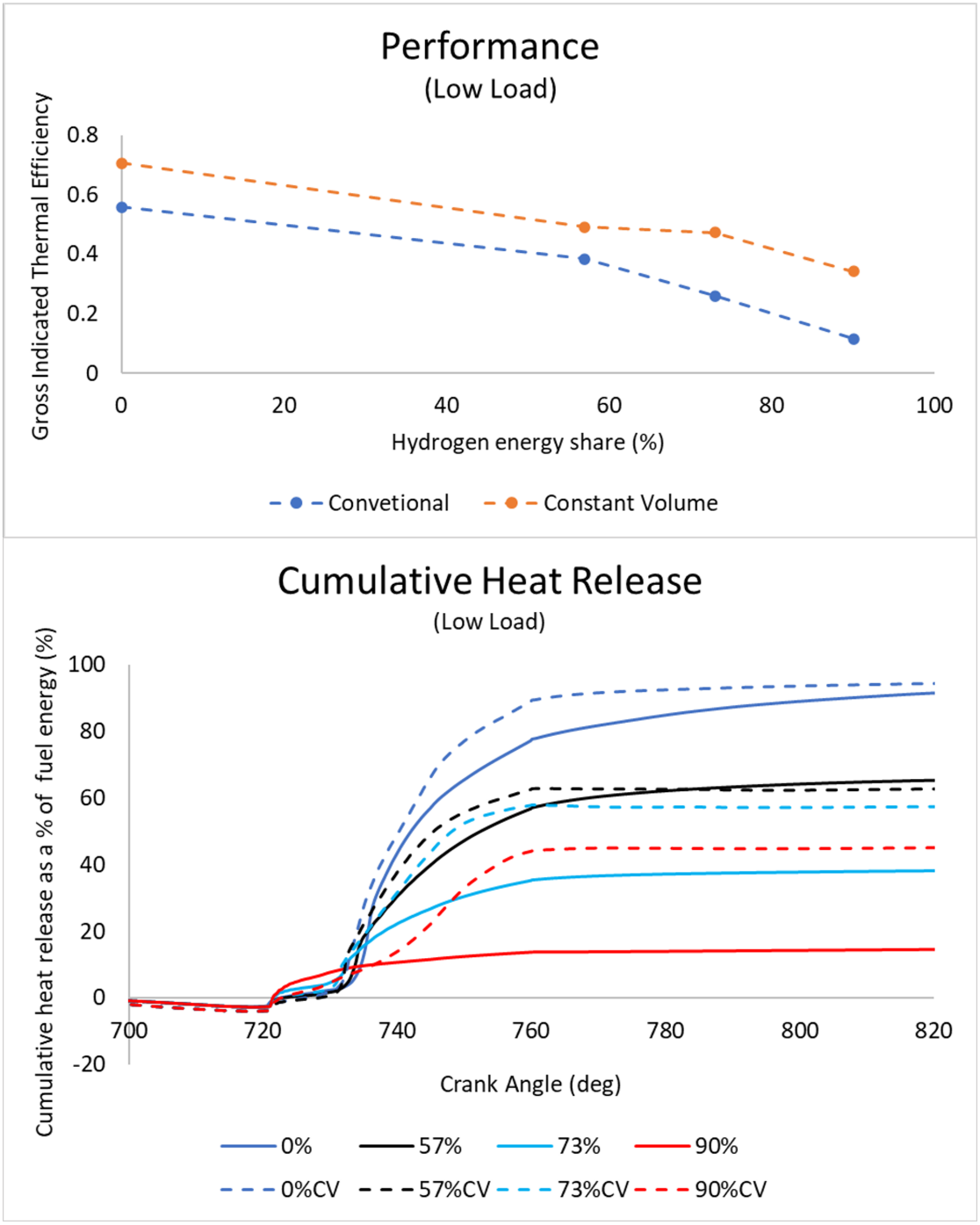

FIGURE 4.31: Performance characteristics for thermal efficiency and cumulative heat release for increasing levels of HES at low load - CVCP dual-fuel

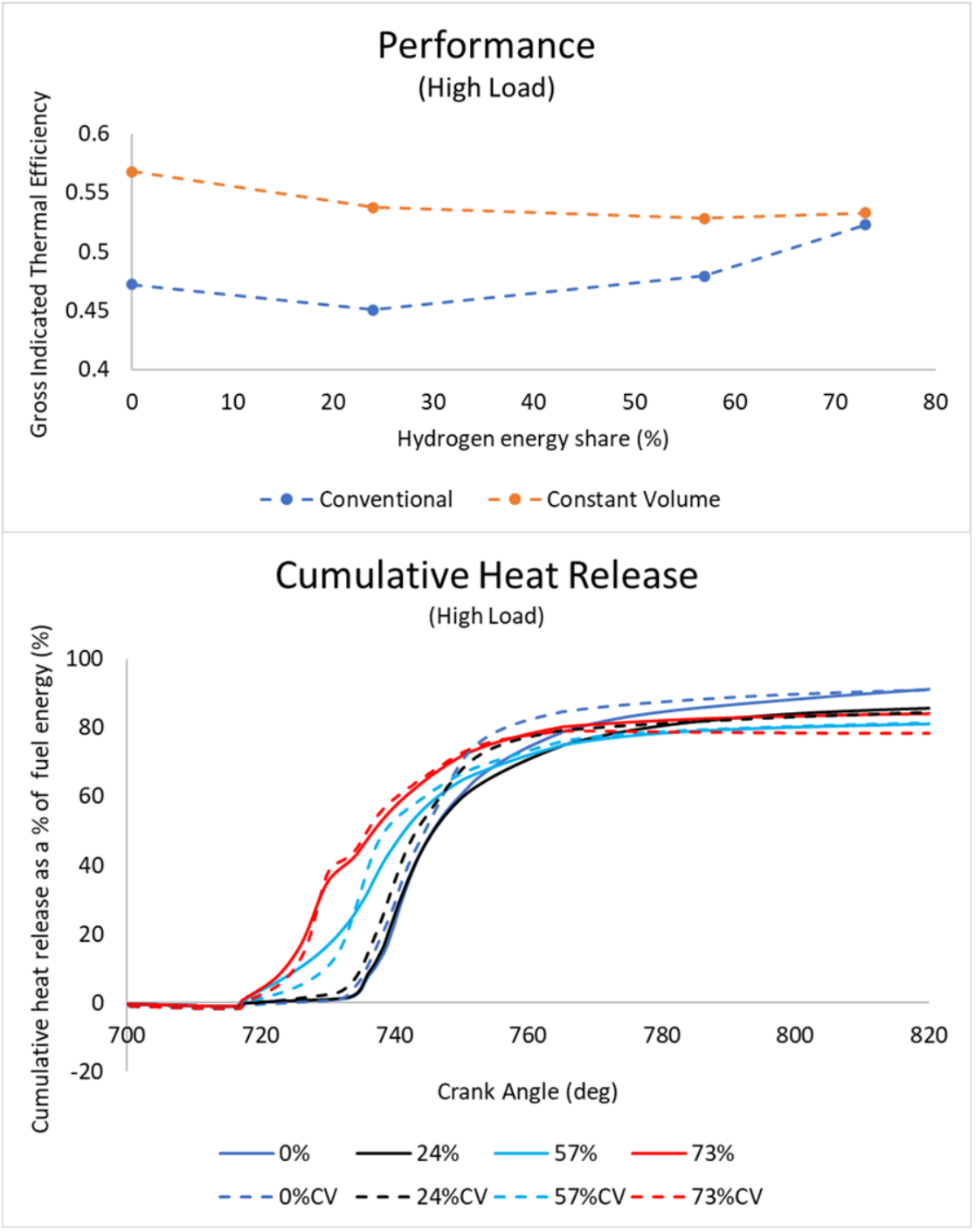

FIGURE 4.32: Performance characteristics for thermal efficiency and cumulative heat release for increasing levels of HES at high load - CVCP dual-fuel

The implementation of a CVCP leads to performance increases across all cases, Figures 4.31 and 4.32. The increase in performance is caused by factors including: increased fuel utilisation, higher in-cylinder pressures and temperatures being built to drive the piston and increased amounts of combustion occurring at these conditions. At HL the relative performance increase of CVCP compared to conventional operation decreases as HES increases, while at LL the opposite is true. At HL in the 57% and 73% HES

cases the pilot adequately ignites the hydrogen air mix without need for the CVCP so the performance increase largely comes from the increased pressures and not so much fuel utilisation. At HL in the conventional setup increasing HES leads to increases to performance, however performance decreases for the CVCP cases as HES increases due to the aforementioned wasted time and thus reduced expansion work as well as increased heat losses to walls. At LL increasing HES leads to a reduction in performance in both operational modes, a result of the diesel injection struggling to properly ignite the hydrogen-air mix. The reduction is less severe in the CVCP cases due to the increased temperatures increasing the likelihood of hydrogen combustion, but further improvements need to be made to completely negate the performance decrease.

As expected, Figures 4.31 and 4.32 show cumulative heat release is higher under CVCP operation throughout combustion across all HESs at LL due to the much-increased fuel utilisation but total heat release decreases as HES increases. Also in the likes of the LL 0% and 57% CVCP cases there is clearly increased levels of initial heat release, however, HRR during the late power stroke is much lower due to greater amounts of wall heat losses and less fuel being available for combustion, i.e. cooling more rapidly, meaning total heat release at EVO is fairly comparable. These effects are amplified at HL in the 57% and 73% cases where the pilot adequately ignites the premixed charge without need for the CVCP, as evidenced by the very similar early cumulative heat release trends prior to 760°CA. The higher in-cylinder temperatures caused by the CVCP and increasing levels of combustion across the entire chamber at higher HESs leads to lower total heat release at EVO for CVCP cases which decreases further as HES increases. This will have an impact on performance and optimising the CVCP such that wall heat losses are minimised requires further attention.

The CVCP performs reasonably across both load conditions at all HESs with good improvements to thermal efficiency and carbon-based emissions compared to the conventional engine. Given proper optimisation with regards to the reducing wasted time at TDC, reducing wall heat losses, further improvement to LL high HES performance and strategies to control NO_x, CVCP operation could prove useful in future diesel-hydrogen dual-fuel engines.

4.4.3 Low load performance improvements at high hydrogen energy share

As noted in the previous section several improvements can be made to engine operation which should lead to improved performance and emissions characteristics in the CVCP configuration. This section will focus on further improving LL performance at a high HES as this is one of the major outstanding issues with current diesel-hydrogen dual-fuel engines [59, 76]. Table 4.7 details the LL 90% HES test cases examined in this section.

TABLE 4.7: Details of ten different test cases considered for LL high HES improvement (5 test cases for the conventional engine and 5 test cases for the CVCP engine)

Case	**1/1CV**	**2/2CV**	**3/3CV**	**4/4CV**	**5/5CV**
Description	Original (LL 90%/ 90%CV)	Injections advanced by 7°CA	Advanced and 3°CA less dwell between pilot + main injection	Advanced and combined pilot + main injections	Advanced and combined pilot + main injections with higher velocity
Injection Period Pilot (°CA)	717-719	710-712		-	-
Injection Period Main (°CA)	727-729	720-722	717-719	710-714	710-713
HES	90%				
Load	Low				

4.4.3.1 Combustion characteristics

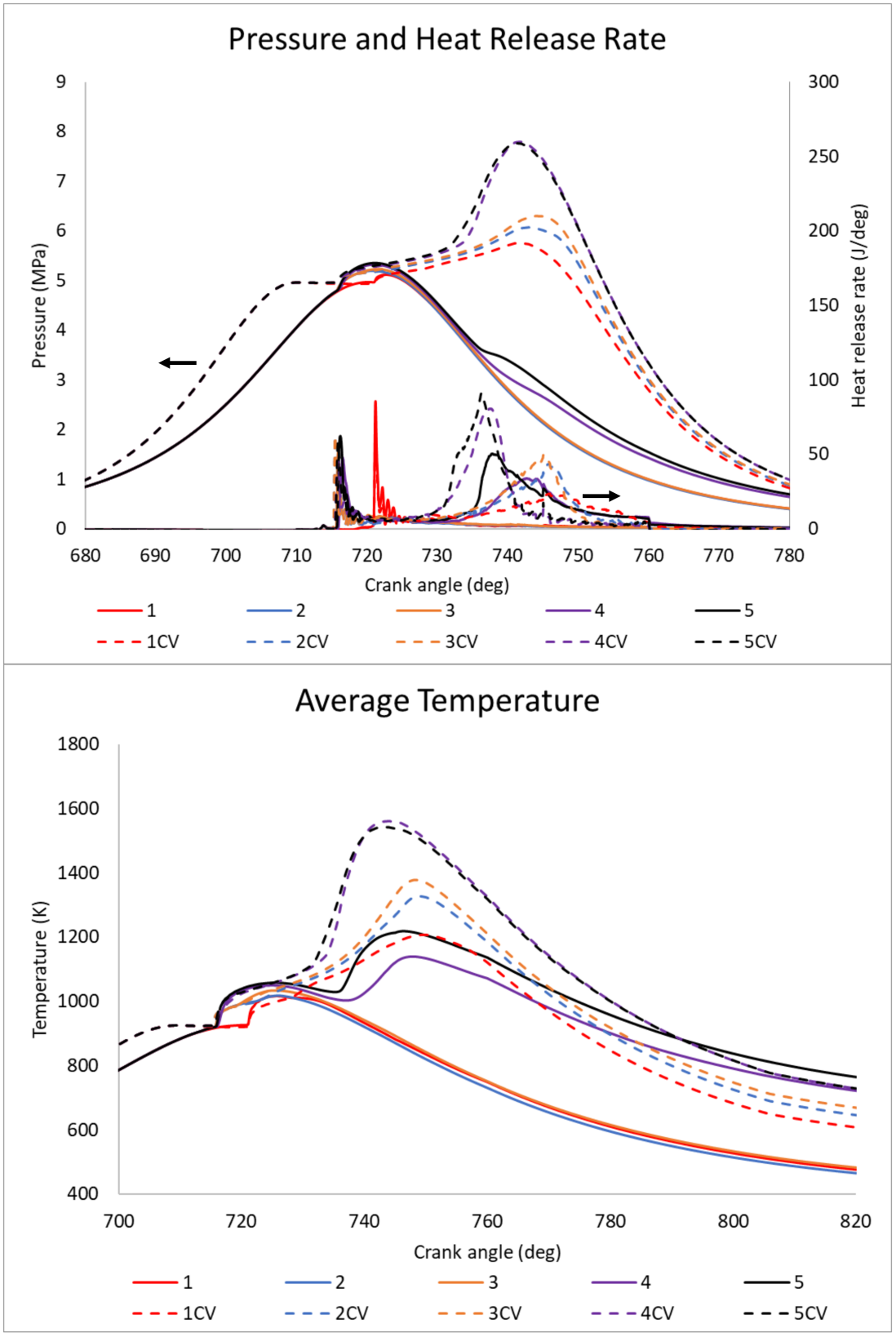

FIGURE 4.33: a) Pressure and HRR and b) average temperature for LL 90% HES - CVCP dual-fuel LL improvements

Figure 4.33 a) shows pressure and HRR traces for each test case while Figure 4.33 b) shows the average in-cylinder temperatures. Cases 2 and 3 in the conventional engine show little to no improvement to hydrogen heat release compared to case 1, i.e. advancing injections does not lead to adequate ignition of the premixed charge. The only potential improvement comes from the advanced injection leading to higher pressures and temperatures at TDC but this is not enough to cause further hydrogen combustion. However, in the CVCP engine the advanced injections lead to considerable improvements. Earlier injections allow for more time for combustion to occur within the CVCP, leading to an extended temperature building phase and much more favourable conditions for hydrogen ignition. HRR/temperatures initially build slowly until enough combustion has occurred to heat the entire cylinder which then leads to rapid combustion of the remaining hydrogen. In comparison to 1CV, 2CV shows higher peak pressure, temperature and heat release while 3CV shows slightly higher levels of each compared to 2CV. The increases in 3CV are due to the shortening of the dwell time between pilot and main injections leading to even more time for combustion within the CVCP. The CVCP ends somewhat early in these cases however which means some hydrogen is left unburned as the flame extinguishes once temperatures begin to fall.

A combination of factors leads to much improved combustion and hydrogen utilisation in cases 4 and 5 in the conventional engine when compared to cases 1, 2 and 3. Increased levels of diesel premixed charge combustion, due to pilot removal, leads to a larger spike in initial HRR and temperature which increases the likelihood for hydrogen ignition and flame propagation. Furthermore, combining the pilot and main injections leads to the entire injection occurring earlier meaning a greater amount of combustion occurs close to TDC and therefore the higher temperatures and pressures which follow improves hydrogen ignition. Additionally, the diesel injection is more focused on one area which increases local temperatures and the chance for local hydrogen combustion which can potentially spread to the rest of the chamber if enough occurs. Compared to case 4, wholesale hydrogen ignition occurs earlier in case 5, indicated by the earlier larger secondary peak in HRR and subsequent increase in power stroke pressure. Clearly more fuel is utilised which suggests injection penetration is as important as expected.

Cases 4CV and 5CV show considerable improvements to combustion when compared to the other CVCP cases. Removal of the pilot increases the diesel premixed charge combustion phase which leads to an increase to in-cylinder temperatures as well as combustion occurring earlier since the overall injection has also been advanced. This means the temperature building phase begins earlier at a higher temperature and leads to the eventual wholesale ignition and rapid combustion of the bulk of the hydrogen-air mix at an earlier stage in the CVCP than the other cases. Due to the earlier combustion much more hydrogen is utilised and this is reflected in the increased HRR and pressure observed in 4CV and 5CV. Compared to 4CV, 5CV has an earlier and larger secondary

peak in HRR which is likely largely due to the improved diesel penetration causing more early hydrogen ignition. Peak temperature is slightly lower in 5CV due to the diesel combustion being spread over a larger portion of the cylinder rather than being confined to one very high temperature region.

There is a considerable gap of roughly 15° between the initial diesel combustion and full hydrogen ignition in cases 4 and 5, indicating that further advancing the injection in the conventional engine would likely be beneficial. This would allow for hydrogen combustion to begin closer to TDC and therefore more would be utilised due to the higher in-cylinder temperatures and the increased pressure should lead to greater work output. This gap also exists in 4CV and 5CV but is smaller, roughly 10°, and HRR peaks occur prior to the end of the CVCP indicating most of the hydrogen has been burned. This could be optimised by injecting the pilot prior to the CVCP and shortening the CVCP duration to allow for a greater amount of expansion work and should also reduce NO_x levels considerably.

4.4.3.2 Emissions

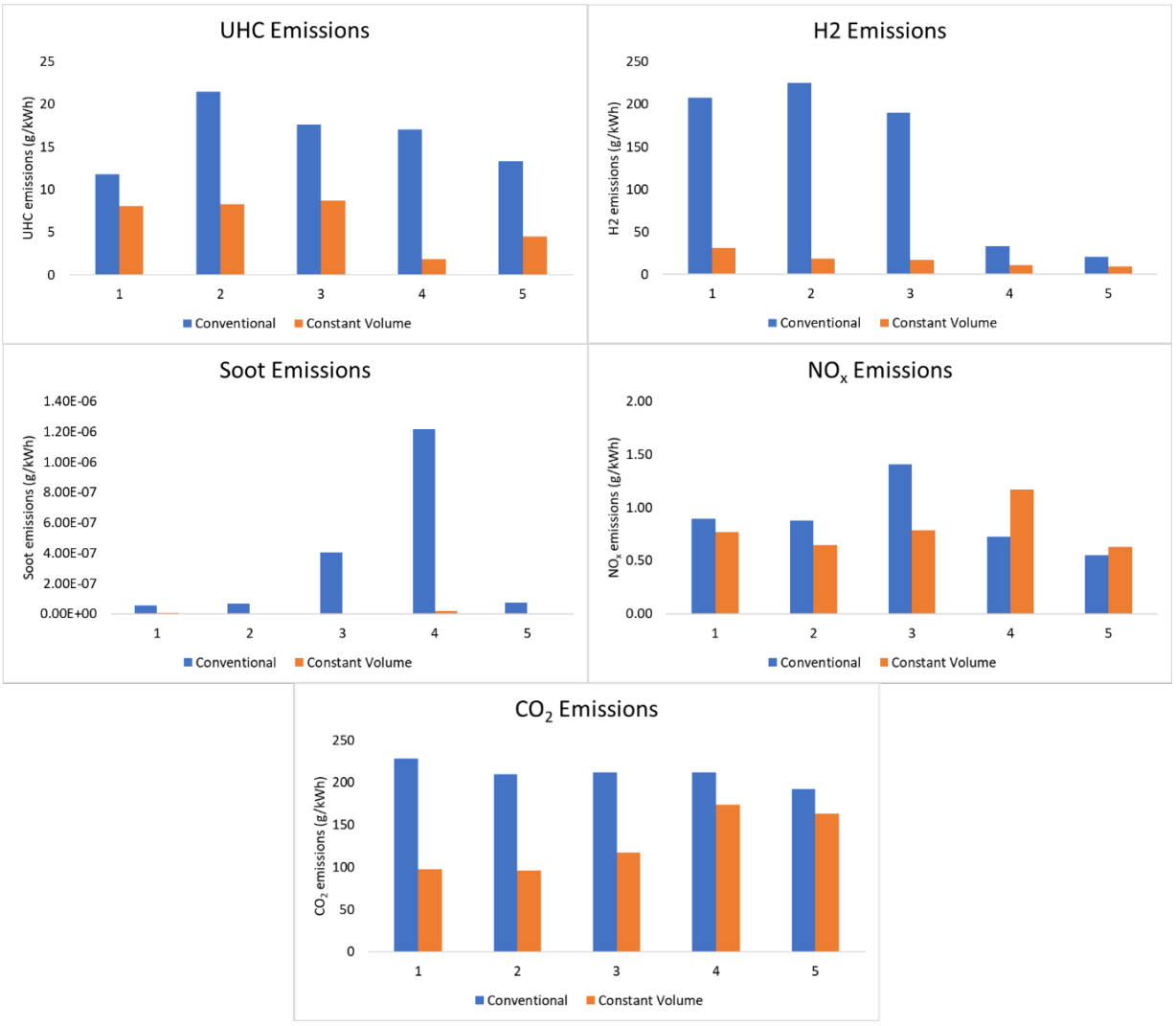

FIGURE 4.34: Emissions levels at EVO for a) UHC, b) H2, c) soot, d) NO_x and e) CO_2 for LL 90% HES - CVCP dual-fuel LL improvements

Advancing the injection leads to an increase to UHC emissions in case 2 in the conventional engine, Figure 4.34 a). This is due to poorer combustion of the pilot injection as combustion occurs further away from TDC compared to case 1. This issue is somewhat alleviated in case 3 due to the main injection occurring before TDC and therefore higher amounts of diesel combustion occurring while pressures/temperatures are at their peak and a more complete combustion of the diesel follows. Case 4 completely removes the pilot which leads to an increase to UHC on a per cycle basis but the improved performance due to hydrogen utilisation reduces the specific output meaning levels are similar to case 3. Removing the pilot causes increased cylinder wetting due to the delayed combustion of the main diesel injection i.e. no pilot means higher ignition delay of the main injection and therefore more of the main injection meets the chamber walls and does not fully combust. Case 5 also suffers from wetting but the increased

hydrogen utilisation, higher power stroke temperatures and increased mixing caused by the higher injection velocity leads to a reduction in UHC compared to 4. Case 2CV shows similar UHC emissions levels to 1CV indicating that there is likely an adequate amount of time for the diesel to combust without the earlier injection. Case 3CV also shows similar specific output but per cycle output is slightly higher due to a reduction in the effectiveness of the pilot. Cases 4CV and 5CV show lower UHC emissions compared to all other CVCP cases even though the pilot has been removed. This is likely due to the considerably higher temperatures caused by high hydrogen combustion efficiency leading to improvements to the conversion of UHCs to CO_2 as well as the performance increases lowering specific output. The increase in 5CV's levels compared to 4CV are due to increased accumulation of fuel in the piston bowl caused by the higher injection velocity and stationary piston, without the benefit of comparatively higher power stroke temperatures unlike in the conventional engine.

Clearly the CVCP cases show much improved hydrogen utilisation across the board compared to the conventional cases, Figure 4.34 b). Each case progressively advances the time at which all diesel is finished being injected and a correlation is observed with regard to hydrogen emissions decreasing with this advancement. This is due to the CVCP maintaining the conditions needed for hydrogen combustion to continue and once the phase ends the hydrogen flame extinguishes soon after as temperatures and pressures fall rapidly, so the earlier the combustion of hydrogen begins the better. Cases 1, 2 and 3 in the conventional engine show unacceptably high hydrogen emissions due to poor bulk mixture ignition. As noted previously, conventional engine cases 4 and 5 improve hydrogen utilisation considerably compared to other conventional cases due to higher amounts of premixed charge diesel combustion, combustion occurring closer to TDC and more focussed injection site. Cases 4CV and 5CV also show a reduction in hydrogen emissions for similar reasons along with the further advancement meaning the bulk of the mixture burns earlier in the CVCP. Increasing injection penetration also leads to a reduction in hydrogen emissions in both conventional and CVCP engines due to more combustion occurring earlier as well as increased mixing of diesel causing more local hydrogen ignition throughout the chamber.

In general soot levels are low in all cases at 90% HES, however, CVCP cases continue to show levels even lower than their conventional counterparts, Figure 4.34 c), a result of the increased temperatures and burning efficiency of both fuels. Reduction of the dwell time between pilot and main injections (3/3CV) leads to an increase in soot for both operational modes while complete removal of the pilot (4/4CV) leads to an even greater increase. The increase in 3/3CV is due to a reduction in premixed diesel combustion during the main injection, while the increase in 4/4CV is mostly due to the more focussed injection site meaning carbon distribution throughout the chamber is poorer and increased wall wetting also leads to soot development (these factors also contributed to 3/3CV to a lesser extent). Cases 5 and 5CV while not benefiting from

the pilot show fairly low soot levels, a result of the increased injection velocity causing a more even carbon distribution throughout the chamber so soot does not form as easily. Case 5 also benefits from higher power stroke temperatures than other conventional cases which slows down the rate of soot production, negating the increases wall wetting may cause.

Cases 1, 2 and 3 show the highest NO_x levels out of all conventional engine cases due to the extremely poor performance and thus specific output is higher even though temperatures are low, Figure 4.34 d). Hydrogen utilisation increases significantly in case 4 and even more so in case 5 which leads to increased temperatures and thus NO_x production, but the improved performance offsets the increase. Case 3 in both the conventional and CVCP engines shows NO_x increase with relatively little performance difference due to the reduction of the benefits which a pilot offers (lower combustion temperatures) when dwell time between pilot and main is reduced. This is also shown in 4CV where the removal leads to a considerable increase to NO_x levels. The increase in 4CV can also be attributed to the higher temperatures caused by the increased hydrogen utilisation and much more rapid hydrogen combustion which causes a higher peak temperature. Case 5CV shows a decrease in NO_x compared to 4CV due to a slightly lower peak temperature and less of a concentrated high temperature zone due to less diesel combusting in one specific area.

CO_2 levels are lower across all CVCP cases compared to conventional cases, Figure 4.34 e). For all cases this is due to the improved performance leading to a lower specific output. For cases 4 and 5 the difference is much less as the vast improvements to hydrogen combustion lead to higher/equivalent temperatures in the late power stroke which aids in breakdown of UHCs and oxidation of CO, therefore much more similar CO_2 levels are observed. Performance increase also lowers the observed levels. Compared to 1CV, all other CVCP cases show increased CO_2 as a result of the longer time allowed for complete combustion within the CVCP and longer time between end of injection and EVO in general.

4.4.3.3 Performance

In the conventional engine advancing the injection and reducing the dwell time between pilot and main does not have a meaningful impact on performance, as shown by cases 2 and 3 in Figure 4.35a) as hydrogen utilisation is not improved. However, cases 4 and 5 show good increases to performance, a result of the much-increased hydrogen combustion efficiency, and therefore higher combustion pressures with case 5 showing the best conventional engine performance. Each case progressively advances injection and improvements to CVCP performance follows. In the CVCP engine advancing the injection leads to significantly more hydrogen utilisation as the temperature

building phase extends, eventually allowing for wholesale ignition of the hydrogen-air mix within the bounds of the CVCP for cases 4CV and 5CV, which leads to very high peak pressures and therefore work output. Figure 4.35b) backs up the findings by clearly showing the correlation between advancement of injection and increase to total heat release. Cumulative heat release trends also show that CVCP cases cause earlier wholesale ignition of the hydrogen-air mix compared to their conventional case counterparts. At LL 90% HES use of advanced injections and increased injection penetration in both the conventional and CVCP engines lead to performances on par with the 0% H_2 conventional engine (Case 5=47.0%, Case 5CV=60.7% vs. 0%H2=54.3%).

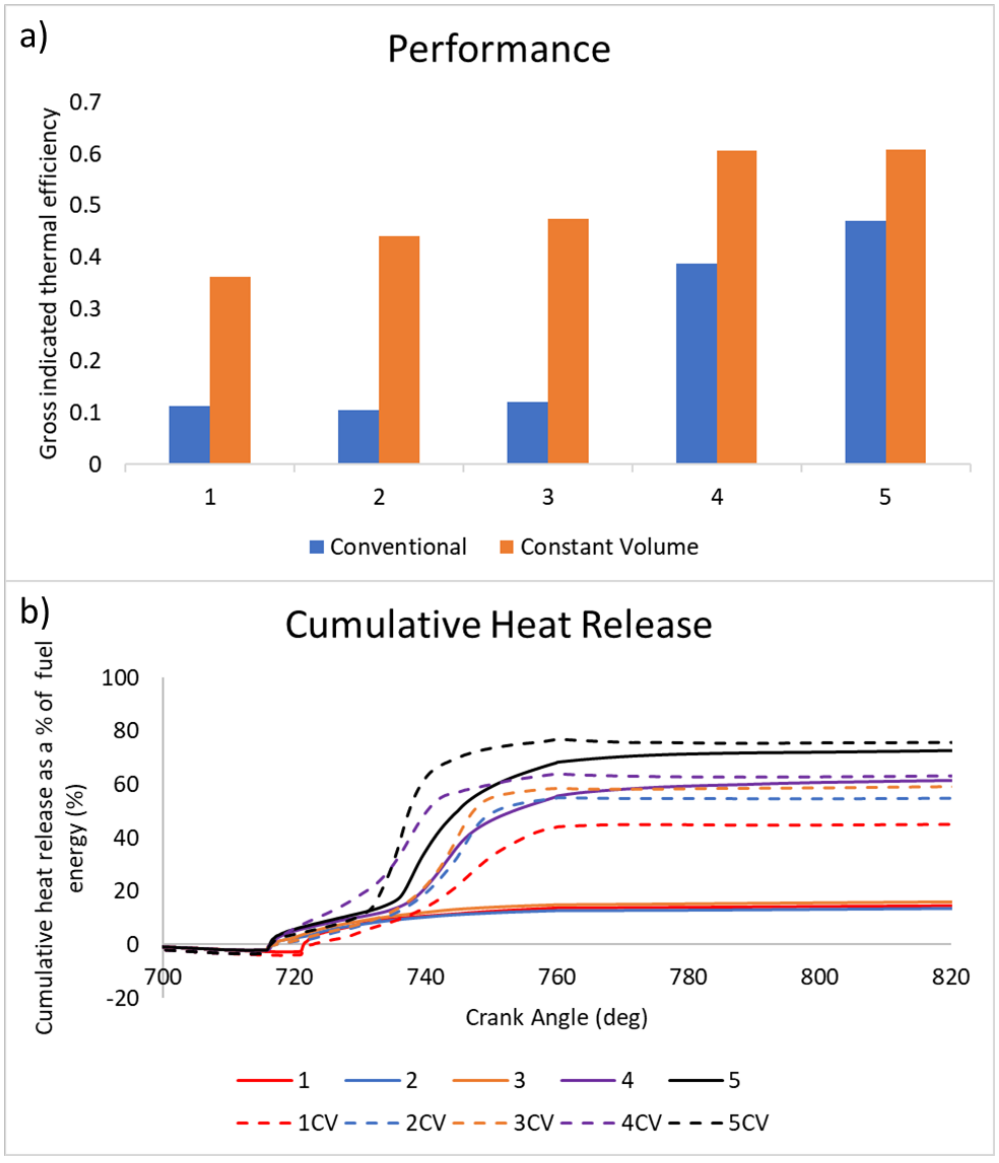

FIGURE 4.35: Performance characteristics for a) thermal efficiency and b) cumulative heat release for LL 90% HES - CVCP dual-fuel LL improvements

4.4.3.4 Contour analysis

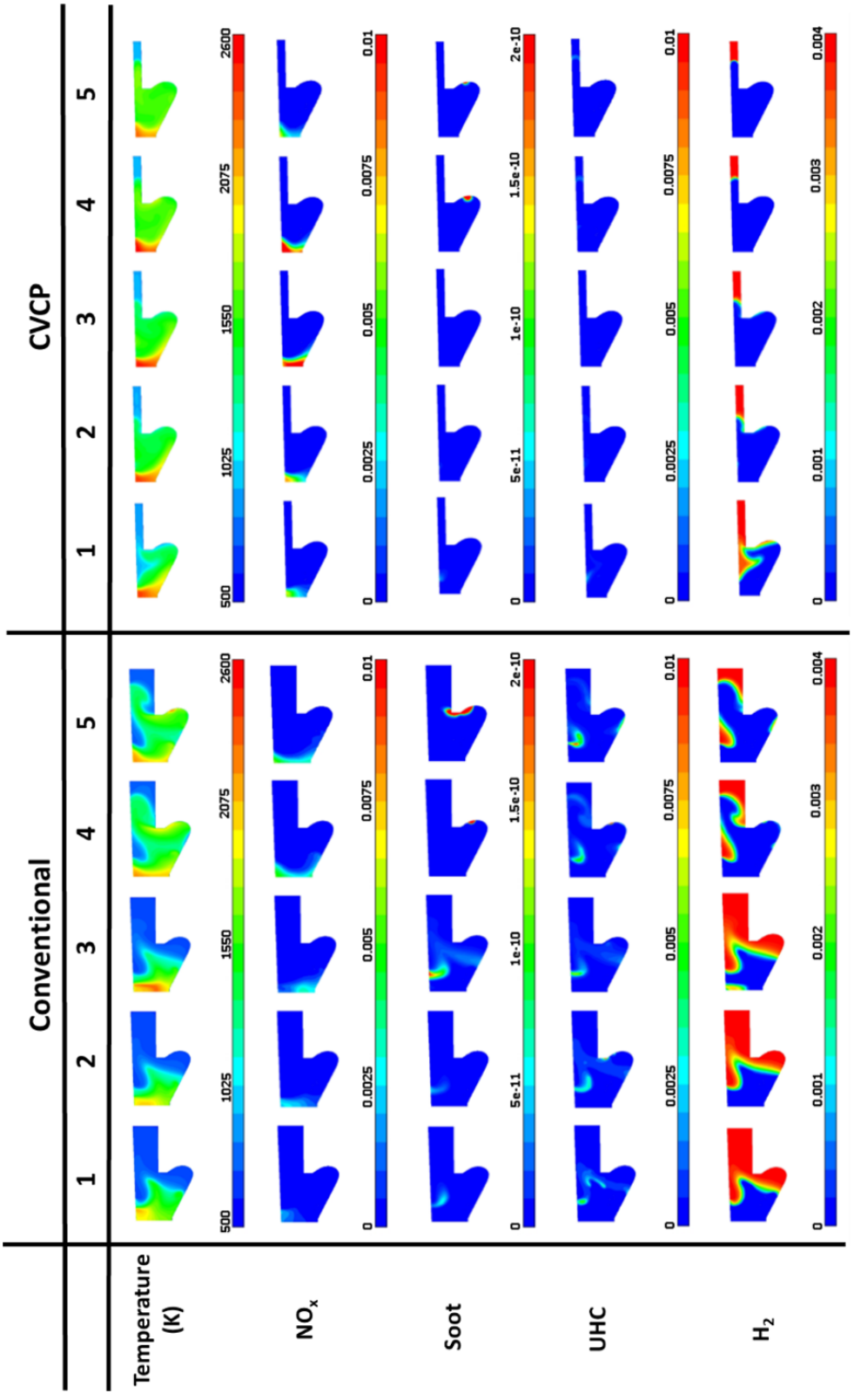

FIGURE 4.36: Contours of temperature, NO_x , soot, UHC and H_2 at 750°CA for LL 90% HES - CVCP dual-fuel LL improvements

Figure 4.36 shows the contours of temperature, NO_x, soot, UHC and H_2 at 750°CA (30° ATDC in the conventional engine and 10° after CVCP ends in the CVCP engine) for the low load 90% HES test cases (see Table 4.7). Temperatures are generally highest close to where the diesel injection originated. Due to poor injection penetration diesel combustion is confined to this specific area and it is the only area in which both hydrogen and diesel combustion occurs. For cases 1, 2 and 3 in the conventional engine there clearly is not much of a temperature increase outside of this region, indicating the flame doesn't spread, and this is backed up by the large high hydrogen concentration areas in the contours. Cases 4 and 5 however show good amounts of temperature increase across nearly all of the cylinder due to the spreading of the hydrogen flame front away from the diesel injection site. Peak temperatures are in similar areas to those of the conventional engine in the CVCP cases, due to multiple fuels combusting close to each other, but are mostly higher and there is a general increase in temperature across the entire cylinder due to the hydrogen flame front spreading well and only struggling to reach the cylinder liner side where flame quenching occurs. There is a clear improvement to hydrogen utilisation in all CVCP cases when compared to 1CV with the hydrogen flame spreading closer to the cylinder liner as injection advancement progresses. The area towards the top-middle of the chamber where the flame front can't spread in 1CV and the conventional cases combusts via autoigniton in the 2-5CV cases and is one of the main reasons why hydrogen emission stays below that of the conventional engine in all cases. 5/5CV does not have as high a peak temperature close to the injector due to there being less diesel combustion occurring in this area. Cases 3 and 4 offer the highest temperatures in both the conventional and CVCP engines due to the diminishment of the pilot injection meaning both more combustion happening over a short period of time and more in the one specific area. As expected, higher NO_x concentration areas correspond to high temperature regions, generally close to the areas in which both diesel and hydrogen combustion occurred. UHC concentrations generally appear on the edge of the hydrogen flame front where oxygen has been consumed due to the spreading flame carrying them throughout the chamber and correlate to areas in which soot production is beginning. Wall wetting is observed in the accumulations of UHCs close to the top/lip of the piston bowl in the cases without pilot injections with a combination of the UHCs and consumed oxygen in these regions causing the onset of soot development.

4.4.4 Summary

A comprehensive numerical modelling study has been carried out to assess the benefits of a constant volume combustion phase being implemented in a diesel-hydrogen dual-fuel compression ignition engine with focus on performance/efficiency and emissions. The numerical modelling framework has been validated with experimental data from a conventional turbocharged compression ignition diesel-hydrogen dual-fuel engine.

The study examined the effects of hydrogen substitution increase at low and high load in the CVCP engine operating with a CVCP period of 30° followed by a performance analysis at low load high hydrogen energy share.

Key findings are summarised as follows:

1. The CVCP strategy was shown to increase gross indicated thermal efficiency at all HESs at both loads compared to conventional engine operation.
2. The CVCP strategy leads to a large reduction in carbon-based emissions with soot, UHC and CO_2 emissions all falling compared to the conventional engine.
3. The CVCP strategy incurs an increase to NO_x emissions compared to conventional engine operation.
4. The CVCP strategy leads to higher peak in-cylinder pressures and temperatures compared to conventional engine operation.
5. Benefits of the CVCP strategy reduce as HES increases at high load. This is due to the diesel injection having no trouble igniting the relatively rich premixed hydrogen-air charge.
6. At LL high HESs the benefits of the CVCP strategy increase greatly. In the conventional engine the reduced diesel pilot injection cannot adequately ignite the lean premixed hydrogen-air charge. Under CVCP operation, however, the higher temperatures and pressures which are built due to the stationary piston allow for much more favourable conditions for dual-fuel pilot ignition and premixed hydrogen-air flame propagation. This is observed in the increased gross indicated thermal efficiency (38% vs. 11% at 90% HES for CVCP and conventional respectively) and considerably reduced levels of hydrogen emission.
7. With further diesel injection optimisation gross indicated thermal efficiencies of up to 61% are achieved at LL 90% HES under CVCP operation and hydrogen utilisation is further improved while not negatively impacting other emissions characteristics.
8. Diesel injection advancement plays a vital role in improving hydrogen utilisation and performance at LL high HESs when using the CVCP strategy. If more time is allowed for combustion within the CVCP the hydrogen-air flame will propagate further before the piston is released from TDC and autoignition in areas where the flame generally can't spread further improve hydrogen utilisation.
9. Injection penetration plays a much bigger role in conventional operation at LL high HESs. This is due to hydrogen combustion being more reliant on an adequate amount of diesel combustion happening throughout the chamber to increase the likelihood of hydrogen ignition. It was also found that increasing the

amount of premixed charge diesel combustion and diesel injections occurring closer to TDC both improve hydrogen combustion significantly in the conventional engine.

Chapter 5

Validation of a Numerical Model for Direct Gaseous Injection in Internal Combustion Engines

5.1 Background

A number of issues were identified in the previous chapter with regards to intake induction diesel-hydrogen dual-fuel operation. One solution which has the potential to improve HES while simultaneously increasing performance, reducing emissions and avoiding the likes of pre-ignition, backfire and knocking is direct hydrogen injection into the combustion chamber. However, current modelling approaches for gaseous direct injection in engines either incur high computational cost or/and are difficult to implement effectively. Therefore, in this section we validate the improved gaseous sphere injection model described in Section 3.5, which should reduce computational cost, be easy to implement and also produce accurate results.

Validation of the modified GSI model is first carried out via comparison of simulations with experimental studies on underexpanded hydrogen and methane freestream jets (Section 5.2) injected into constant volume chambers. Freestream simulations are chosen due to their simplicity which allows for penetration and spreading of the jet to be assessed fairly; studies on hydrogen and methane are used to show the applicability of the model to disparate gases. Next comparisons are made to experimental optical mixture formation imaging in a hydrogen direct injection engine (Section 5.3). An early direct injection case is chosen as it isolates the mixture formation process in a realistic engine setup and allows for mixing and flow field development to be assessed. Finally, combustion in a diesel pilot ignited methane direct injection compression ignition engine is simulated and the various combustion and emissions characteristics are compared against the experimental data (Section 5.4). A combustion analysis in a

realistic engine is carried out as it can be used to assess the performance of the model in its eventual end use-case, showing its wide applicability to the various problem sets.

5.2 Freestream hydrogen and methane jets

Two experimental freestream studies on underexpanded gas jets are chosen to assess jet penetration and spreading when using the improved GSI model. The first is Tsujimura et al. [139] which examines underexpanded hydrogen jets injected into nitrogen and the second is Rogers [63] which studies high pressure ratio compressed natural gas (CNG) jets injected into nitrogen. These experimental studies are chosen as they are good sources of both experimental measurement and optical imaging of the gas jets and will help show the applicability of the improved GSI model to the two gaseous fuels most likely to be utilised in engines under various injection conditions.

5.2.1 Numerical setup

Numerical setups for the freestream test cases are presented. A 120 $\times$ 80 $\times$ 80 mm cuboid geometry was created in ANSYS SpaceClaim and a hex mesh was generated using ANSYS meshing Figure 5.1. The geometry represents the constant volume vessels used in the two freestream studies and is large enough such that walls will not impact the injected gas jets development. Three mesh densities with even cell sizes of 0.75 mm ($\approx$ 1800k cells), 1 mm ($\approx$ 800k cells) and 2 mm ($\approx$ 100k cells) were tested with a single case from each experimental study to ensure the GSI models applicability and insensitivity to mesh refinement at mesh densities typical for engine simulation. All mesh densities provided reasonable agreement with experimental data and only minor variations were observed between the 2 mm and 1 mm meshes and next to no variation between the 1 mm and 0.75 mm meshes. The 1 mm mesh was deemed to give a sufficiently mesh independent solution and is used for all the freestream tests presented.

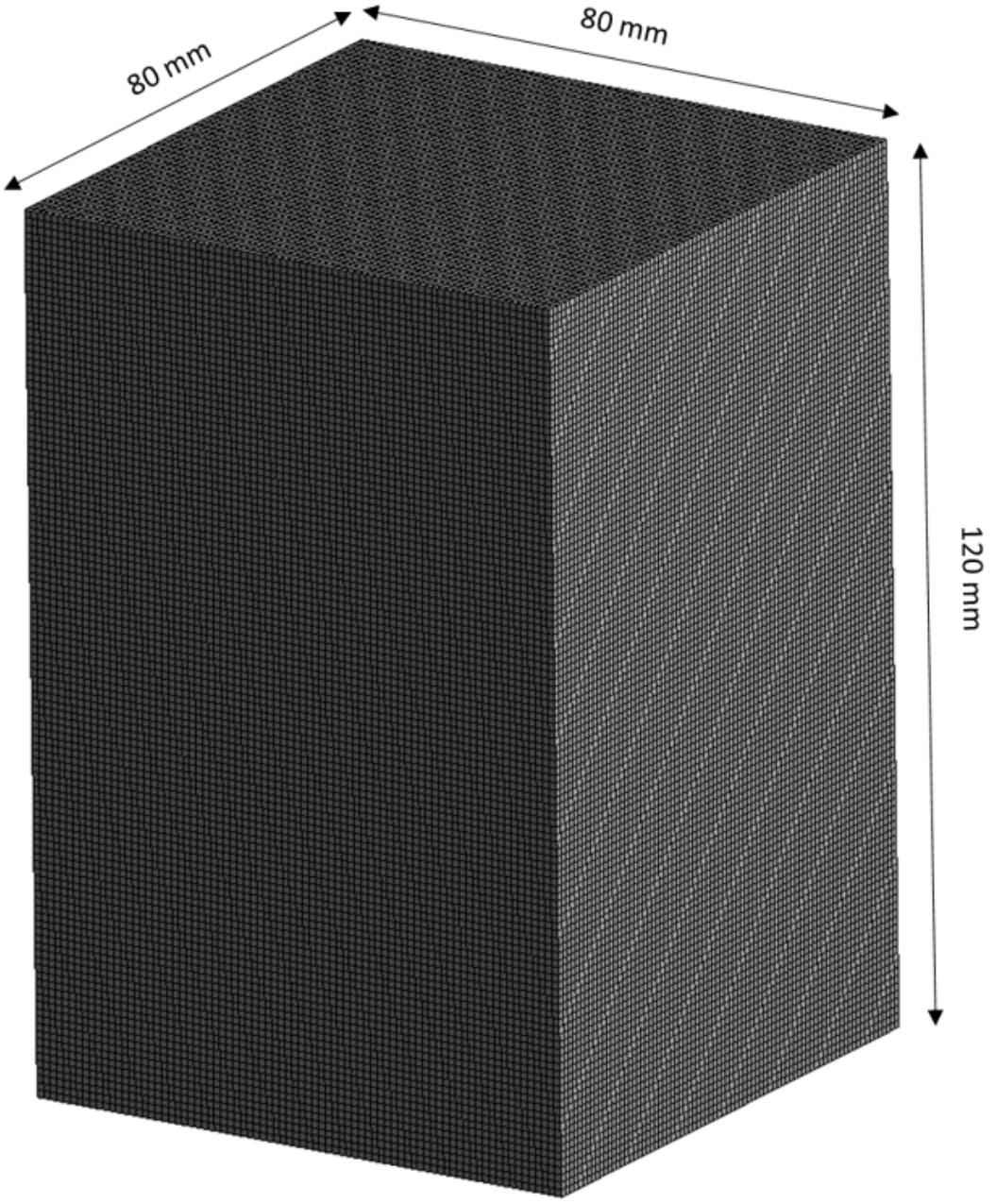

FIGURE 5.1: Mesh of constant volume vessel used in freestream studies, 1 mm cell size.

Table 5.1 outlines the relevant operating conditions for each freestream case. As instantaneous injector mass flow rate was not measured for either study the initial injector transients are not modelled. Instead a constant steady mass flow rate is prescribed based on the overall average mass flow rates which were measured in the studies. Mach disk quantities are calculated using the previously described methods (Section 3.5). No slip boundary conditions with no heat transfer allowed are set at the solid walls enclosing the chamber. A constant time step size of 1e-6 s is used throughout.

TABLE 5.1: Summary of freestream test cases.

Operating Conditions	**Tsujimura [139]**	**Rogers [63]**
Ambient gas	Nitrogen	Nitrogen
Ambient temperature (K)	298	298
Ambient pressure (MPa)	1	0.1, 0.05, 0.025
Injected gas	Hydrogen	Methane
Upstream temperature (K)	298	298
Actual nozzle exit diameter (mm)	0.3, 0.7, 1	1
Injection total pressure (MPa)	8	4
Total pressure ratio	8	40, 80, 160
Discharge coefficient	0.9	0.482
Steady mass flow rate (kg/s)	3.50e-4, 1.91e-3, 3.89e-3	5.41e-3

Jet axial penetration length is measured normal to the nozzle exit plane to the furthest axial position with greater than 0.005 mass fraction of the injected gas. Half jet dispersion angle is calculated using the same method as the given experimental study (Tsujimura and Rogers use different methods which are detailed in each article/thesis) and the jet boundary is taken to be at 0.005 mass fraction of the injected gas. Further details about the full modelling setup can be found in Chapter 3.

5.2.2 Validation

Figures 5.2 a) and 5.3 a) show that the initial jet penetration trends are overpredicted for all cases. This is most likely due to injector ramp up/energizing time not being accounted for but could also be because of difficulties in carrying out experimental measurement of the highly complicated initial flow development or a need to tune the cone angle setting on a case by case basis to limit initial penetration. However, after roughly 0.5 ms in both studies penetration matches experimental results rather well which indicates the fully developed region is predicted reasonably. Penetration in the Tsujimura 0.3 mm case is largely underpredicted which could be due to changes in discharge coefficient as nozzle geometry varies, which is not accounted for, and Tsujimura also notes that the 0.3 mm orifice has the greatest normalised jet volume and spreading rate which may indicate a need to tune cone angle at smaller orifice sizes. In the Rogers PR160 test, Figure 5.3 a), the jet does not have time to fully develop before being influenced by the wall in the experiments, nonetheless, simulation results appear to be converging towards the experimental trend had it been able to continue. Even with the noted issues jet penetration is well captured for both hydrogen and methane at various pressure ratios and injector nozzle diameters.

Figures 5.2 b) and 5.3 b) show the measured and calculated half jet dispersion angles for hydrogen and methane freestream jets respectively. At areas close to the end of the core length, where transition of the gaseous droplets occurs, there tends to be an overprediction in spreading. This is likely partly due to the neglect to model injector transients but also results from the deacceleration of the injected gas upon transition. This is not so dissimilar to a real underexpanded jet where vortex rings form at the tip of the jet, nevertheless, dispersion is somewhat higher than expected at this point. Figure 5.2 b) shows that the simulated values of jet dispersion tend to fluctuate in the early parts of the injection before beginning to converge to a lower value after roughly 0.5 ms. Experiments also show this fluctuating behaviour to a lesser degree and the behaviour is expected due to the jet needing time to fully develop during the transition region following the core. The methane cases, Figure 5.3 b), also exhibit this behaviour in both experiments and simulations but due to the very high pressure ratios there does not appear to be time for this fluctuation to stop before the end of the tests. The simulations tend to show an increase in dispersion angle as pressure ratio increases, however, the experimental results show an inconsistent trend. In further tests of even higher pressure ratios carried out by Rogers, it was found that generally dispersion angle does increase with pressure ratio which indicates the simulation trends are reasonable. Considering a constant cone angle of $\theta_e = 12^\circ$ is set throughout all the simulations jet dispersion is relatively well represented and, while not ideal, should be adequate for use in further study and failing that can be tuned on a case by case basis.

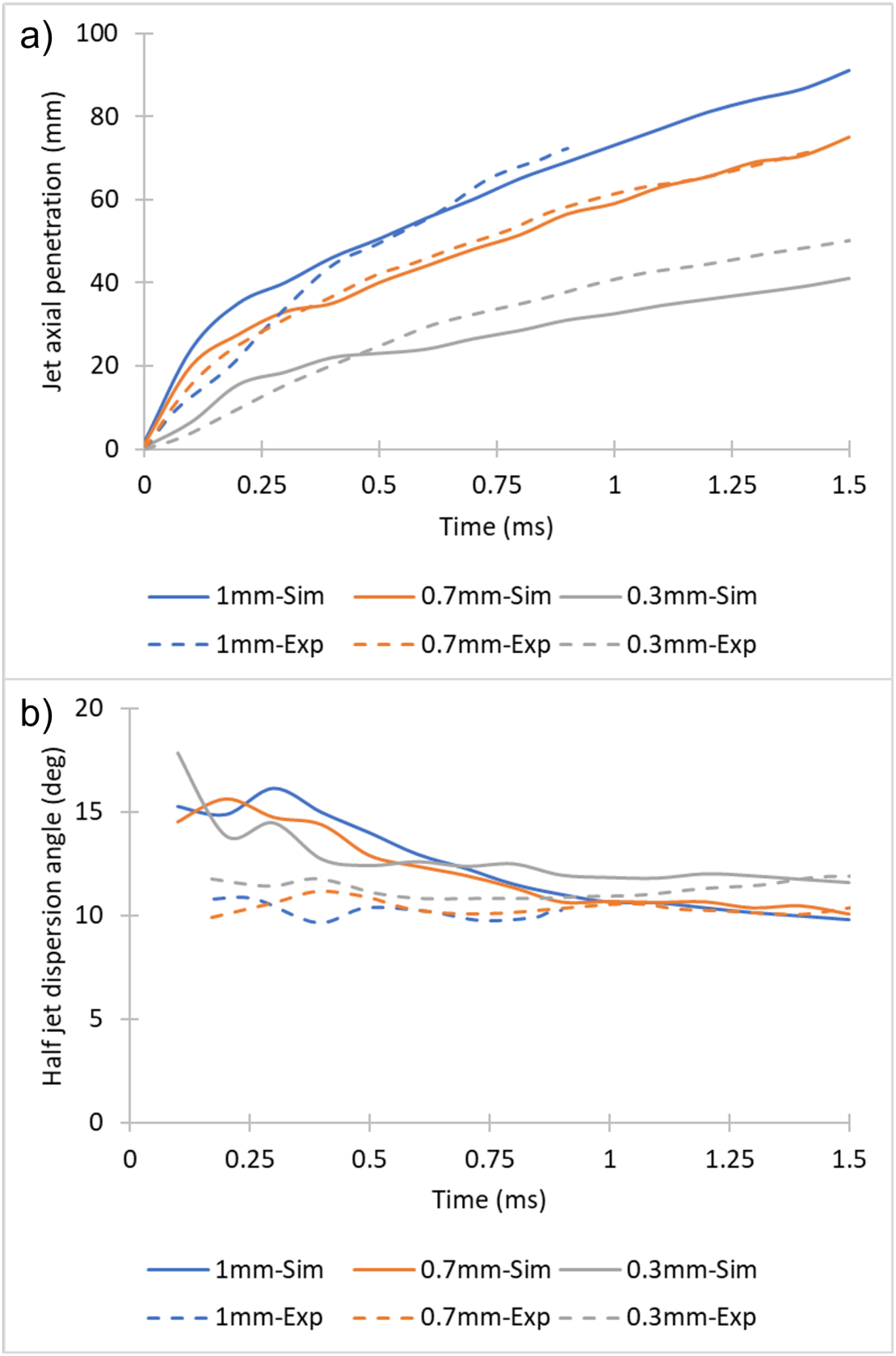

FIGURE 5.2: Hydrogen freestream simulation temporal development comparison with experimental data [139] for a) jet tip axial penetration and b) half jet dispersion angle for 1 mm, 0.7 mm and 0.3 mm nozzle exit diameters at $\eta_0 = 8$.

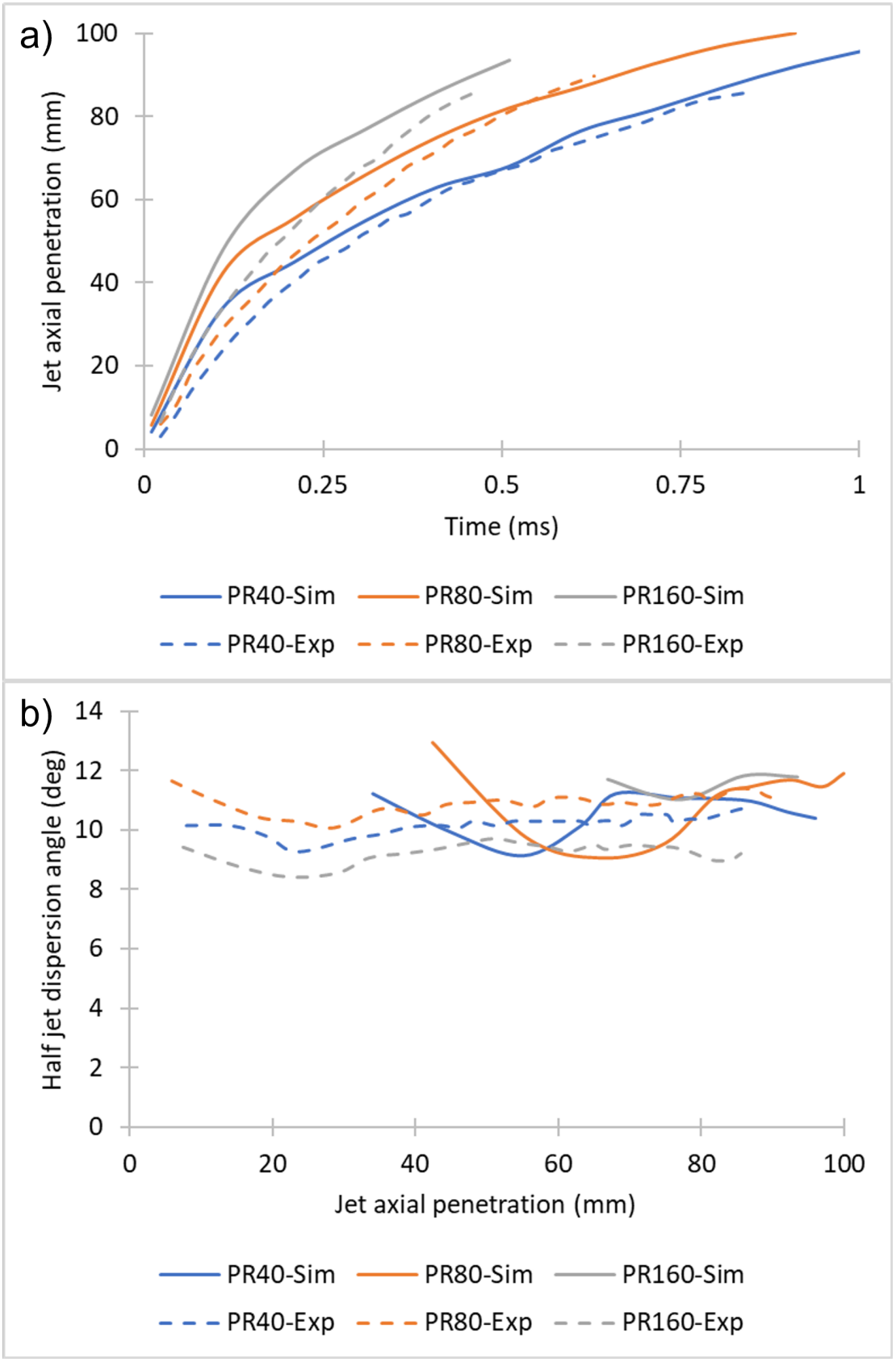

FIGURE 5.3: Methane freestream simulation comparison with experimental data [63] for a) jet tip axial penetration temporal development and b) half jet dispersion angle axial development measured at 70% of the jet tips penetration at $\eta_0 = 40$, 80 and 160.

Figure 5.4 compares the experimental shadowgraph images taken by Tsujimura for the 0.7 mm nozzle and the mass fraction contours of the present CFD results. As previously noted, and illustrated by Figure 5.4, there is a clear overprediction of the initial jet penetration, yet as time progresses the jet penetration of the experiment "catches up" and proceeds at a very similar rate to the simulations. The spreading rate demonstrates a similar story with the 0.4 ms simulation snapshot showing a much wider jet than its experimental counterpart, however, at 0.8 ms and 1.2 ms the predicted jet widths are very similar to that of the experimental shadowgraph images.

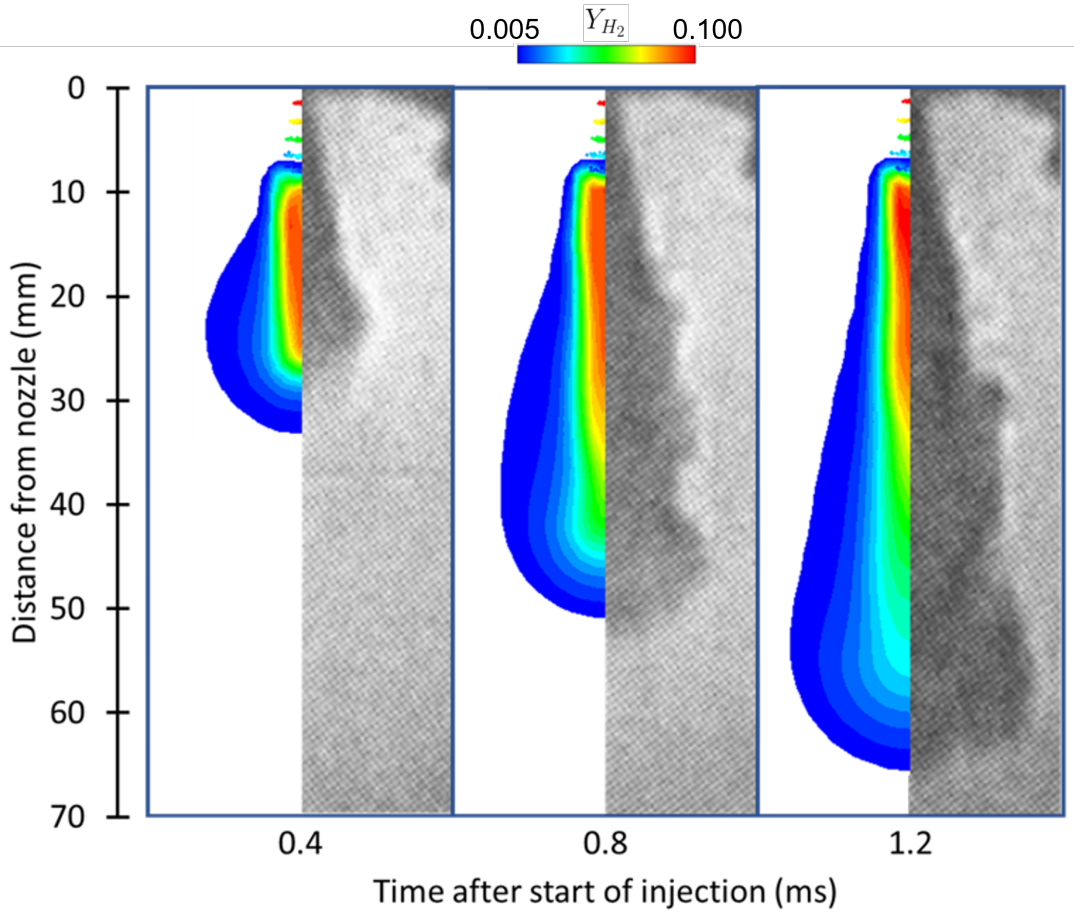

FIGURE 5.4: Hydrogen freestream comparison of experimental shadowgraph imaging and CFD simulation mass fraction contours for the 0.7 mm nozzle exit diameter at $\eta_0 = 8$. Source: Tsujimura et al. [139].

Figure 5.5 backs up the findings of Figure 5.3 a) and b) and shows the expected increase in jet penetration rate as pressure ratio is increased even though injection pressure (and thus mass flow rate) are constant between all cases.

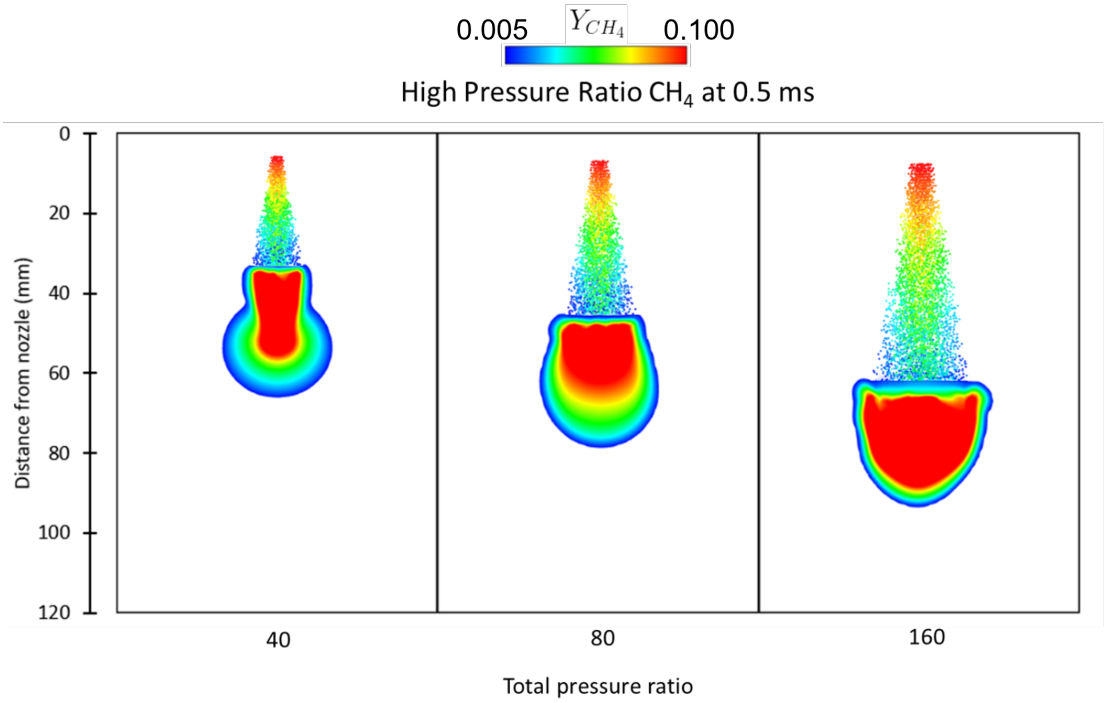

FIGURE 5.5: Comparison of methane freestream jets 0.5 ms after the start of injection at $\eta_0 = 40$, 80 and 160. Shown are simulation mass fraction contours and particles coloured by velocity (250 – 775 ms^{-1}).

Overall, the modified GSI model results, in terms of jet penetration and spreading rate, are in good agreement with the experimental freestream studies across a wide range of pressure ratios, disparate injected gases and multiple nozzle diameters. This implies the improved GSI model should be sufficient for predicting gaseous injections when extended to more practical applications such as direct injection in engines.

5.3 Mixture formation in a hydrogen direct injection engine

An experimental study on the direct injection of hydrogen into an optically accessible spark ignition combustion chamber is used to assess the improved GSI model's ability to accurately predict mixture formation in a realistic engine setup. The study chosen is that of the engine combustion network (ECN) on mixture formation in a hydrogen direct injection engine [121, 214, 215] as this is an excellent source of publicly available experimental and optical measurement which also provides an accurate engine geometry. The ECN study uses particle image velocimetry (PIV) for flow-field measurement and planar laser-induced fluorescence (PLIF) to capture images of the fuel mole fraction distribution. Another advantage of the ECN study is the ability to test the GSI model improvements in a high pressure ratio (≈ 81) engine case.

5.3.1 Numerical setup

Numerical setup for the mixture formation of hydrogen direct injection into a spark ignition engine is presented. Initially, the full combustion chamber along with intake/exhaust valves and ducts is meshed using ANSYS meshing, Figure 5.6 a), leading to a grid with about 1100k cells at IVC. A layered sliding hex mesh is created at the valves to allow for valve motion as well as in the main chamber to simulate piston motion, while the rest of the geometry is meshed using tets, Figure 5.6 b). This mesh is then used to compute the in-cylinder flow field which develops due to the gas exchange process. One full 720°CA cycle starting from EVO is run to remove any initial transients, followed by another from EVO to IVC. After this a higher quality but reduced grid, roughly 1300k cells at IVC with a max cell size of 1.4 mm, detailing only the combustion chamber is produced, Figure 5.6 c), and the previous results of the gas exchange process are interpolated as initial conditions. A further refined grid with roughly 2000k cells at IVC was also tested but results did not differ significantly. The compression stroke is then simulated from IVC to top dead centre which includes the full hydrogen injection and mixture formation process. A constant time step size of 0.25°CA is used throughout the simulations and is only lowered to 0.025°CA from the start of injection until 10°CA after the end of injection. Results are then compared to the experimental measurements and optical imaging. Throughout this analysis the convention that 720°CA is TDC of the compression stroke is followed.

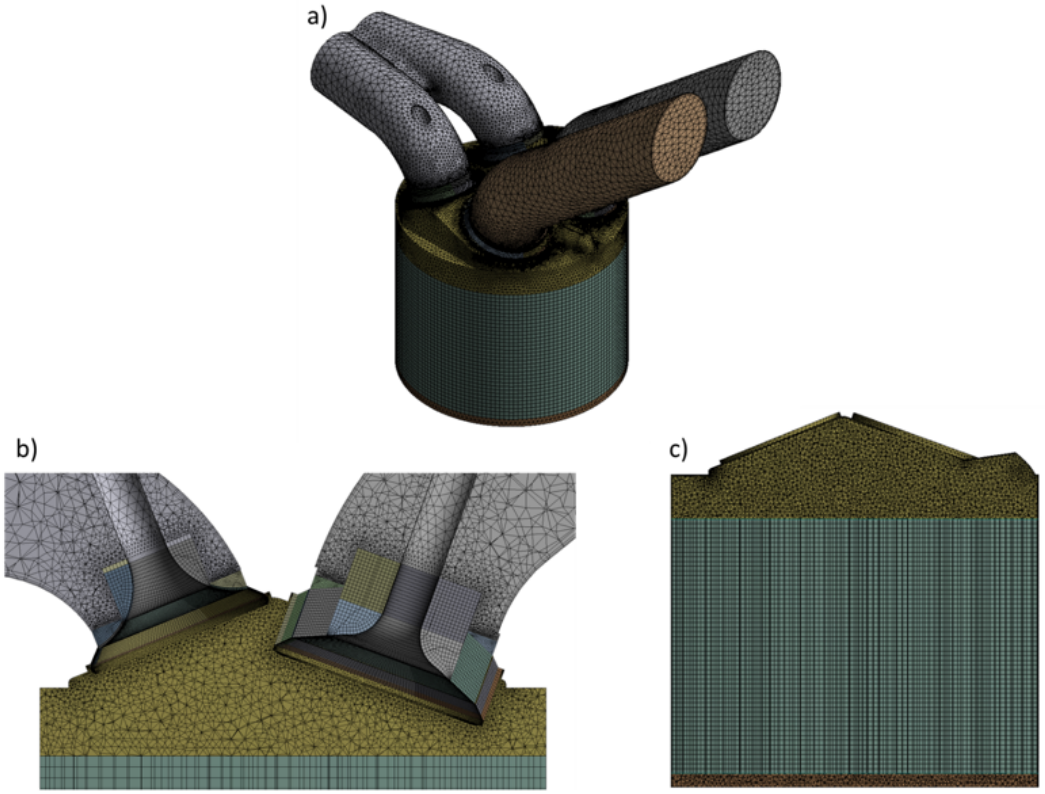

FIGURE 5.6: a) Full geometry mesh including valves, ducts and chamber for gas exchange process, b) cut-plane view of full mesh demonstrating valve layering motion, c) cut-plane view of reduced chamber only mesh for hydrogen mixture formation analysis.

During the gas exchange simulation, experimentally measured pressure profiles are set at the inlets of the intake ducts and outlet of the exhaust duct, Figure 5.7, and temperatures at the inlets and outlet are set to 309.15 K. In both stages of the simulation all chamber, piston head and valve wall temperatures are set to a constant 353.15 K and in the gas exchange process duct walls are set to 309.15 K. The bulk gas used is nitrogen and the engine runs at a speed of 1500 RPM. Table 5.2 summarises the operating conditions and engine geometry and further information about the experimental setup can be found at the ECN website [214].

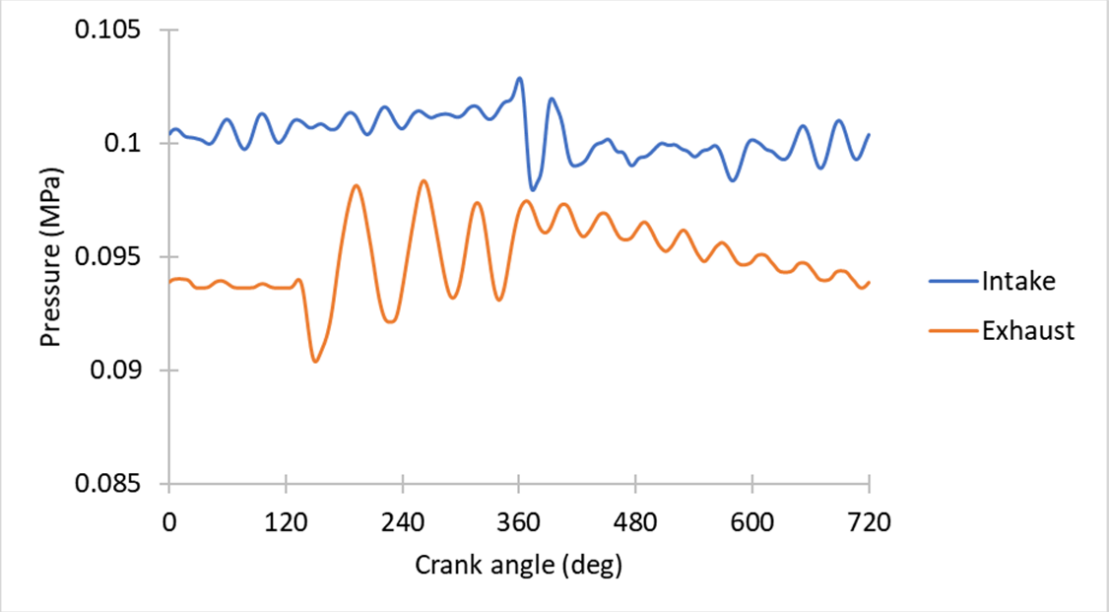

FIGURE 5.7: Experimentally measured pressure profiles used as boundary conditions at inlet and exhaust ducts.

TABLE 5.2: Summary of ECN mixture fraction test case.

Operating conditions	**ECN**
Bore x stroke (mm)	92 x 85
Displacement volume (L)	0.56
Compression ratio	11
Engine speed (RPM)	1500
Ambient gas	Nitrogen
Initial ambient temperature (K)	309.15
Initial ambient pressure (MPa)	0.1
Intake valve timing (CA)	open: 346° / close: 580°
Exhaust valve timing (CA)	open: 130° / close: 364°
Injected gas	Hydrogen
Upstream temperature (K)	300
Actual nozzle exit diameter (mm)	1.46
Injection total pressure (MPa)	10
Total pressure ratio	≈ 81
Discharge coefficient	0.248
Steady mass flow rate (kg/s)	2.56e-3
Injection period (CA)	583°-600.5°

The actual nozzle exit diameter is 1.46 mm and is directed at a 50° angle with respect to the cylinder axis downwards towards the intake squish region (90° included spray

angle). The prescribed hydrogen injection mass flow rate is shown in Figure 5.8 and the remainder of the initial injection quantities are calculated at the Mach disk via the previously described methods in Section 3.5. Further details about the full modelling setup can be found in Chapter 3.

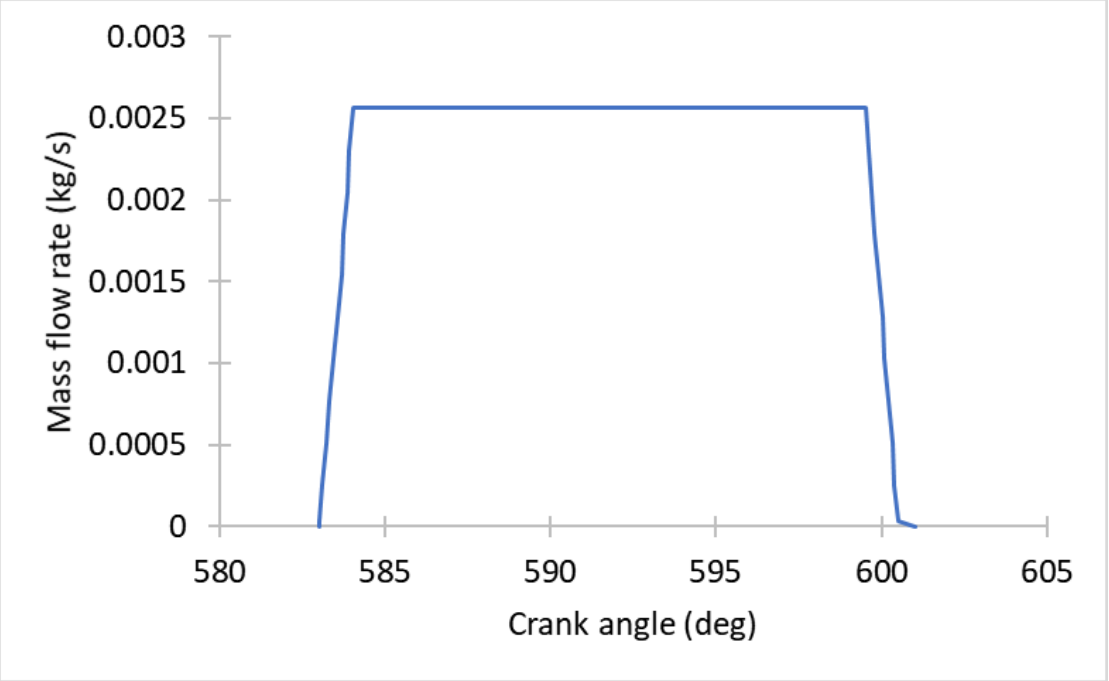

FIGURE 5.8: Mass flow rate profile for hydrogen injection.

5.3.2 Validation

Figure 5.9 shows the mean velocity vector field on the cylinder symmetry plane (in-plane) at IVC calculated by the CFD gas exchange simulation and that of the experimentally measured field. The simulation matches reasonably well with the experiments and captures the recirculation zones at the bottom and top of the chamber. There is a slight shift of the recirculation zones downwards and to the right in the simulations but overall, the velocity field is predicted adequately. Calculated pressure throughout the cycle also matches with the data provided by the experiments. Data from the gas exchange process is then interpolated to the reduced grid for initial conditions in the mixture formation simulations.

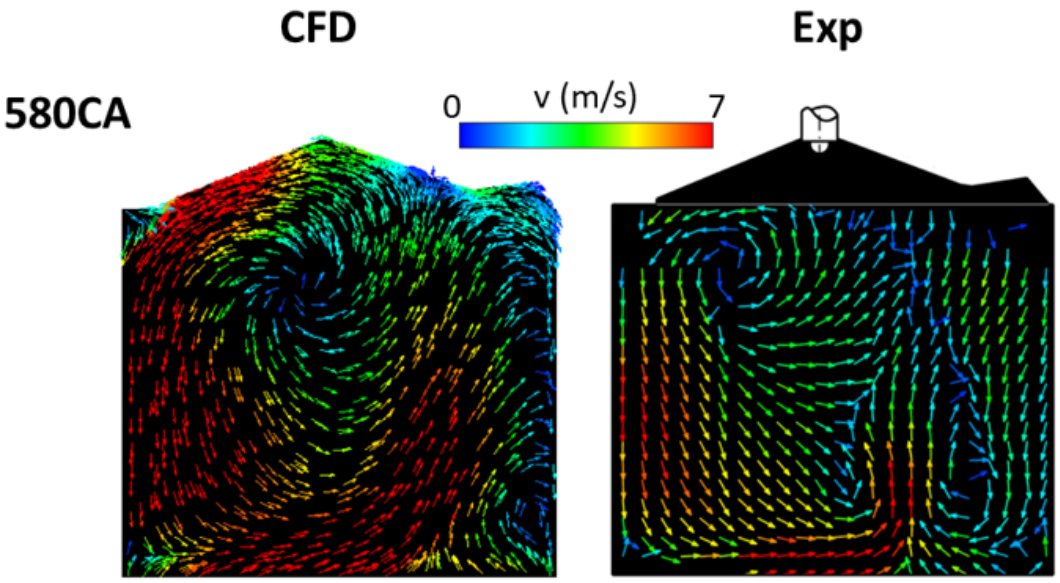

FIGURE 5.9: Initial mean in-plane velocity vector field at IVC calculated by CFD after initial gas exchange modelling compared with experimental PIV measurement.

In-plane mean velocity vector fields calculated by the simulations and the measured experimental values during the hydrogen injection and mixture formation process are presented in Figure 5.10. At each crank angle the velocity field is predicted well, with the general flow development induced by the injected gas jets penetration, such as recirculation zones and the wall jet, being reproduced. Velocity magnitudes are largely also well captured.

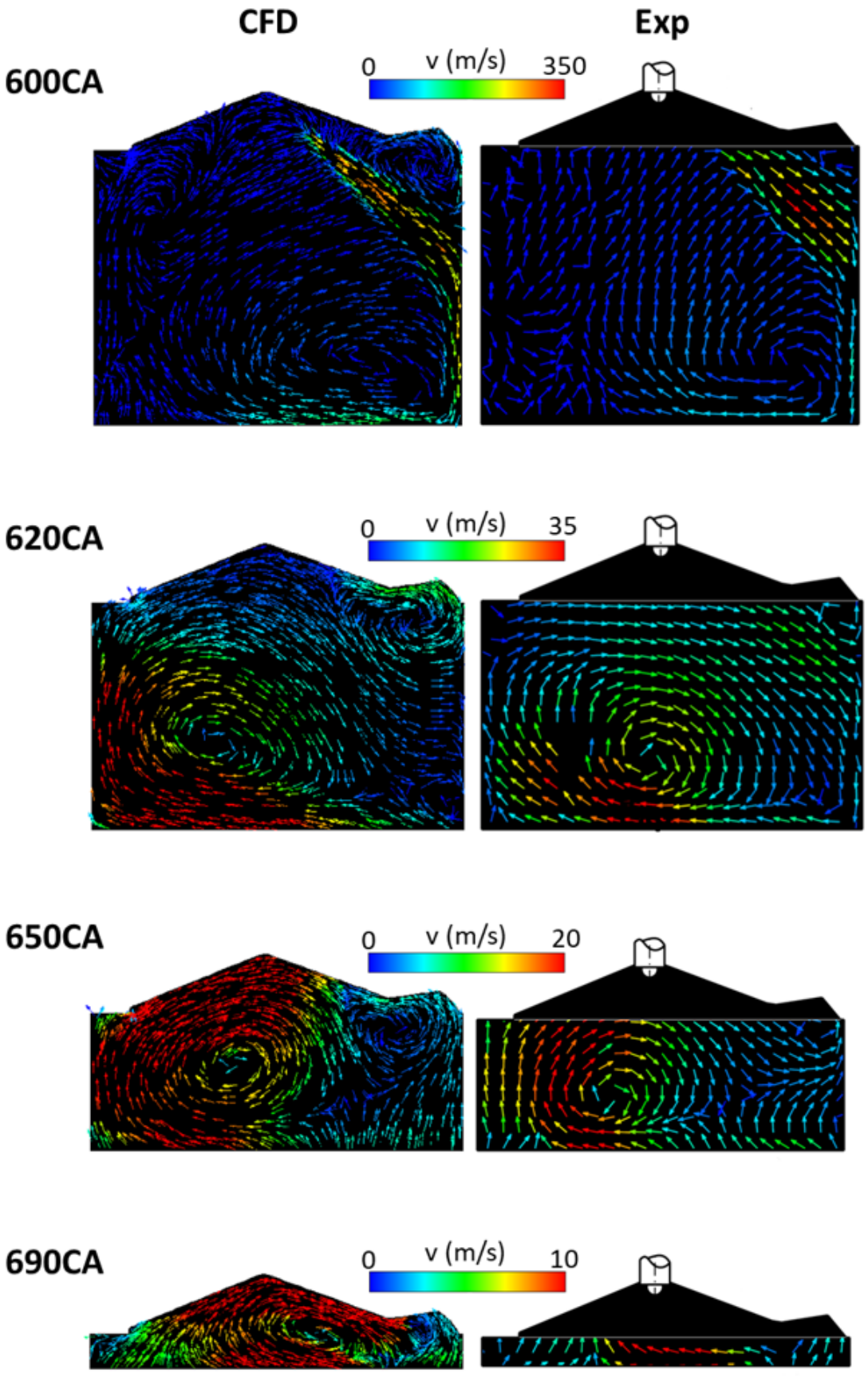

FIGURE 5.10: Mean in-plane velocity vector field calculated by CFD during compression stroke including hydrogen injection from 583°CA to 600.5°CA compared with experimental PIV measurement.

In-plane hydrogen mole fractions are shown in Figure 5.11. One of the major differences observed is the lack of hydrogen close to the injector at 600°CA. This is expected due to the estimated core length extending deep into the chamber, thus no droplet transition, and is backed up by the rich hydrogen concentration measured in the experiments at the center of the jet all the way up to the chamber wall. It should be noted that the jet core should have a mole fraction of 1 and the experiments may not show this due to difficulties in measuring the value experimentally, influence of the wall on the core structure or the high injector discharge coefficient leading to a reduced core. There is also a hydrogen rich portion of the wall jet formed directly after impingement which is not well captured by the CFD indicating the potential need for enhanced wall treatments (the higher concentration is predicted by the CFD but the colour scale does not show this well as the peak value is underpredicted compared to the experiments). Nonetheless, the general mixture formation excluding these regions is well predicted at 600°CA. At 620°CA the hydrogen's progress penetrating the chamber, traversing the top of the piston and up the left wall, as well as the secondary zone at the top right corner is in good agreement with the experimental measurement. However, again there is an underprediction in the richness of the mixture along the wall preceding the head of the jet. There is also a general lack of hydrogen dispersion in the chamber. The simulation at 650°CA suffers from much of the same issues as the previous crank angles whereby the rich region behind the head of the jet is not well defined and the concentration in the lean areas is lower compared to the experiments indicating a lack of hydrogen dispersion. The final measured mixture formation at 690°CA matches the simulations rather well with the two clear rich and two clear lean regions present.

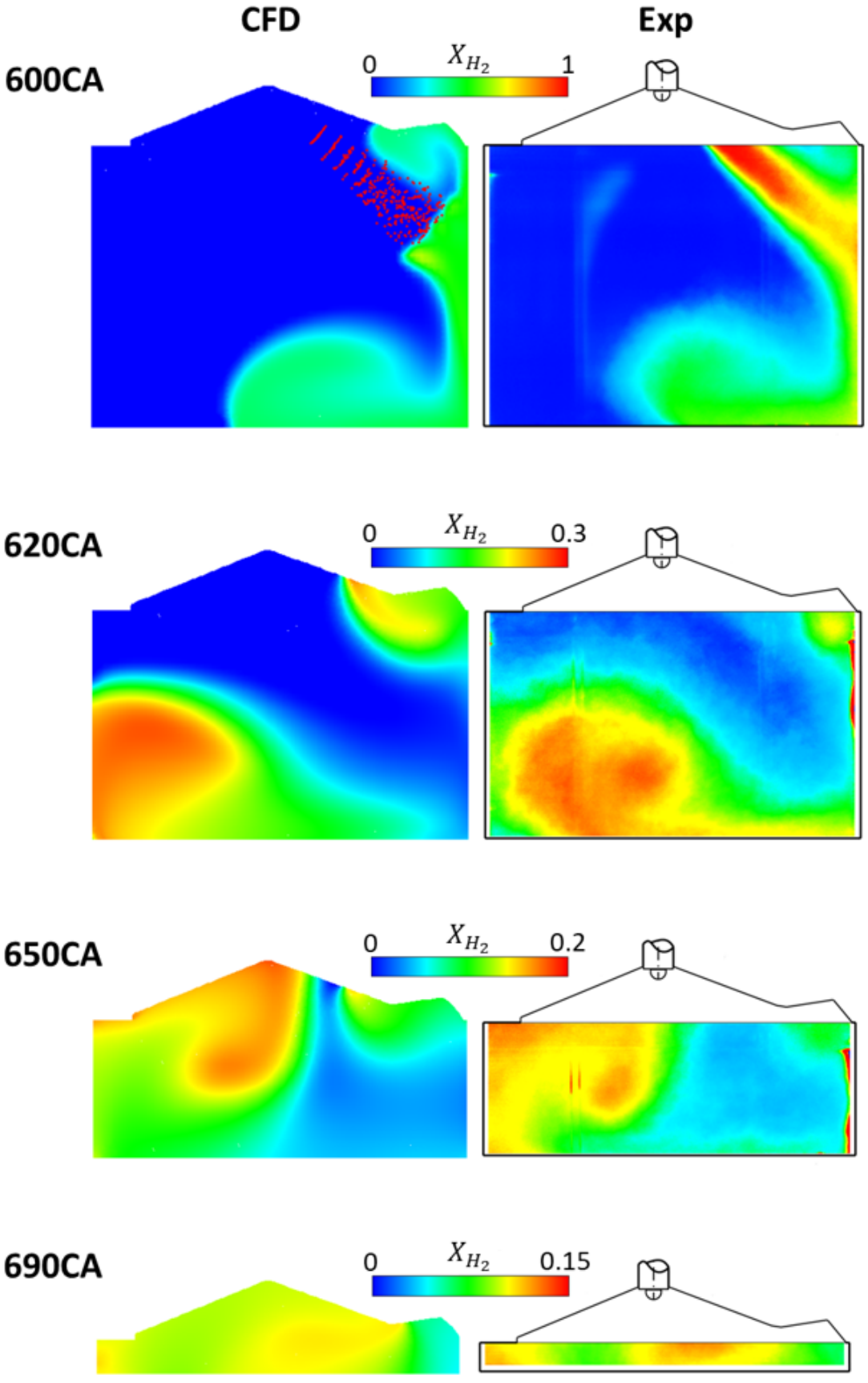

FIGURE 5.11: Hydrogen mole fraction (X_{H_2}) contours for hydrogen injection from 583°CA to 600.5°CA during the compression stroke calculated by CFD compared with experimental PLIF measurement.

Other RANS based CFD studies using refined injector inlets appear to suffer from similar issues in terms of adequately predicting jet dispersion and wall jet features [121, 215, 216]. This indicates that the problem is likely not to do with the GSI model and more so shows a need for enhanced wall treatments, fine tuning of the turbulence model, introduction of multi-component diffusion or use of a more detailed mass flow rate profile to achieve more accurate results as the simplified ramp up/down may be inadequate.

Overall agreement of the mixture formation and flow field between the present CFD study and experiments is very good with only minor differences being observed throughout the entire process. This indicates the improved GSI model can be a valuable tool in efficiently exploring direct injection gaseous fuelled engine nozzle configurations and injection strategies.

5.4 Combustion in a dual-direct injection compression ignition engine

An experimental study on combustion in a dual direct injection diesel-methane compression ignition engine is used to assess the ability of the improved GSI model at predicting combustion characteristics in direct injection gaseous fuelled engine. The study chosen is that of Faghani [109] as it is one of the few experimental works on gaseous direct injection and combustion in an engine which provides sufficient details for numerical model validation. Other works by the same group also serve to provide further information about the engine and its setup [105, 106].

5.4.1 Numerical setup

Numerical setup for the reacting compression ignition dual direct injection diesel-methane engine is presented. As there are 7 evenly spaced diesel and gas injectors in the engine a sector geometry representing $1/7^{th}$ of the combustion chamber is created in ANSYS SpaceClaim and meshed using ANSYS meshing, Figure 5.12. The sector contains one gas and one diesel injector both with an included spray angle of 140° and an interlace angle of 0°. The Westport HPDI 2.0 injector used in the experiments is depicted in Figure 5.13. Periodic boundary conditions are set at the side faces of the sector and constant temperature boundary conditions of 600 K and 650 K are set at the sector top face and piston bowl walls respectively and 500 K at the remainder of the chamber walls. Exhaust gas recirculation (EGR) level is adjusted by varying the initial charge composition, temperature and pressure using values measured in the experimental reference. Simulations are run from IVC to EVO and layering is used to compute piston motion during the compression and expansion strokes. Results are then compared to the experimental measurements. The prescribed diesel and methane injection mass

flow rates are shown in Figure 5.13 and the remainder of the initial injection quantities are calculated at the Mach disk via the previously described methods (Section 3.5). The injection profiles are based on those detailed in the reference study [109]. The gas injection takes place around TDC because a non-premixed mode of combustion is targeted as it allows for much finer control over the combustion and engine operating parameters compared to an early injection, or intake inducted, premixed combustion strategy. Throughout this analysis the convention that 720°CA is TDC of the compression stroke is followed. Table 5.3 summarises the operating conditions and engine geometry.

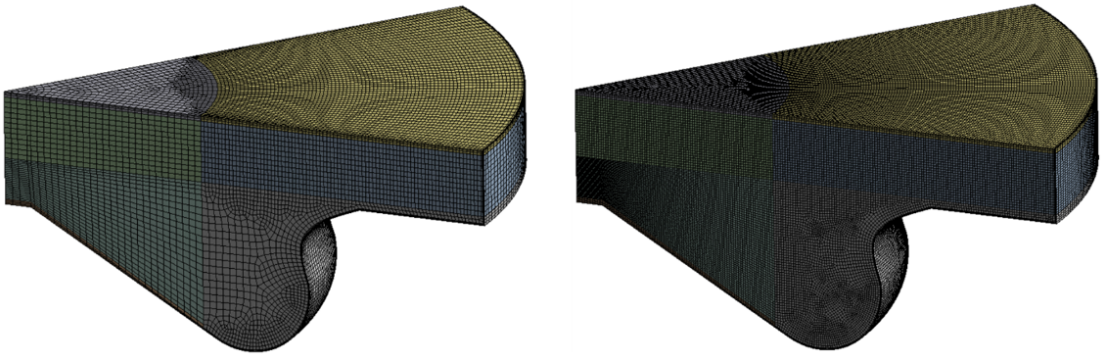

FIGURE 5.12: Sector mesh at 700°CA used in combustion simulations. Left shows the "coarse" grid used to compute the compression stroke prior to injection and right shows the "fine" keygrid, with a maximum mesh size of 0.35 mm, used during injection and combustion.

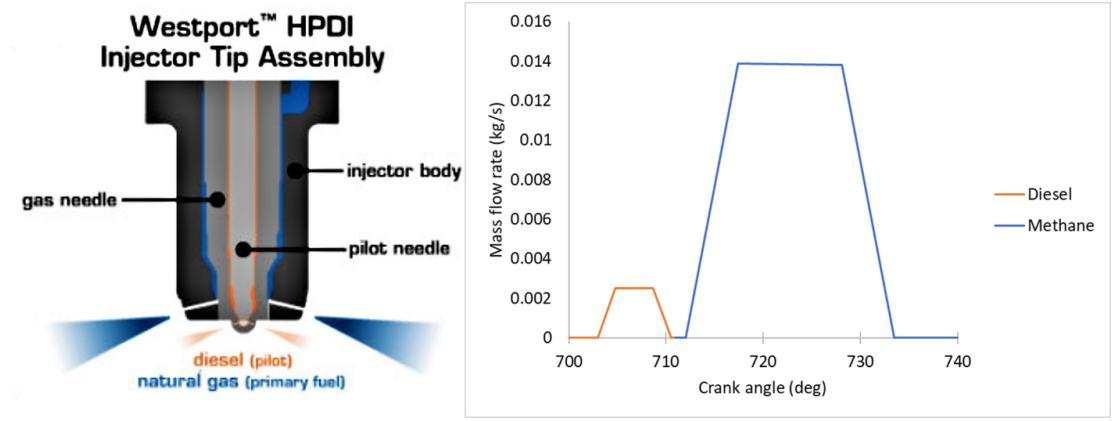

FIGURE 5.13: Schematic of the Westport HPDI 2.0 injector used in experiments (Source: Westport Inc [217]) and injection mass flow rate profiles for diesel and methane used in the simulations.

TABLE 5.3: Summary of dual direct injection diesel-natural gas combustion case.

Operating conditions	**Faghani [109]**	
Bore x stroke (mm)	137 x 169	
Connecting rod (mm)	262	
Displacement volume (L)	2.5	
Swirl ratio	1.5	
Compression ratio	17	
Engine speed (rpm)	1500	
IVC-EVO (CA)	630°-860°	
Ambient gas	Air + EGR	
EGR (%)	0, 18, 25	
Initial ambient pressure (MPa)	0.382, 0.448, 0.450	
Initial ambient temperature (K)	431, 441, 428	
Ambient gas composition	**O_2**: 0.233, 0.205, 0.198 **N_2**: 0.767, 0.760, 0.7583 **CO_2**: 0.00, 0.0194, 0.0240 **H_2O**: 0.00, 0.0156, 0.0194	
Injection Properties	**Gas**	**Liquid**
Number of injectors	7	7
Injected fuel	Methane	Diesel
Upstream temperature (K)	370	320
Actual nozzle exit diameter (mm)	0.73	0.16
Injection total pressure (MPa)	25	27
Total pressure ratio		
Mass of fuel injected-sector (kg)	2.48e-5	1.57e-6
Discharge coefficient	0.87	0.8
Steady mass flow rate (kg/s)	1.39e-2	2.5e-3

Accurate combustion results can be obtained through direct use of detailed chemistry given the mesh is adequately refined such that the majority of the turbulence scales are resolved to minimise sub-grid effects [124, 131, 218, 219]. In this study we employ a RANS based turbulence model, species transport finite-rate combustion and a detailed methane/n-heptane chemistry mechanism to simulate combustion in a diesel-natural gas dual direct injection engine. The discrete phase modified GSI model and discrete phase liquid injection model are used to represent the methane and n-heptane fuel injections respectively. Further details about the full modelling setup can be found in Chapter 3.

5.4.2 Validation

An extensive mesh sensitivity study is carried out using 4 different grid resolutions; coarse, medium, fine and very fine with maximum cell sizes of 1 mm, 0.4 mm, 0.35 mm and 0.3 mm respectively, Table 5.4. To allow for reasonable computation times keygrids are used in all but the coarse mesh simulation. In the medium, fine and very fine cases the coarse grid is used from IVC to 700°CA (3° before pilot injection starts) before being replaced by a finer mesh, Figure 5.12. This fine mesh is then used throughout both injections and the power stroke until EVO with a variable layering height which begins to coarsen after injections have finished. A variable time step size is used with 0.25°CA steps from IVC to 702°CA followed by 0.025°CA steps until 755°CA then 0.25°CA again until EVO.

TABLE 5.4: Mesh densities for the mesh independence study.

Mesh	Cell count at TDC	Max cell size (mm)	Run time
Coarse	50k	1	≈7h
Medium	300k	0.4	≈29h
Fine	400k	0.35	≈51h
Very Fine	550k	0.3	≈69h

As can be seen in Figure 5.14 all grids apart from the most coarse predict in-cylinder pressure and heat release fairly well for the 18% EGR test case. The coarse grid predicts a slightly later ignition of the methane injection compared to the other grids and generally underpredicts the rate of combustion until around the time that the gaseous injection finishes, leading to a lower pressure than desired. Only small variation between the medium and fine grid is observed. The variation is largely during the diesel injection where the medium grid has a similar peak HRR but lower level of mixing controlled diesel combustion than the fine grid which leads to lower pressures. The difference between the fine and very fine grids is even smaller with the only significant change being a slightly earlier diesel ignition which leads to a lower peak diesel HRR in the very fine grid. This could be due to grid effects but may simply be due to the cycle to cycle variation which the discrete phase model can cause. Results indicate that the RANS scales are adequately resolved when using a maximum cell size of 0.35 mm, in line with the expected 0.1 – 1 mm minimum length scale discussed in the literature [124, 131, 218, 219], so for the remainder of this study the 0.35 mm fine mesh is used and deemed insensitive to further mesh refinement.

Comparing fine mesh simulation results to the experimental study, the heat released from the combustion of the pilot injection is overpredicted leading to an overprediction in pressure during this period. This could be due to a number of reasons such as the use of n-heptane as a surrogate for the diesel blend used in the experiments which

has a slightly smaller lower heating value than n-heptane as well as a likely different cetane number and thus expected ignition delay. For the gaseous injection, ignition delay and peak heat release are predicted well, however, heat release rate during the mixing-controlled combustion phase is somewhat underpredicted and tends to remain at a higher level for longer when compared with experimental results. This again could be due to the use of methane as a surrogate for natural gas whose composition can vary greatly, or potentially a need to tune the likes of the cone angle in the GSI model for the specific case or to use a more accurate mass flow rate profile which accounts for the transients at the start and end of injection. It's also true that Mach disk properties (injection properties) will vary during combustion and thus a more complete approach would use a moving injector position as Mach disk length decreases, as well as variable Mach disk diameter, velocity and temperature rather than the expected averages used in these simulations. Another potential reason for the underprediction in mixing controlled combustion rate is the mixing layer surrounding the jet core being neglected which could lead to an offset in the combustion similar to the observed difference. Introducing a secondary transition criterion which would allow for particles at the outer limits of the core to be shed and transition to the bulk phase at a specific rate may be a good approach. Implementing these improvements should lead to better agreement with the experimental results and could be the focus of future work. All in all, the combustion trends are captured well indicating the potential for the improved GSI models use in direct injection engine studies.

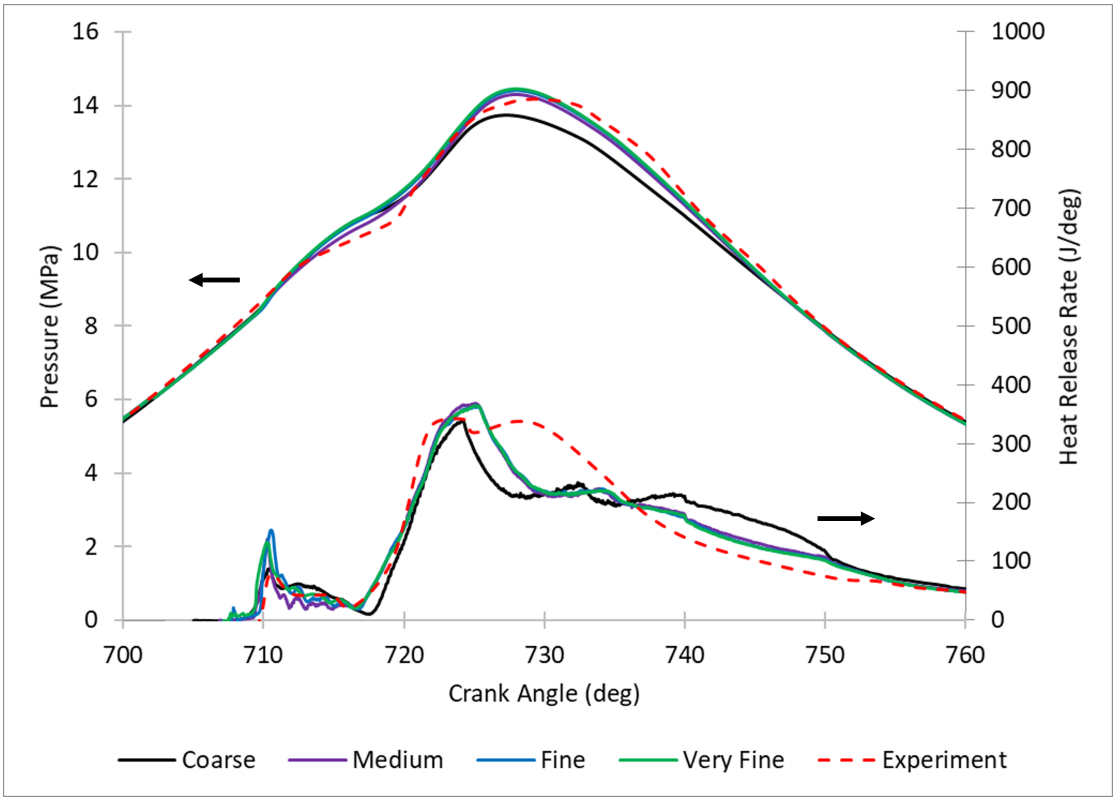

FIGURE 5.14: Pressure and heat release rate predictions and mesh sensitivity study for the 18% EGR test case with comparison to experimental data.

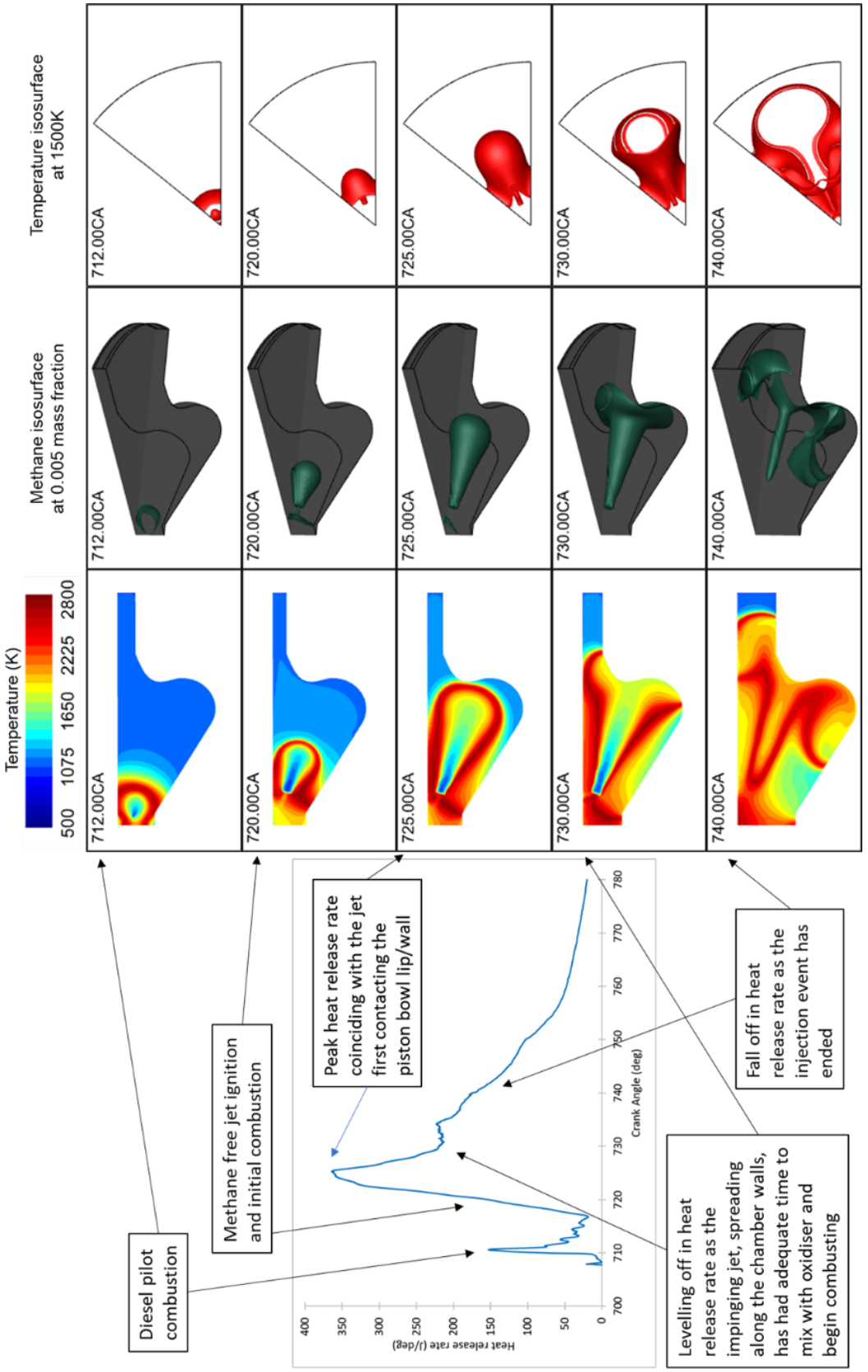

FIGURE 5.15: Breakdown of the diesel pilot ignited direct injection methane jet combustion process using calculated HRR (left), cylinder axis plane temperature contour slices (middle left), methane jet isosurfaces at 0.005 mass fraction (middle right) and top-view flame temperature isosurfaces at 1500 K (right).

Furthermore, Figure 5.15 shows the various stages of combustion are captured well by the model. Initially the pilot diesel combustion occurs, beginning at roughly 708°CA and peaking around 712°CA. The pilot combustion is largely confined to the near injector region/center of the chamber, see first row. The main injection of methane then begins and interacts with the high temperature region where the pilot combustion is occurring leading to ignition of the jet around 718°CA. Heat release rate then begins to climb rapidly due to the injector finishing its ramp up to peak mass flow rate, which is further enhanced by the free jet penetrating deeper into the chamber and mixing with oxidiser, second row of Figure 5.15. The majority of the combustion occurs at the outer edges of the jet where stoichiometry is achieved as the core of the jet is still too rich for combustion. The peak heat release rate coincides with the jets first contact with the piston bowl lip/wall at about 725°CA, third row, which is then followed by a rapid fall off in combustion rate, due to both quenching of the flame front at the wall and also the accumulation of methane in the region which can't combust due to a lack of oxidiser. As shown in the fourth row the jets momentum eventually leads to the spreading of the fuel both deeper into the piston bowl and up towards the top of the chamber. This allows for the flame front to spread and the fall in heat release rate levels off around 730°CA. Row 5 shows the flame front travelling towards the chamber liner and also curling up in the piston bowl and travelling back towards the injectors. As the main injection has ended heat release rate falls off and combustion starts to occur in the core/center of the jet as the rich core has decayed and is no longer too rich for combustion to take place.

Assessing the CFD modelling framework along with the improved GSI model's ability to predict pollutant emissions under differing conditions is important for gaining insight into various engine operating strategies. As pollutant soot and NO_x predictions are decoupled from the main flow solution the absolute values predicted are not of much importance, but the trends predicted should still follow those of the experimental data. As can be seen in Figures 5.16 a) and b), the overall trends of both NO_x and soot emission as EGR rate is increased are predicted fairly well with NO_x showing a decrease between 0% and 25% EGR rates and soot showing an increase. The percentage decrease in NO_x is also well predicted with simulations showing a decrease of 82% between 0% and 25% EGR rates and experiments showing a decrease of 80%. The findings are in line with the expected effect of EGR on NO_x development, whereby reduction in oxidiser leads to lower combustion temperatures which is further aided by the dissociation of H_2O and CO_2 during combustion and the higher heat capacity of exhaust gases acting as heat sinks. The percentage increase in soot is underpredicted in comparison to experiments which likely indicates a need to tune model parameters, include a soot mechanism in the chemical kinetics, improve initial charge composition as EGR rate is increased or various other factors. However, the general increasing trend of soot emissions being captured is deemed sufficient for the current work. Increased

soot emissions with increased EGR use is expected due to the decrease of oxygen availability leading to an increase in fuel rich areas and thus soot formation as well as the reduced in-cylinder temperatures being better suited for soot development.

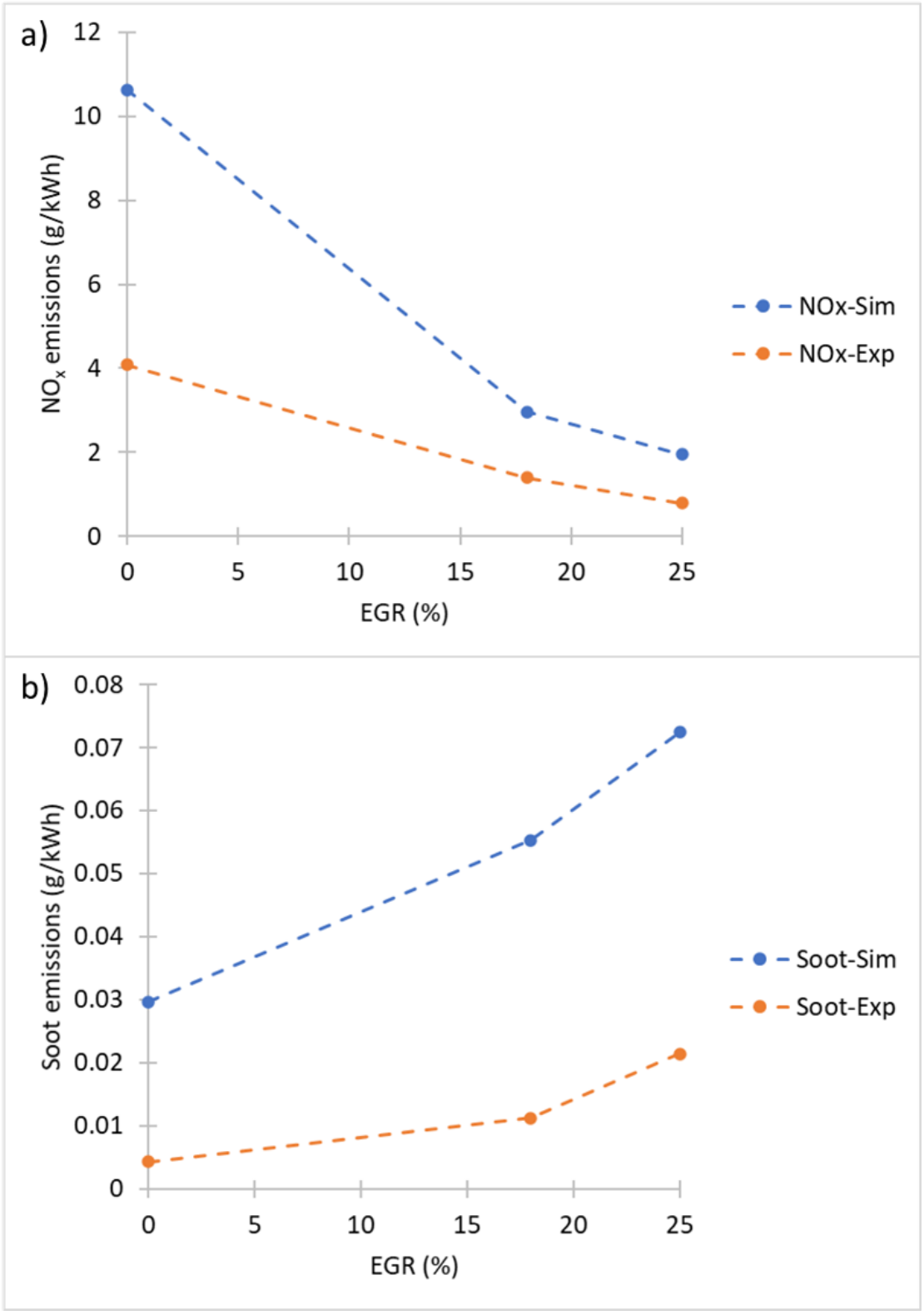

FIGURE 5.16: Pollutant trend predictions of a) NO_x and b) soot at EVO for increasing levels of EGR compared with experimental measurement.

Overall, the CFD model predicts the gaseous combustion and emissions characteristics relatively well and thus indicates that the improved GSI model should be suitable for use in the investigation of combustion in direct injection gaseous fuelled engines

5.5 Summary

The capability of the improved discrete phase gaseous sphere injection (GSI) model to accurately predict the direct injection of gaseous fuels, such as hydrogen and natural gas, into internal combustion engines has been demonstrated. A change to the core length estimation which determines when gaseous droplets transition to the bulk phase was introduced. An empirical estimate based on recent experimental and numerical data is proposed which accounts for the variation in the jet core length due to total pressure ratio change. Other theoretical estimates are also used to determine injection and discrete phase particle properties. The improved GSI model was implemented into a CFD code and used to simulate the gaseous direct injection process at various engine relevant conditions. Both freestream and engine experimental studies are considered for model validation. The main findings of the paper are summarised as follows:

1. The gaseous fuel injection process was successfully simulated by the improved GSI model across a wide range of cases including both hydrogen and methane direct fuel injection.

2. Fairly coarse meshes are sufficient for the modelling of mixture formation and penetration of gaseous fuels using the improved GSI model.

3. The improved GSI model can deal with a wide range of pressure ratios, nozzle exit conditions and gases.

4. Good agreement with experimental data is met without need for turbulence model alteration or model tuning given the proposed modifications to core length, drag and initial injection quantities are applied.

5. Good agreement with experimental data is found in terms of penetration and spreading in freestream studies.

6. Mixture formation in a non-reacting hydrogen direct injection spark ignition engine, as well as the velocity field, are reproduced well by the modified GSI model.

7. Simulation of combustion and emissions characteristics in a dual direct injection methane-diesel compression ignition engine is carried out and predictions correlate well with the experimental measurements.

8. Future improvements to the model could account for variations in Mach disk properties as pressure ratio changes throughout a given simulation by using a variable Mach disk length, velocity, diameter and temperature.

9. Implementing a secondary transition criterion which allows for the shedding of some particles from the core, to model the mixing layer, may aid in improving combustion characteristics.

10. There is also likely a need to use more accurate mass flow rate profiles which account for the opening and closing injector transients to reproduce specific flow characteristics, but simplified profiles still show reasonable agreement with experiments.

11. Similarly, tuning of cone angle may also be necessary to properly reproduce spreading rate in some cases.

12. Additionally, further experimental and high fidelity numerical studies focussed on the fundamental mixing and non-premixed combustion processes of underexpanded gaseous jets is required for a more complete validation of the GSI model.

Chapter 6

Numerical Modelling of Diesel-Hydrogen Dual-Fuel Combustion with Hydrogen Direct Injection

6.1 Background

Gaining insight into processes occurring during dual direct injection diesel-hydrogen CI engine operation is vital for the advancement of hydrogen internal combustion engine technology. HPDI of the gaseous fuel close to TDC should allow for greater power output and higher hydrogen substitution rates across all load conditions when compared to either early compression stroke direct injection or intake induction operation. Currently investigations of such engines are scarce and even fewer detailed CFD modelling studies or studies aimed at optimising operation have been carried out.

In this chapter an explorations of various parameters which can impact the combustion process, performance and emissions in a dual direct injection diesel-hydrogen CI engine is carried out. Examples of such parameters are the likes of gas injector properties/orientation and injection strategies, intake charge pressure and temperature, exhaust gas recirculation and CVCP. Recommendations are then provided for future dual direct injection diesel-hydrogen dual fuel engine operating strategies and injector designs which maximise performance and hydrogen energy share while minimising pollutant emission outputs.

In this chapter we use the dual direct injection diesel-natural gas CI engine configuration [109] which was previously employed in Chapter 5 when validating the improved gaseous sphere injection model. First a comparison of hydrogen and methane

operation is made at HL and LL for 95%, 97% and 99% gaseous energy share. This is then followed by a parametric exploration of strategies which can potentially improve performance and HES while keeping emissions outputs low. Finally, an optimisation study is carried out at 99% HES for both loads, guided by the findings of the parametric study. The optimisation study performs sweeps of varying EGR rate, duration between pilot and main injections (PSEP) and gaseous start of injection (GSOI) with the target of reducing NO_x emissions while maintaining or improving performance. The ultimate goal of this work is to find out whether it is possible to introduce very high hydrogen energy content at both low and high load conditions using hydrogen direct injection compared to the likes of intake induction hydrogen operation without compromise of engine performance and emissions.

6.2 Numerical setup

The numerical setup and validation study carried out in Section 5.4 for the diesel-natural gas engine is carried over to this chapter and used as the basis for the hydrogen direct injection study. Ideally validation would have been carried out using a HPDI dual-fuel diesel-hydrogen engine, however, the literature is distinctly lacking in this regard. The diesel-natural gas engine model validation should be adequate as the chemical mechanism contains a detailed hydrogen oxidation mechanism [43] and both the medium and fine mesh showed good agreement with experimental results indicating that the fine mesh should be able to adequately resolve the higher velocity and temperature gradients present during hydrogen injection and combustion (see Table 5.4 and Figure 5.14). Using this setup also means that an in-depth comparison of methane and hydrogen HPDI can be made and key differences identified. Further details about the full modelling setup can be found in Chapter 3.

Injection pressure is increased to 40 MPa based on the analysis carried out in Section 2.3.2 to ensure the nozzle is choked during operation. Conversely, nozzle diameter is reduced to 0.577 mm to keep mass flow rates equivalent to the validation case (for methane; hydrogen will always be less due to density differences) as this should keep combustion phasing somewhat similar. This ensures a fairer comparison between cases as steady mass flow rate will not change during a given case due to unchoking of the nozzle and also represents an injection pressure and nozzle diameter which should be targeted in practical applications.

All HL cases use a total energy of 1304 J (diesel + gaseous fuel) and all LL cases 434 J. While the HL case uses the same initial absolute pressure (3.82 bar) and temperature (431 K) as the validation simulations unless stated otherwise, the LL case uses slightly lower initial absolute pressure (3 bar) and temperature (390 K) to model what would be expected in a practical engine setup where turbocharging level is used as a way to

control load in conjunction with smaller fuel injections. At this point it's likely good to point out that the IVC provided by the experimental validation study is further into the compression stroke than is standard (90°CA after bottom dead center). So while it may seem as if the initial turbocharging levels are quite high they equate to effective compression ratios of 38.7 at HL and 30.4 at LL which are fairly standard for diesel engine operation. From here on it's simply assumed that the engine operates on a late intake valve close cycle similar to some Miller cycle implementations.

6.3 Hydrogen compared to methane

Combustion, performance and emissions characteristics of HPDI operation of the two fuels is examined across 3 gaseous energy shares (95%, 97% and 99%) and also at high and low load conditions. It's worth mentioning that real-world diesel injectors may struggle to properly inject the small volumes of fuel required at the likes of LL 99% energy share [220], but this problem is outside of the scope of the current study,

The first two tests simulate equivalent injection conditions (same injection pressure and diameter) for hydrogen and methane which leads to a slightly lower energy flow rate and longer duration for the hydrogen injection (case 0 and case 1), while the second set changes various injection parameters such that energy flow rate and duration of the hydrogen injections are equivalent to the baseline methane case (case 2, 3 and 4). Table 6.1 outlines the injection conditions for the test cases.

TABLE 6.1: Injection conditions for methane-hydrogen comparisons.

Case	**Fuel**	**P_0 (MPa)**	**D_e (mm)**	**$\dot{m}$ (kg/s)**	**Energy flow rate (MJ/s)**	**Energy per gaseous injection (J)** 95% HL | LL	97% HL | LL	99% HL | LL
0	CH_4	40	0.577	0.013900	0.695	1236 | 412	1265 | 422	1291 | 430
1	H_2	40	0.577	0.005042	0.605	1236 | 412	1265 | 422	1291 | 430
2	H_2	46	0.577	0.005792	0.695	1236 | 412	1265 | 422	1291 | 430
3	H_2	40	0.619	0.005792	0.695	1236 | 412	1265 | 422	1291 | 430
4	H_2	80	0.437	0.005792	0.695	1236 | 412	1265 | 422	1291 | 430

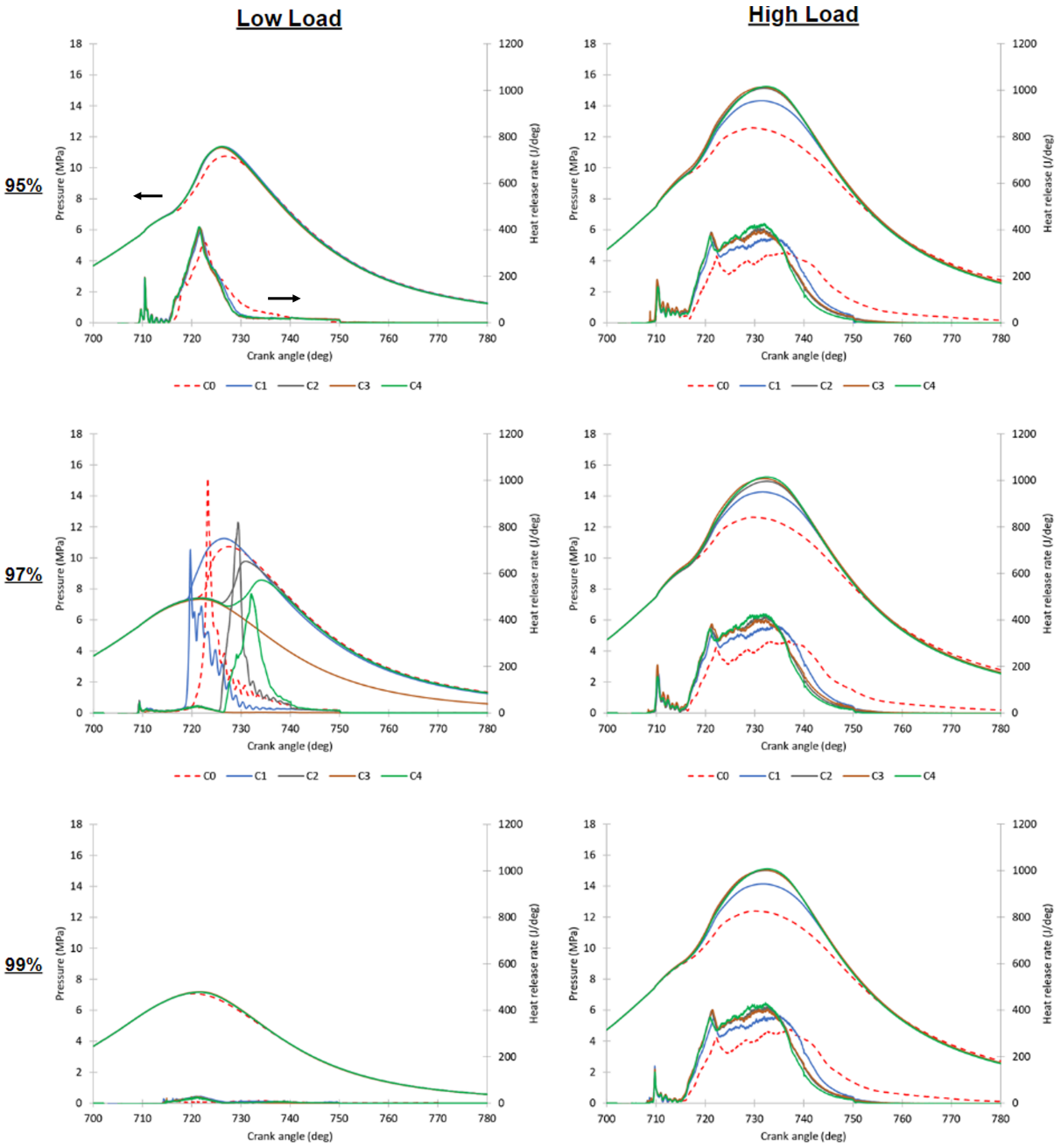

FIGURE 6.1: Calculated pressure and HRR trends for methane-hydrogen comparisons at 95%, 97% and 99% gaseous energy shares.

We first compare the combustion process of methane and hydrogen at 95% gaseous energy share as consistent and stable combustion is present at both load conditions. From observation of the heat release rate graphs, Figure 6.1, it's clear that the diesel pilot adequately ignites the gaseous injections for both fuels almost instantly upon their injection into the combustion chamber. Due to hydrogen's lower minimum ignition energy this ignition occurs about 0.3° earlier for the hydrogen injections compared to methane. There is also increased HRR before full ignition of the jet at HL due to small amounts of hydrogen enhancing the diesel combustion. Figure 6.2 shows time series

temperature contours which highlight the differences in the combustion process at HL (analogous to LL at this energy share). Clearly the diesel injection provides an adequately high temperature region in the vicinity of the injected gases trajectory close to the injectors (715°CA contours). Upon contact with this region the gas jet quickly ignites with little to no premixed combustion present (the rich lower temperature core stays intact throughout, 716°CA - 717°CA contours, with no early HRR spike) and a non-premixed diffusion flame forms. The lack of premixed combustion is mostly due to the lack of air entrainment due to the underexpanded flow structures close to the injector.

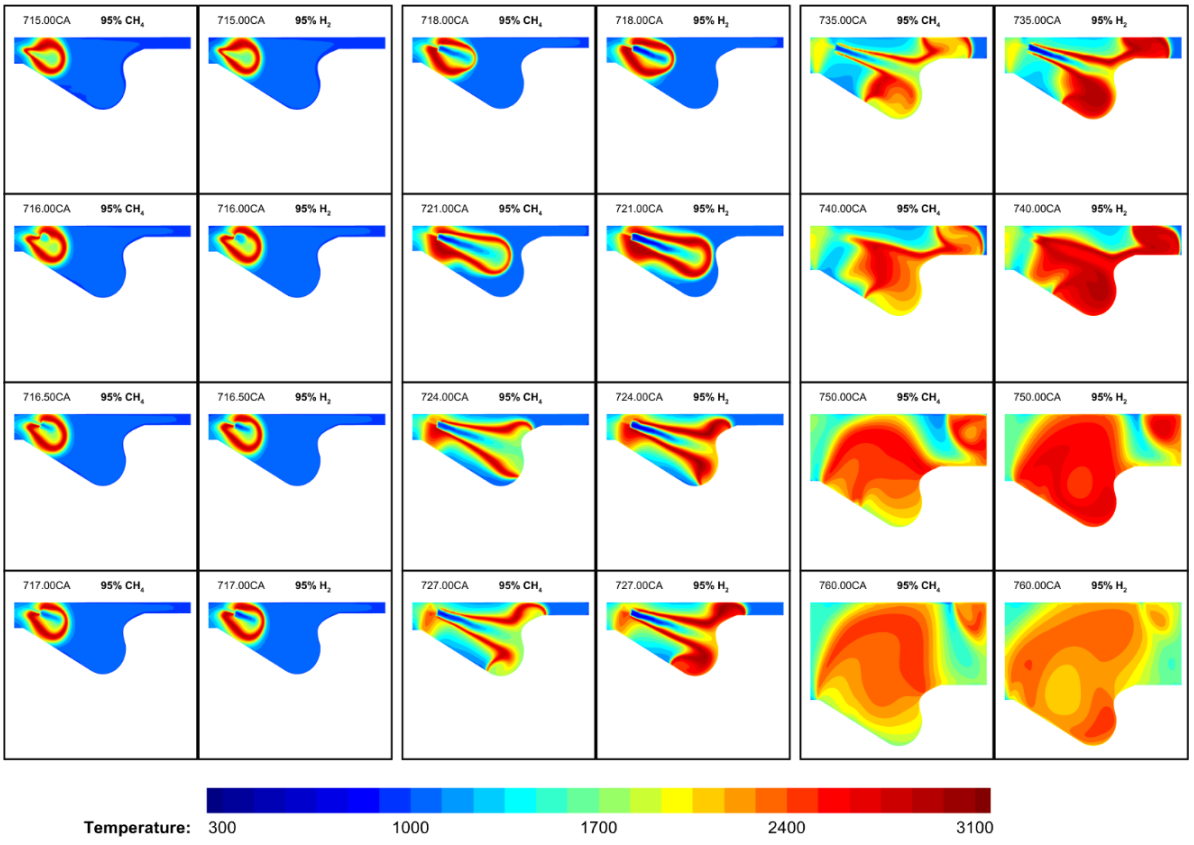

FIGURE 6.2: Temperature contours for methane and hydrogen at high load 95% gaseous energy share (case 0 & 1).

The formation of a flame indicates the end of the ignition delay phase and beginning of the free-jet combustion phase (716-721°CA contours). The higher injection velocity of the hydrogen (higher speed of sound) leads to a much faster penetration rate than the methane which likely contributes to the faster ignition and is certainly a factor in the higher pressure rise rate (climb to peak HRR) due to the rate of mixing with oxidiser being much higher as the flame penetrates the chamber. The non-premixed flame is also thicker in the hydrogen case as evidenced by the reduced low temperature core width and wider high temperature region surrounding it on either side and in-front (721°CA contours). This is due partly to hydrogen's higher mass diffusivity and thus

further reach with regard to mixing but is mostly due to its much wider flammability limit allowing for far richer combustion towards the core and leaner combustion towards the outer edge of the jet. This is also the reason for the higher peak HRR value in the hydrogen cases which occurs just before the jets contact with the chamber wall. The peak HRR correlates with the point at which the non-premixed flame is largest, i.e. before the leading edge is quenched by the chamber wall (721°CA vs. 724°CA contours), and as noted hydrogen's flame is much wider than its methane counterparts. This peak in HRR also occurs earlier for the hydrogen cases due to the increased penetration rate and thus earlier contact with the chamber wall.

Upon contacting the wall the front of the flame quenches and HRR begins to fall due to a smaller flame volume and an accumulation of fuel which is too rich to combust at the rate it was previously, indicating the end of the free-jet combustion phase and beginning of the wall-jet combustion phase (724°CA-735°CA contours). This process is very pronounced for the methane case where a clear low temperature region forms around the piston bowl walls. However, due to hydrogen's far lower quenching distance and wider flammability limit combustion is still occurring along the wall, although at a reduced rate compared to the free-jet combustion. The impinging jets momentum forces fuel along the walls in all directions; into the piston bowl and back towards the injectors, laterally towards other sectors of the chamber and towards the top cylinder and liner walls. This spreading of the fuel allows for adequate mixing of fuel and oxidiser which leads to a levelling off in HRR at a moderate level (better shown in the HL graphs as the injection ends too early to show this at LL). As combustion is focussed within the piston bowl a high temperature area develops which is especially apparent for hydrogen due to its ability to burn at much higher fuel-air equivalence ratios (most obvious in the 735°CA contours). This increase in fuel utilisation leads to higher HRR levels during the wall-jet combustion for the hydrogen cases compared to methane. During this phase (or later after the end of injection) due to spreading out of the fuel and flame front, interaction with fuel from other injectors is likely and may enhance the combustion rate in some cases (can be seen somewhat in the climbing HRR towards the end of the phase). This process is more likely for hydrogen which spreads faster because of the increased jet velocity and thus increases the chance of meeting other injector fuels before the end of the injection event while the jets still have a high momentum.

As the injection ends HRR falls off rapidly signalling the end of the of the wall-jet combustion phase and start of the late combustion phase (740°CA-760°CA contours continuing until EVO). Even though the hydrogen injection ends later the fall off in HRR occurs earlier and is much more rapid than the methane case. This is due to the oxidation of the remaining UHCs producing heat whereas comparatively almost all of the hydrogen has been oxidised due its much shorter and simpler chemical breakdown pathway. In general, initially for both fuels the rich core stays intact for a short while after the end of injection but over time it begins to decay until eventually being engulfed

by the remaining flame (740°CA contours). There is often a secondary peak right before fall off in HRR which is due to the rapid combustion that occurs when the jet core collapses which is enhanced by the wall-jet/combined injector jets convection into this region. Small amounts of combustion continue for the remainder of the power stroke, as evidenced by the fairly high temperature regions. It's clear however that both from the quickly reducing temperatures in the hydrogen cases (760°CA contours), and much lower HRR that greater amounts of combustion are occurring in the methane cases at this stage due to the aforementioned oxidation of UHCs. There is however still a low temperature region formed in the piston bowl region for the methane case (rich pooling of UHCs where combustion cannot reach) which is not present for the hydrogen case (760°CA contours). Minimal interaction of the hydrogen close to the cylinder liner and the hydrogen in the piston bowl/injection region is observed after the injection event ends, with two clear separate zones of recirculation forming.

Figure 6.3 depicts the impact of the impinging hydrogen jet on the flow field during and after the gaseous injection event. Initially, prior to impingement, the free-jet displaces the air around it, pushing air both ahead of itself towards the piston bowl/chamber liner and also around itself and back towards the injectors. This is partly attributed to the minimal air entertainment in the early development of the jet, as evidenced by the lack of premixed combustion and rich core. Upon impingement, the jet curls up in the piston bowl, spreading out as it impinges on the wall. The momentum of the jet pushes hydrogen along the wall in all directions: back towards the injectors, up towards the piston liner and outwards towards other sectors of the chamber. Recirculation zones form in the piston bowl and towards the top of the chamber near the liner which slows the rate of combustion as fuel rich areas form. After a time the outward spreading leads to contact of the jet with those from other injectors, and this interaction slows the lateral movement but further propels the jet back up the slope towards the injectors. Finally the injection event ends and the lack of momentum and decaying core leads to high levels of recirculation along the trajectory of the jet which combines with the fuel which was pushed back towards the injectors. This process enhances the combustion rate somewhat and also leads to the formation of a large high temperature zone as can be seen in the 740°CA/750°CA contours in Figure 6.2.

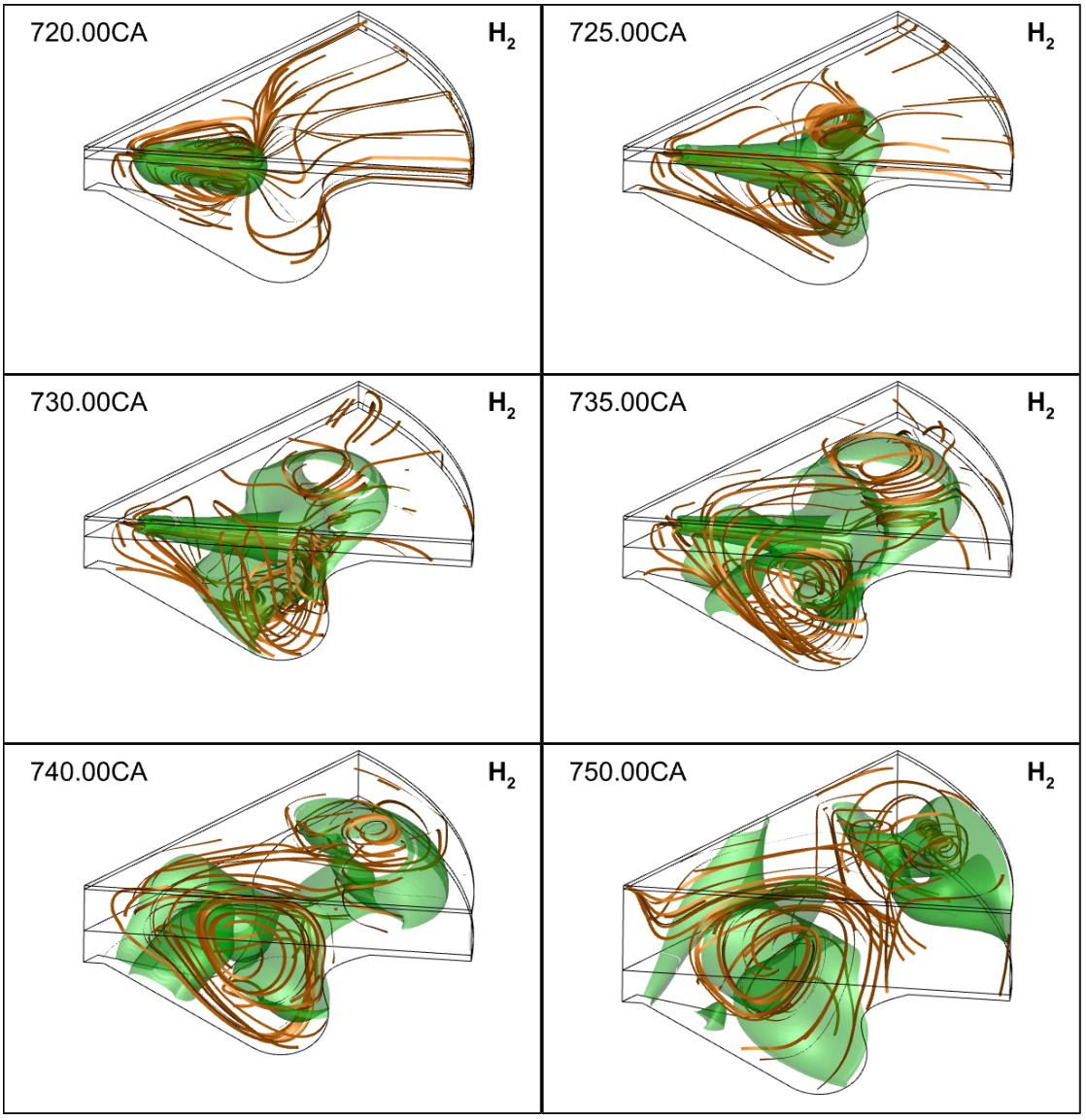

FIGURE 6.3: Streamlines and hydrogen isosurface at a mass fraction of 0.001 showing the jet induced flow field at HL 95% HES.

Next we address the change in combustion characteristics as gaseous energy share is increased. From observing the HRR and pressure curves presented in Figure 6.1 it can be seen that increasing gaseous energy share makes very little difference to combustion characteristics at HL for either fuel or at the varying injection conditions. This is because the reducing volume pilot diesel injection continues to produce enough heat to ignite the gaseous injection. This is evidenced by the very similar ignition delays of the gaseous jet observed across all HL cases. A completely different story is observed at LL due to the smaller pilot injection compared to HL. At 95% gaseous energy share the diesel pilot adequately ignites the jet with very similar jet ignition delays to the HL cases. However, further decrease of the pilot volume leads to much longer gaseous jet ignition delays at 97% energy share leading to high levels of premixed combustion and high pressure rise rates/HRR peaks. Hydrogen won't produce soot/CO/UHCs

like diesel during this type of combustion mode, however, the issue is hydrogen's wide flammability limits and very high burning velocity meaning too much fuel is likely to combust over a very short period of time. This type of combustion is undesirable as the rapid and rich premixed combustion which occurs generally leads to high engine noise and possibly damage, while also causing difficulties with controlling engine operation as the ignition timing becomes unpredictable. NO_x emission during this type of combustion mode may be lower than the high temperature combustion which occurs in a non-premixed flame, however, this will only be the case if the amount of premixing is somewhat controlled to not allow for the majority of the fuel volume to burn in a much shorter period. The inconsistent and difficult to control engine operation is highlighted by the wide variance in ignition delays observed between cases and the likes of case 3 (which is not too different from the other cases) not even showing full ignition of the jet with only a minimal amount of hydrogen combustion occurring in the vicinity of the pilot injection. Similar to case 3 at 97% energy share, all 99% LL cases show almost no hydrogen combustion due to the much reduced diesel injection providing too little energy for ignition of the injected jet.

The temperature contours shown in Figure 6.4 shows the stark difference between the ignition and combustion process as gaseous energy share increases at LL for methane and hydrogen injections (case 0 & case 1). At 99% the diesel injection offers so little temperature rise that by the time the gaseous injection begins there is essentially no hot products combusting (top right 720°CA) leading to no ignition for either fuel. At 97% operation improves a lot compared to 99% as the pilot provided enough energy to ignite the jet. However, the ignition is delayed as shown by the 720°CA methane contour (same is observed for hydrogen at earlier crank angles than shown) which also reduces initial jet penetration as the acceleration of the jet via combustion occurs later than in the 95% cases. This late ignition leads to a much higher gaseous fuel burning rate early in the injection as can be observed in the 730°CA and 740°CA contours where the temperatures in the center of the sector are higher than the same regions at 95% energy share. The reduced penetration rate also contributes to the more focussed central combustion site as there is greater fuel dispersion which is why the flame is somewhat wider at 97% energy share. There are also lower temperatures in the near injector region throughout at 97% energy share both because the initial combustion occurs slightly later into the gaseous injection trajectory and also due to the reduction in diesel meaning there is a smaller multiple fuel burning region.

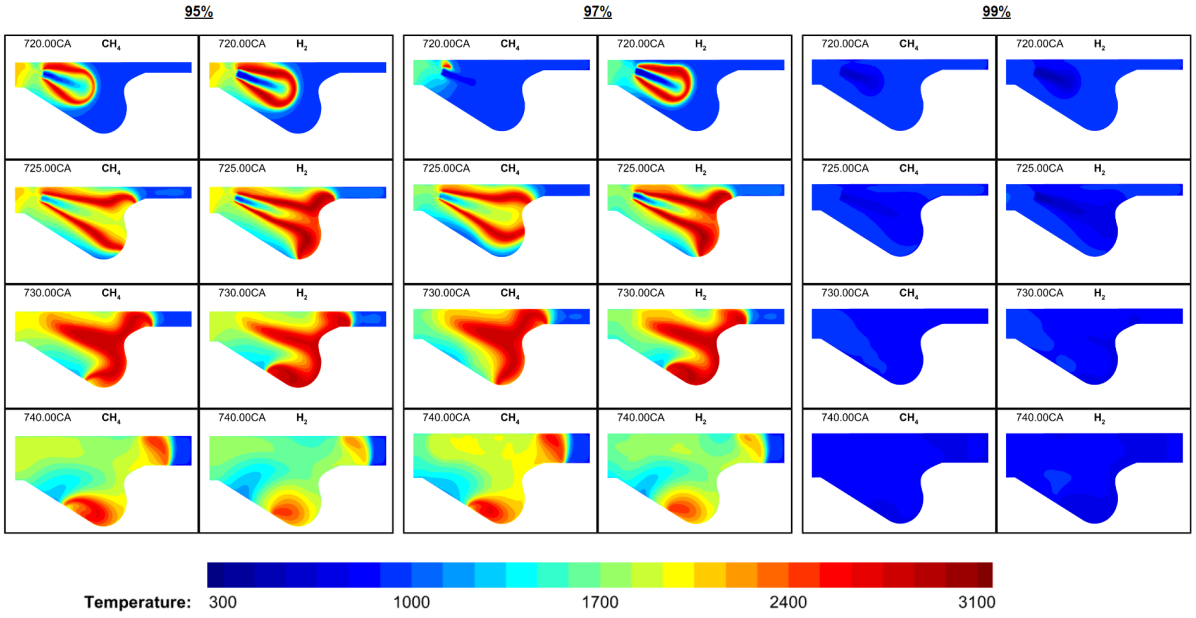

FIGURE 6.4: Temperature contours comparing methane and hydrogen at low load 95%, 97% and 99% gaseous energy share (case 0 & 1).

At this point we note that thermal efficiency is calculated using the gross indicated work, i.e. integrating only pressure/volume between IVC and EVO, thus the values are somewhat higher than would be expected in a practical engine as the various losses aren't accounted for. The engine operating on an overexpanded cycle (50° longer expansion stroke compared to compression) also contributes. However, trends captured are more important than the absolute value so this shouldn't be of concern. The same can be said for presenting the likes of work or power output as the gross indicated version of these quantities are linearly linked to the gross indicated thermal efficiency.

Figure 6.5 presents the calculated emissions and thermal efficiency of each case at HL. Clearly as expected hydrogen leads to much higher NO_x emissions than methane due to the much faster and higher temperature combustion, however, the reduction of supplied carbon leads to a considerable decreases to all carbon based emissions. Due to the high fuel burning efficiency at HL this also means hydrogen emissions are lower in the hydrogen cases as the breakdown of UHCs ends up outweighing any unburned injected hydrogen fuel (this could also be an indication that the reduced n-heptane mechanism needs work but nonetheless indicates high fuel utilisation in the hydrogen cases). Performance also sees a small uplift across most hydrogen cases compared to methane. The performance increase is smaller than might be expected when comparing the pressure graphs but this is due to the increased late power stroke pressures in the methane cases as the oxidation of UHCs and CO continues to produce heat, and therefore work, all the way up to EVO.

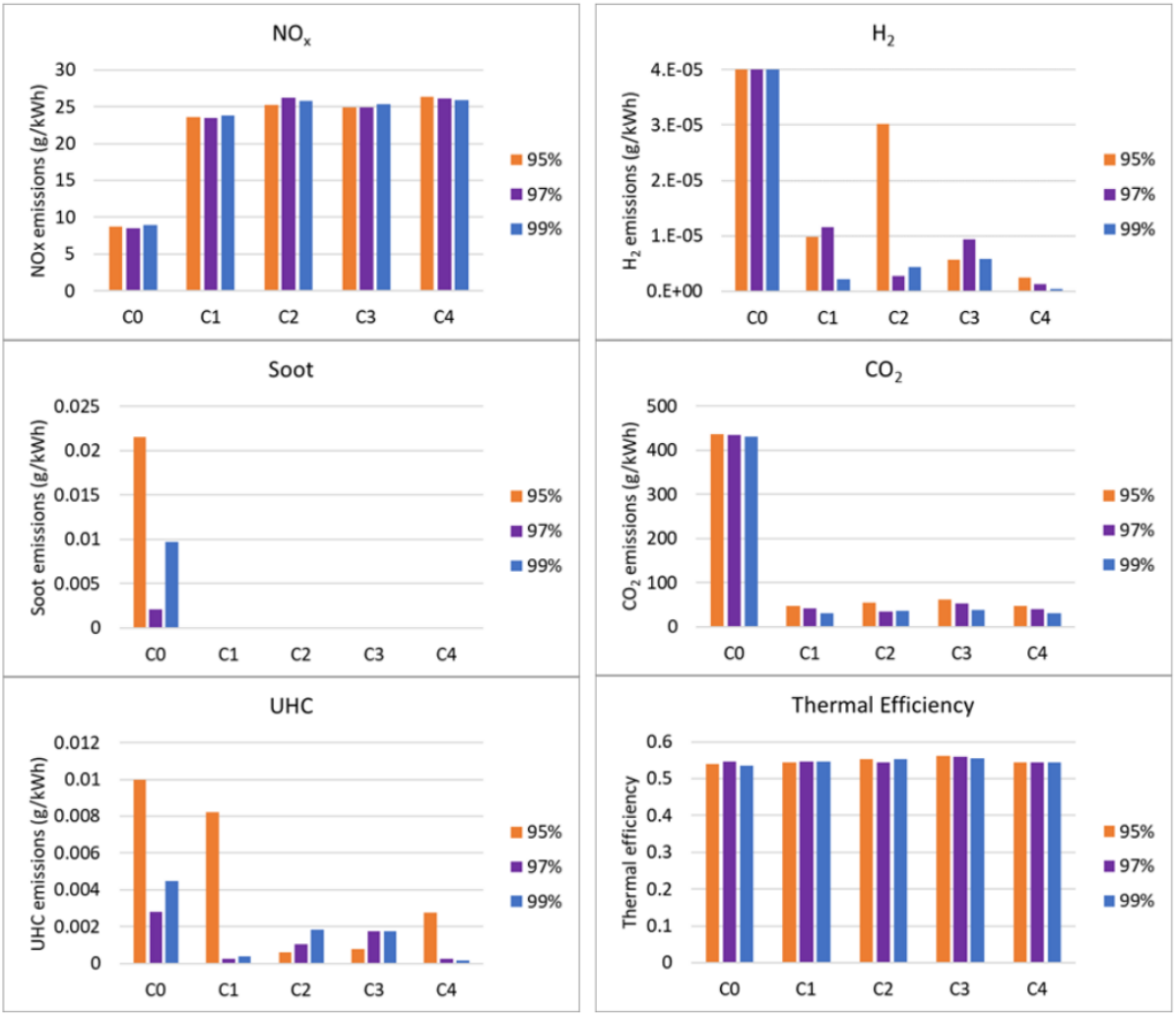

FIGURE 6.5: Calculated HL thermal efficiency and NO_x, soot, UHC, CO_2 and H_2 emissions at EVO for 95%, 97% and 99% gaseous energy shares - methane hydrogen comparisons.

There is relatively little change between each hydrogen case across all the energy shares. The two key points to note are the injection rate increase leading to increased NO_x emissions due to the increased rate of burning causing higher in-cylinder pressures and temperatures, and very similar performance (in some cases reduced) compared to the original hydrogen case. This indicates C2, C3 and C4 are not effective strategies going forwards.

However, one of the significant findings is the decrease in UHC emissions as the injection rate is increased at 95% HES. Not only do the higher temperatures aid in this process but the increased convection due to the higher jet momentum and larger mach disk diameters in C2, C3 and C4 improve the mixing in the near injector area leading to improvements to the pilot burning. Pilot combustion products also often get entrained in the jet (also improved by momentum/diameter) and are burned as it penetrates the chamber further improving utilisation. This process is shown in Figure 6.6

where it's clear that in C1 more of the UHCs are accumulating in the near injector region whereas in C3 more UHCs are entrained in the hydrogen jet and are being pushed into the piston bowl. The entrained UHCs then burn efficiently with the hydrogen jet as they penetrate the chamber. At higher energy shares, where the pilot penetration is reduced, poorer pilot burning is sometimes observed leading to higher UHC emissions due to the combustion products getting stuck behind the injector. This is a result of the increased mach disk/core length reducing gaseous jet combustion close to the injector compared to lower pressure ratio/nozzle diameter cases and in some cases the higher momentum jet pushes more air around itself and back towards the injector area, essentially trapping the already poorly penetrating pilot products behind the jet in the injector region (see Figure 6.3).

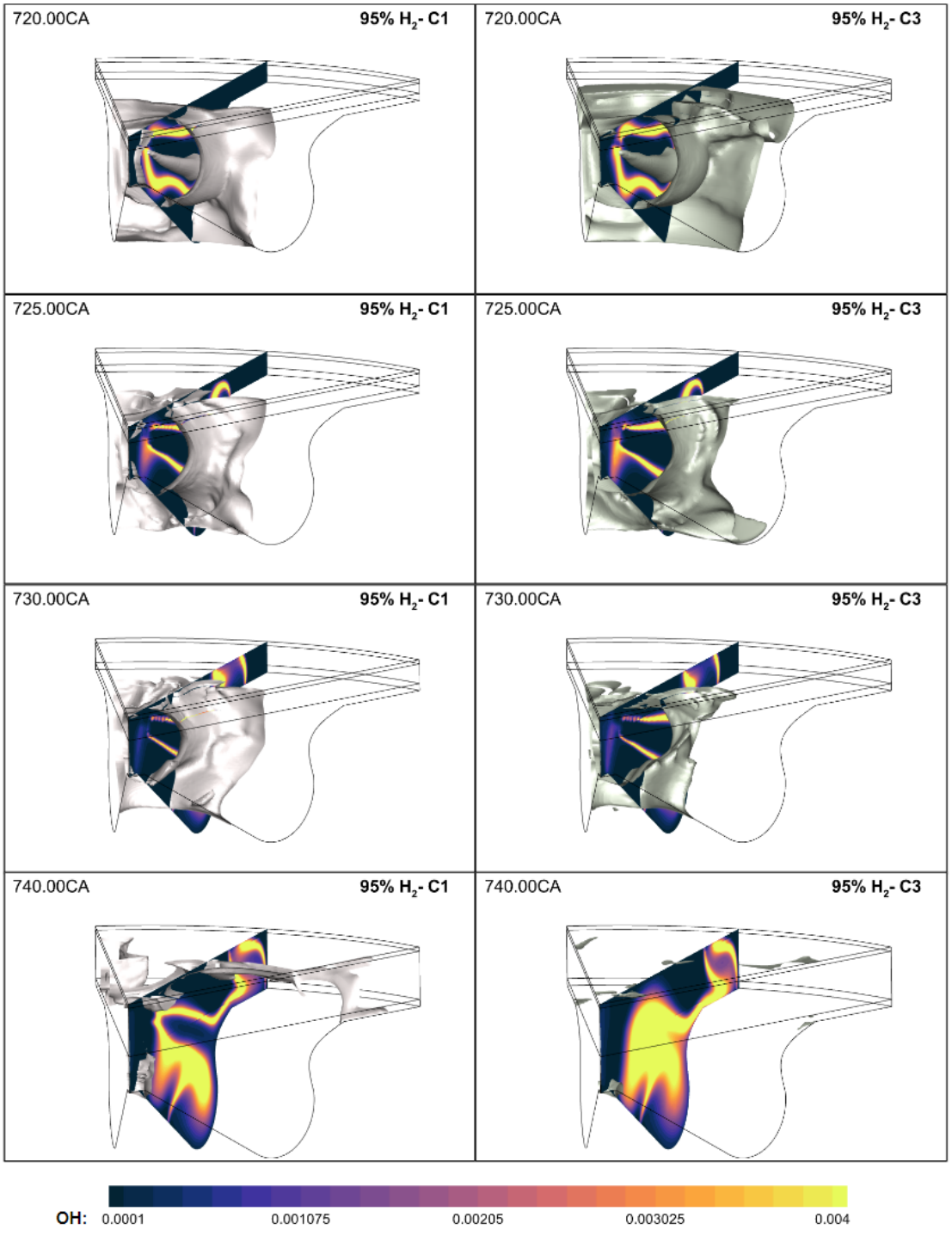

FIGURE 6.6: UHC isosurfaces at 0.05% mass fraction with OH mass fraction contours at 95% HES HL cases 1 and 3.

Figure 6.7 presents the calculated emissions and thermal efficiency of each case at LL. Comparing the 95% methane and hydrogen cases it's clear that NO_x increases while carbon based emissions generally decrease similar to the higher load condition. UHCs don't tend to follow the same trend which is due to a similar process to the one shown in Figure 6.6. The reduced LL pilot penetration means pilot combustion products get

caught behind the injector and the reduced penetration of the gaseous injection means the flame struggles to curl up in the piston bowl and make it back towards the injector and burn the pilot fuel in the same way it does at HL (compare 740°CA contours in Figure 6.2 with Figure 6.4). This means UHC oxidation is much more reliant on late power stroke combustion which is much poorer for hydrogen cases. Performance tends to decrease compared to methane due to the overall poorer fuel utilisation.

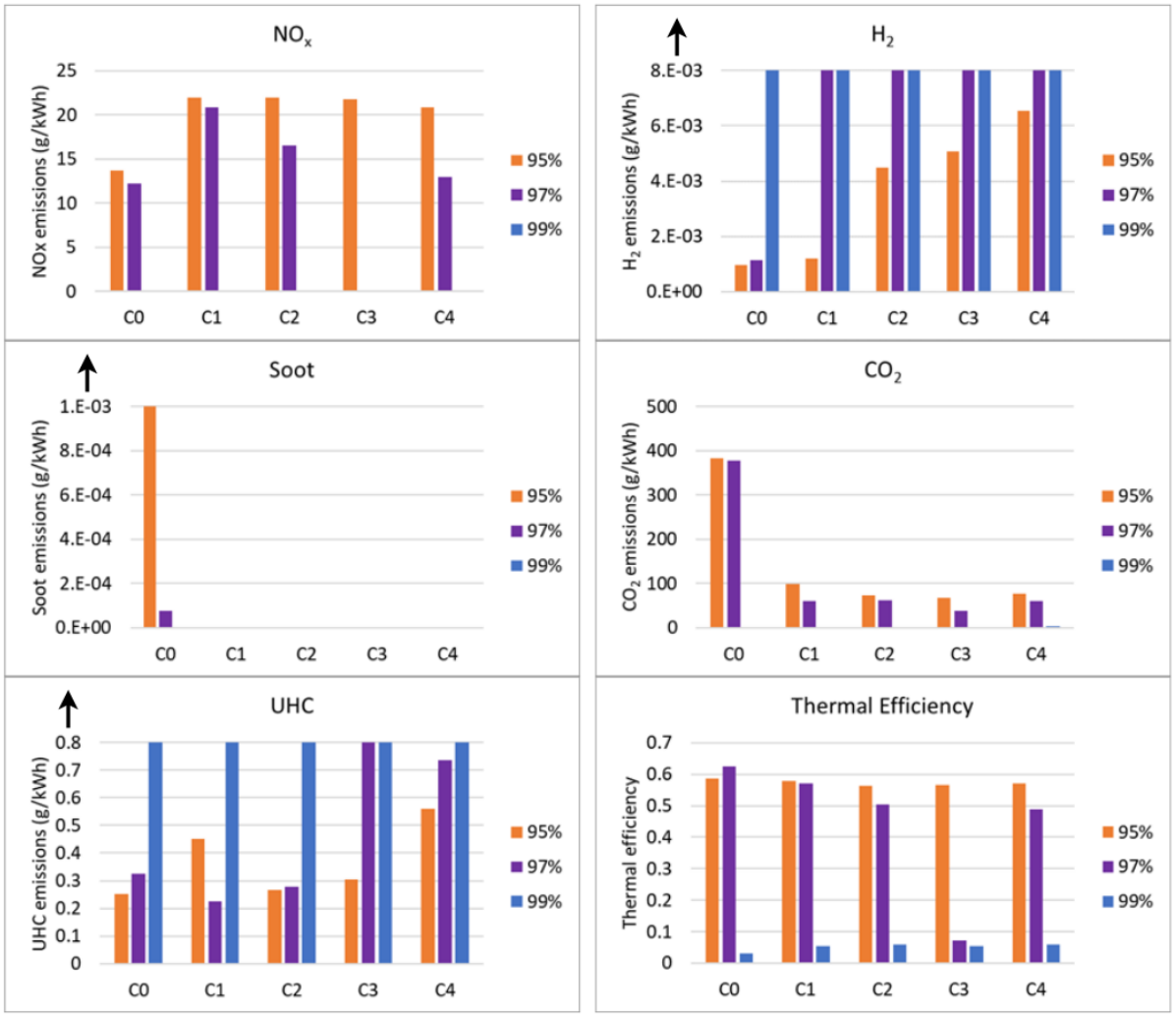

FIGURE 6.7: Calculated LL thermal efficiency and NO_x, soot, UHC, CO_2 and H_2 emissions at EVO for 95%, 97% and 99% gaseous energy shares - methane hydrogen comparisons.

Clearly 99% energy share shows poor combustion all around and therefore the likes of UHC and H_2 emissions increase dramatically while thermal efficiency drops to near 0 levels. Improvements are clearly required for LL operation at this high an energy share.

At 97% the unstable combustion leads to far poorer fuel utilisation which causes high hydrogen and UHC emissions combined with a reduction in performance when compared to 95% energy share. NO_x emissions do tend to reduce, but this is mostly due

to the delayed onset of combustion and lower levels of fuel burning reducing temperatures. This is not the correct way to go about reducing NO_x but does indicate that a later injection timing should be beneficial given adequate ignition can be achieved and also implies that premixed combustion modes may offer some potential for NO_x reduction.

Figure 6.8 compares contours of temperature and emissions at EVO for the baseline methane and hydrogen cases (C0 and C1) at LL 95% and 97% energy share. Methane cases have higher late power stroke temperatures for both fuels which are higher at the lower energy share because of the early rapid premixed combustion in the 97% cases. Hydrogen cases have much higher NO_x levels which cover a larger area of the chamber due to the increased penetration and wider flame than methane. Hydrogen case CO_2 emissions are much lower than methane and they are confined to the near injector region. Both fuels show a general decrease of CO_2 at increasing energy share as a result of much poorer fuel utilisation but also due to lower carbon levels in the chamber in general. Soot is extremely low in all but the 95% methane case and it is confined to the low temperature region close to the cylinder liner and along the chamber walls close to the injector where unburned fuel has pooled. An area of unburned hydrogen forms at the top of the cylinder close to the liner in the 97% hydrogen case due to the unstable combustion meaning some of the unburned fuel gets trapped above the piston bowl at too low a temperature to burn.

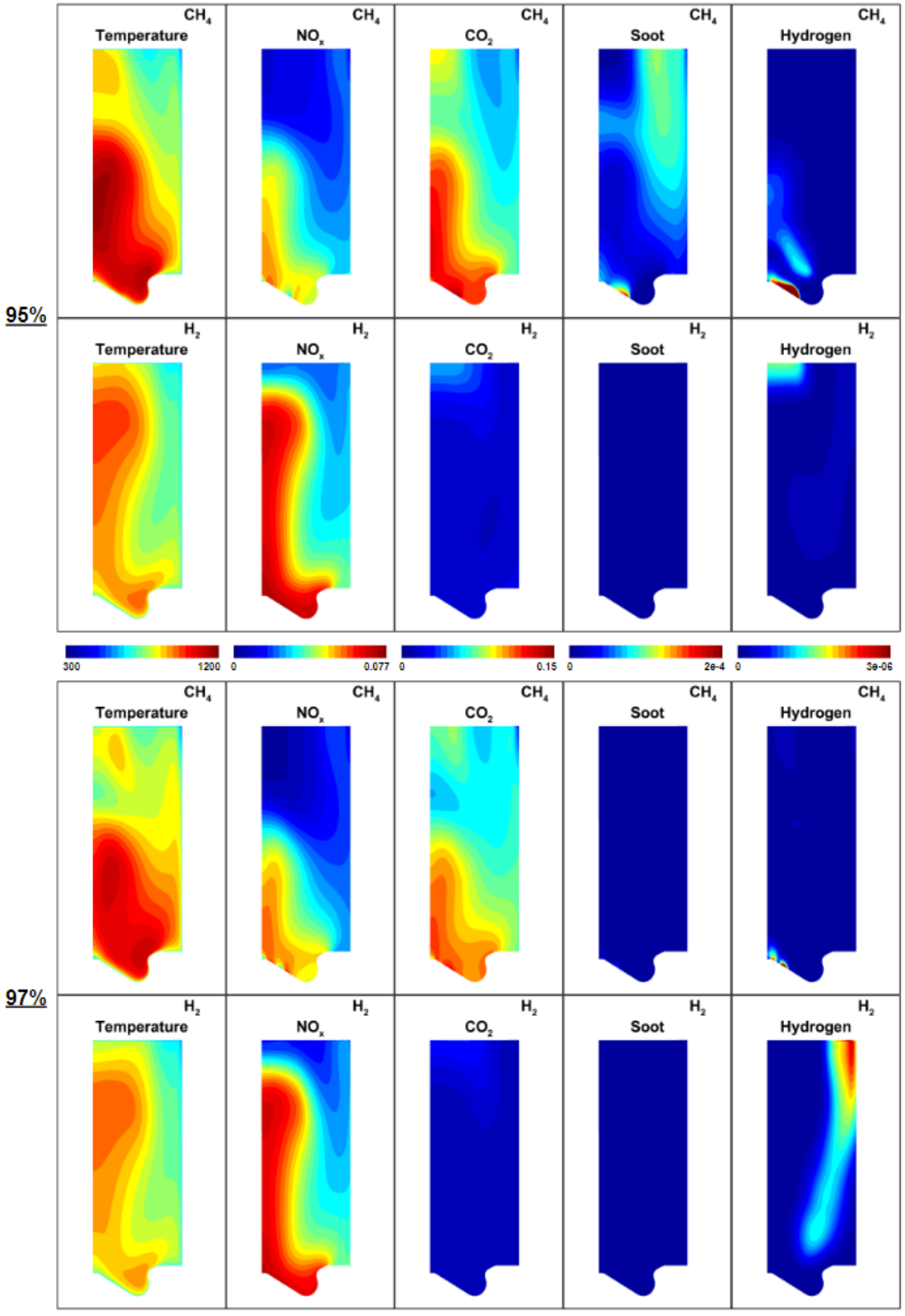

FIGURE 6.8: Contours of temperature, NO_x, CO_2, soot and hydrogen at EVO for LL 95% and 97% energy share of hydrogen and methane (cases 0 and 1).

Comparing the contours for C1, C2, C3 and C4 at HL 99% HES, Figure 6.9, it's clear

that simply increasing injection rate doesn't necessarily improve combustion and mixing of the hydrogen with oxidiser. In fact, the jets increased momentum causes the hydrogen, which in C1 gets caught close to the liner, to deflect off the walls and move back towards the injector region where there is a lack of oxidiser because of the combustion which already took place there. The highest NO_x levels occur close to the top of the chamber along the trajectory of the hydrogen injection and to a lesser extent along the piston bowl walls. This is amplified as the injection rate is increased as the combustion is less spread out compared to C1 with the liner deflected hydrogen likely also enhancing the NO_x production in the region. These contours clearly indicate that slowing the hydrogen injection rate or increasing the coverage/mixing of the injection should be an effective way to control NO_x while also potentially improving hydrogen utilisation. The increased CO_2 levels shown at the top left of the contours are a clear indication of improved pilot utilisation when jet momentum is increased leading to improved mixing of the pilot combustion products with higher cylinder temperatures also contributing. This improved mixing and utilisation of UHCs is reflected in the soot contours also, where for the most part soot levels reduce with the increase in jet momentum due both to less initial formation and greater oxidation.

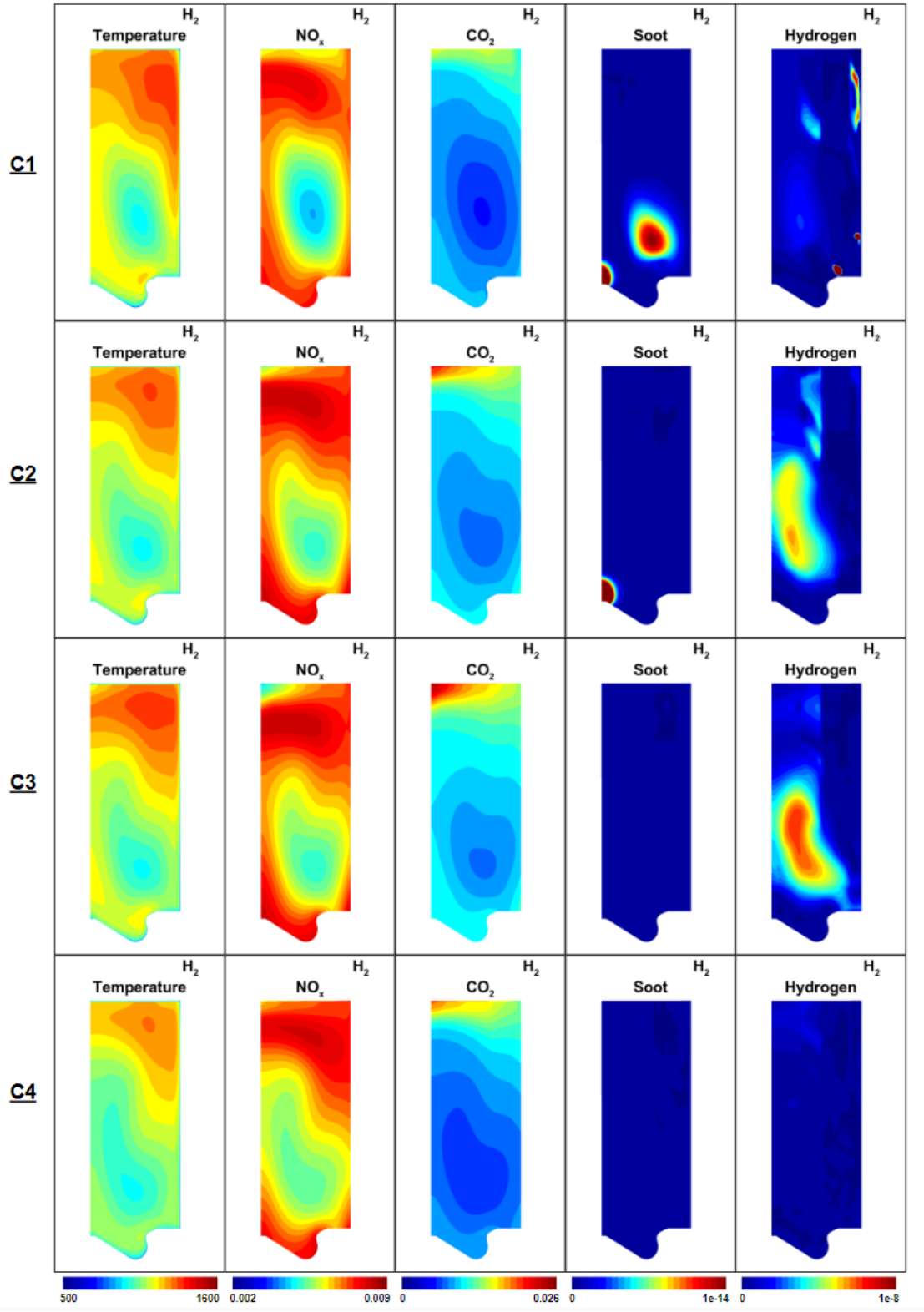

FIGURE 6.9: Contours of temperature, NO_x, CO_2, soot and hydrogen at EVO for HL 99% energy share of hydrogen (cases 1, 2, 3 and 4).

Three clear problems which need to be addressed with respect to high hydrogen energy share dual-direct injection operation are identified:

1. Poor low load performance at high hydrogen energy shares due to inadequate jet ignition by the reduced pilot.
2. Unstable combustion at low load as hydrogen energy share is increased due to delayed jet ignition by the reduced pilot.
3. Much higher NO_x output compared to methane due to hydrogen's much faster burning rate, wider flammability limit and higher temperature combustion.

The above issues will be investigated in the following sections via exploration and optimisation of various parameters/approaches pertinent to engine operation.

6.4 Parametric study of injector properties/injection strategies

The approach taken in this section is to isolate various parameters and view their effectiveness at improving high HES combustion characteristics and their ability to reduce NO_x output. The most promising strategies will then be carried over to the final section which aims to optimise the engine combustion process.

One of the parameters not investigated further is injection pressure. While injection pressure has a considerable effect on combustion it is not varied in the following tests. This is because increasing injection pressure will likely lead to undesirable NO_x increase (as evidenced by case 2 and 4 in the previous section) and a reduction will lead to unchoked flow in many cases and thus would would be harder to fairly examine with the current modelling approach while also introducing uncertainty with regard to metering in a practical engine. If however the engine is targeting lower TDC pressures than the currently studied engine a lower injection pressure would likely be an effective way to control the combustion rate.

All tests (apart from split injection - only HL 99%; gaseous start of injection - only HL 99% & LL 95%, 97% and 99%; turbocharging/inlet heating - only HL & LL 99%) were carried out at 95%, 97% and 99% HES at both load conditions. Similar to the previous section very little difference is observed at any of the HES at HL and little to no combustion is observed at LL 99% apart from one case where slight improvement is noted and 97% shows inconsistency again in most cases. As a result for the most part conclusions will be drawn from the 99% HL cases and the 95% LL cases. Figure 6.10 shows a plot of HRR for all the cases carried out (excluding the parameters listed above) with some select cases/trends highlighted.

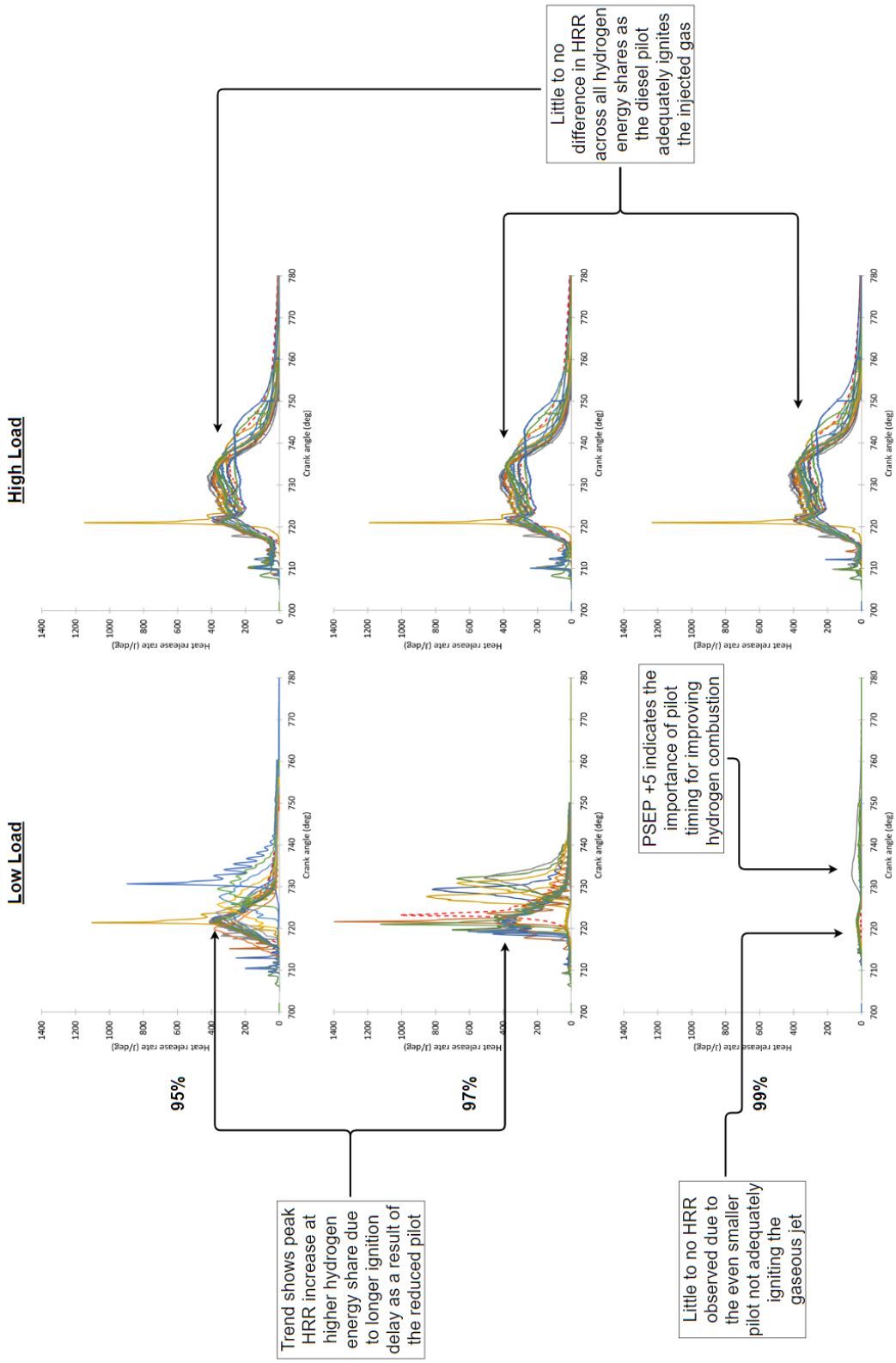

FIGURE 6.10: HRR comparisons for parametric studies at HL & LL for 95%, 97% and 99% HES (trend observations only).

Figure 6.11 summarises the NO_x emissions and performance of the parameters varied

in this section at LL 95% HES and Figure 6.12 does the same for HL 99% HES. Carbon based emissions are of less concern due to the values being relatively low compared to methane operation where much more carbon is present within the chamber. Hydrogen emissions tend to correlate with thermal efficiency for the most part and so also are not focussed on. From here on hydrogen and carbon emissions will only be discussed when they vary significantly from the baseline hydrogen case (C1) with the emphasis being placed on NO_x emissions, performance and stable combustion. Table 6.2 gives a brief summary of the results of the parametric study.

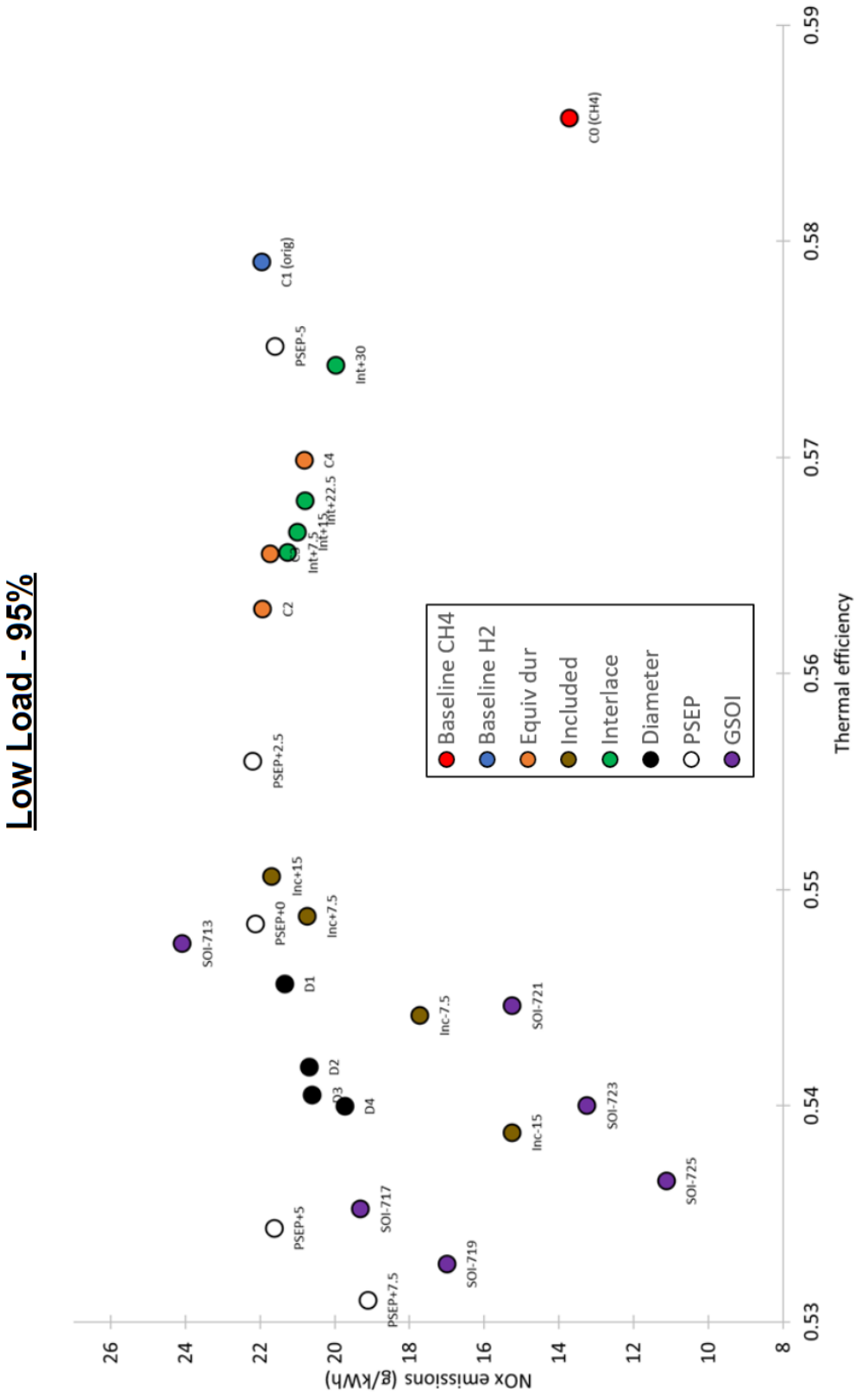

FIGURE 6.11: NO_x emissions plotted against thermal efficiency for the various parameters at LL 95% HES.

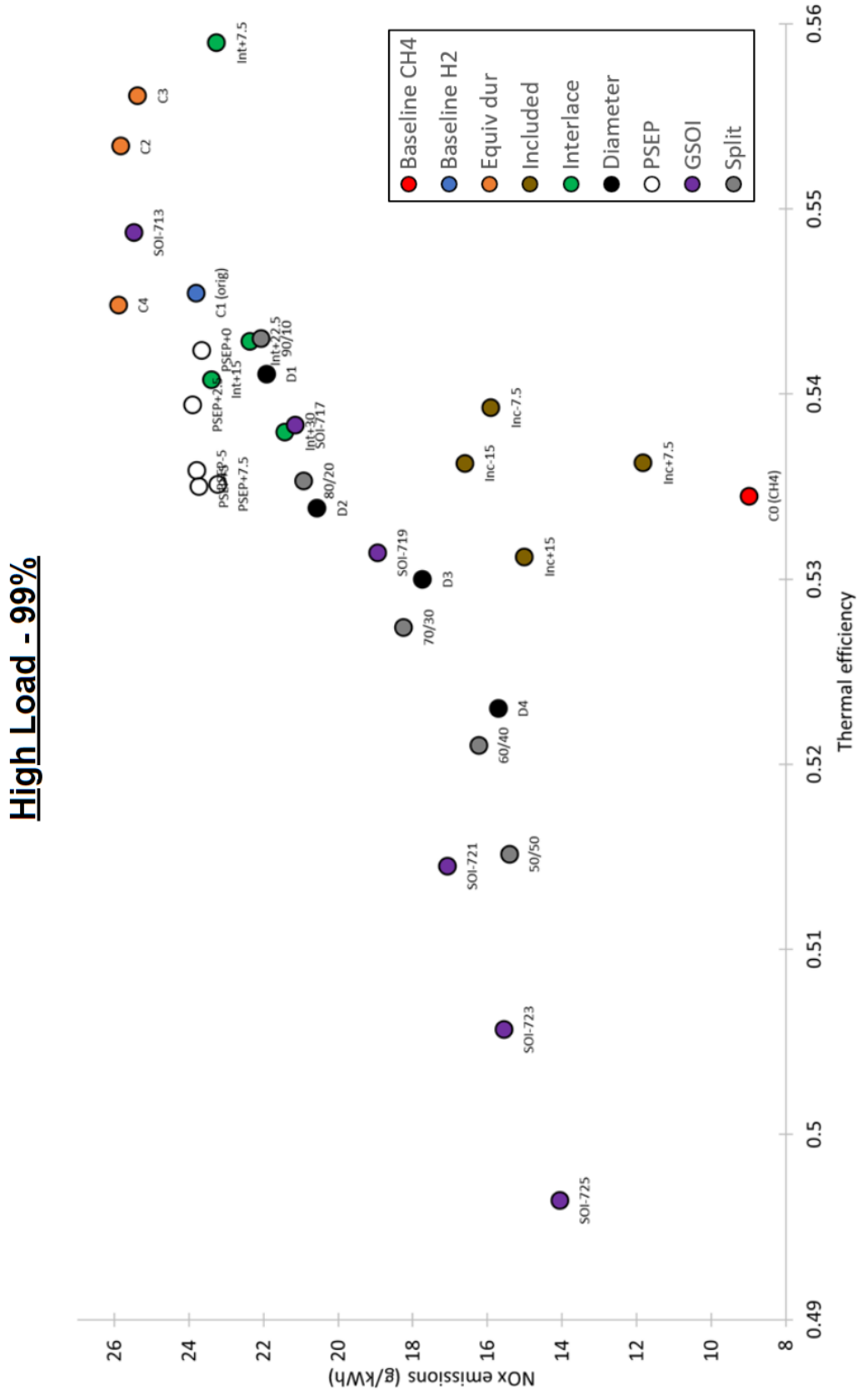

FIGURE 6.12: NO_x emissions plotted against thermal efficiency for the various parameters at HL 99% HES.

TABLE 6.2: Summary of parametric investigations.

Parameter	NO_x	Performance	Comment
Included angle	Potential significant decrease	Potential significant increase	Interaction of gas jet with chamber walls has a significant influence on combustion
Interlace angle	Potential small decrease	Potential small increase	Smaller angles than studied here are likely worth investigation
Nozzle diameter reduction	Significant decrease	Moderate decrease	Reduces mass flow rate which limits combustion rate
PSEP	Potential decrease	Potential increase	Must be optimised based on a given setup/chamber conditions
GSOI	Potential significant decrease	Potential significant increase	Must be optimised based on a given setup/chamber conditions
Split injection increase in 2nd injection volume	Significant decrease	Moderate decrease	Similar to nozzle diameter reduction but offers increased flexibility at the cost of increased complexity
Intake temperature decrease	Moderate decrease	Moderate increase	Increasing temperature can also improve performance if it aids in ignition of the gaseous injection
Intake pressure increase	Small increase	Moderate increase	Intake pressure reduction can reduce NO_x emissions and could be studied further
CVCP	Significant increase	Moderate increase	Can lead to poor gaseous injection combustion, but given further optimisation could be a good strategy

6.4.1 Included angle

When discussing included angle in this analysis we are referring to the relative included angle between the pilot and gaseous injections, Figure 6.13. The original cases use a relative included angle of 0°, i.e. parallel pilot and gaseous injections (at an actual

included angle of 90°). In this study, cases with both diverging (-15° and -7.5°) and converging (+7.5° and +15°) included angles are investigated by changing the angle of the gaseous injection.

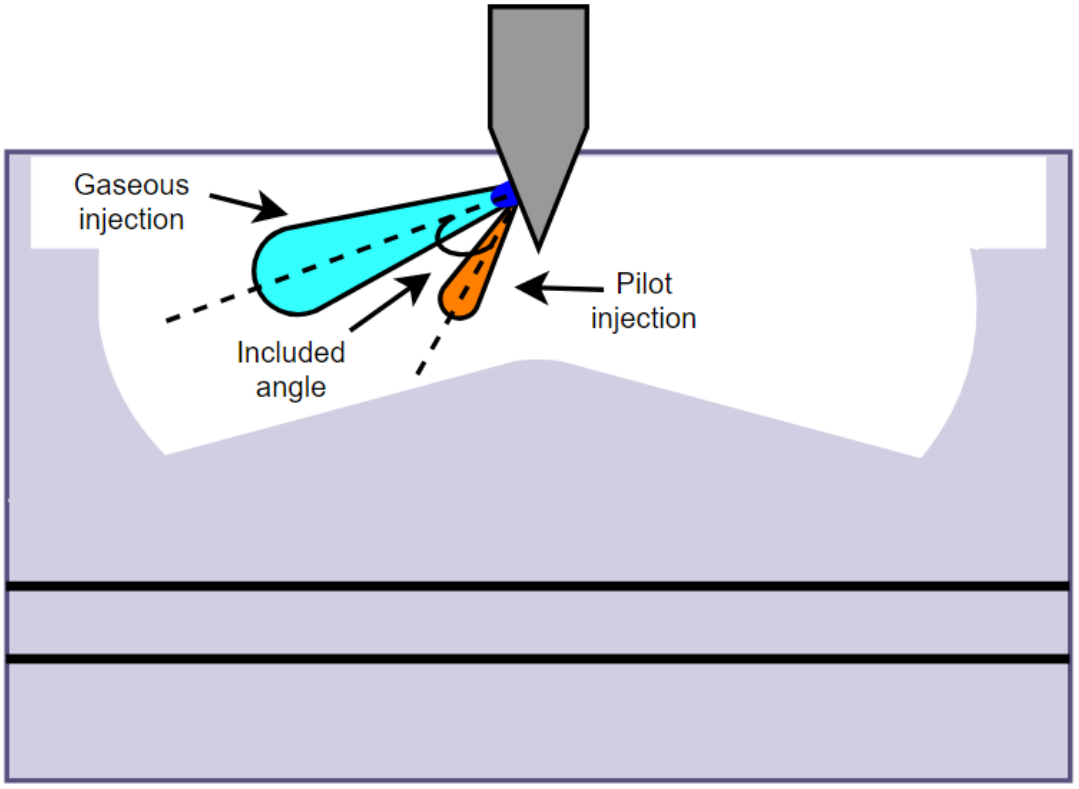

FIGURE 6.13: Relative included angle schematic - viewed from the cylinder centerline-plane.

As shown by Figure 6.14, included angle has a considerable impact on combustion characteristics at both loads. Generally the HRR variations aren't based on interaction with the pilot, but more so interaction of the gaseous jet with the chamber walls. The contours depicted in Figure 6.15 help to explain the differences at the included angles studied.

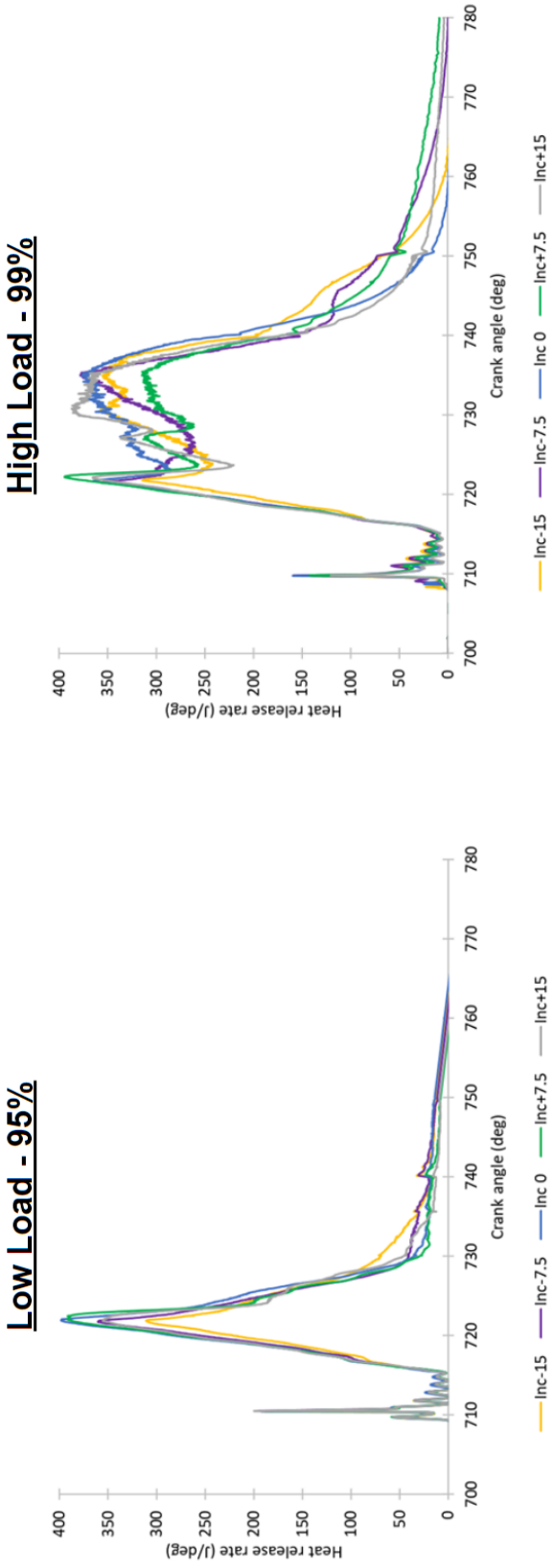

FIGURE 6.14: Calculated HRR for LL 95% and HL 99% HES - included angle.

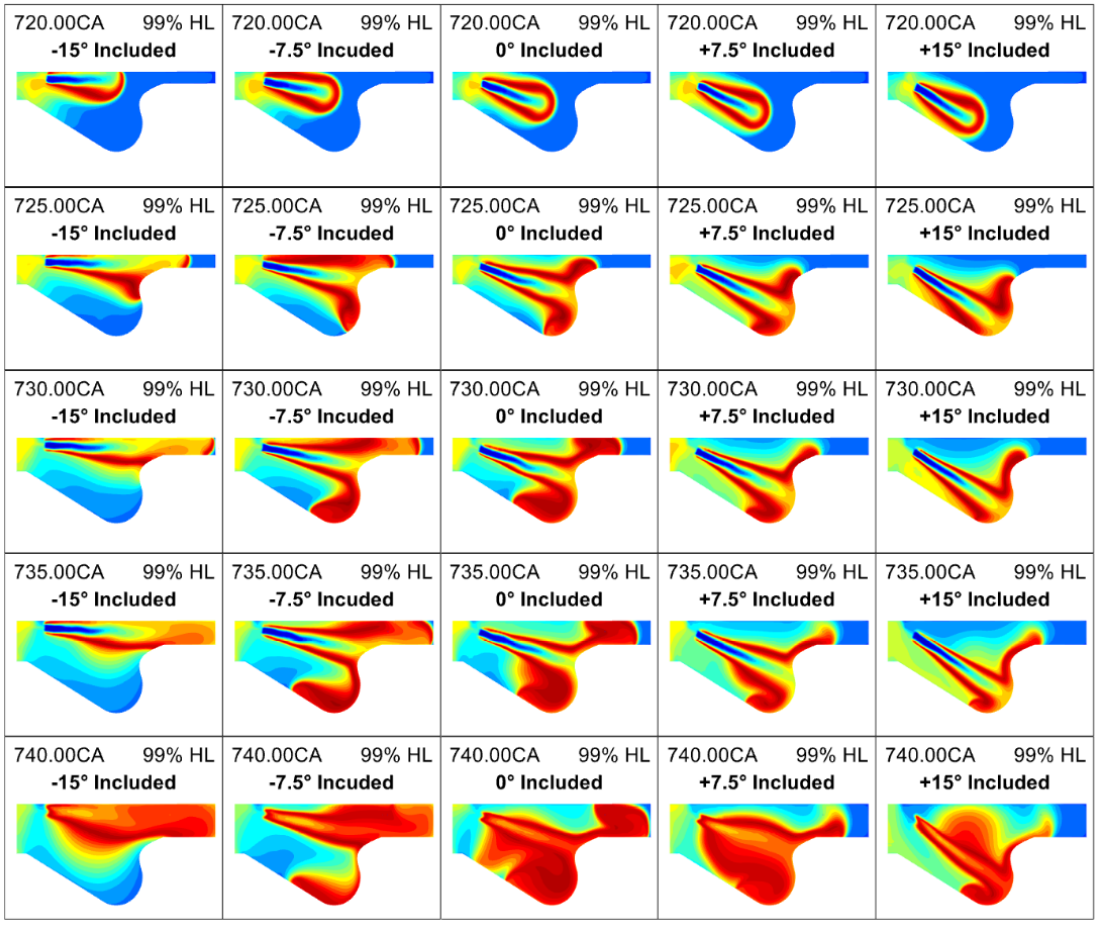

FIGURE 6.15: Contours of temperature for the included angle cases at HL 99% HES.

At -15° the jet contacts the top chamber wall early in its trajectory leading to a quenching of the top half of the flame. As a result a slower initial pressure rise rate is observed compared to the original case (Inc 0) due to the much reduced momentum of the jet and the lower flame width which is then followed by a reduced peak level of HRR for the same reasons. The peak however occurs at roughly the same time as the other cases as the jet still contacts the piston bowl wall/lip at a similar time, quenching the front of the flame. The reduced jet momentum also leads to an increase in dispersion and thus the lower half of the flame is somewhat thicker than the other cases without wall influence which is why the HRR peak and rise rate are still reasonable. The jet and flame then spread into the top gap close to the cylinder liner becoming squeezed and then spreading out laterally along the top wall and liner rather than in the piston bowl like the original case. This process leads to a similar level of heat release during the wall-jet combustion phase when compared with the other cases. There is also a slightly increased HRR just after the end of injection partly due to the generally slower combustion rate previously meaning more fuel is available but also due to the lower jet momentum meaning the jet-jet interaction is somewhat delayed.

At -7.5° there is much less flame interaction with the top wall leading to only a moderate reduction in peak HRR compared to the original case. This is followed by roughly equal amounts of the flame spreading into the top gap and piston bowl regions which leads to a somewhat low initial wall-jet combustion phase HRR as the lateral spreading and thus interaction with other jets is delayed. As the piston moves away from TDC the jet becomes more directed towards the top gap and most of the combustion now occurs in this region. Similar to the previous case the spreading as the jet squeezes into the small gap reduces temperatures compared to the more focussed combustion occurring in the piston bowl in the in some of the other cases. This squeezing aids in the lateral spreading and interaction with other jets begins around the same time as the injection event ends leading to a relatively high peak HRR at the end of the wall-jet phase. As the jet-jet interaction was delayed extra combustion is observed during the fall off in HRR similar to the -15° case.

At +7.5° the free-jet combustion phase is extended somewhat as the jet is directed towards the furthest away portion of the wall. As a result the free-jet flame volume is largest in this case and is quenched the latest leading to both the highest and latest peak HRR. However, this case shows the lowest levels of wall-jet HRR, partly due to more fuel being burned as a free-jet, but also due to the angle of contact with the piston bowl wall meaning fuel struggles to traverse the walls. Thus very little combustion occurs in the top of the chamber and there is a pooling of fuel in the bowl. This pooled fuel in the piston bowl can be seen burning at a high temperature in the 740°CA contour and also in the higher level of late power stroke HRR observed.

At +15° there is some early quenching of the bottom half of the jet with the piston bowl wall which slopes towards the injectors, but less so than the likes of the -15° case with the top wall. This case behaves similarly to the +7.5° case in that there is a long free-jet combustion phase, however, the peak is slightly lower due to the bottom half quenching. Then because of where the jet contacts the bowl wall, there is increased lateral spreading and almost no traversal of the wall in other directions leading to the greatest fall off from peak HRR. Similar levels of wall-jet HRR to the original case are observed after the jet has had time to spread adequately, however, a somewhat faster fall off occurs after the end of injection as the jet momentum reduces and it can no longer spread out.

At both loads the case with the highest performance and highest NO_x is the original (Inc 0). This is a result of the increased jet mobility (angle of impingement with the wall and alignment with pilot induced flow) allowing it to spread both towards the top of the chamber and to the bottom. Increased pilot utilisation is also noted due to the parallel injection allowing for increased entertainment of UHCs. These factors all improve combustion efficiency but also increase combustion temperatures and NO_x. At LL the converging cases (+7.5° and +15°) only serve to reduce performance with little to no reduction in NO_x, whereas, the diverging cases offer considerable NO_x reduction with

further performance penalties. At HL included angle is much more effective with all cases considerably reducing NO_x for only a small reduction in performance. The most effective case is likely +7.5° at HL but this is not a good fit at LL and since included angle is not a parameter which can be varied between loads, the optimal case needs to cater for all. In this regard, -7.5° likely offers the best mix of performance and NO_x reduction. Additionally, -15° may also be suitable, but because of the flame quenching on the top wall much increased hydrogen emissions are observed.

The findings of the included angle study also indicate that engine geometry optimisation is required as the influence of the chamber walls on the hydrogen combustion cannot be understated. Future work should explore this avenue e.g. optimise for more free-jet or wall-jet combustion, lateral spreading, etc.

6.4.2 Interlace angle

Interlace angle refers to the relative angle between pilot and gaseous injections when viewed from the top plane of the cylinder/sector, Figure 6.16. The original cases use an interlace angle of 0°. Four additional interlace angles of 7.5°, 15°, 22.5° and 30° are investigated.

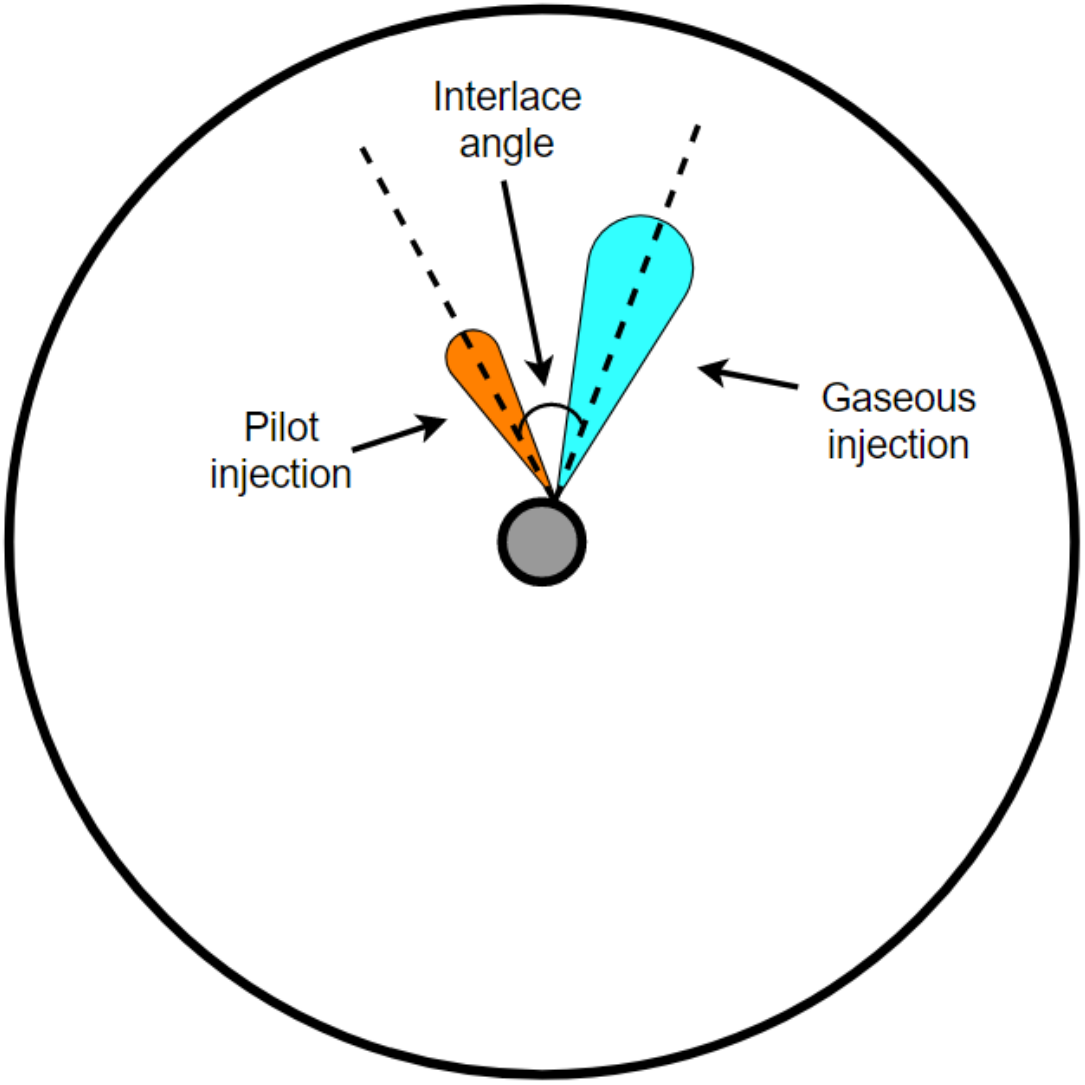

FIGURE 6.16: Interlace angle schematic - viewed from the cylinder top-plane.

Unlike included angle, interlace angle has relatively little impact on HRR as shown in Figure 6.17. The minor differences observed as interlace angle increases are a slightly lower and earlier initial peak HRR but slightly higher peak at the end of the wall jet combustion phase. This is then followed by a faster fall off from the secondary peak which levels off at a higher level than the lower interlace angle cases.

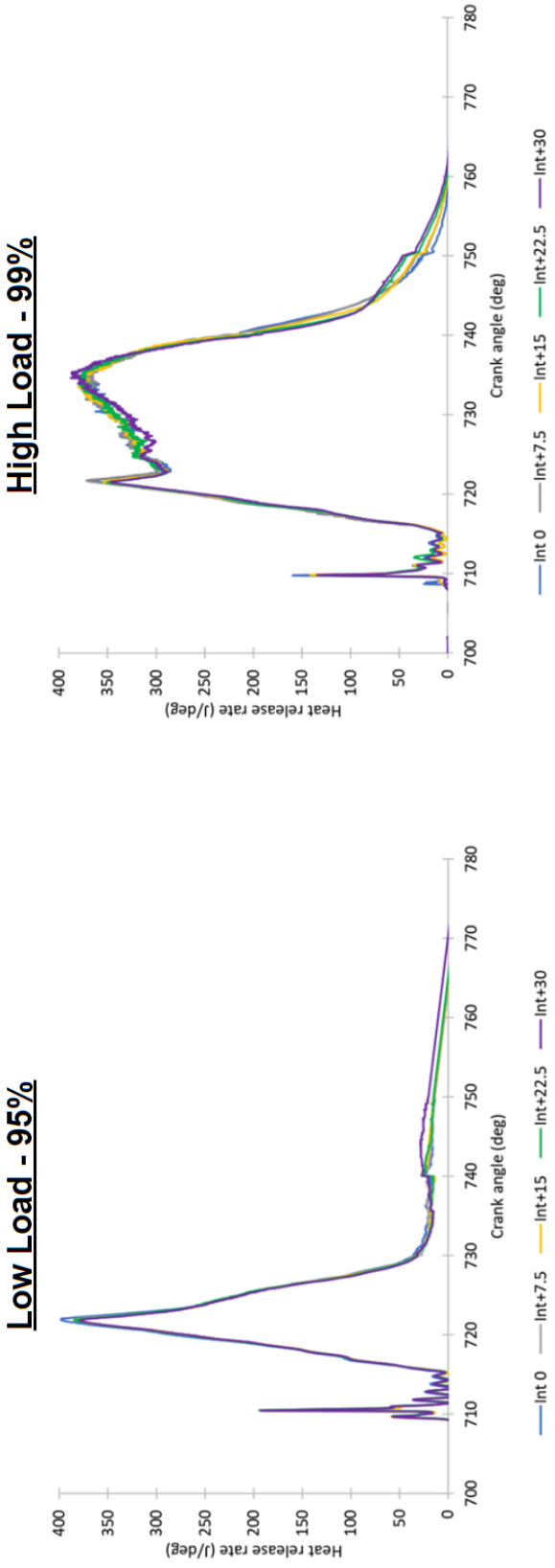

FIGURE 6.17: Calculated HRR for LL 95% and HL 99% HES - interlace angles

The differences can be explained by the temperature isosurfaces depicted in Figure

6.18. As interlace angle increases there is less interaction of the hydrogen jet with the higher temperature pilot combustion region. This reduced overlap slows down the combustion rate and thus the jets momentum somewhat. The jet is also not aligned with the flow induced by the pilot injection or the higher temperature/lower density pilot combustion region, which will contribute to the reduction in jet momentum. It's worth noting that hydrogen's very low density likely also plays a part as it will be more affected by the variation in ambient gas density than other higher density gaseous fuels such as methane. As a result, on impingement with the wall there is less curling up of the jet in the piston bowl and thus movement back towards the injector, but instead more of the jet is pushed into the top gap and towards the cylinder liner. This leads to increased "mushrooming"/squeezing of the jet in the top gap region and a further spreading out of the flame, but decreased temperatures in the injector and piston bowl region. This spreading along the liner side of the cylinder leads to increased interaction with jets from other injectors after the injection ends, whereas this interaction is mostly limited to the piston bowl region in the lower interlace angle cases. The reduced jet momentum somewhat delays the interactions which leads to the slightly higher combustion rate around 750°CA.

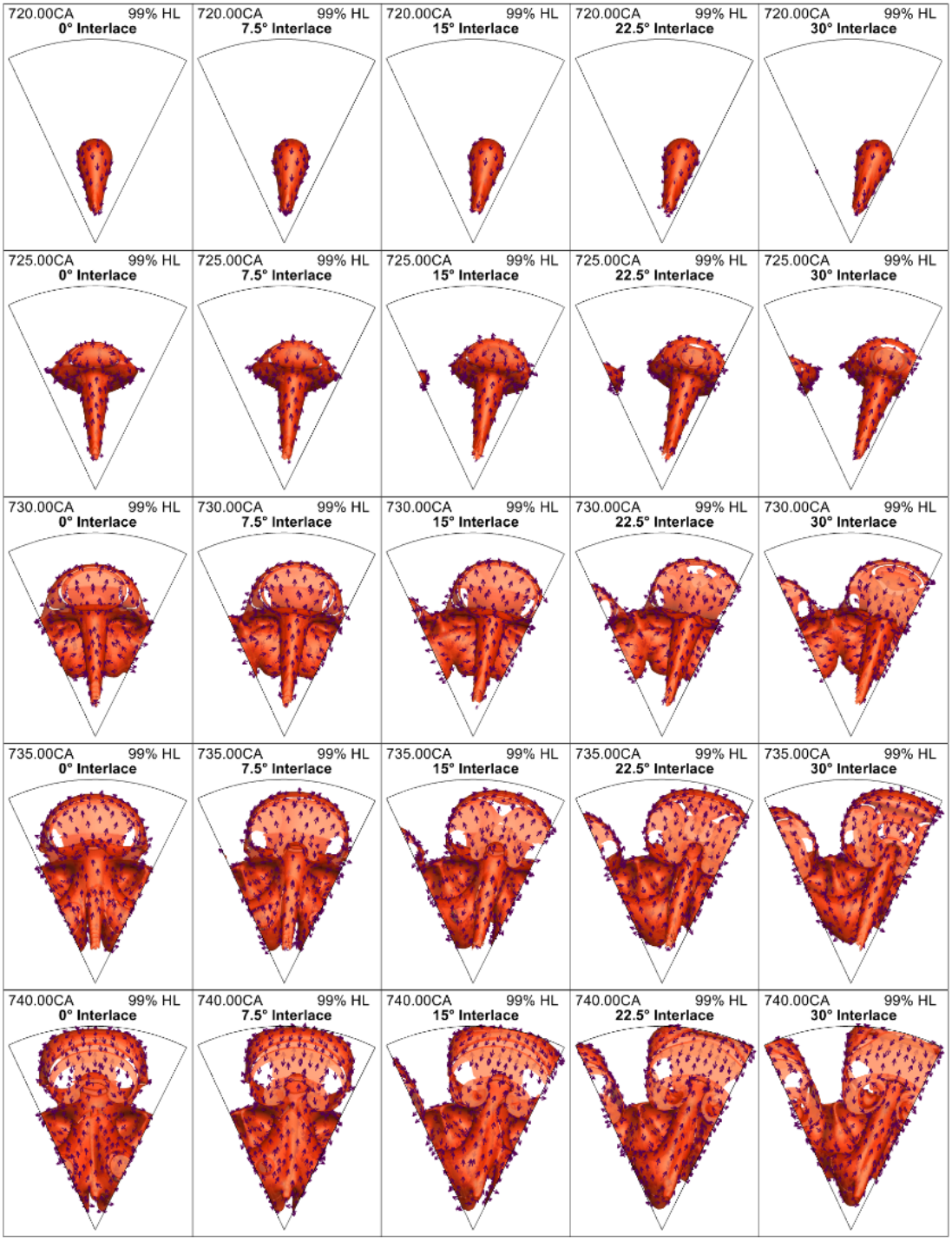

FIGURE 6.18: Temperature isosurfaces at 2500 K with velocity vectors for the interlace angle tests at HL 99% HES.

At LL the original case offers the best performance but highest NO_x emissions which is a result of the parallel injections and higher fuel utilisation due to convection/entrainment of UHCs. When the injections are diverging performance increases between 7.5° and 30° because of the increased jet interaction and combustion rate after the injection has ended (which is generally limited at LL due to reduced jet penetration). Specific

NO_x output actually decreases at the same time due to the combustion not causing too high a temperature increase and the performance increase outweighing any negatives. At HL performance increases at 7.5° but subsequently decreases for any further increase while NO_x reduces in all cases. The increase to performance indicates there is merit to this strategy but also shows there is a fine balance between too much and too little overlapping of the pilot and gaseous injection trajectories. Too little overlap leads to poorer pilot convection and thus soot/UHCs increase and performance decreases whereas too much of an overlap can lead to increased NO_x (original case). Of the interlace angles studied none offer performance increases at both loads but there is promise in terms of NO_x reduction. Results also indicate that smaller interlace angles than are studied in this thesis may be beneficial and thus require further investigation.

6.4.3 Nozzle diameter

Nozzle diameter reduction slows the rate of injection (and therefore increases injection duration) and as a result allows for combustion rate to be controlled, lowering in-cylinder temperatures and thus NO_x emission, while avoiding any potential unchoking of the nozzle which a reduction in injection pressure may cause. Another quality of smaller nozzle diameters is the reduction in the flame volume due to the jet cores smaller width, and as noted previously the flame volume determines peak HRR, meaning combustion will also be controlled in this way. Here 4 additional nozzle diameters are studied which are 0.95, 0.9, 0.85 and 0.8 times smaller than the original nozzle diameter (D1, D2, D3 and D4 respectively). Table 6.3 outlines the nozzle diameter injection parameters while Figure 6.19 shows the calculated HRRs.

TABLE 6.3: Injection conditions for nozzle diameter study.

Case	**Fuel**	**P_0 (MPa)**	**D_e (mm)**	**$\dot{m}$ (kg/s)**	**Energy flow rate (MJ/s)**	**Energy per gaseous injection (J)** 95% HL | LL	97% HL | LL	99% HL | LL
D0	H_2	40	0.577	0.005042	0.6050	1236 | 412	1265 | 422	1291 | 430
D1	H_2	40	0.548	0.004550	0.5460	1236 | 412	1265 | 422	1291 | 430
D2	H_2	40	0.519	0.004084	0.4901	1236 | 412	1265 | 422	1291 | 430
D3	H_2	40	0.491	0.003643	0.4372	1236 | 412	1265 | 422	1291 | 430
D4	H_2	40	0.462	0.003227	0.3872	1236 | 412	1265 | 422	1291 | 430

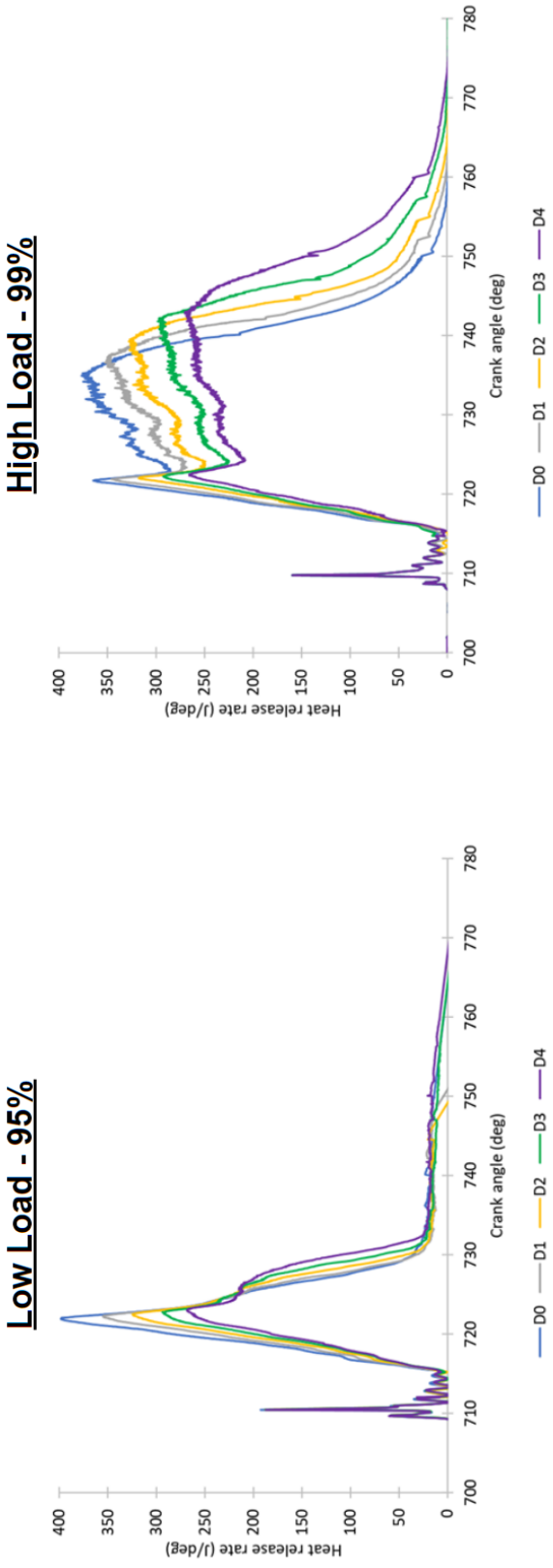

FIGURE 6.19: Calculated HRR for LL 95% and HL 99% HES - nozzle diameters.

Nozzle diameter reduction increases injection duration and also reduces overall penetration length and penetration rate due to a reduction in the jets momentum and core length. The increased duration does a good job at controlling combustion as there is less unburned fuel within the chamber at any one time. The reduced penetration rate also contributes, leading to lower max pressure rise rates (peak HRR delayed) as the free-jet combustion phase lasts longer due to the jets first impingement with the chamber wall occurring later. Peak HRR is also lowered due to a reduction in the max flame volume because of the smaller jet diameter. The lower jet momentum, penetration, diameter and general fuel availability means that combustion rate is slowed considerably during the wall-jet combustion phase. A lower jet momentum also reduces lateral spreading and thus jet-jet interactions are curtailed somewhat. All of these factors serve to lower in-cylinder temperatures and thus much reduced NO_x levels are observed. This also however incurs increases to hydrogen emission due to the worse mixing of fuel and oxidiser and lower temperatures leading to poorer combustion efficiency and performance decreases.

6.4.4 Start of pilot injection timing/duration between pilot and gaseous injection

Pilot separation (PSEP) refers to the time between end of the pilot injection and start of the gaseous injection. When referring to PSEP a negative means prior to gaseous injection and positive after. In this study the naming convention uses the 95% cases separation time in the case names (that is to say the case names aren't representative of the actual timings at 97% and 99% but simply indicate an increasing or decreasing separation). Figure 6.20 shows example mass flow rate profiles for the 99% HL case.

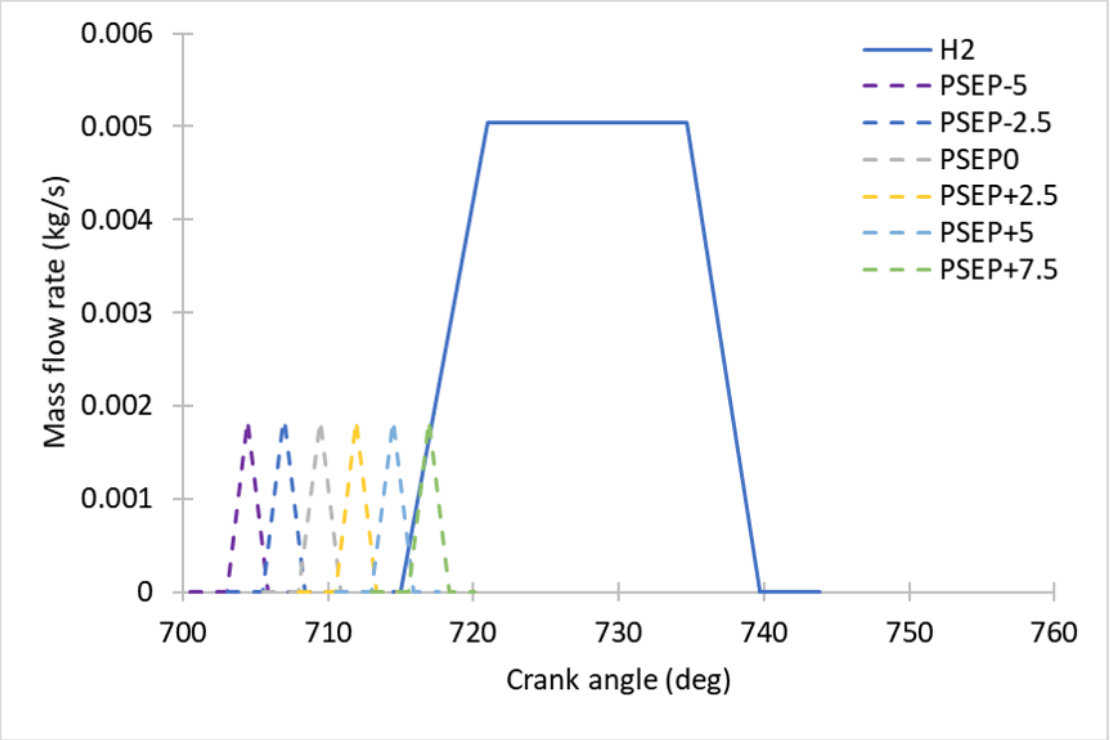

FIGURE 6.20: Mass flow rate profiles for PSEP study - HL 99% HES shown.

PSEP is an integral parameter which can ensure smooth engine operation at high HESs given pilot timing is optimised to give the best chance at igniting the gaseous jet. Figure 6.21 shows the calculated HRR for the 95% LL and 99% HL cases. Delaying the pilot such that it occurs close to or after the start of the hydrogen injection generally leads to unstable combustion due to the increased levels of premixing. Advancing the pilot either increased NO_x levels at HL or again lead to a greater level of premixed combustion at LL due to cooling of the pilot injection area/the area being more offset from the hydrogen injection. We also note that a fairly late pilot injection (after hydrogen SOI) may be required to cause ignition for high HES at LL (see Figure 6.10) without need for further engine modification and thus this strategy could be investigated in future work. Clearly PSEP has the potential to alter combustion characteristics rather dramatically and thus must be included in the later optimisation process. Optimal PSEP will depend on the likes of chamber conditions, interlace/included angle, load, energy share, etc.

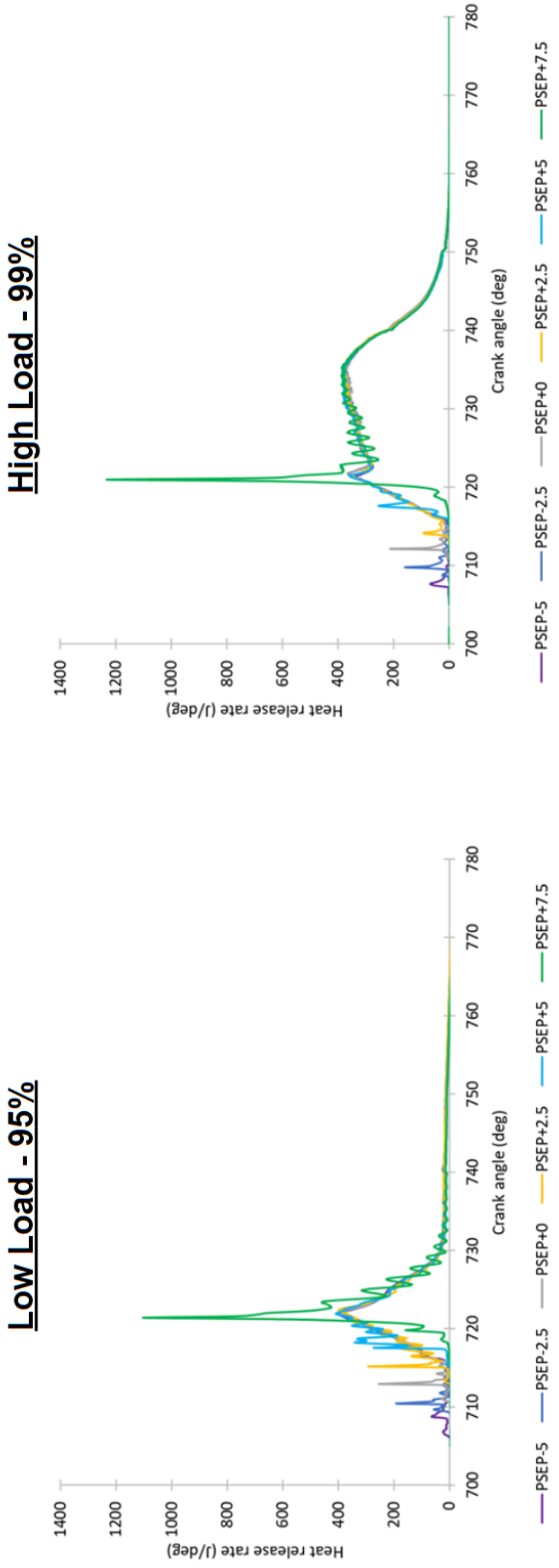

FIGURE 6.21: Calculated HRR for LL 95% and HL 99% HES - PSEP.

6.4.5 Start of gaseous injection timing

Gaseous start of injection (GSOI) plays a major role in engine operation. Figure 6.22 shows example profiles for the HL 99% HES injection timings simulated and Figure 6.23 presents the calculated HRR at HL 99% and LL 95% HES.

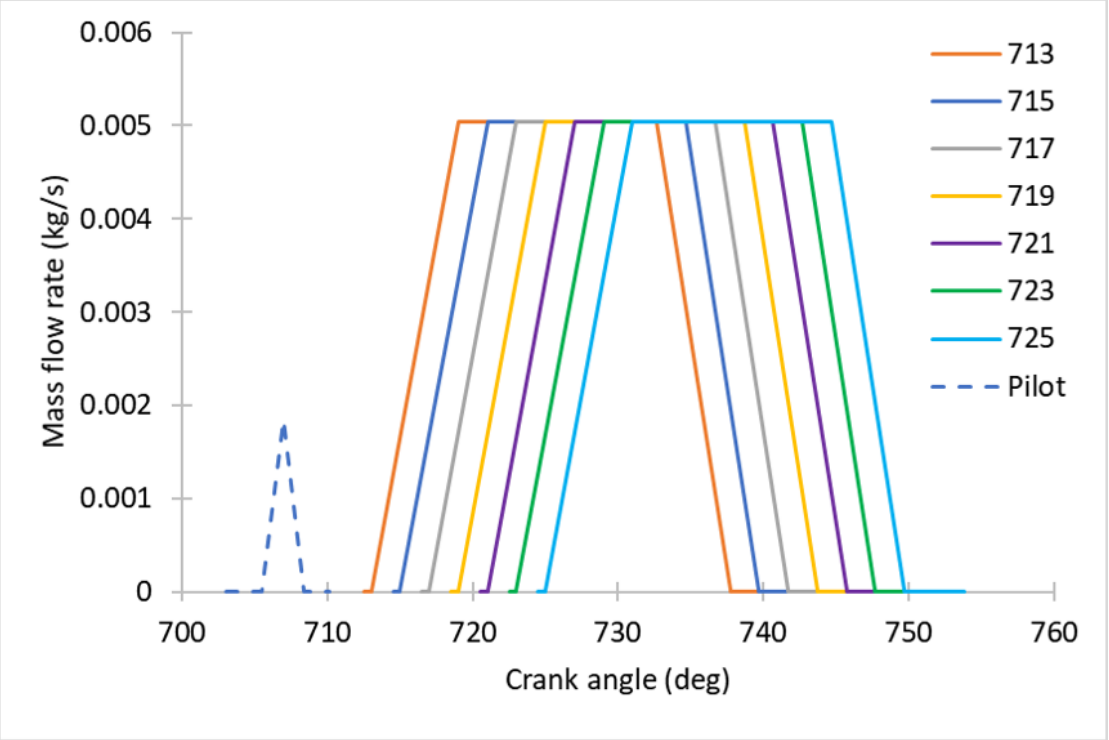

FIGURE 6.22: Mass flow rate profiles for GSOI study HL 99% HES shown.

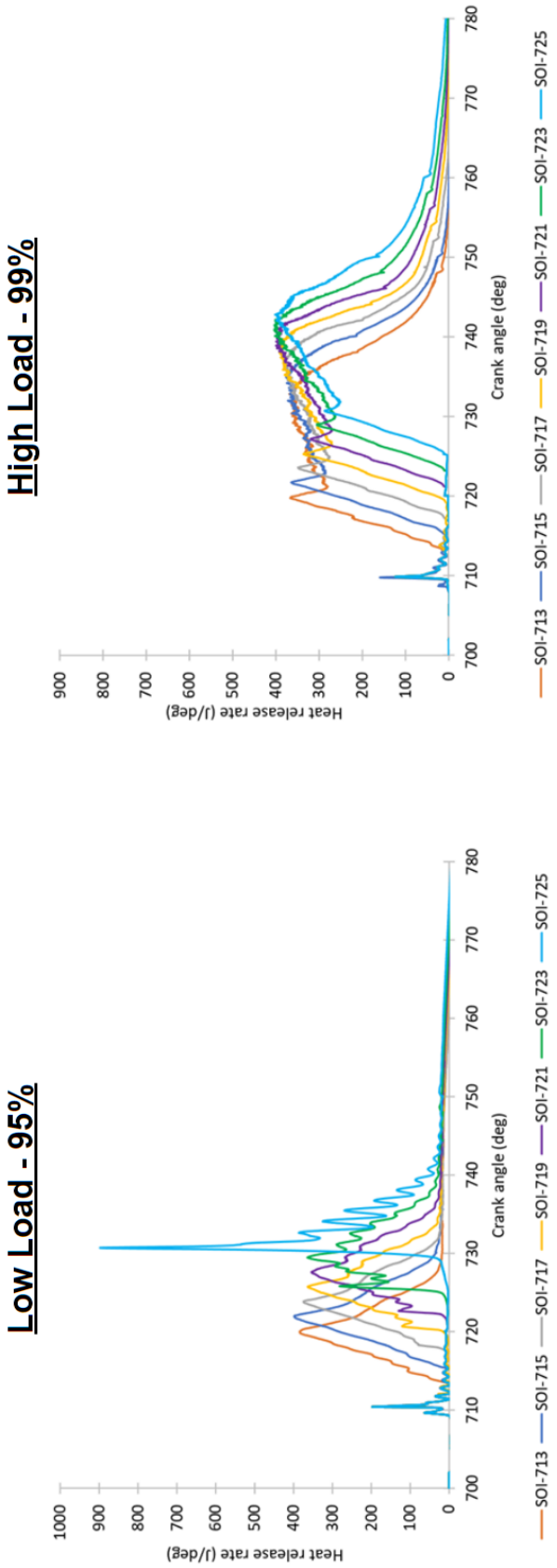

FIGURE 6.23: Calculated HRR for LL 95% and HL 99% HES - GSOI.

At HL delaying the start of the gaseous injection leads to a decrease in the initial peak HRR at the end of the free-jet combustion phase, but an increase in the secondary peak which occurs towards the end of the wall-jet combustion phase. The initial peak HRR reduces due to chamber pressures and temperatures progressively falling lower, as well as there being reduced amounts pilot combustion products available to enhance the hydrogen jet combustion. One of the main factors is the decreasing cylinder pressure which leads to higher Mach disk velocities and longer core lengths as pressure ratio increases (peak cylinder pressure of 15.2 MPa at 713 GSOI vs. 9.35 MPa at 725 GSOI). This means that less mixing of the jet with oxidiser can occur in the initial part of the free-jets trajectory and thus the flame volume is smaller leading to the lower peak HRR. This reduction in HRR is counteracted by the increased jet momentum at impingement which pushes the fuel further along the walls enhancing the mixing of fuel with oxidiser and also leads to a greater amount of interaction with jets from separate injectors, both of which contribute to the increased HRR during this phase. Ignition delay tends to stays almost constant throughout the GSOI sweep with minimal amounts of premixed combustion starting to become apparent at the later injections.

While similar processes are occurring at LL ignition delay increases considerably as GSOI is advanced and the premixed combustion starts to dominate leading unstable operation. There is an initial sharp climb to the first peak observed at GSOIs of 717+ which grows larger as the injection is advanced further as a result of increasingly lower amounts of heat being released from the static pilot injection at GSOI. Similar to HL, there is a decrease in the free-jet combustion peak HRR as pressure ratio increases (excluding the two latest injections) but due to the injection ending before the jets momentum can carry it around the chamber we do not observe the same wall-jet combustion peak as at HL.

Delaying the GSOI is shown to be an effective strategy for decreasing NO_x emissions but also incurs a loss of performance so a trade-off needs to be made. At LL the bigger problem is ensuring the premixed combustion doesn't take over the combustion process and cause unstable engine operation. As the pilot injection was static during these tests PSEP also increased as the injection was delayed which is mostly the reason for this unstable operation. Therefore, a fair test would include a PSEP optimisation sweep prior to a GSOI sweep. The optimal pilot timing would then be advanced/delayed at the same rate as the gaseous injection, keeping PSEP constant, to ensure good ignition and combustion characteristics.

6.4.6 Split gaseous injection-HL 99% hydrogen energy share only

A split injection strategy has the potential to limit combustion rate and reduce areas of locally high temperature as the injection is targeted in more than one area. As LL

already has a short injection duration splitting the injection up would likely mean injector ramp wouldn't finish so it isn't simulated here. It's also clear from the previous tests that HL 99% performs well and thus is the only energy share tested. Figure 6.24 shows the mass flow rate profiles of the split injections studied which range from the original single injection (100/0) to a 50/50 split while Figure 6.25 shows the calculated HRR.

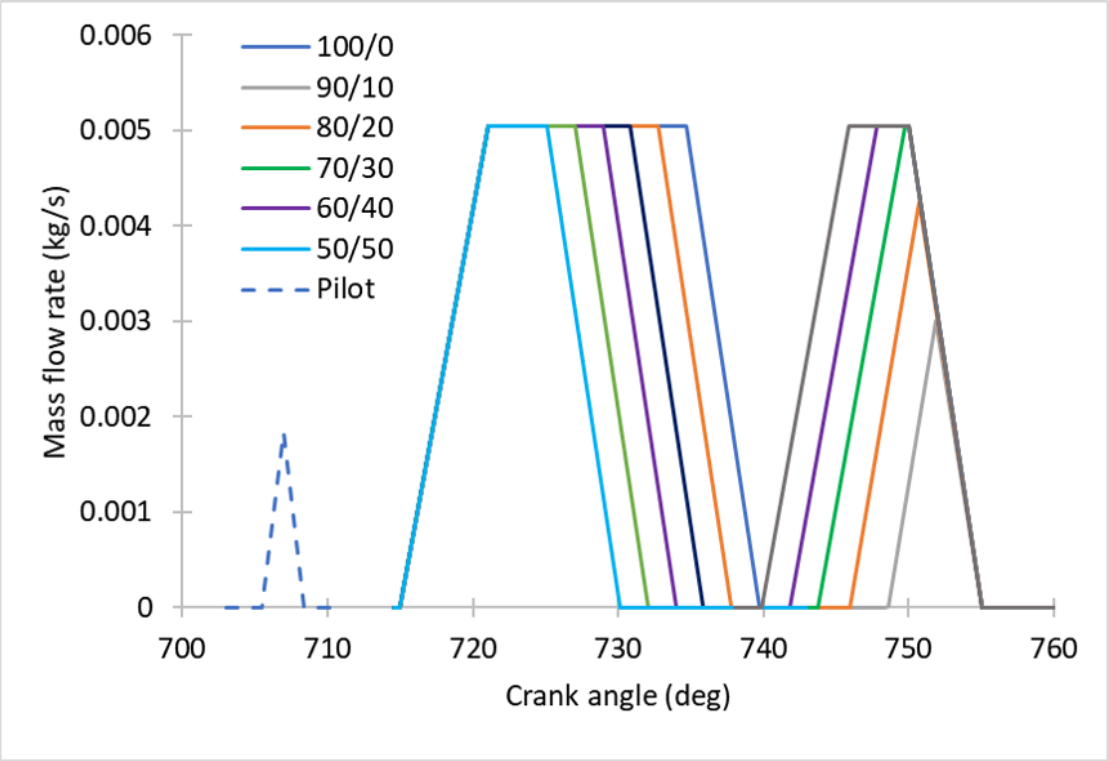

FIGURE 6.24: Split injection mass flow rate profiles for HL 99% HES.

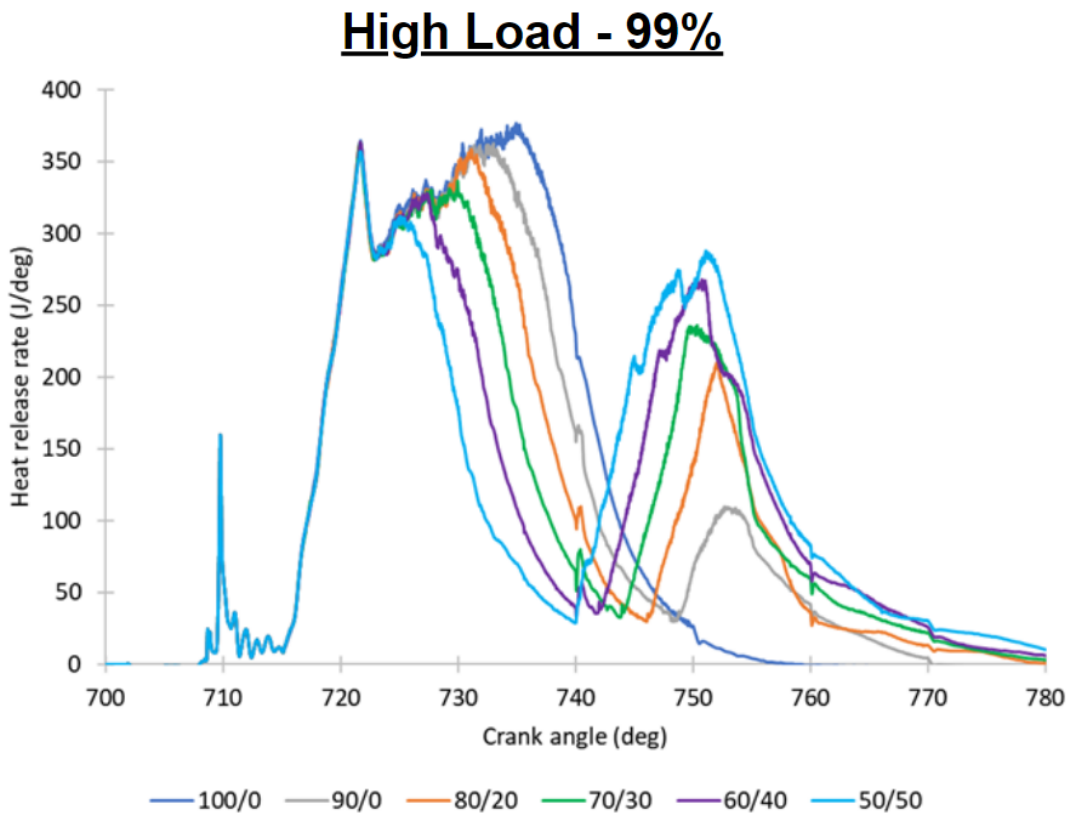

FIGURE 6.25: Calculated HRR for HL 99% HES - split - split injection.

The split injection strategy reduces the amount of combustion occurring at TDC and similar to nozzle diameter decrease also limits the amount of unburned fuel within the chamber at any one time. Peak and average temperatures are reduced as a larger fuel volume is transferred to the second injection leading to a considerable reduction in NO_x. However, performance also decreases (while hydrogen emissions increase) at a similar rate indicating a trade off will need to made. Further investigation of this strategy through varying the gap between injections and further increasing the second injection volume could lead to performance or further NO_x emission improvements.

6.5 Effects of initial charge temperature and pressure at 99% hydrogen energy share

In this section all simulations are carried out using 99% HES at low and high loads with the main goal of improving engine operation at LL while maximising hydrogen energy share. The idea is to identify an appropriate way to utilise the maximum amount of hydrogen at all load conditions with better combustion performance and lower emissions. In the following we investigate the impacts of initial charge temperature and pressure at 99% hydrogen energy share.

6.5.1 Inlet pre-heating/cooling

A number of initial chamber temperatures are tested to investigate their effect on combustion characteristics at both load conditions.

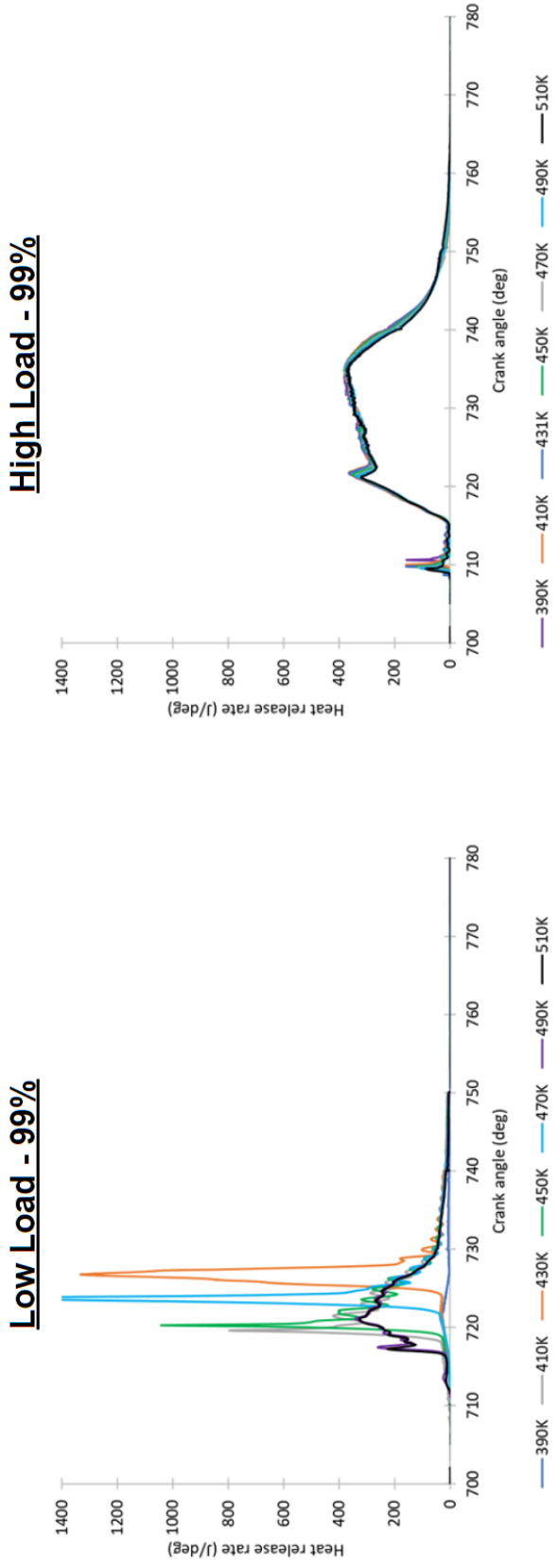

FIGURE 6.26: Calculated HRR for LL and HL 99% HES - inlet temperature.

At LL ignition of the hydrogen jet is poor at higher substitution rates due to the reduced local temperature increase which an extremely reduced diesel pilot can achieve. Therefore inlet pre-heating is used as an attempt to improve combustion efficiency. Figure 6.26 shows the calculated HRR. The results show that increasing the overall temperature of the combustion chamber allows for autoignition of the hydrogen jet rather than relying solely on the pilot diesel combustion as an ignition source. This is evidenced by the sharp rise in HRR as the hydrogen autoignites, causing an initial peak in HRR similar to what would be expected in the premixed combustion phase during diesel combustion after an initial ignition delay phase ($\approx 2^{\circ}$ for the 490 K and 510 K cases) where the fuel has time to heat up and mix with oxidiser. An initial inlet temperature of 490 K, which equates to an average in-cylinder temperature of 1095 K at the start of the hydrogen injection, seems to be the tipping point for when reasonably stable combustion can be achieved as prior to this ignition delays are too long. Further increase to inlet temperature leads to increased NO_x emissions and a reduction in performance, Figure 6.27, due to a lower oxidiser mass and thus reduced overall combustion rate as higher inlet temperatures reduce the intake air density. This shows that it's likely possible to operate a single fuel non-premixed hydrogen engine without need to use a diesel pilot, however, due to the increased overall chamber temperature higher NO_x emissions than desired will be emitted.

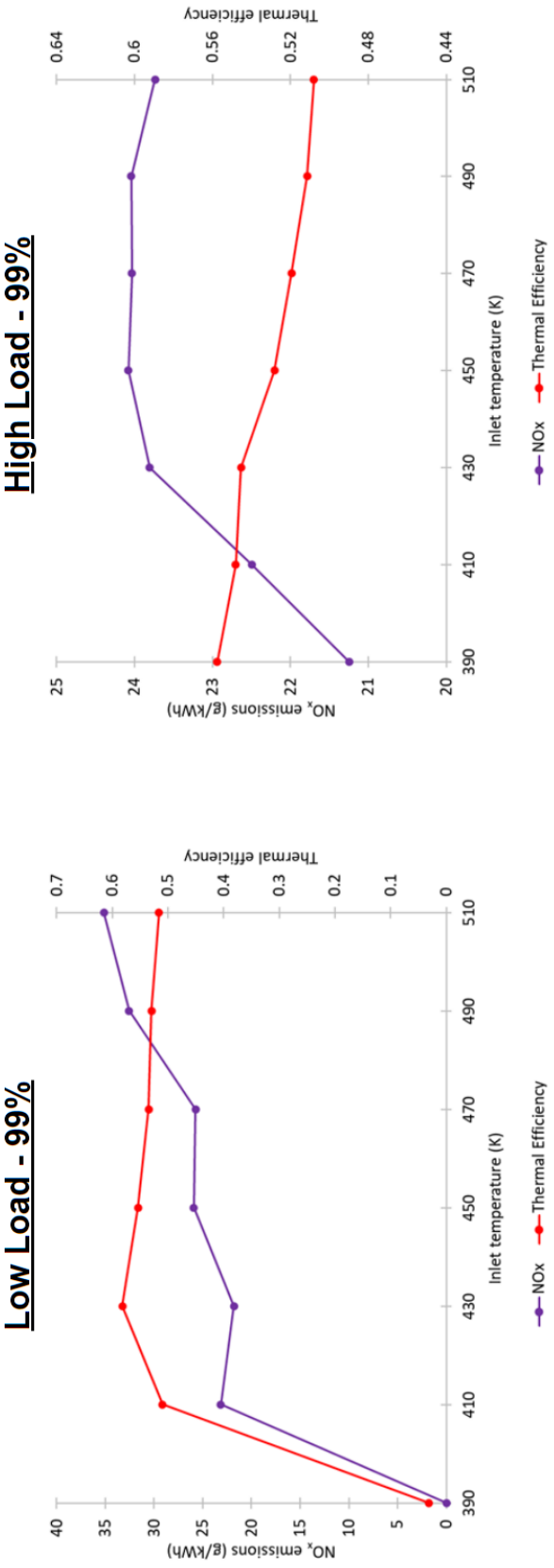

FIGURE 6.27: Calculated NO_x and thermal efficiency for LL and HL 99% HES - Inlet temperature.

At HL inlet pre-heating leads to a reduction in inducted oxidiser which results in generally reduced combustion rates and poorer performance (Figure 6.26 and 6.27). Pilot ignition delay also reduces as inlet temperature increases. The general increase in chamber temperatures leads to increased NO_x emissions which shows pre-heating isn't a good option at HL as improving fuel utilisation isn't required. However, inlet cooling led to the opposite; a reduction in NO_x emissions because of the lower average in-cylinder temperatures but a small increase to performance due to the greater oxygen charge. Further cooling for HL operation could be investigated in future work.

6.5.2 Turbocharging/effective compression ratio

Six different initial intake pressures are tested at each load condition. At HL absolute initial pressures of 3.5, 3.82 (original), 4.5, 5, 5.5 and 6 bar are tested which equate to effective compression ratios of 35.5, 38.7, 45.6, 50.7, 55.8 and 60.8. At LL initial absolute pressures of 3 (original: 30.4 effective compression ratio), 3.5, 4, 4.5, 5 and 5.5 are used. Figure 6.28 shows the calculated HRR for the various turbocharging rates at both load conditions.

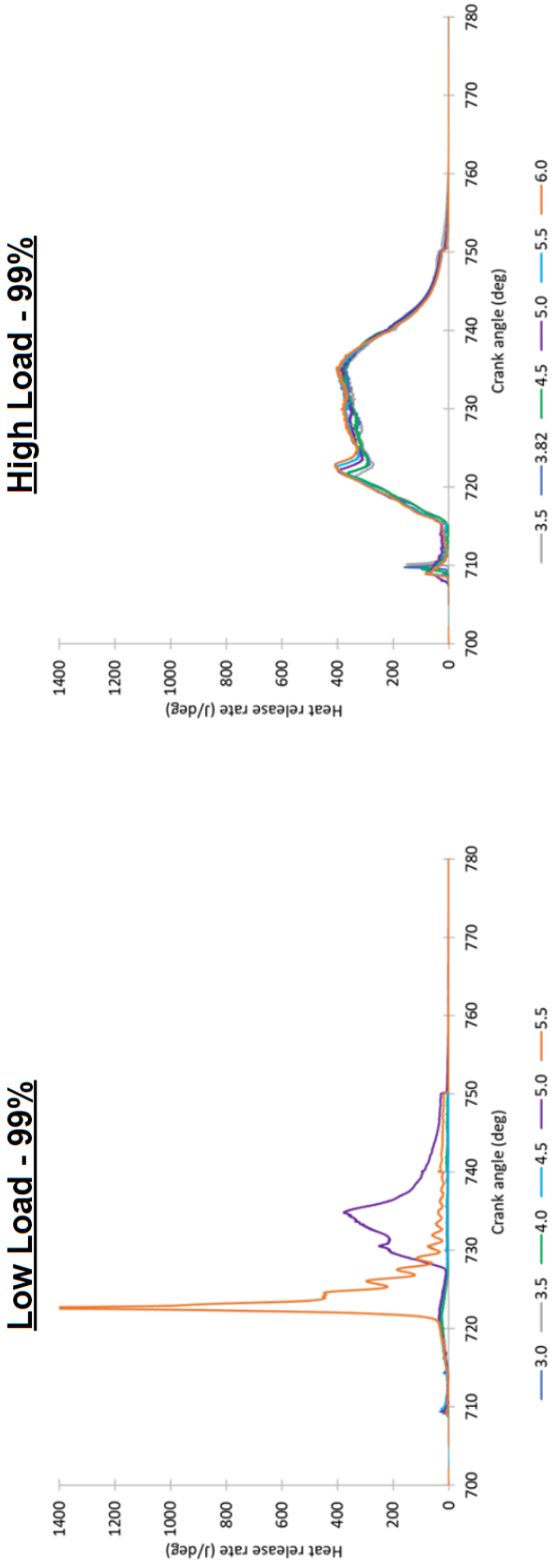

FIGURE 6.28: Calculated HRR for LL and HL 99% HES - intake pressure.

At HL the increased oxidiser levels at higher effective compression ratios lead to a general increase in the combustion rate throughout each phase with higher HRR levels across all phases of combustion. The increased cylinder pressures lead to a reduction in pressure ratio and thus the jets penetration rate also reduces. This is evidenced by roughly equivalent pressure rise rates during the free-jet combustion phase but the peak HRR, when the jet impinges on the chamber wall, occurs slightly later meaning a higher percentage of the combustion occurs during this phase. These factors serve to somewhat control NO_x emissions, Figure 6.29, as a lower penetration rate controls the rate of mixing and jet-jet interactions which in turn somewhat slows the rate of combustion compared to what it would be at a higher pressure ratio. The improvements to combustion efficiency are clearly reflected in the much improved performance while the controlling of the combustion rate means NO_x emissions do not increase significantly. Decreasing the initial pressure leads to a dramatic reduction in NO_x emissions but also leads to a performance reduction and significantly increases carbon based and hydrogen emissions so trade-offs need to be made in this regard.

At LL the increased oxidiser levels improve the pilot combustion leading to enough of a rise in cylinder temperature to cause ignition of the jet at the two highest intake pressure cases. However, combustion is unstable with very long ignition delays observed causing high levels of hydrogen emission. The considerable improvements to combustion compared to the lower turbocharging cases are promising however, and should be beneficial when combined with other strategies aimed at improving operation at LL high HES.

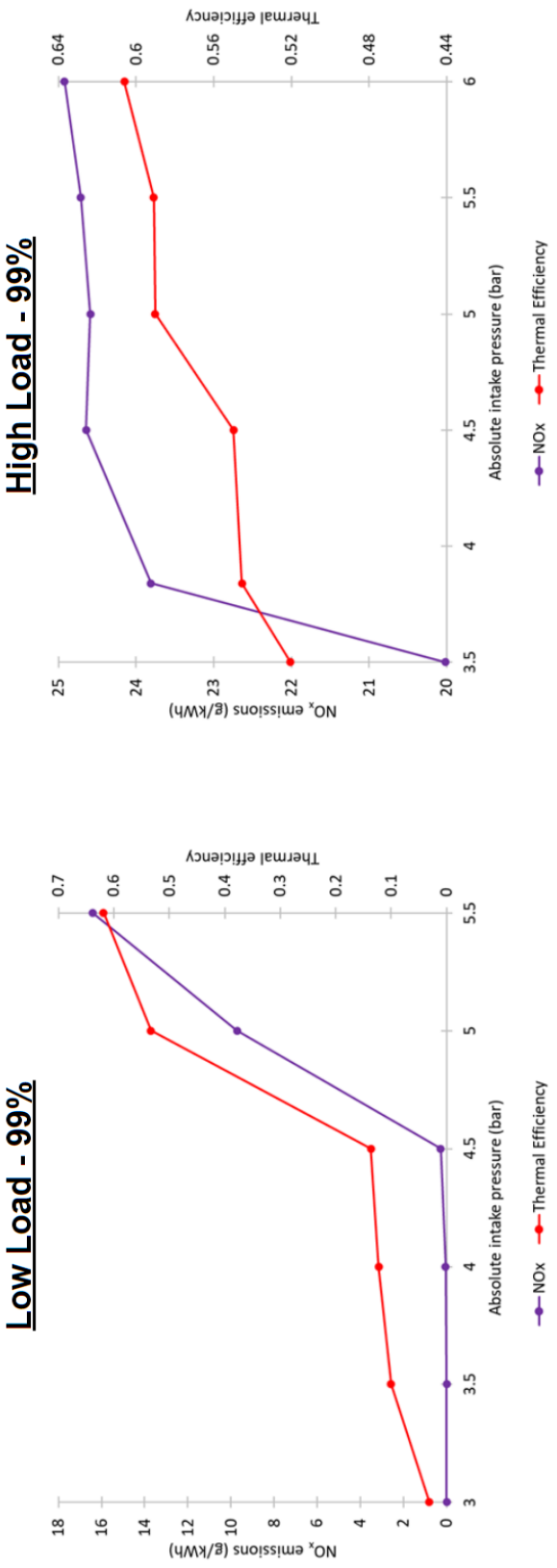

FIGURE 6.29: Calculated NO_x and thermal efficiency for LL and HL 99% HES - intake pressure.

6.6 Optimal conditions for performance and NO_x reduction at 99% hydrogen energy share

Using the knowledge gained from the previous tests an attempt is made to optimise the engine in terms of minimising NO_x while maximising performance and not allowing for egregious increases of CO, UHC, soot and H_2 emissions at both low and high load conditions. A mostly non-premixed mode of combustion is targeted for the gaseous injection as this ensures smooth engine operation. Future work could look to study the impacts of aiming for small-medium amounts of premixing to limit NO_x production. However, this strategy would require a fine balance between many parameters to ensure consistent gaseous jet ignition timing as well as a study on the variance of the ignition timing in multi-hole configurations and thus is outside the scope of the current study.

Exhaust gas recirculation is introduced to further reduce NO_x levels and a constant volume combustion phase is also tested to assess the benefits of the strategy for HPDI operation. Following this, duration between pilot and main injection along with start of the gaseous injection are tested again to find optimal timings at the new chamber conditions. Figure 6.30 provides a summary of the optimisation process.

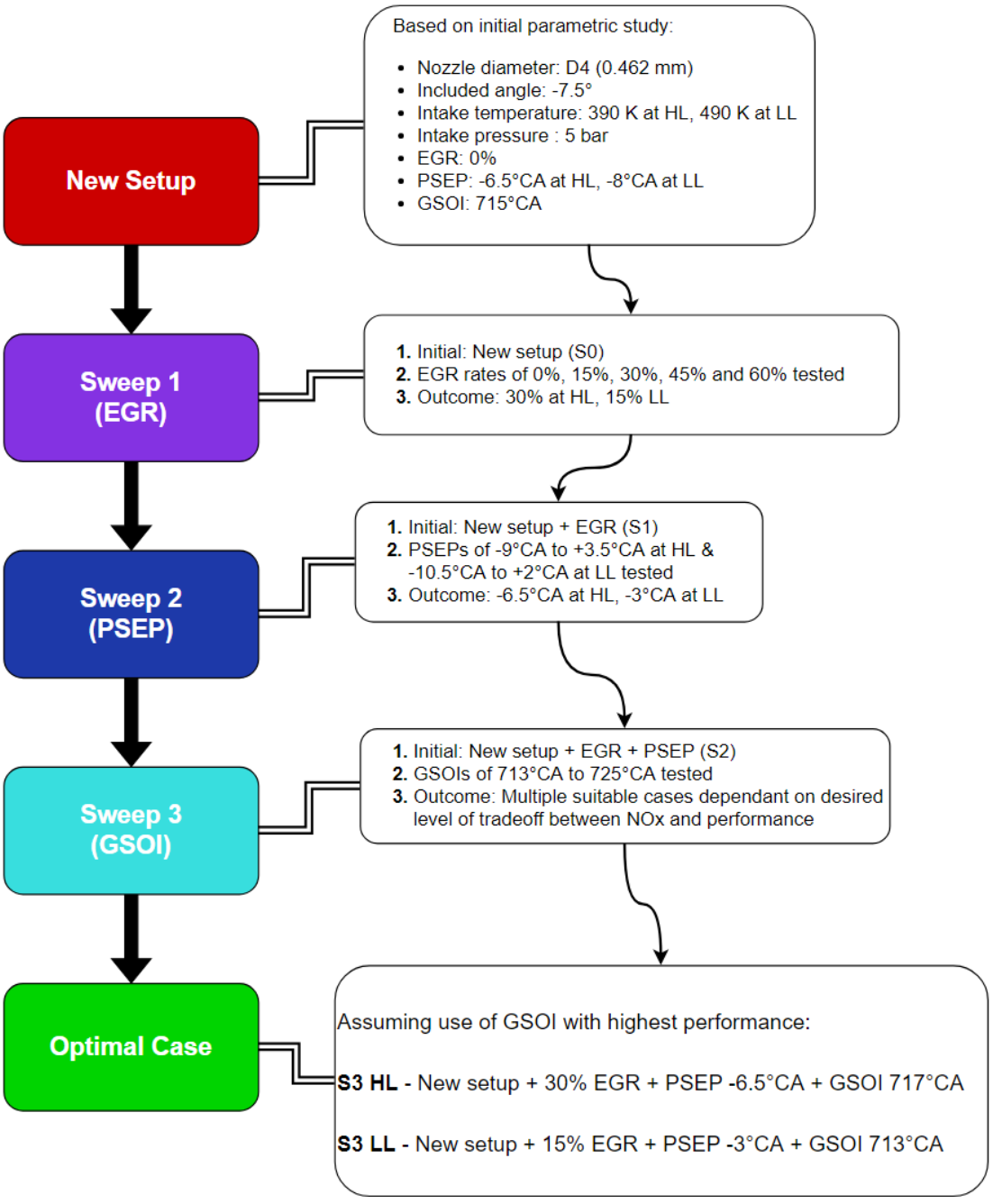

FIGURE 6.30: Summary of optimisation study.

6.6.1 New parameter setup based on previous results

The following section provides reasoning for the specific setup chosen as a starting point for the optimisation study.

Split injection and nozzle diameter reduction offer similar benefits in terms of NO_x improvement without greatly impacting performance. In the proceeding study we choose to use the the 0.8× nozzle diameter reduction (D4) as limiting the number of injection

events (needle opening and closing) should increase the lifetime of a given injector and thus cost/reliability of a system. However, we do note that a split injection strategy offers much more flexibility in terms of engine operation at differing loads and speeds meaning it can be customised to fit a changing injection window (Figure 2.7) unlike nozzle diameter which cannot be altered on the fly. Therefore, depending on the use case, either flexibility or cost/longevity can be optimised for at the design stage.

Delaying the pilot such that it occurs close to or after the start of the hydrogen injection generally leads to unstable combustion due to the increased levels of premixing. Advancing the pilot either increased NO_x levels at HL or again lead to a greater level of premixed combustion at LL due to cooling of the pilot injection area. The optimal PSEP will be intrinsically linked to the the EGR rate due to the change in oxidiser level altering ignition delay as well as the new initial pressure and temperatures used. Thus PSEP change is the second step in the optimisation process after an optimal EGR rate is decided upon and prior to gas start of injection optimisation.

Gaseous start of injection has the potential to reduce NO_x emissions greatly when delayed but does lead to a reduction in performance in doing so. We choose to carry out another sweep of the GSOI as the final step in the optimisation process after the ideal EGR rate and PSEP for a given load is decided upon.

Included angle variation changed combustion characteristics considerably due to interactions of the gas jet and flame with the chamber walls. As injector orientation is a parameter which cannot be varied between loads in a practical engine the same included angle is chosen for both load cases. An included angle difference of -7.5° offered the best mix of performance and NO_x emissions when accounting for both loads and therefore is used for the remainder of the test cases.

Interlace angle lead to relatively little change in combustion characteristics so is left unchanged to allow for easier comparison with previous results (contours etc.). The strategy definitely has its merits however, with improved performance being observed at HL (but reduced at LL) for the smallest interlace angle studied as well as small NO_x reductions at both loads. This indicates that potentially smaller interlace angles may have provided further improvements and thus should be studied in the future. With that said, the flow field which varying interlace angle develops should also be investigated further in a more detailed study of a full combustion chamber with multiple injections as a sector simulation is somewhat limited in this regard.

At HL inlet cooling to 390 K allowed for an increase in oxidiser concentration while reducing average in-cylinder temperatures which lead to an increase in performance while reducing NO_x. At LL inlet heating was required to improve gas jet ignition and fairly smooth operation was found starting at 490 K. These two initial temperatures are carried over for their respective load conditions in the next studies.

Increasing turbocharging level to above 5 bar (effective compression ratio > 50) allowed for improvements to the pilot-diesel combustion leading to much improved hydrogen utilisation at LL. At HL increasing turbocharging level considerably improves performance while only increasing NO_x emissions slightly. For the rest of the test cases a turbocharging level of 5 bar is used due to the noted improvements to performance while ensuring the critical nozzle exit pressure ratio continues to be exceeded and also to make sure the engine remains at realistic conditions. The noted improvements to NO_x emissions at reduced effective compression ratios for HL could also be the subject of further study but is left to future work.

Chapter 4 showed CVCP operation has the potential to increase performance while improving hydrogen utilisation and reducing carbon based emissions. A CVCP phase of 20° duration starting at 720°CA is implemented in the EGR study and compared to the results of the conventional engine.

Exhaust gas recirculation is an effective way to limit combustion temperatures and thus control NO_x emissions. EGR reduces oxidiser levels by replacing part of the inducted air charge with exhaust gases from the previous cycle. Reduced oxidiser levels then mean that there is less available oxidiser for fuel to mix with and thus reduces the rate of combustion. EGR also reduces in-cylinder temperatures and combustion rate through dissociation of CO_2 and H_2O (the main constituents of exhaust gases; mostly H_2O at 99% HES) during combustion and the higher heat capacity of the exhaust gases also causes them to act as a heat sink. When utilising hydrogen many of EGRs negative qualities such as increased soot and UHC emissions as rates increase are much reduced due to a large reduction of carbon being involved in the combustion process and thus also reduced levels in the exhaust gases. Hydrogen's wide flammability limits and high stoichiometric air/fuel ratio should also mean a high combustion quality is maintained even when oxidiser levels are reduced. As a result relatively high EGR rates should be applicable given the reduced quality of the pilot diesel combustion still allows for adequate ignition of the hydrogen jet. Therefore, a sweep of EGR rates up to 60% is carried out and is the first step in the optimisation process.

6.6.2 Sweep 1 - exhaust gas recirculation

EGR rates of 0%, 15%, 30%, 45% and 60% are investigated for both the conventional and CVCP engine cycles at high and low load. Figure 6.31 compares the pressure and HRR for the conventional and CVCP EGR cases while Figure 6.32 presents the calculated NO_x emissions and thermal efficiency.

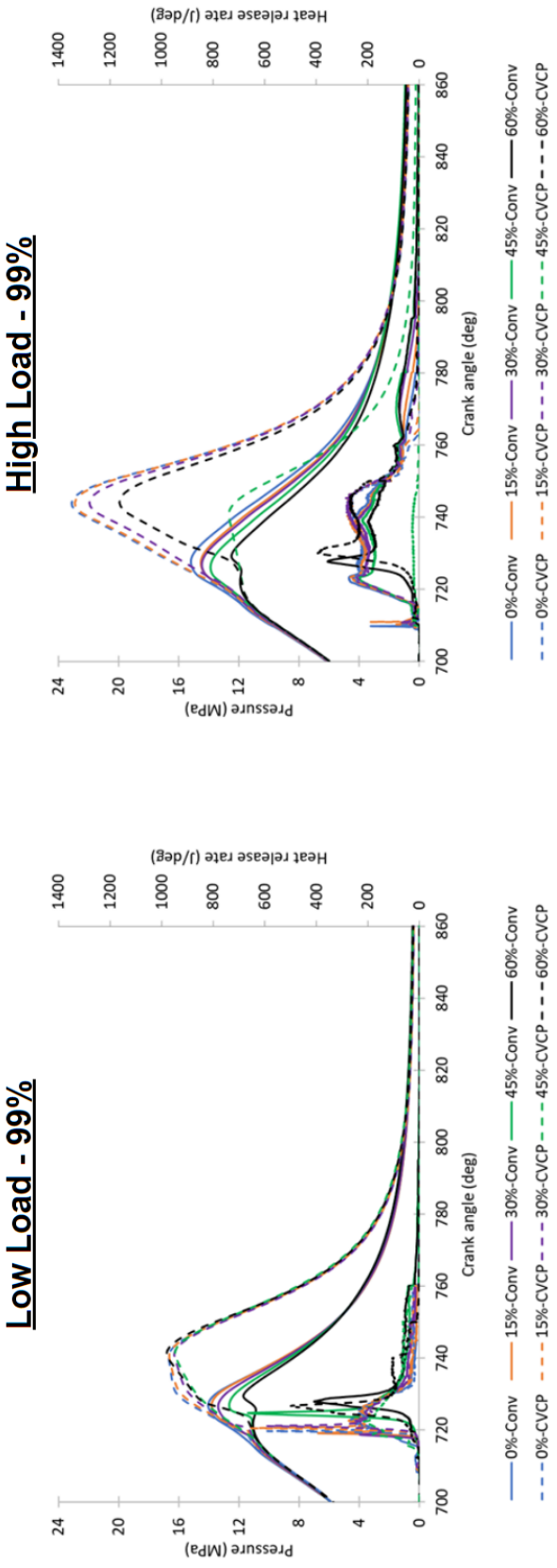

FIGURE 6.31: Calculated pressure and HRR for LL and HL 99% HES - EGR sweep with conventional and CVCP comparison.

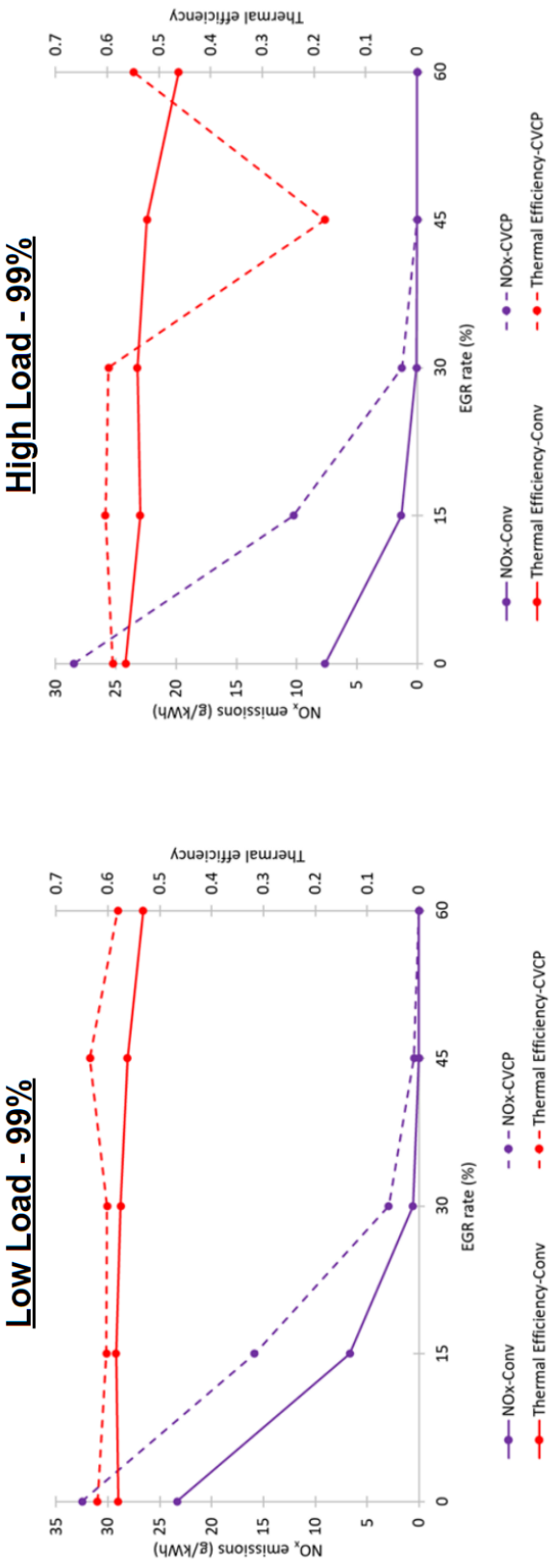

FIGURE 6.32: Calculated NO_x and thermal efficiency for LL and HL 99% HES - EGR sweep with conventional and CVCP comparison.

6.6.2.1 Constant volume combustion phase

CVCP operation did an excellent job at increasing performance in most HL cases while also reducing carbon emissions and improving hydrogen utilisation. This is due to the higher pressures/temperatures and the burning of a greater amount of the hydrogen earlier in the power stroke comparative to the conventional engine. In the conventional engine increasing EGR rate shifts more of the combustion phase into the late power stroke and relies more heavily on the injections interaction with jets from other sectors. While this behaviour is still observed in CVCP operation the initial rapid movement of the piston away from TDC (at 740°CA) greatly increases the hydrogen combustion rate due to a sudden increase of both mixing with oxidiser and jet-jet interactions leading to much less fuel being available for burning later in the power stroke. However, CVCP operation increases the likelihood of unchoking of the nozzle due to high pressures towards the end of the injection/CVCP and increases NO_x emissions by roughly 4-20 times the amount of the respective conventional EGR case. Inconsistent combustion is also observed at higher EGR rates which is a result of the combination of a reduced oxygen charge and lower convection of the hot diesel pilot products due to the stationary piston and lesser pressure ratio causing a reduction in jet momentum.

Unlike in the diesel-hydrogen intake induction engine studied in Chapter 4, CVCP operation does not significantly improve LL operation for the dual-direct injection engine. A considerable amount of premixed combustion and HRR spikes are observed at most EGR rates due to ignition delay increasing considerably. The only exception is at 45% where the EGR increase delays the pilot ignition till roughly the same time as the hydrogen injection leading to adequate ignition. However similar to HL CVCP operation, in general the reduced convection appears to lower the diesel pilots ability to ignite the hydrogen jet leading to ignition delays even longer than most of the conventional engine cases.

CVCP operation is filtered out of the optimisation study at this stage as even with the increased performance and H_2/carbon reduction the NO_x emissions run counter to the goals of the optimisation process and are unacceptable when comparing each EGR rate to their respective conventional case. The added complexity of needing to deal with a much greater pressure ratio variance than in the conventional engine and inconsistent/unstable combustion only cements this decision. To add to this CVCP implementation is not something which can be altered after the design stages and thus must work at all load conditions and the current results show relatively poor low load operation. There is however promise here and a more detailed study entirely focused on improving CVCP operation and controlling the NO_x and injection issues would be conducive. Possible solutions could include either a split injection strategy or a combination of an even smaller nozzle diameter and higher injection pressures, geometry/injector orientation changes to increase swirl, etc. Aside from the previously suggested

improvements for non-premixed combustion, the CVCP strategy would likely also be well suited to an earlier injection strategy where unchoking would not be an issue. That is to say, future investigations could use the findings of Chapter 4 combined with a direct hydrogen injection during the early compression stroke rather than during intake to improve HES and combustion efficiency of dual-fuel premixed operation further.

6.6.2.2 Conventional

In the conventional engine, i.e. the engine without CVCP, at LL the diesel injection only adequately ignites the hydrogen jet at 0% EGR rate where the HRR graph shows little to no premixed combustion occurring much like most of the HL cases previously examined. As the EGR rate increases the reduced temperature of the diesel combustion means that the hydrogen reverts back to autoigniting, similar to the inlet heating cases, as evidenced by the increasing ignition delay and high sudden HRR spikes. It should also be noted that even in the 15% and 30% cases the ignition delay increases by roughly 1°CA compared to the similarly autoigniting original 490 K case, whereas at 0% EGR the quick ignition of the hydrogen jet by the pilot means that ignition delay decreases by about the same margin leading to the almost solely non-premixed combustion. Performance actually increases slightly while NO_x reduces at 15% EGR rate but while NO_x continues to decrease so does performance as the autoigniting combustion mode takes over at the higher EGR rates. Hydrogen emission increases rapidly with the increase in EGR rate and while this may be acceptable due to the reduction in NO_x, the unstable combustion mode is not, indicating that for such a high HES the LL case with EGR requires further work. Since the 15% case shows quite promising performance and NO_x outputs it's chosen for the next stage of the optimisation study where improved pilot timings should be able to improve the ignition delay and unstable combustion problem. The 0% EGR rate could have been carried over to the next stage as it represents the type of engine operation which is desired but the poor NO_x outputs make it a less attractive option than the higher potential 15% EGR case. Clearly however, it's been shown that purely non-premixed jet combustion at LL 99% HES is possible and given further improvements to operation should be achievable at higher EGR rates.

At HL the diesel injection adequately ignites the hydrogen jet leading to the desired non-premixed combustion mode in all but the 60% EGR rate test. At 60% the reduced oxidiser concentration means that the hydrogen jet struggles to ignite leading to gradual low levels of combustion occurring until eventual wholesale ignition of the jet. The full ignition of the jet occurs roughly 7°CA later than the other cases and only shows a slightly higher peak HRR. Hydrogen ignition delay is largely unchanged between 0% and 45% rates and the peaks in HRR also occur at roughly the same time due to jet

impingement timing barely changing, but the peaks themselves decrease. Wall-jet combustion phase HRR also lowers with EGR rate increase but as previously noted, after the injection ends much higher levels of HRR are observed due to more fuel remaining in the chamber and interaction of the jets from separate injectors. The expected trends of NO_x reduction with reducing efficiency and poorer hydrogen utilisation as EGR rate increases is observed. 30% EGR rate appears to be the sweet spot where performance and hydrogen utilisation deterioration has only kicked in slightly while NO_x emissions have decreased to very low levels. Any further EGR rate increase beyond this point incurs considerable performance and hydrogen emission penalties with relatively little NO_x improvement. Therefore, along with the 15% conventional LL case the 30% EGR rate will be carried over to the proceeding studies.

6.6.3 Sweep 2 - duration between pilot and main injection

Six PSEPs are investigated at each load condition. Since only one HES is used in this section the PSEPs have been renamed such that they all indicate the actual separation between the end of the pilot and start of the gaseous injection in degrees. Figure 6.33 depicts the calculated pressure and HRR for the PSEP sweeps and Figure 6.34 shows the calculated NO_x, hydrogen and thermal efficiency.

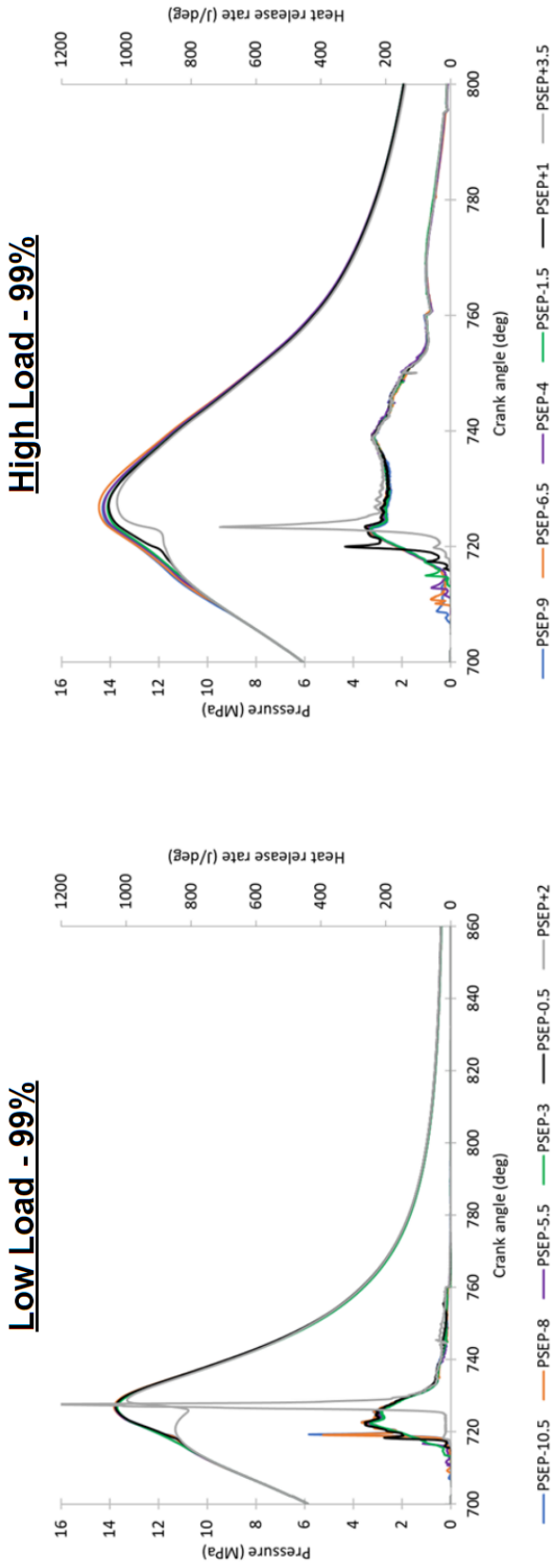

FIGURE 6.33: Calculated pressure and HRR for LL and HL 99% HES - PSEP sweep.

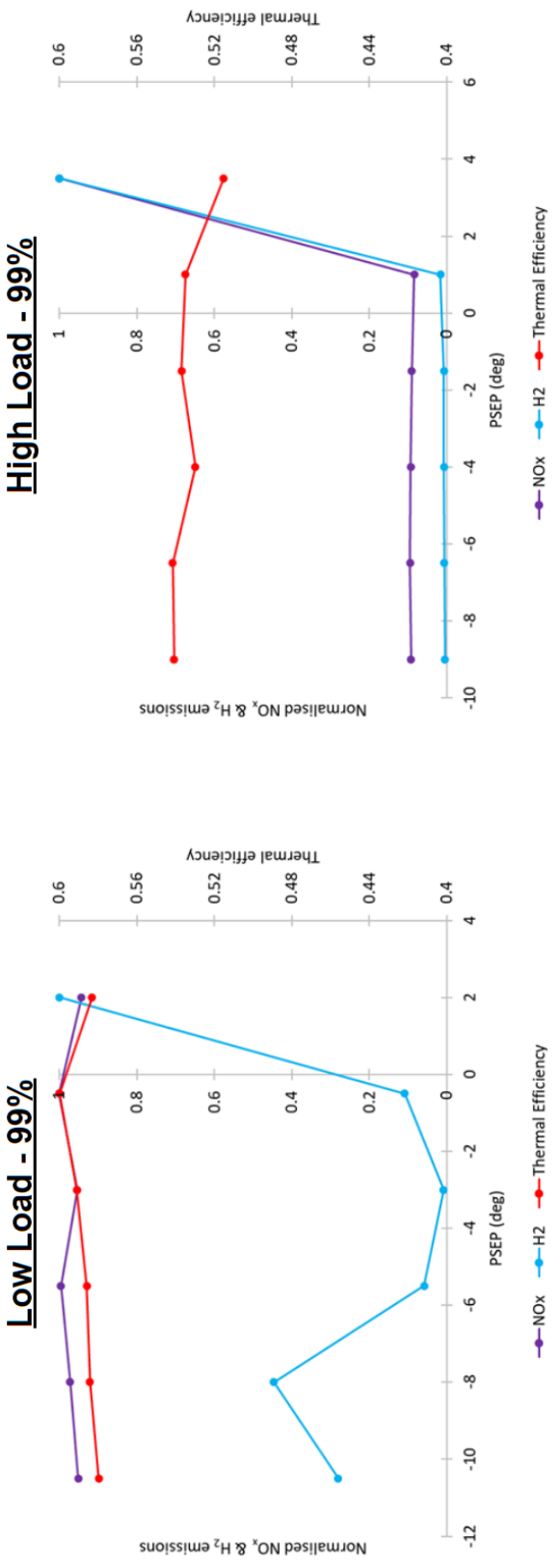

FIGURE 6.34: Calculated normalised NO_x/hydrogen emissions and thermal efficiency for LL and HL 99% HES - PSEP sweep.

At LL 15% EGR rate a PSEP of -5.5°, -3° and -0.5° all lead to good ignition of the hydrogen jet and the combustion stability improves significantly. At -5.5° PSEP there is a small amount of premixed combustion initially but ignition delay of the hydrogen jet is brought down significantly compared to the original -8° case and there is no longer a reliance on autoignition of the hydrogen. At -3° PSEP, due to the pilot's peak HRR occurring as the hydrogen injection begins, the hydrogen jet ignites almost instantly leading to little to no premixed combustion. At -0.5° PSEP the pilot ignites the hydrogen jet well but since there is a reasonable amount of premixing before the pilot combustion begins there is a fairly high initial sharp rise in HRR. This rise is lower than the autoigniting cases (-10.5° and -8°) but considerably higher than the other pilot ignited cases mentioned. When the pilot is advanced further (+2° PSEP) similar results to the previous PSEP study (Section 6.4.4) are observed where ignition of the hydrogen jet is greatly delayed leading to unstable combustion and high peak HRRs. There is a moderate increase to HRR during the free-jet and wall-jet combustion phases in the -0.5° case. This is partly due to a greater amount of diesel combustion occurring at the same time as hydrogen but is also a result of increased convection of the pilot products into the piston bowl region due to the sync up of the two injections. This process enhances the wall-jet combustion leading to lower levels of hydrogen emission but also incurs higher peak temperatures due to the multiple regions containing two burning fuels (close to injector and piston bowl) and high initial HRR spike. The -3° case offers the most stable combustion combined with the lowest NO_x levels of the 3 good cases while only having slightly reduced performance compared to -0.5° so is carried over to the next study.

At HL 30% EGR rate the amount of premixed combustion occurring increases dramatically once PSEP is increased beyond a threshold value of -1.5°. Delaying the pilot leads to unacceptably large spikes in HRR in the +3.5° case as too much premixing has been allowed before pilot combustion ignites the hydrogen jet. A PSEP of +1° shows a similar trend albeit with a much reduced peak compared to +3.5°. The remaining cases (-9°, -6.5°, -4° and -1.5°) all show relatively little premixing and very similar HRR curves excluding pilot timing. The -9° and -1.5° cases show virtually identical free-jet and wall-jet combustion heat release with -1.5° having slightly higher levels for the same reasons as the later pilot LL cases. PSEPs of -6.5° and -4° show the highest peak and wall-jet combustion phase HRRs which are attributed to an optimal mix of diesel combustion close to the injection and convection of hydrocarbons into the piston bowl. The original -6.5° case has the slightly higher peak and cumulative heat release which is mostly a result of the earlier pilot increasing pressure and temperature slightly more. A PSEP of -6.5° offers the best performance and lowest hydrogen emissions with relatively little increase in NO_x emissions so is carried over to the next phase of the optimisation study.

6.6.4 Sweep 3 - start of gaseous injection

All gaseous start of injections at both loads offer relatively smooth engine operation (excluding 725°CA LL) due to the optimal PSEP ensuring adequate ignition of the injected hydrogen before much mixing can occur. Thus operation with low NO_x emissions, reasonable performance and stable combustion is realised at 99% hydrogen energy share across both high and low load conditions. Figure 6.35 presents the calculated pressure and HRR for the PSEP sweeps and Figure 6.36 the calculated NO_x, hydrogen and thermal efficiency.

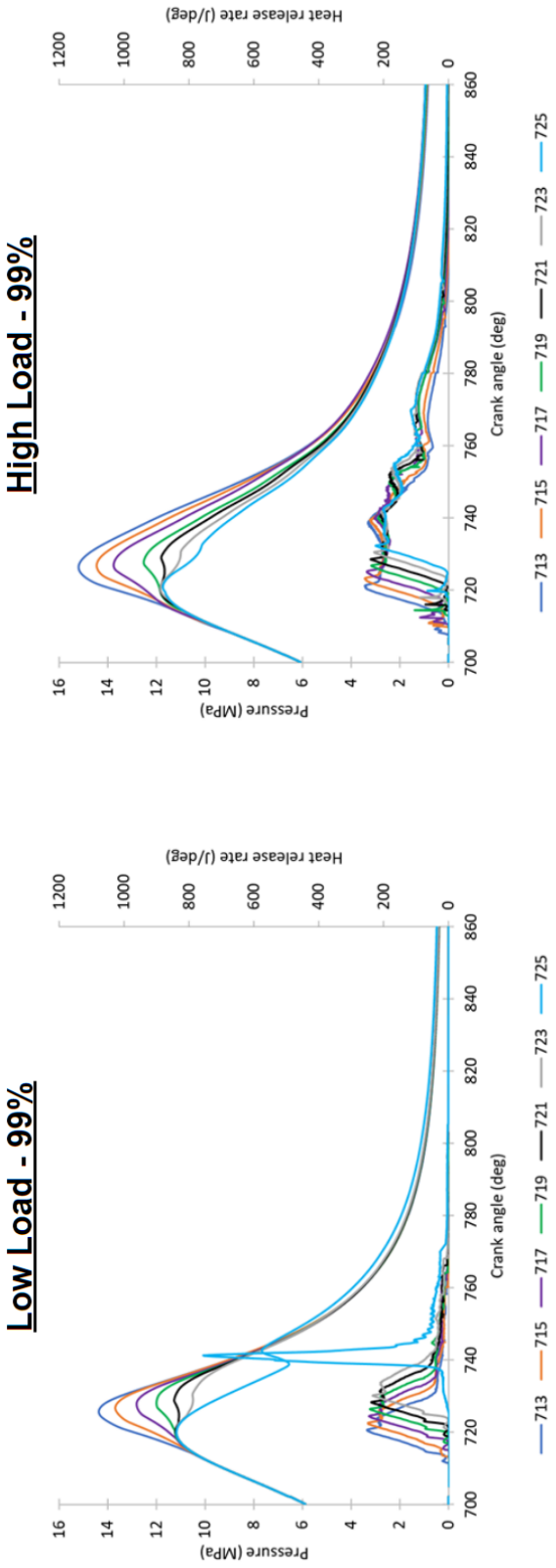

FIGURE 6.35: Calculated pressure and HRR for LL and HL 99% HES - GSOI sweep.

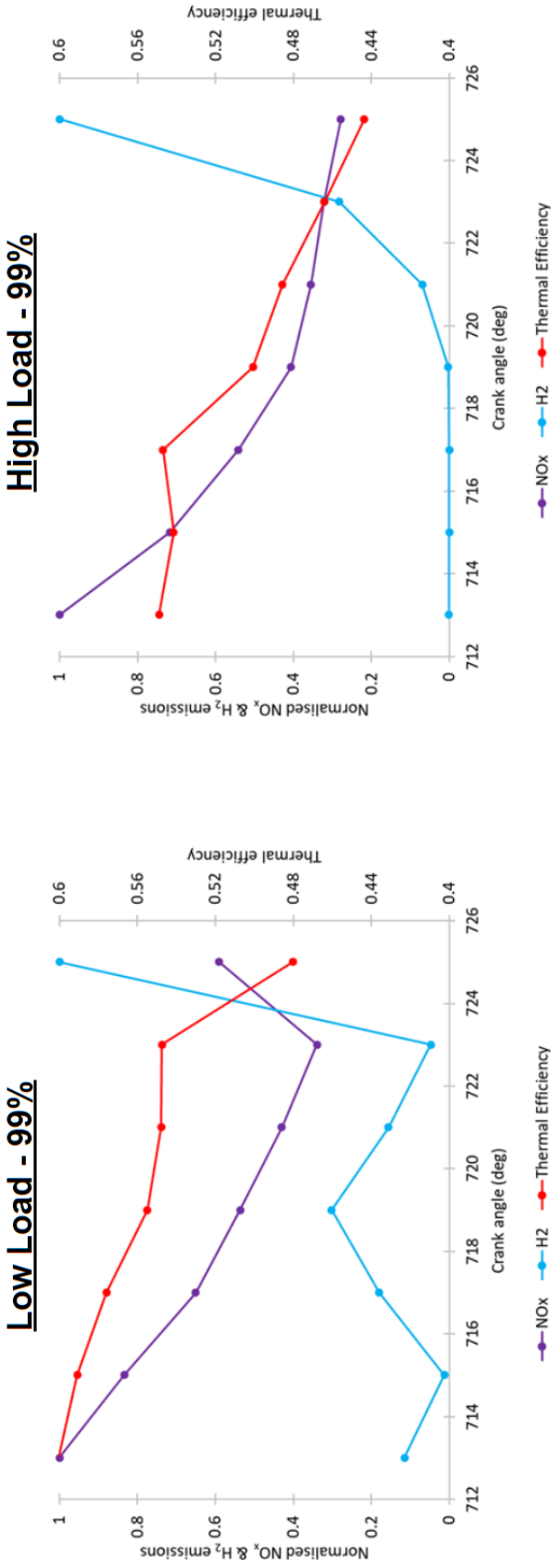

FIGURE 6.36: Calculated normalised NO_x/hydrogen emissions and thermal efficiency for LL and HL 99% HES - GSOI sweep.

Generally, a later hydrogen injection reduces NO_x emissions but also decreases performance and vice versa. Only the LL 725°CA case shows significant deterioration in combustion quality which is due to average cylinder temperatures falling too low as the piston moves away from TDC. At both loads after GSOI is advanced beyond a certain point thermal efficiency begins to fall rapidly and hydrogen emissions climb sharply. At HL 717°CA GSOI offers roughly the best performance while still keeping hydrogen emissions low and NO_x to a moderate level. At LL there isn't a clear best case as the performance and NO_x increase/fall off at a similar rate and thus it's harder to make a tradeoff. For the following analysis the highest performing cases (HL 717°CA and LL 713°CA) are deemed optimal as the NO_x emissions relative to C1/S0 at HL and S0 at LL are very low anyway.

The initial baseline hydrogen case from the original study (C1) is compared with the initial case in the optimisation sweeps (S0), the optimal EGR case (S1) and the optimal EGR + PSEP case (S2) and the optimal EGR + PSEP + GSOI case (S3). Figure 6.37 breaks down the clear improvements provided by the initial parametric study and the following parametric optimisation at both load conditions.

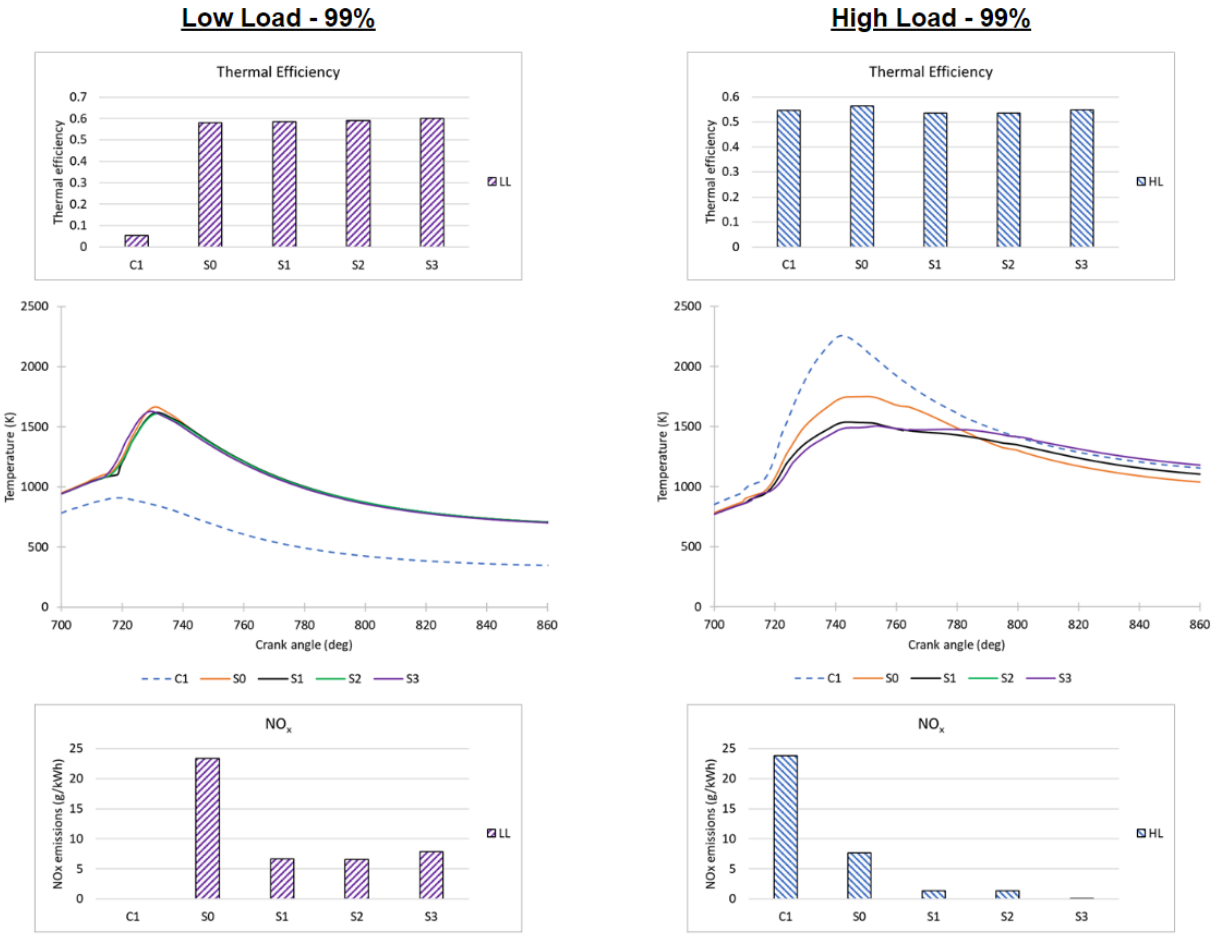

FIGURE 6.37: Calculated NO_x, thermal efficiency and average temperature comparison between original case and each stage of the optimisation sweep.

At low load more of a focus was placed on improving performance as initially little to no combustion occurred in the original 99% HES case, as can be seen in the average temperature graph. Thermal efficiency was increased from 5.4% all the way to 60.0% in the final optimisation sweep while managing to keep NO_x levels to about $1/3^{rd}$ the level they were initially at after the new setup was implemented. Further improvements to NO_x should be possible if higher EGR levels are implemented through finer tuning of the EGR rate, PSEP or the various other parameters to ensure stable operation. Also one of the later GSOI cases could be used in return for a loss of performance as they have already been shown to provide effective NO_x deductions.

At high load performance was already adequate in the original case so more emphasis was placed on improving NO_x emissions. Consistent decreases to NO_x levels were found throughout the optimisation process with the likes of the initial study findings (diameter, inlet cooling, included angle, etc.), EGR and later GSOI all having a large impact on emission with clear reductions in average in-cylinder temperature noted with each parameters addition. Thermal efficiency was also maintained at a high level throughout with the final optimal case having both almost no NO_x emission compared to the original case but also slightly higher performance (54.9% vs. 54.5% for S3 and C1 respectively). Further performance improvement or increased HES could likely be attained through the likes of geometry optimisation and further injection strategy exploration.

6.7 Summary

Diesel-hydrogen dual fuel compression ignition engine operation with dual direct injection at very high hydrogen energy share is investigated via numerical modelling and simulation. Detailed comparisons between methane and hydrogen direct injection are made. This is followed by a parametric study on various key injection and engine operational variables. The findings of the initial parametric study are then applied to a parametric optimisation which aimed to improve high hydrogen energy share (99%) performance/operation and reduce emissions at high load (HL) and low load (LL) conditions.

Key findings are as follows:

1. A non-premixed mode of combustion was targeted through main hydrogen injection after pilot diesel injection close to top dead center. 4 main phases of dual direct-injection non-premixed combustion are identified, namely: a) gaseous jet ignition delay, b) free-jet combustion, c) wall-jet combustion and d) late combustion phases.

2. The ignition delay is generally short leading to very little premixed combustion, i.e. no initial HRR spike/peak which is normally observed in pure diesel operation. This is mostly due to the minimal air entertainment in the jet close to the injector resulting from the compressible underexpanded flow structures.

3. Free-jet combustion follows from ignition and heat release is largely dependant on the volume of the non-premixed flame which the jet forms - peak HRR is realised when the flame is at its largest.

4. Wall-jet combustion begins with the jets first impingement on the chamber wall which quenches the front of the non-premixed flame leading to a reduction in its volume and thus a fall off from peak HRR. This phase is dominated by the interaction of the injected jet with the piston wall. The rate of combustion is controlled now by a combination of a) the momentum of the impinging jet and its ability to traverse the walls and mix with oxidiser and b) the volume of the jet flame (minus the front of the flame which is now quenched). Interaction with jets from other injectors is also likely due to the spreading out along the chamber walls and can enhance combustion rate.

5. The late combustion phase is signalled by the end of the gaseous injection. At the start of this phase the remaining jet core deteriorates until being engulfed by the diffusion flame which also tends to combine with the fuel travelling along the piston bowl walls which is quickly losing momentum, resulting in the fast burning of the remaining fuel which is then followed by a rapid fall off in HRR which remains at a low level until EVO. Again interaction with jets from other injectors tends to enhance the phase's initial rapid combustion process.

6. Due to hydrogen's faster penetration rate (higher speed of sound) than methane, peak HRR occurs earlier, i.e. earlier impingement on the piston bowl wall. Hydrogen also has a higher peak due to the flames greater width and thus maximum value as hydrogen has much wider flammability limits. Wall-jet combustion HRR is also higher for similar reasons as hydrogen can burn at richer conditions (fuel pooling along the wall), has a smaller quenching distance meaning it can burn closer to the wall and also continues to have a larger jet flame. Late phase HRR is lower however, as UHC oxidation is a much slower process than hydrogen oxidation.

7. In general hydrogen combustion leads to much higher NO_x levels than methane but lower carbon based emissions. Performance increases at HL but decreases slightly at LL (in the initial cases studied) due to poorer fuel utilisation at lower temperature conditions.

8. High load operation doesn't deteriorate at hydrogen energy shares up to 99% due to adequate ignition by the diesel pilot. However, at LL operation the diesel pilot volume reduces too much and combustion begins to become unstable with

HES increase from 95% to 97% as ignition delay increases and causes too much premixed gaseous combustion, further increase to 99% leads to little to no combustion of the gaseous jet.

9. Interlace angle can reduce NO_x slightly with increasing angle but generally leads to a similar loss of performance.

10. Included angle impacts NO_x and performance greatly due to interaction of the flame with chamber walls. If the injection is correctly targeted NO_x can be reduced while performance is maintained, the exact angle of which will be largely geometry dependant which also indicates geometry optimisation is key for improving direct hydrogen injection operation.

11. Nozzle diameter is an effective way to limit combustion rate while only moderately reducing performance.

12. Similarly split injection strategies can be used in much the same way.

13. Duration between pilot and gaseous injection (PSEP) is essential for proper engine operation, especially as pilot volume reduces at the likes of LL or and high HES. Optimal timing will be dependant on chamber conditions but ideally peak pilot HRR should occur roughly at the start of the gaseous injection when dealing with very small pilot volumes if a non-premixed mode of combustion is targeted.

14. Given proper PSEP timing is found gaseous start of injection (GSOI) can significantly reduce NO_x emissions when delayed but comes with a tradeoff in performance.

15. Inlet pre-heating can greatly enhance LL high HES performance, while cooling can increase performance and lower NO_x when gaseous ignition isn't of as great a concern because the pilot combustion is adequate, e.g. at HL.

16. Turbocharging increase generally improves performance while not greatly increasing NO_x and can also be effective at LL high HES. Lowering initial pressures can also reduce NO_x emissions in cases where the injection is adequate but will also reduce performance.

17. Constant volume combustion phase can increase performance and reduce carbon/hydrogen emission. However, NO_x increase is inevitable and issues with ignition are observed due to reduced convection, and pressures which may lead to unchoking of the nozzle were noted.

18. EGR is a very effective strategy in terms of reducing NO_x while not greatly reducing performance given an optimal rate is found. In this study at 99% HES, 30% EGR rate at HL and 15% at LL were found to give the best results.

19. Through implementation of the above findings an optimal case was found for 99% HES LL and HL operation which used a smaller nozzle diameter, a diverging (from pilot) included angle aimed close to the top wall, intake cooling at HL/heating at LL, turbocharging increase, EGR, an optimal PSEP and an optimal GSOI.

20. At LL an emphasis was placed on improving performance and engine operation as the original case had little to no combustion. An increase in performance from 5.4% in the original case all the way to 60.0% in the optimal case was found while keeping NO_x emissions relatively low.

21. At HL a reduction in NO_x was targeted as combustion performance was already fairly good. A considerable NO_x reduction was found across all steps in the optimisation process all the while maintaining performance, with the final optimal case showing a slight improvement in performance over the original much higher NO_x case.

22. Exploration of the minimum possible diesel pilot volume required for adequate ignition of the hydrogen jet at various engine and injection conditions should be the target of future work.

23. Further studies should investigate geometry optimisation (and injector orientation as they go hand in hand) as fully understanding the differences and impacts of free-jet and wall-jet combustion in direct gaseous injection operation is pivotal for achieving ideal engine operation.

24. A more detailed modelling approach using resolved injector inlets and potentially LES should be applied to study the flow structures created by the high velocity compressible jet on the air in the chamber, e.g. recirculation zones, air entrainment, convection away/infront of the jet, etc. These are somewhat observed in the likes of the streamline and interlace angle contours presented but this is difficult to study when only using a simplified injector model which doesn't fully simulate the compressible flow structures as well as a sector mesh which can't truly account for jet-jet interaction and their impact on the flow field.

25. As many of the cases examined show unstable combustion modes it would be good to study a full multi-hole configuration to see the variance in combustion of each jet. This way a strategy where little variance between combustion of each individual injection could be optimised for as the current study can't account for this variation.

26. A strategy which has potential and wasn't investigated in the current study is the targeting of some premixed combustion in an attempt to curtail NO_x emissions as hydrogen doesn't produce UHC/soot/CO during rich premixed combustion like diesel. Deciding on the correct amount of premixing which doesn't cause unstable combustion and high hydrogen emission while also being able to consistently

control ignition timing across multiple injections is required, i.e. likely requires multi-hole modelling to ensure little variance.

27. More detailed heat transfer modelling is also required as, with hydrogen especially due to its low quenching distance, there are high temperatures in the near wall regions. Proper optimisation of geometry, injection parameters and materials in this regard will likely aid in operational improvements.

28. Investigation of more parameters regarding the likes of injector orientation should be carried out, e.g. opposing diesel and gas injectors.

29. Comparisons with other fuels, e.g. ammonia or ignition using bio-fuels rather than diesel, etc.

30. More detailed emissions modelling integrated into the chemical kinetic mechanism should be featured in future work.

31. Further experimental investigation is needed for better validation of CFD models also.

Chapter 7

Conclusions

Diesel-hydrogen dual-fuel combustion in compression ignition (CI) engines is an effective way to reduce reliance on fossil fuels, lower carbon based emissions and potentially improve performance. In this thesis detailed numerical investigations of both intake manifold diesel-hydrogen dual-fuel CI engine operation and dual direct injection diesel-hydrogen CI engine operation were carried out. Additionally a low computational cost, accurate high pressure gaseous direct injection model was improved upon and validated for use in engine simulations and applied to the study of a dual direct injection diesel-hydrogen dual-fuel engine.

A novel constant volume combustion phase (CVCP) strategy was applied to an intake induction diesel-hydrogen dual-fuel CI engine and was shown to be an effective solution for the low load issues present during this type of operation. Optimisation of the various parameters controlling the CVCP operation were also carried out. Detailed summaries on the CVCP study can be found in Section 4.3.5 and 4.4.4.

Following this the high pressure direct injection gaseous sphere injection model (GSI) for engine simulations was improved upon and validated. The model proves accurate, easy to implement and computationally inexpensive and could facilitate the further study of direct injection gaseous fulled engines. A summary of the model development and validation is provided in Section 5.5.

Finally, the GSI model was applied to the study of a dual direct injection diesel-hydrogen dual-fuel CI engine operating in non-premixed mode at very high hydrogen energy shares. The combustion process of hydrogen in this type of engine was mapped out and compared to that of the combustion process of the same engine using methane direct injection rather than hydrogen. This was followed by a detailed parametric investigation and parametric optimisation of various relevant engine parameters for high hydrogen energy share at low and high load conditions. Guidelines for operation and a detailed summary of the work are provided in Section 6.7.

7.1 Summary of outcomes

The objectives of the work were met as follows:

7.1.1 Objecitve 1 - develop a physics based gaseous direct injection model to simulate high pressure direct injection of gaseous fuels in internal combustion engines

Model development was carried out on the gaseous sphere injection model which utilises the Lagrangian discrete phase model to simulate gaseous injection for application to engine simulations. Computational fluid dynamic studies are required to fully understand and optimise the combustion process in high pressure direct injection engines, however, the fine grids required to adequately simulate the underexpanded gas jets which tend to result from direct injection make this a difficult and cumbersome task. A distinct lack of numerical engine studies is identified which can mostly be attributed to this meshing requirement and the need to modify the geometry and remesh whenever injector geometry/orientation is altered. The model aims to be far less computationally costly than a fully resolved approach which is generally infeasible for engine simulations while also being easy to implement and accurate. The capability of the GSI model to accurately predict the direct injection of gaseous fuels, such as hydrogen and natural gas, into internal combustion engines has been demonstrated. A change to the core length estimation which determines when gaseous droplets transition to the bulk phase was introduced. An empirical estimate based on recent experimental and numerical data is proposed which accounts for the variation in the jet core length due to total pressure ratio change. Other theoretical estimates are also used to determine injection and discrete phase particle properties. The improved GSI model was implemented into a CFD code and used to simulate the gaseous direct injection process at various engine relevant conditions.

7.1.2 Objective 2 - validate the developed gaseous direct injection model over a range of experimental conditions relevant to engine operation

Validation of the modified GSI model is first carried out via comparison of simulations with experimental studies on underexpanded hydrogen and methane freestream jets injected into constant volume chambers. Freestream simulations are chosen due to their simplicity which allows for penetration and spreading of the jet to be assessed fairly; studies on hydrogen and methane are used to show the applicability of the model to disparate gases. Next comparisons are made to experimental optical mixture formation imaging in a hydrogen direct injection engine. An early direct injection case is

chosen as it isolates the mixture formation process in a realistic engine setup and allows for mixing and flow field development to be assessed. Finally, combustion in a diesel pilot ignited methane direct injection compression ignition engine is simulated and the various combustion and emissions characteristics are compared against the experimental data. A combustion analysis in a realistic engine is carried out as it can be used to assess the performance of the model in its eventual end use-case, showing its wide applicability to the various problem sets.

The improved GSI model performs reasonably well across all cases examined which cover various pressure ratios, injector diameters, injection conditions and disparate gases (hydrogen and methane) while also allowing for relatively coarse meshes (cheaper computational cost) to be used when compared to those needed for fully resolved modelling of the gaseous injection process.

The model is then applied to the study of a dual-direct injection diesel-hydrogen dual-fuel engine and allows for a wide ranging parametric study to be carried out without need to alter the geometry or remesh when injector details are varied.

7.1.3 Objective 3 - perform numerical simulations and evaluate a novel constant volume combustion phase strategy for high hydrogen energy share diesel-hydrogen dual-fuel CI engines

A detailed numerical study was carried out to investigate the performance of a diesel-hydrogen dual-fuel compression ignition engine operating under a novel combustion strategy in which diesel injection and most of the combustion occur at a constant volume. First a detailed validation of the numerical model for diesel-hydrogen dual-fuel engine operation was carried out. From this a parametric study was carried out to determine optimal start time and duration of the constant volume combustion phase (CVCP). Following this a further study was performed to investigate the effects of the CVCP at up to 90% hydrogen energy share (HES) on engine performance and emissions at low and high load with comparisons to the conventional engine. The results demonstrate that the CVCP strategy can improve thermal efficiency at all HESs and load conditions with far lower carbon-based emissions. Conventional dual-fuel engines struggle at low load high HESs due to the reduced diesel injection failing to ignite the leaner premixed charge. Through use of a CVCP thermal efficiency at low load 90% HES increased from 11% to 38% with considerably reduced hydrogen emission due to the increased temperatures and pressures allowing for the wholesale ignition of the hydrogen-air mix. It was also found that increasing the time allowed for combustion within the CVCP, by advancing the diesel injection, can lead to even further thermal efficiency gains while not negatively impacting emissions.

7.1.4 Objective 4 - perform numerical simulations and generate novel operational strategies for very high hydrogen energy share diesel-hydrogen dual direct injection CI engines

A distinct lack of experimental and numerical investigation into dual-direct injection diesel-hydrogen dual-fuel engines operating in non-premixed mode was noted. As a result, diesel-hydrogen dual fuel compression ignition engine operation with dual direct injection at very high hydrogen energy share was investigated via numerical modelling and simulation. Detailed comparisons between methane and hydrogen direct injection were made. This was followed by a parametric study on various key injection and engine operational variables. The findings of the initial parametric study were then applied to a parametric optimisation which aimed to improve high hydrogen energy share (99%) performance/operation and reduce emissions at high and low load conditions.

Four distinct phases of combustion were found which differ from that of pure diesel operation. Interaction of the gas jets with the chamber walls is discovered to be by far the most important factor in this type of engine operation. When combined, the likes of nozzle diameter reduction, split injection strategies, gaseous injection included angle, timing between diesel pilot and gaseous injection, start time of gaseous injection, inlet pre-heating/cooling, turbocharging and EGR were all found to be effective ways to improve performance and combustion stability/consistency while increasing hydrogen energy share and reducing NO_x emissions at both high and low load. Very low carbon based emissions were also noted when compared to that of diesel-methane operation. The various results and insights which the study provides can be used to guide any further investigations on this type of engine.

7.2 Summary of novel fundamental scientific contributions

The key original findings of the thesis are outlined:

1. A novel combustion strategy utilising a constant volume combustion phase was applied to the operation of a pure diesel engine as well as both an intake manifold and direct injection diesel-hydrogen dual-fuel engine.
2. The CVCP strategy was shown to be a potential solution to the poor low load operation issues which plague intake induction diesel-hydrogen CI engines when hydrogen energy share is increased.
3. Improvements were made to the GSI model for high pressure direct injection of gaseous fuels. Validation and application to practical flows were carried out and the model proves accurate, computationally efficient and easy to implement.

4. One of the first studies on dual direct injection diesel-hydrogen dual-fuel operation targeting non-premixed combustion in a CI engine was carried out.
5. The combustion process and flow induced by the hydrogen injection is mapped out in detail.
6. The study on direct hydrogen injection is the first to explore various engine parameters and perform a parametric optimisation.
7. Guidelines for optimal operation of a dual direct injection diesel-hydrogen dual-fuel CI engine operating in non-premixed mode are provided, details for how each parameter can impact operation are noted and the areas required for future study are outlined.

7.3 Future work

Potential areas for future study are discussed:

7.3.1 Constant volume combustion phase

1. Investigation focussed on heat transfer through the walls and minimising it during CVCP operation is needed.
2. Hydrogen energy share improvement at high load while not producing egregious NO_x emissions needs to be looked into during diesel-hydrogen intake induction operation.
3. Further optimisation with regards to direct hydrogen injection operation at low and high loads is required with a target of reducing NO_x, improving gas jet ignition timing consistency and reducing maximum pressure during the CVCP such that unchoking of the nozzle isn't an issue.
4. Investigation and enhancement of turbulence while the piston is stationary at TDC would also likely improve emissions/performance in both types of dual-fuel and pure diesel operation so should be studied.

7.3.2 Gaseous sphere injection model

1. Future improvements to the model could account for variations in Mach disk properties as pressure ratio changes throughout a given simulation by using a variable Mach disk length/diameter and cone angle. A condition for mass flow rate change if/when the nozzle unchokes because the critical pressure ratio is no longer exceeded should also be included.

2. There is also likely a need to use more accurate mass flow rate profiles which account for the opening and closing injector transients to reproduce specific flow characteristics and the impact of doing so should be assessed.

3. Improved cone angle estimation/more investigations into what exactly causes cone angle variations are required so that a theoretical model which can consistently predict its value can be built and applied.

4. Implementing a secondary transition criterion which allows for the shedding of some particles from the core, to model the mixing layer, may aid in improving combustion characteristics.

5. Side-by-side comparison of the GSI model with refined inlet modelling so that differences can be noted and potential improvement areas explored.

6. Additionally, further experimental and high fidelity numerical studies focussed on both the microscopic and macroscopic elements of the mixing and non-premixed combustion processes of underexpanded gaseous jets is required for a more complete validation of the GSI model.

7. Implementation and validation of the model in open source computational codes.

7.3.3 Dual direct injection diesel-hydrogen dual-fuel combustion

1. Exploration of the minimum possible diesel pilot volume required for adequate ignition of the hydrogen jet at various engine and injection conditions should be the target of future work as this will aid in maximising hydrogen energy share.

2. Further studies should investigate geometry optimisation (and injector orientation as they go hand in hand) as fully understanding the differences and impacts of free-jet and wall-jet combustion in direct gaseous injection operation is pivotal for achieving ideal engine operation.

3. A more detailed modelling approach using resolved injector inlets and potentially LES should be applied to study the flow structures created by the high velocity compressible jet on the air in the chamber, e.g. recirculation zones, air entrainment, convection away/infront of the jet, etc. These are somewhat observed in the likes of the streamline and interlace angle contours presented but this is difficult to study when only using a simplified injector model which doesn't fully simulate the compressible flow structures as well as a sector mesh which can't truly account for jet-jet interaction and their impact on the flow field.

4. As many of the cases examined show unstable combustion modes it would be good to study a full multi-hole configuration to see the variance in combustion of each jet. This way a strategy where little variance between combustion of each

individual injection could be optimised for as the current study can't account for this variation.

5. A strategy which has potential and was not investigated in the current study is the targeting of some premixed combustion in an attempt to curtail NO_x emissions as hydrogen doesn't produce UHC/soot/CO during rich premixed combustion like diesel. Deciding on the correct amount of premixing which doesn't cause unstable combustion and high hydrogen emission while also being able to consistently control ignition timing across multiple injections is required, i.e. likely requires multi-hole modelling to ensure little variance.

6. More detailed heat transfer modelling is also required as, with hydrogen especially due to its low quenching distance, there are high temperatures in the near wall regions. Proper optimisation of geometry, injection parameters and materials in this regard will likely aid in operational improvements.

7. Investigation of more parameters regarding the likes of injector orientation should be carried out, e.g. opposing diesel and gas injectors.

8. Comparisons with other fuels, e.g. ammonia or ignition using bio-fuels rather than diesel, etc.

9. More detailed emissions modelling integrated into the chemical kinetic mechanism should be featured in future work.

10. Further experimental investigation is needed for better validation of CFD models also.

Appendices

Appendix A

GSI User-Defined Function

ANSYS Fluent allows for customisation of a number of its standard features through use of user defined functions (UDFs) written in C programming language. UDFs utilise pre-made macros to access solver data and functionality. Detailed breakdowns of the macros used in the following UDFs can be found in the Fluent UDF Manual [221] which also provides the procedure for hooking each function to the solver.

A.1 C source code

```
/************************************************************************
UDFs for the implementation of the GSI discrete phase model.
Including DPM laws, law switching criteria, sources & drag law.
Also includes variable dynamic mesh layering height.
Implemented in Fluent 19.1.
************************************************************************/
#include "udf.h"
#include "dpm.h"
#include "dynamesh_tools.h"

/* Global Variables */

/********** CHANGE THESE FOR THE SPECIFIC CASE **********/

static real up_pres = 25e6;          /* Upstream total pressure */
static real gamma1 = 1.3;            /* Ratio spec heat for given gas */
static real v_e = 503.157;           /* Isentropic nozzle exit velocity */
static real c_d = 0.867;             /* Discharge coefficient */
static real oper_pres = 0;           /* Operating pressure set in Fluent */
static real d_inj = 0.73e-3;         /* Actual nozzle exit diameter */
static real mach_length = 0.71e-3; /* Average Mach disk length */
static T_e = 370;                    /* Nozzle exit/upstream temperature */

/* Setting the below average values initially in-case injection at 1st time
```

```
step, otherwise value doesn't matter as it will be changed */

 real avg_dens = 29.75;     /* To be adjusted - average density in domain */
 real v_M = 572.159;        /* To be adjusted - Mach disk velocity */
 real avg_pres = 1.11e+7;   /* To be adjusted - average pressure in domain*/
 real eta = 2.252;          /* To be adjusted - pressure ratio */
 real c_L = 0.00548;        /* To be adjusted - core length */
 real dens_multi = 1126;    /* To be adjusted - multiplier for part density*/
 real eta_e  = 1.2;         /* To be adjusted - nozzle exit pressure */
 real T_M = 300;            /* To be adjusted - Mach disk temperature */


 DEFINE_DYNAMIC_ZONE_PROPERTY(nonconst_height, dt, lh)
 {
/* UDF for implementing varying dynamic mesh cell layering height. */

#if !RP_HOST
 /* Local variables for saving time and crank angle then setting layering
 height*/
 real ca;
 real time;
 real init_ca = 740; /*** Input CA where variable layering height starts ***/
 real cur_ca;    /* Number of CAs after start of variable layering height */

 time = DYNAMESH_CURRENT_TIME;             /* Find current solver time */
 ca = TIME_TO_ABSOLUTE_CRANK_ANGLE(time); /* Convert time to CAs */
 cur_ca = ca - init_ca;

 /* *lh controls the layering height */

 if(ca < init_ca)
  *lh = 0.35e-3;
 else
  *lh = 0.35e-3 + (pow(cur_ca, 1.3)) * 6e-6;

#endif
}


 DEFINE_ADJUST(avg_pressure_udf,d)
 {
  /* UDF to compute the volume integral of pressure and density then find
 average over volume to adjust core length, dens multi and Mach vel/temp */

#if !RP_HOST

 real sum_pres = 0.;
 real sum_vol = 0.;
 real sum_dens = 0.;
 real total_pres = 0.;
 real total_vol = 0.;
```

```
real total_dens = 0.;
real eta_e = 0.;

cell_t c ;              /* Access to cell structure */
Thread *t ;             /* Access to thread structure */


/* Loop over all threads and all cells in each thread
then sum to find the total in each thread */

thread_loop_c(t,d)
{
begin_c_loop(c,t)
 sum_dens += C_R(c,t)*C_VOLUME(c,t);
 sum_pres += C_P(c,t)*C_VOLUME(c,t);
 sum_vol  += C_VOLUME(c,t);
end_c_loop(c,t)
}

/* Sum calculated values over all threads */

total_pres = PRF_GRSUM1(sum_pres)
total_dens = PRF_GRSUM1(sum_dens);
total_vol  = PRF_GRSUM1(sum_vol);

/* Find domain averages */

avg_dens = ((total_dens)/(total_vol));
avg_pres = oper_pres + ((total_pres)/(total_vol));

/* Calculate total pressure ratio */
eta = (up_pres)/(avg_pres);

/* Calculate core length */
c_L = (5 * sqrt(eta) * d_inj) - mach_length;

/* Calculate particle density multiplier (5e-6 particle diameter assumed) */
dens_multi = (31800 * (c_L) * (v_M + (c_d * v_e)))/(v_M - (v_e * c_d));

/* Calculate exit pressure ratio */
eta_e = (up_pres * (pow(2/(gamma1 + 1), gamma1/(gamma1-1))) /(avg_pres));

 /* Calculate new Mach velocity and temp - Yuceil */
v_M = v_e * (1 + ((eta_e) -1)/((eta_e) * gamma1));
T_M = T_e * (1 + ((gamma1 - 1)/2) * (1 - (((v_M)/(v_e)) * ((v_M)/(v_e)))));

#endif
}


DEFINE_DPM_INJECTION_INIT(initial_vel_temp,I)
```

```
{
/* UDF for adjusting initial particle velocity and temperature*/
#if !RP_HOST
Particle *p;

real p_vel_mag = 0.;
real adjust_vel = 0.;
int i;


/*loop over all particles initially */
loop(p,I->p_init)
{
/* Set particle to Mach temp */
P_T(p) = T_M;

/* Find currently assigned velocity magnitude */
p_vel_mag=sqrt((SQR(P_VEL(p)[0])) + (SQR(P_VEL(p)[1])) + (SQR(P_VEL(p)[2])));

/* v_M is the velocity we want the particle to be at */
adjust_vel = (v_M) / (p_vel_mag);

/* Adjust particle vel mag while keeping same direction */
for(i=0;i<3;i++)
P_VEL(p)[i] = (adjust_vel) * (P_VEL(p)[i]);
}
#endif
}

DEFINE_DPM_PROPERTY(udfdens,c,t,p,T)
{
/* UDF to set initial density of particle based on domain density
 (5e-6 part diam assumed)*/

#if !RP_HOST
real part_dens = 1759;       /* particle density */

dens_multi = (31800 * (c_L) * (v_M + (c_d * v_e)))/(v_M - (v_e * c_d));

part_dens = dens_multi * avg_dens;

return part_dens;
#endif
}


DEFINE_DPM_DRAG(constdrag,Re,p)
{
/* UDF to define constant particle drag law */

#if !RP_HOST
```

```
178  real drag_force = 0.;
179
180  drag_force = (18.0 * 0.424 * (Re) )/24;
181
182  return (drag_force);
183 #endif
184  }
185
186
187  DEFINE_DPM_LAW(gsivapourisation, p, coupled)
188  {
189  /* UDF for GSI evapouration law */
190
191 #if !RP_HOST
192
193  P_MASS(p) = 0.;     /* fully vapourise particle */
194
195 #endif
196  }
197
198
199 DEFINE_DPM_LAW(gsidens, p , coupled)
200  {
201  /* UDF for GSI particle density adjustment law.
202  It's likely sufficient to only adjust initial particle density
203  but this may be needed for longer core lengths */
204
205  #if !RP_HOST
206
207  P_RHO(p) = avg_dens * dens_multi;   /* adjust particle density */
208
209  #endif
210  }
211
212
213  DEFINE_DPM_SWITCH(dpm_switch, p, coupled)
214  {
215  /*  UDF for determining which law the particle should follow,
216  i.e. when particle should be vapourised */
217
218 #if !RP_HOST
219
220  /*** Inputs for additional vaporisation criteria to avoid particle wall
221  contact. ***/
222
223  real inj_angle = 0.872665;   /* input injection angle wrt cylinder axis */
224  real bore = 98882e-3;        /* input bore of engine */
225  real user_dist_wall = 5e6;   /* input max allowable particle penetration */
226
227  /*** ^^ generally not required due to small core length, but avoids the need
228  to have boundary condition switching criteria when wall film model
```

```
229 is used with liquid fuel injections ***/
230
231 real dist_to_wall = 0.;      /* calculated distance to cylinder liner */
232 real part_pos_actual[ND_ND]; /* particle displacement from injector */
233 real mag_dist = 0.;          /* particle distance from injector */
234 real vel_mag = 0.;           /* particle velocity magnitude */
235
236
237
238 /* distance to liner wall along inj axis starting at chamber centerline */
239 dist_to_wall = (0.5 * bore)/(sin(inj_angle)) - mach_length;
240
241 /* find current particle velocity magnitude */
242 vel_mag = NV_MAG(P_VEL(p));
243
244 /* find particle displacement vector */
245 NV_VV(part_pos_actual, =, P_POS(p), -, P_INIT_POS(p));
246
247 /* find magnitude of displacement vector, i.e. distance from injector */
248 mag_dist = NV_MAG(part_pos_actual);
249
250
251 /* if particle is further than a core length away from injector
252 or if velocity drops below a threshold value
253 or if in close proximity to chamber wall
254 then transition particle to continuous phase, otherwise continue.
255 Law user 2 is the vapourisation law and law user 1 the density law */
256
257 if ( mag_dist > c_L || mag_dist > 0.85 * dist_to_wall ||
258 mag_dist > user_dist_wall || vel_mag < 0.05 * v_e )
259  P_CURRENT_LAW(p) = DPM_LAW_USER_2;
260 else
261  P_CURRENT_LAW(p) = DPM_LAW_USER_1;
262
263 #endif
264 }
265
266
267 DEFINE_DPM_SOURCE(dpm_source, c, t, S, strength, p)
268 {
269 /* UDF for defining the particle sources to the continuous phase */
270 #if !RP_HOST
271
272 real mp_dot_total;       /* mass source to the continuous phase */
273
274 /* if the particle currently obeys GSI vapourisation law then...*/
275
276 if (P_CURRENT_LAW(p) == DPM_LAW_USER_2)
277 {
278   /* mass source term,
279   difference in mass between entry and exit from cell times number of
```

```
280     particles */
281
282     mp_dot_total = (P_MASS0(p)-P_MASS(p)) * strength;
283
284     /* species source term,
285     vapourising species needs to be the first species in the materials list
286     in Fluent or change the "[0]" to the species number - 1 */
287
288     S->species[0]  += mp_dot_total;
289   }
290
291 #endif
292   }
293
294 /* TO DO:
295
296     Additional functions for varying injection diameter, position and angle
      should be written to better account for changing chamber conditions/Mach
      disk quantities. Additionally variable mass flow rate profiles which
      change when/if pressure ratio falls below the critical pressure ratio and
       thus unchokes should also be made. Some problems involving incorrect
      injected masses were found when applying these variable quantities and
      due to time constraints implementation is left to future work. With that
      said the additions should be relatively easy to make (in Fluent use "
      define_dpm_injection_init" similar to the velocity and temperature
      function above).
297 */
```

Appendix B

Additional Validation

B.1 Freestream GSI mesh sensitivity study

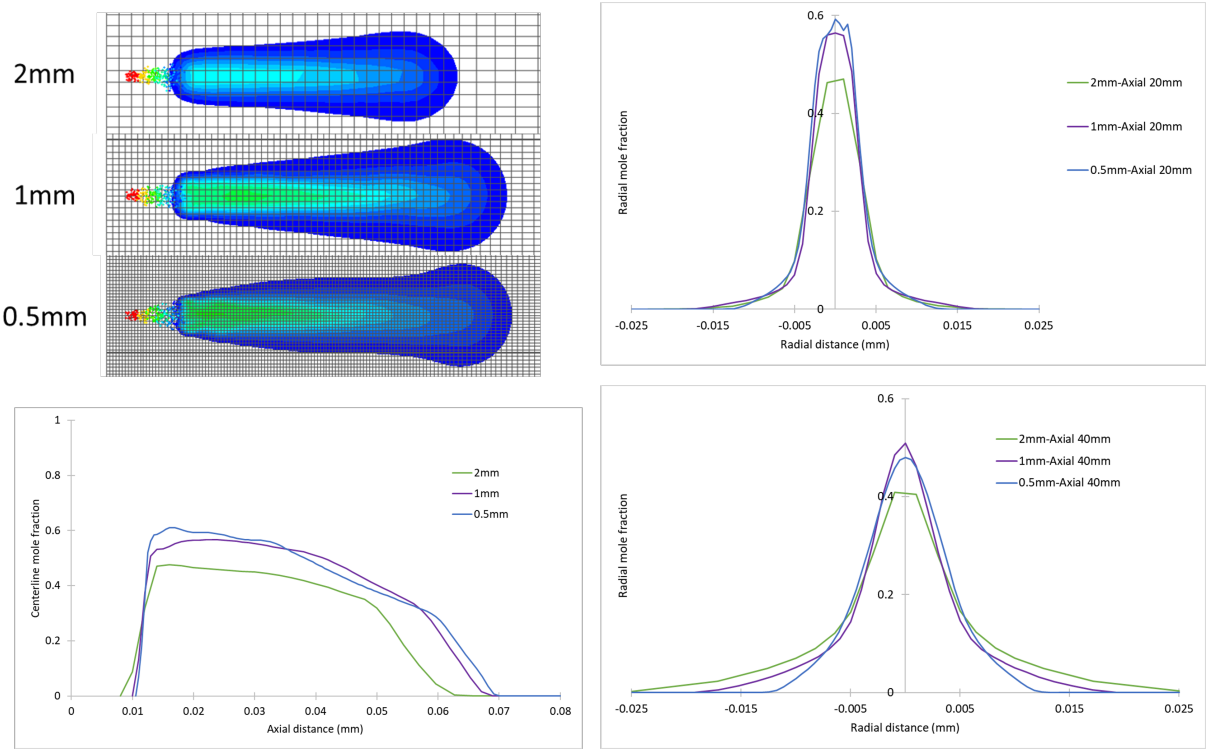

FIGURE B.1: Freestream study comparing mass fraction contours, centerline mole fraction and radial mole fraction at 20 mm and 40 mm downstream of the nozzle exit at three mesh densities (2 mm, 1 mm and 0.5 mm).

Figure B.1 compares various important features of accurate injection modelling. The coarse mesh doesn't adequately predict the flow, but both the 1 mm and 0.5 mm predict fairly similar flow fields and are starting to show convergence. The indication is that

the 1 mm mesh is likely adequate for reasonable predictions but further refinement could be useful.

B.2 Comparison of expected average and variable Mach disk quantities in the GSI model

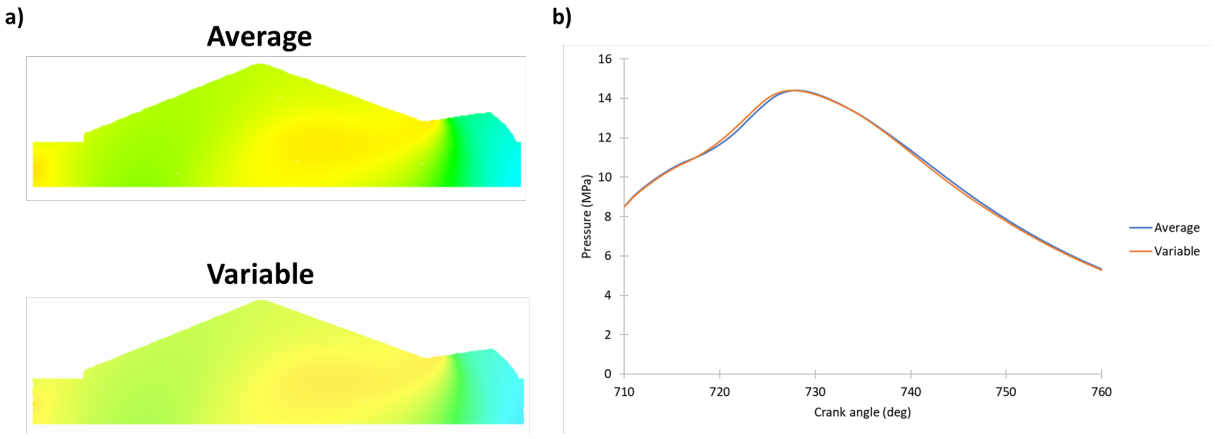

FIGURE B.2: Comparison of results for expected average and variable Mach disk quantities in a) ECN and b) Faghani validation cases

A comparison is made between the GSI model when formulated with expected average and variable Mach disk quantities. Variable is the preferred option and is used throughout the parametric investigations as chamber conditions are not known a priori. Figure B.2 compares the mixture formation at the end of the ECN simulations as well as the pressure trends in the 18% EGR Faghani reacting engine simulation. Very little difference is observed between the two cases with the only noticeable difference being the slightly higher pressure for the variable case in the early parts of combustion. This is due to the higher initial injection velocity as pressure ratio starts off higher than the average case, this is then balanced as chamber pressures rise and the pressure ratio falls below the average case and is reflected in the slightly lower pressure just after the peak is reached.

B.3 ECN Spray H mesh sensitivity study

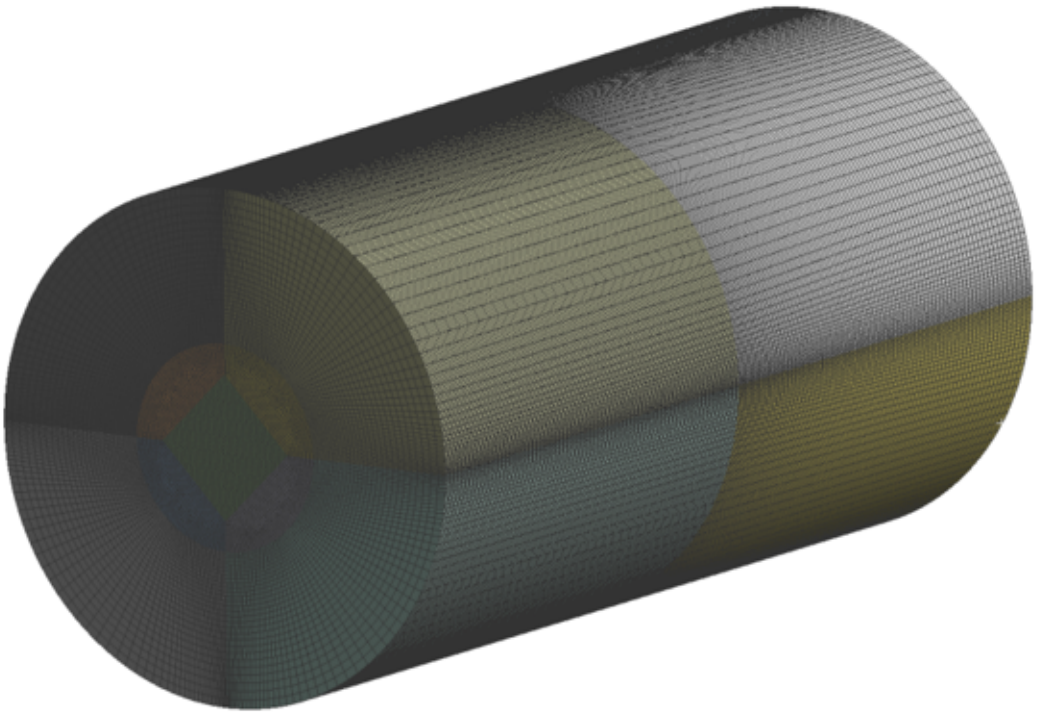

FIGURE B.3: ECN Spray H mesh.

Validation of the combustion and liquid spray modelling approaches is carried out using the ECN Spray H experimental database [214, 222, 223]. Figure B.3 shows the o-grid mesh used to perform the simulations. Figures B.4 and B.5 show the non-reacting and reacting results respectively. Good agreement is found for the 0.25 mm and 0.5 mm mesh densities. Non-reacting axial penetration and centerline mass fraction are predicted well, as are reacting ignition delay and lift off length as EGR rate is increased with the finer mesh performing slightly better across all cases. Additionally the finite rate combustion modelling approach shows its applicability to the cases studied throughout this work.

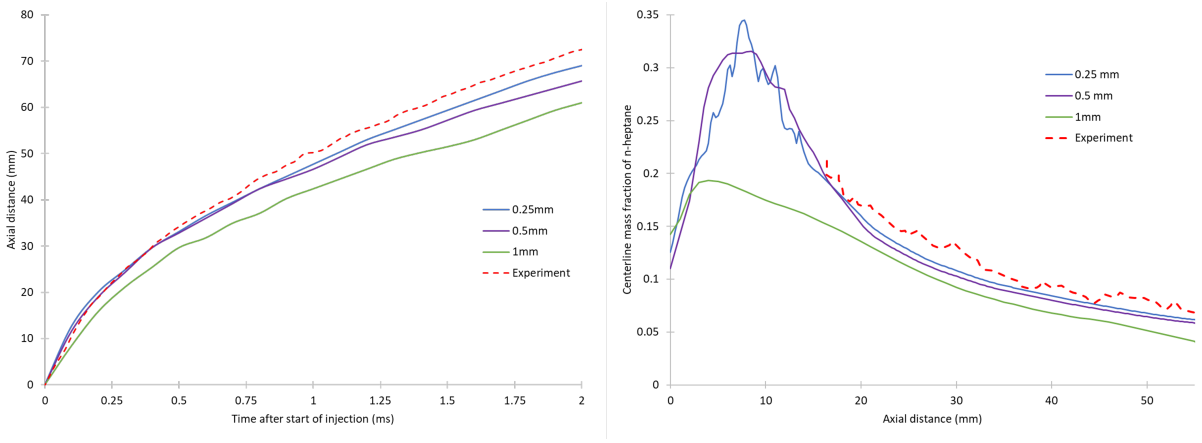

FIGURE B.4: Comparison of 1 mm, 0.5 mm and 0.25 mm to the ECN Spray H axial penetration (left) and centerline mass fraction (right) non-reacting experimental measurements [222, 223].

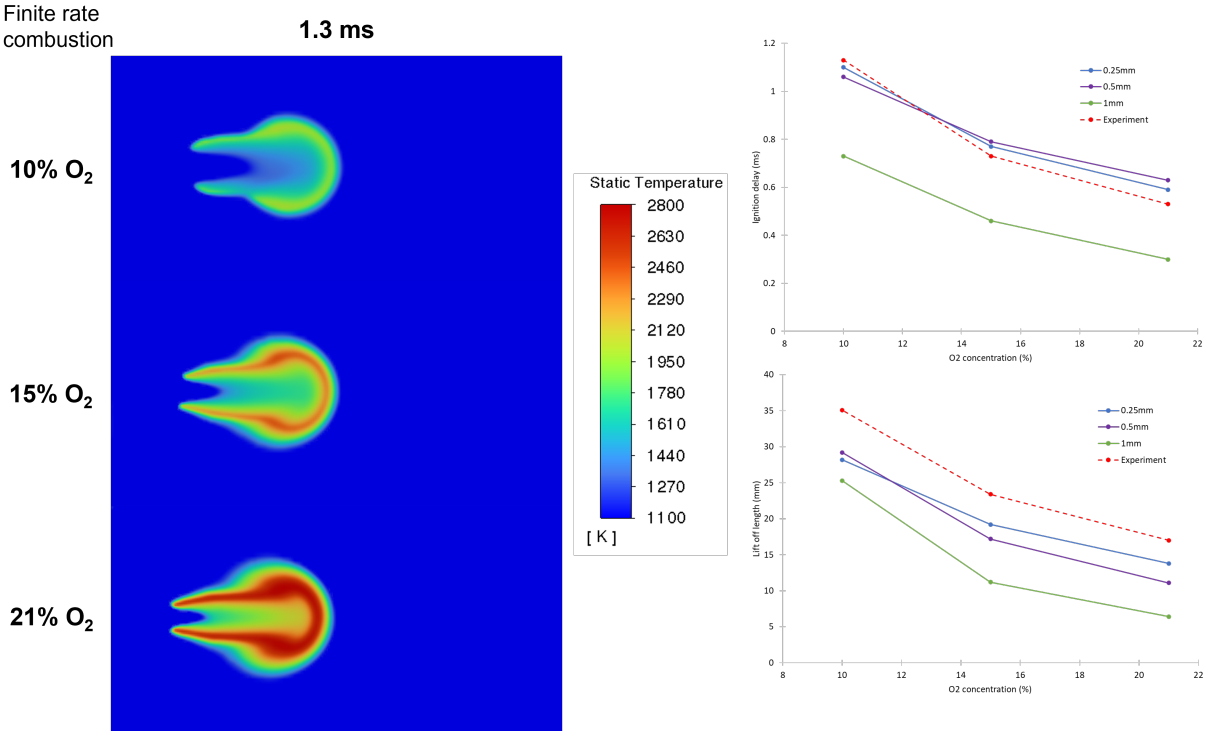

FIGURE B.5: Finite rate combustion modelling setup validation using the ECN Spray H reacting experimental measurements for ignition delay and lift off length [222, 223].

Appendix C

Additional Modelling Details

C.1 Swirl

Swirl is introduced in the sector simulations which don't model the gas exchange process through an initial patch to the velocity field. A swirl number taken from the experimental setup used in the validation of each case is applied,

Swirl is calculated via the following equation

$$\vec{u} = \vec{r} \times \vec{\omega} \tag{C.1}$$

where $\vec{r}$ is the radial distance vector from the cylinder axis and $\vec{\omega}$ is the angular velocity about the cylinder axis whose magnitude can be expressed as

$$|\omega| = \text{Swirl Number} \times \frac{2\pi \times RPM}{60}, \tag{C.2}$$

and

$$\vec{\omega} = (|\omega|) \left(\textit{cyl-axis-x } \widehat{i} + \textit{cyl-axis-y } \widehat{j} + \textit{cyl-axis-z } \widehat{k} \right). \tag{C.3}$$

Equation (C.1) is then used to patch x, y and z components of the velocity field after initialisation.

Figure C.1 provides a depiction of the initial patched velocity field and the turbulence generated as the flow is "squished" prior to injection close to TDC using a swirl number of 1.5 in the gaseous direct injection study

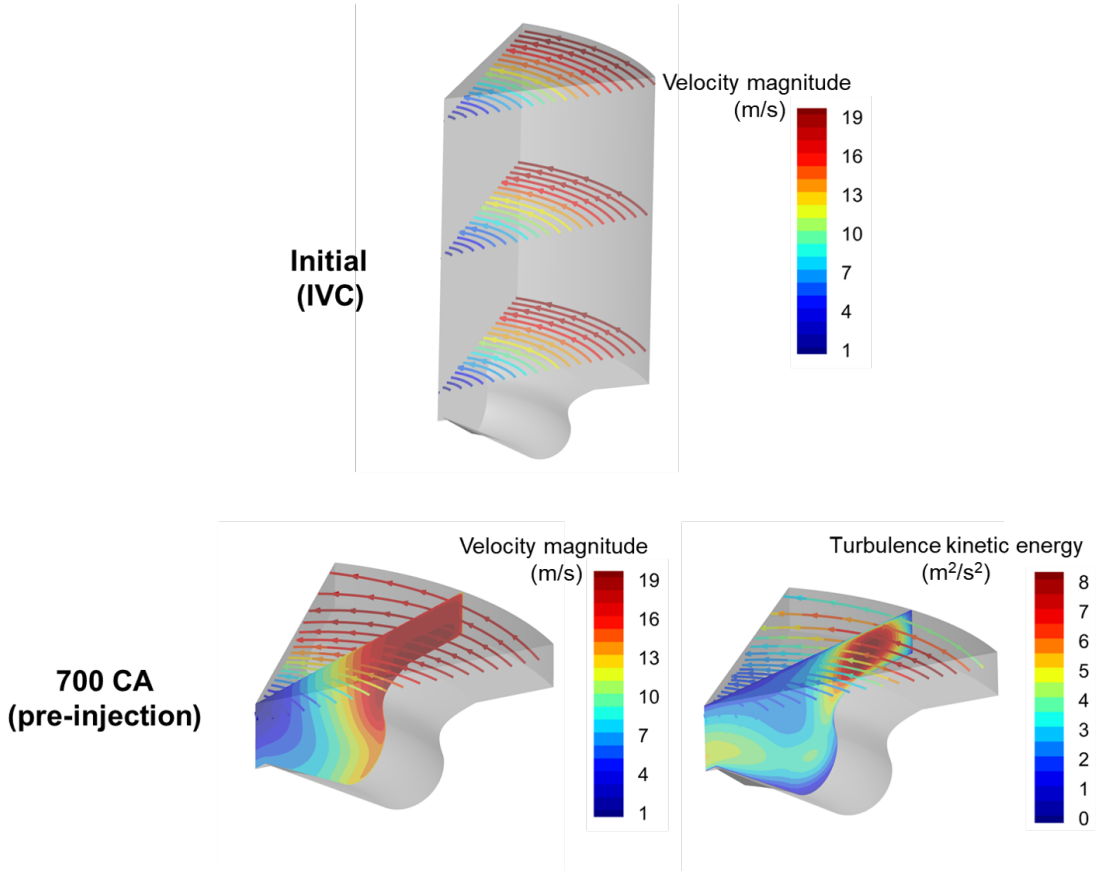

FIGURE C.1: Flow field generated by applying swirl at IVC.

C.2 Diesel Unsteady Flamelet PDF Table

Figure C.2 shows the PDF table generated during the initial pure diesel study.

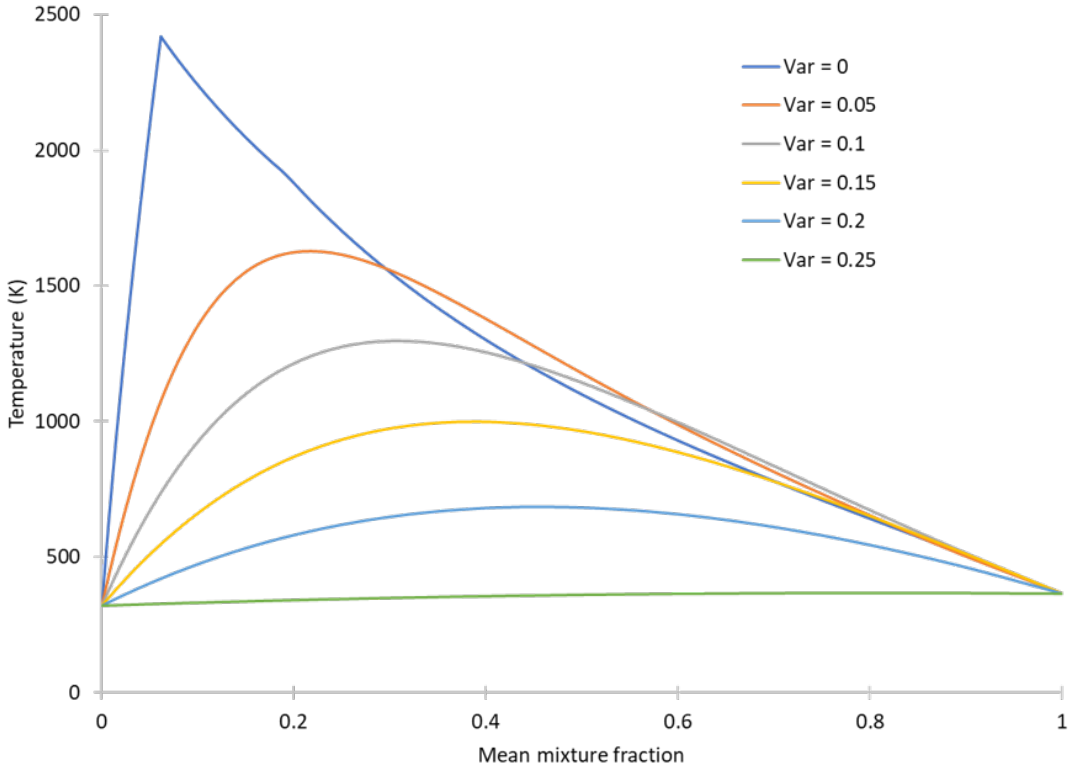

FIGURE C.2: Generated PDF table - diesel unsteady flamelet model.

Bibliography

[1] IEA. *Global Energy Review 2021*. Paris: IEA, 2021. https://www.iea.org/reports/global-energy-review-2021.html (Accessed 31/05/2021).

[2] BP. *BP Statistical Review of World Energy 2020*. BP, 2020. https://www.bp.com/en/global/corporate/energy-economics/statistical-review-of-world-energy.html (Accessed 31/05/2021).

[3] W. R. Institute. *Climate Watch Washington, DC:* 2020. https://www.climatewatchdata.org (Accessed 31/05/2021).

[4] L. Al-Ghussain. "Global Warming: Review on Driving Forces and Mitigation". In: *Environmental Progress & Sustainable Energy* 38.1 (2019), pp. 13–21. ISSN: 1944-7450. DOI: 10.1002/ep.13041.

[5] *The Paris Agreement to the United Nations Framework Convention on Climate Change*. Dec. 12, 2015. https://unfccc.int/process-and-meetings/the-paris-agreement/the-paris-agreement.html (Accessed 31/05/2021).

[6] W. R. Institute. *CAIT Data*. Climate Watch. GHG Emissions. Washington, DC: 2020. https://www.climatewatchdata.org/ghg-emissions (Accessed 06/06/2021).

[7] T. Sinigaglia et al. "Production, Storage, Fuel Stations of Hydrogen and Its Utilization in Automotive Applications-a Review". In: *International Journal of Hydrogen Energy* 42.39 (Sept. 28, 2017), pp. 24597–24611. ISSN: 0360-3199. DOI: 10.1016/j.ijhydene.2017.08.063.

[8] A. L. Dicks and D. A. J. Rand. *Fuel Cell Systems Explained*. John Wiley & Sons, Mar. 14, 2018. 492 pp. ISBN: 978-1-118-70697-8. Google Books: l2pRDwAAQBAJ.

[9] A. Murugan and A. S. Brown. "Review of Purity Analysis Methods for Performing Quality Assurance of Fuel Cell Hydrogen". In: *International Journal of Hydrogen Energy* 40.11 (Mar. 22, 2015), pp. 4219–4233. ISSN: 0360-3199. DOI: 10.1016/j.ijhydene.2015.01.041.

[10] C. Acar and I. Dincer. "The Potential Role of Hydrogen as a Sustainable Transportation Fuel to Combat Global Warming".
In: *International Journal of Hydrogen Energy*. Hydrogen Energy Technologies for Mitigating Global Warming 45.5 (Jan. 29, 2020), pp. 3396–3406. ISSN: 0360-3199. DOI: 10.1016/j.ijhydene.2018.10.149.

[11] S. E. Hosseini and B. Butler. "An Overview of Development and Challenges in Hydrogen Powered Vehicles".
In: *International Journal of Green Energy* 17.1 (Jan. 2, 2020), pp. 13–37. ISSN: 1543-5075. DOI: 10.1080/15435075.2019.1685999.

[12] J. Heywood. *Internal Combustion Engine Fundamentals*.
McGraw-Hill Education, Apr. 1, 1988. 968 pp. ISBN: 978-0-07-028637-5. Google Books: u9FSAAAAMAAJ.

[13] P. Dimitriou and T. Tsujimura.
"A Review of Hydrogen as a Compression Ignition Engine Fuel". In: *International Journal of Hydrogen Energy* 42.38 (Sept. 21, 2017), pp. 24470–24486. ISSN: 0360-3199. DOI: 10.1016/j.ijhydene.2017.07.232.

[14] H. L. Yip et al. "A Review of Hydrogen Direct Injection for Internal Combustion Engines: Towards Carbon-Free Combustion".
In: *Applied Sciences* 9.22 (22 Jan. 2019), p. 4842. DOI: 10.3390/app9224842.

[15] C. J. Ramsay et al. "A Numerical Study of a Compression Ignition Engine Operating with Constant Volume Combustion Phase: Effects of Constant Volume Phase on Combustion Performance and Emissions".
In: *Fuel* 280 (Nov. 15, 2020), p. 118657. ISSN: 0016-2361. DOI: 10.1016/j.fuel.2020.118657.

[16] C. J. Ramsay et al. "A Numerical Study on the Effects of Constant Volume Combustion Phase on Performance and Emissions Characteristics of a Diesel-Hydrogen Dual-Fuel Engine". In: *International Journal of Hydrogen Energy* 45.56 (Nov. 13, 2020), pp. 32598–32618. ISSN: 0360-3199. DOI: 10.1016/j.ijhydene.2020.09.021.

[17] C. J. Ramsay and K. K. J. R. Dinesh. "High Pressure Direct Injection of Gaseous Fuels Using a Discrete Phase Methodology for Engine Simulations".
In: *International Journal of Hydrogen Energy* (Nov. 18, 2021). ISSN: 0360-3199. DOI: 10.1016/j.ijhydene.2021.10.235.

[18] C. Acar and I. Dincer. "Review and Evaluation of Hydrogen Production Options for Better Environment".
In: *Journal of Cleaner Production* 218 (May 1, 2019), pp. 835–849. ISSN: 0959-6526. DOI: 10.1016/j.jclepro.2019.02.046.

[19] D.-Y. Lee, A. Elgowainy, and Q. Dai. "Life Cycle Greenhouse Gas Emissions of Hydrogen Fuel Production from Chlor-Alkali Processes in the United States". In: *Applied Energy* 217 (May 1, 2018), pp. 467–479. ISSN: 0306-2619. DOI: 10.1016/j.apenergy.2018.02.132.

[20] S. Z. Baykara. "Hydrogen: A Brief Overview on Its Sources, Production and Environmental Impact". In: *International Journal of Hydrogen Energy*. The 2nd International Hydrogen Technologies Congress (IHTEC-2017) 43.23 (June 7, 2018), pp. 10605–10614. ISSN: 0360-3199. DOI: 10.1016/j.ijhydene.2018.02.022.

[21] F. Colmati et al. "Production of Hydrogen and Their Use in Proton Exchange Membrane Fuel Cells". In: *Advances In Hydrogen Generation Technologies* (Nov. 5, 2018). DOI: 10.5772/intechopen.76663.

[22] I. Dincer and C. Acar. "Review and Evaluation of Hydrogen Production Methods for Better Sustainability". In: *International Journal of Hydrogen Energy* 40.34 (Sept. 14, 2015), pp. 11094–11111. ISSN: 0360-3199. DOI: 10.1016/j.ijhydene.2014.12.035.

[23] T. Bourgeois et al. "The Temperature Evolution in Compressed Gas Filling Processes: A Review". In: *International Journal of Hydrogen Energy* 43.4 (Jan. 25, 2018), pp. 2268–2292. ISSN: 0360-3199. DOI: 10.1016/j.ijhydene.2017.11.068. Review Paper EU.

[24] *The First Commercial Type V Composite Pressure Vessel*. https://www.compositesworld.com/articles/next-generation-pressure-vessels (Accessed 31/05/2021).

[25] E. Rivard, M. Trudeau, and K. Zaghib. "Hydrogen Storage for Mobility: A Review". In: *Materials* 12.12 (June 19, 2019), p. 1973. ISSN: 1996-1944. DOI: 10.3390/ma12121973. pmid: 31248099.

[26] A. M. Elberry et al. "Large-Scale Compressed Hydrogen Storage as Part of Renewable Electricity Storage Systems". In: *International Journal of Hydrogen Energy* 46.29 (Apr. 26, 2021), pp. 15671–15690. ISSN: 0360-3199. DOI: 10.1016/j.ijhydene.2021.02.080.

[27] B. C. Tashie-Lewis and S. G. Nnabuife. "Hydrogen Production, Distribution, Storage and Power Conversion in a Hydrogen Economy - A Technology Review". In: *Chemical Engineering Journal Advances* (Aug. 24, 2021), p. 100172. ISSN: 2666-8211. DOI: 10.1016/j.ceja.2021.100172.

[28] J. O. Abe et al.
"Hydrogen Energy, Economy and Storage: Review and Recommendation".
In: *International Journal of Hydrogen Energy* 44.29 (June 7, 2019), pp. 15072–15086.
ISSN: 0360-3199. DOI: 10.1016/j.ijhydene.2019.04.068.

[29] O. Barrera et al. "Understanding and Mitigating Hydrogen Embrittlement of Steels: A Review of Experimental, Modelling and Design Progress from Atomistic to Continuum".
In: *Journal of Materials Science* 53.9 (May 1, 2018), pp. 6251–6290.
ISSN: 1573-4803. DOI: 10.1007/s10853-017-1978-5.

[30] M. Aziz, A. T. Wijayanta, and A. B. D. Nandiyanto. "Ammonia as Effective Hydrogen Storage: A Review on Production, Storage and Utilization".
In: *Energies* 13.12 (12 Jan. 2020), p. 3062. DOI: 10.3390/en13123062.

[31] K. E. Lamb, M. D. Dolan, and D. F. Kennedy.
"Ammonia for Hydrogen Storage; A Review of Catalytic Ammonia Decomposition and Hydrogen Separation and Purification".
In: *International Journal of Hydrogen Energy* 44.7 (Feb. 5, 2019), pp. 3580–3593.
ISSN: 0360-3199. DOI: 10.1016/j.ijhydene.2018.12.024.

[32] F. C. S. Committee. "Fueling Protocols for Light Duty and Medium Duty Gaseous Hydrogen Surface Vehicles J2601_201612".
In: *SAE International* Standards (Dec. 6, 2016), p. 267.
DOI: 10.4271/j2601_201612.

[33] L. Zhao et al.
"Review on Studies of the Emptying Process of Compressed Hydrogen Tanks".
In: *International Journal of Hydrogen Energy* 46.43 (June 23, 2021), pp. 22554–22573. ISSN: 0360-3199. DOI: 10.1016/j.ijhydene.2021.04.101.

[34] *US Department of Energy*. Hydrogen Storage.
URL: https://www.energy.gov/eere/fuelcells/hydrogen-storage (visited on 09/07/2021).

[35] M. Chaichan.
"The Impact of Equivalence Ratio on Performance and Emissions of a Hydrogen-Diesel Dual Fuel Engine with Cooled Exhaust Gas Recirculation".
In: *International Journal of Scientific and Engineering Research* 6 (June 18, 2015), pp. 938–941.

[36] J. P. J. van Lipzig et al. "Laminar Burning Velocities of N-Heptane, Iso-Octane, Ethanol and Their Binary and Tertiary Mixtures".
In: *Fuel* 90.8 (Aug. 1, 2011), pp. 2773–2781. ISSN: 0016-2361.
DOI: 10.1016/j.fuel.2011.04.029.

[37] W. M. Haynes. *CRC Handbook of Chemistry and Physics, 95th Edition*. CRC Press, June 4, 2014. 2666 pp. ISBN: 978-1-4822-0868-9. Google Books: bNDMBQAAQBAJ.

[38] *Alternative Fuels Data Center*. Fuel Properties Comparison. June 23, 2018. URL: https://www.afdc.energy.gov/fuels/fuel_properties.php (visited on 06/23/2018).

[39] S. R. Turns. *An Introduction to Combustion: Concepts and Applications*. 3 edition. New York: McGraw-Hill Education, Mar. 1, 2011. 752 pp. ISBN: 978-0-07-338019-3.

[40] D. W. Green and R. H. Perry. *Perry's Chemical Engineers' Handbook, 8th Edition*. McGraw-Hill Education, 2008. ISBN: 978-0-07-142294-9.

[41] T. B. Imhoff, S. Gkantonas, and E. Mastorakos. "Analysing the Performance of Ammonia Powertrains in the Marine Environment". In: *Energies* 14.21 (21 Jan. 2021), p. 7447. ISSN: 1996-1073. DOI: 10.3390/en14217447.

[42] K. Takizawa et al. "Quenching Distance Measurement of Highly to Mildly Flammable Compounds". In: *Fire Safety Journal* 71 (Jan. 1, 2015), pp. 58–68. ISSN: 0379-7112. DOI: 10.1016/j.firesaf.2014.11.013.

[43] A. Kéromnès et al. "An Experimental and Detailed Chemical Kinetic Modeling Study of Hydrogen and Syngas Mixture Oxidation at Elevated Pressures". In: *Combustion and Flame* 160.6 (June 1, 2013), pp. 995–1011. ISSN: 0010-2180. DOI: 10.1016/j.combustflame.2013.01.001.

[44] C. Olm et al. "Comparison of the Performance of Several Recent Hydrogen Combustion Mechanisms". In: *Combustion and Flame* 161.9 (Sept. 1, 2014), pp. 2219–2234. ISSN: 0010-2180. DOI: 10.1016/j.combustflame.2014.03.006.

[45] L. Wei and P. Geng. "A Review on Natural Gas/Diesel Dual Fuel Combustion, Emissions and Performance". In: *Fuel Processing Technology* 142 (Feb. 1, 2016), pp. 264–278. ISSN: 0378-3820. DOI: 10.1016/j.fuproc.2015.09.018.

[46] G. A. Karim. "Combustion in Gas Fueled Compression: Ignition Engines of the Dual Fuel Type". In: *Journal of Engineering for Gas Turbines and Power* 125.3 (Aug. 15, 2003), pp. 827–836. ISSN: 0742-4795. DOI: 10.1115/1.1581894.

[47] G. A. Karim. "Hydrogen as a Spark Ignition Engine Fuel". In: *International Journal of Hydrogen Energy* 28.5 (May 1, 2003), pp. 569–577. ISSN: 0360-3199. DOI: 10.1016/S0360-3199(02)00150-7.

[48] H. M. Cho and B.-Q. He. "Spark Ignition Natural Gas Engines—A Review". In: *Energy Conversion and Management* 48.2 (Feb. 1, 2007), pp. 608–618. ISSN: 0196-8904. DOI: 10.1016/j.enconman.2006.05.023.

[49] A. Boretti.
"Advances in Hydrogen Compression Ignition Internal Combustion Engines".
In: *International Journal of Hydrogen Energy* 36.19 (Sept. 1, 2011),
pp. 12601–12606. ISSN: 0360-3199. DOI: 10.1016/j.ijhydene.2011.06.148.

[50] J. C. Beale and R. D. Reitz. "Modeling Spray Atomization with the
Kelvin-Helmholtz/Rayleigh-Taylor Hybrid Model".
In: *Atomization and Sprays* 9.6 (1999). ISSN: 1044-5110, 1936-2684.
DOI: 10.1615/AtomizSpr.v9.i6.40.

[51] C. R. Ferguson and A. T. Kirkpatrick.
Internal Combustion Engines: Applied Thermosciences.
John Wiley & Sons, July 7, 2015. 474 pp. ISBN: 978-1-118-53331-4.
Google Books: 9rLLCQAAQBAJ.

[52] B. R. Petersen, I. W. Ekoto, and P. C. Miles.
"An Investigation into the Effects of Fuel Properties and Engine Load on UHC
and CO Emissions from a Light-Duty Optical Diesel Engine Operating in a
Partially Premixed Combustion Regime".
In: *SAE International Journal of Engines* 3.2 (2010), pp. 38–55. ISSN: 1946-3936.
JSTOR: 26275545.

[53] P. T. Williams et al. "The Influence of PAH Contamination of Lubricating Oil on
Diesel Participate PAH Emissions". In: *SAE Transactions* 98 (1989), pp. 464–472.
ISSN: 0096-736X. JSTOR: 44472044.

[54] H. Kosaka, T. Aizawa, and T. Kamimoto. "Two-Dimensional Imaging of
Ignition and Soot Formation Processes in a Diesel Flame".
In: *International Journal of Engine Research* 6.1 (Feb. 1, 2005), pp. 21–42.
ISSN: 1468-0874. DOI: 10.1243/146808705X7347.

[55] P. P. Duvvuri et al.
"Modeling Soot Particle Size Distribution in Diesel Engines".
In: *Fuel* 243 (May 1, 2019), pp. 70–78. ISSN: 0016-2361.
DOI: 10.1016/j.fuel.2019.01.104.

[56] Y. B. Zeldovich. *Selected Works of Yakov Borisovich Zeldovich Ch 26. Oxidation of
Nitrogen in Combustion and Explosions"*. Vol. 1.
Selected Works of Yakov Borisovich Zeldovich.
Princeton University Press, July 14, 2014, pp. 404–410. ISBN: 978-1-4008-6297-9.

[57] S. A. Ciatti, S. A. Miers, and H. K. Ng.
"Influence of EGR on Soot/NOx Production in a Light-Duty Diesel Engine".
In:
ASME 2005 Internal Combustion Engine Division Fall Technical Conference.
American Society of Mechanical Engineers Digital Collection, Nov. 11, 2008,
pp. 415–423. DOI: 10.1115/ICEF2005-1327.

[58] T. Tsujimura and Y. Suzuki.
"The Utilization of Hydrogen in Hydrogen/Diesel Dual Fuel Engine".
In: *International Journal of Hydrogen Energy*. Special Issue on The 21st World Hydrogen Energy Conference (WHEC 2016), 13-16 June 2016, Zaragoza, Spain 42.19 (May 11, 2017), pp. 14019–14029. ISSN: 0360-3199.
DOI: 10.1016/j.ijhydene.2017.01.152.

[59] P. Dimitriou et al. "Combustion and Emission Characteristics of a Hydrogen-Diesel Dual-Fuel Engine". In: *International Journal of Hydrogen Energy* 43.29 (July 19, 2018), pp. 13605–13617. ISSN: 0360-3199.
DOI: 10.1016/j.ijhydene.2018.05.062.

[60] M. Choi, K. Mohiuddin, and S. Park.
"Effects of Methane Ratio on MPDF (Micro-Pilot Dual-Fuel) Combustion Characteristic in a Heavy-Duty Single Cylinder Engine".
In: *Scientific Reports* 11.1 (1 May 7, 2021), p. 9740. ISSN: 2045-2322.
DOI: 10.1038/s41598-021-89161-z.

[61] S. Frankl et al. "Investigation of Ammonia and Hydrogen as CO2-free Fuels for Heavy Duty Engines Using a High Pressure Dual Fuel Combustion Process".
In: *International Journal of Engine Research* 22.10 (Oct. 1, 2021), pp. 3196–3208.
ISSN: 1468-0874. DOI: 10.1177/1468087420967873.

[62] R. Babayev et al. "Computational Characterization of Hydrogen Direct Injection and Nonpremixed Combustion in a Compression-Ignition Engine".
In: *International Journal of Hydrogen Energy* 46.35 (May 20, 2021), pp. 18678–18696. ISSN: 0360-3199. DOI: 10.1016/j.ijhydene.2021.02.223.

[63] T. Rogers. "Mixture Preparation of Gaseous Fuels for Internal Combustion Engines Using Optical Diagnostics". PhD thesis. RMIT University, 2014.

[64] M. El Hannach et al. "Life Cycle Assessment of Hydrogen and Diesel Dual-Fuel Class 8 Heavy Duty Trucks".
In: *International Journal of Hydrogen Energy* 44.16 (Mar. 29, 2019), pp. 8575–8584.
ISSN: 0360-3199. DOI: 10.1016/j.ijhydene.2019.02.027.

[65] I. Staffell et al.
"The Role of Hydrogen and Fuel Cells in the Global Energy System".
In: *Energy & Environmental Science* 12.2 (Feb. 13, 2019), pp. 463–491.
ISSN: 1754-5706. DOI: 10.1039/C8EE01157E.

[66] C. M. White, R. R. Steeper, and A. E. Lutz.
"The Hydrogen-Fueled Internal Combustion Engine: A Technical Review".
In: *International Journal of Hydrogen Energy* 31.10 (Aug. 1, 2006), pp. 1292–1305.
ISSN: 0360-3199. DOI: 10.1016/j.ijhydene.2005.12.001.

[67] V. Chintala and K. A. Subramanian. "A Comprehensive Review on Utilization of Hydrogen in a Compression Ignition Engine under Dual Fuel Mode". In: *Renewable and Sustainable Energy Reviews* 70 (Apr. 1, 2017), pp. 472–491. ISSN: 1364-0321. DOI: 10.1016/j.rser.2016.11.247.

[68] W. B. Santoso, R. A. Bakar, and A. Nur. "Combustion Characteristics of Diesel-Hydrogen Dual Fuel Engine at Low Load". In: *Energy Procedia*. International Conference on Sustainable Energy Engineering and Application (ICSEEA) 2012 32 (Jan. 1, 2013), pp. 3–10. ISSN: 1876-6102. DOI: 10.1016/j.egypro.2013.05.002.

[69] C. Liew et al. "Exhaust Emissions of a H2-enriched Heavy-Duty Diesel Engine Equipped with Cooled EGR and Variable Geometry Turbocharger". In: *Fuel* 91.1 (Jan. 1, 2012), pp. 155–163. ISSN: 0016-2361. DOI: 10.1016/j.fuel.2011.08.002.

[70] K. A. Subramanian and V. Chintala. "Reduction of GHGs Emissions in a Biodiesel Fueled Diesel Engine Using Hydrogen". In: (Oct. 13, 2013), V002T02A005. DOI: 10.1115/ICEF2013-19133.

[71] T. Miyamoto et al. "Effect of Hydrogen Addition to Intake Gas on Combustion and Exhaust Emission Characteristics of a Diesel Engine". In: *International Journal of Hydrogen Energy*. 3rd Iranian Fuel Cell Seminar 36.20 (Oct. 1, 2011), pp. 13138–13149. ISSN: 0360-3199. DOI: 10.1016/j.ijhydene.2011.06.144.

[72] H. Park, J. Kim, and C. Bae. "Effects of Hydrogen Ratio and EGR on Combustion and Emissions in a Hydrogen/Diesel Dual-Fuel PCCI Engine". In: (Sept. 1, 2015). DOI: 10.4271/2015-01-1815.

[73] A. A. Hairuddin, T. Yusaf, and A. P. Wandel. "A Review of Hydrogen and Natural Gas Addition in Diesel HCCI Engines". In: *Renewable and Sustainable Energy Reviews* 32 (Apr. 1, 2014), pp. 739–761. ISSN: 1364-0321. DOI: 10.1016/j.rser.2014.01.018.

[74] U. S. Jyothi and K. Vijaya Kumar Reddy. "Experimental and CFD Analysis of Re-entrant Combustion Chamber on Diesel Enriched with Hydrogen". In: *Journal of The Institution of Engineers (India): Series C* 102.1 (Feb. 1, 2021), pp. 121–129. ISSN: 2250-0553. DOI: 10.1007/s40032-020-00629-9.

[75] T. Tsujimura and Y. Suzuki. "Development of a Large-Sized Direct Injection Hydrogen Engine for a Stationary Power Generator". In: *International Journal of Hydrogen Energy*. Production, Storage and Valorization of Hydrogen Energy (PSVHE) 44.22 (Apr. 26, 2019), pp. 11355–11369. ISSN: 0360-3199. DOI: 10.1016/j.ijhydene.2018.09.178.

[76] P. Dimitriou, T. Tsujimura, and Y. Suzuki.
"Low-Load Hydrogen-Diesel Dual-Fuel Engine Operation – A Combustion Efficiency Improvement Approach". In: *International Journal of Hydrogen Energy* 44.31 (June 21, 2019), pp. 17048–17060. ISSN: 0360-3199.
DOI: 10.1016/j.ijhydene.2019.04.203.

[77] V. Chintala and K. A. Subramanian. "An Effort to Enhance Hydrogen Energy Share in a Compression Ignition Engine under Dual-Fuel Mode Using Low Temperature Combustion Strategies".
In: *Applied Energy* 146 (May 15, 2015), pp. 174–183. ISSN: 0306-2619.
DOI: 10.1016/j.apenergy.2015.01.110.

[78] P. Sharma and A. Dhar.
"Compression Ratio Influence on Combustion and Emissions Characteristic of Hydrogen Diesel Dual Fuel CI Engine: Numerical Study".
In: *Fuel* 222 (June 15, 2018), pp. 852–858. ISSN: 0016-2361.
DOI: 10.1016/j.fuel.2018.02.108.

[79] J. E. Dec. "Advanced Compression-Ignition Engines—Understanding the in-Cylinder Processes".
In: *Proceedings of the Combustion Institute* 32.2 (Jan. 1, 2009), pp. 2727–2742.
ISSN: 1540-7489. DOI: 10.1016/j.proci.2008.08.008.

[80] V. Chintala and K. A. Subramanian. "Hydrogen Energy Share Improvement along with NOx (Oxides of Nitrogen) Emission Reduction in a Hydrogen Dual-Fuel Compression Ignition Engine Using Water Injection".
In: *Energy Conversion and Management* 83 (July 1, 2014), pp. 249–259.
ISSN: 0196-8904. DOI: 10.1016/j.enconman.2014.03.075.

[81] M. Mohamed Ibrahim and A. Ramesh. "Investigations on the Effects of Intake Temperature and Charge Dilution in a Hydrogen Fueled HCCI Engine". In: *International Journal of Hydrogen Energy* 39.26 (Sept. 3, 2014), pp. 14097–14108.
ISSN: 0360-3199. DOI: 10.1016/j.ijhydene.2014.07.019.

[82] H. Mabadi Rahimi, S. A. Jazayeri, and M. Ebrahimi.
"Hydrogen Energy Share Enhancement in a Heavy Duty Diesel Engine under RCCI Combustion Fueled with Natural Gas and Diesel Oil". In: *International Journal of Hydrogen Energy* 45.35 (July 10, 2020), pp. 17975–17991.
ISSN: 0360-3199. DOI: 10.1016/j.ijhydene.2020.04.263.

[83] R. D. Reitz and G. Duraisamy.
"Review of High Efficiency and Clean Reactivity Controlled Compression Ignition (RCCI) Combustion in Internal Combustion Engines".
In: *Progress in Energy and Combustion Science* 46 (Feb. 1, 2015), pp. 12–71.
ISSN: 0360-1285. DOI: 10.1016/j.pecs.2014.05.003.

[84] J. Gao et al. “Review of the Backfire Occurrences and Control Strategies for Port Hydrogen Injection Internal Combustion Engines”.
In: *Fuel* 307 (Jan. 1, 2022), p. 121553. ISSN: 0016-2361.
DOI: 10.1016/j.fuel.2021.121553.

[85] A. Menaa et al. “CFD Analysis of Hydrogen Injection Pressure and Valve Profile Law Effects on Backfire and Pre-Ignition Phenomena in Hydrogen-Diesel Dual Fuel Engine”.
In: *International Journal of Hydrogen Energy* 44.18 (Apr. 5, 2019), pp. 9408–9422.
ISSN: 0360-3199. DOI: 10.1016/j.ijhydene.2019.02.123.

[86] M. Li et al. “A Comprehensive Review of Pilot Ignited High Pressure Direct Injection Natural Gas Engines: Factors Affecting Combustion, Emissions and Performance”.
In: *Renewable and Sustainable Energy Reviews* 119 (Mar. 1, 2020), p. 109653.
ISSN: 1364-0321. DOI: 10.1016/j.rser.2019.109653.

[87] A. Welch et al. *Challenges in Developing Hydrogen Direct Injection Technology for Internal Combustion Engines*. SAE Technical Paper 2008-01-2379.
Warrendale, PA: SAE International, Oct. 6, 2008. DOI: 10.4271/2008-01-2379.

[88] A. Mohammadi et al. “Performance and Combustion Characteristics of a Direct Injection SI Hydrogen Engine”.
In: *International Journal of Hydrogen Energy* 32.2 (Feb. 1, 2007), pp. 296–304.
ISSN: 0360-3199. DOI: 10.1016/j.ijhydene.2006.06.005.

[89] H. Rottengruber et al. *Direct-Injection Hydrogen SI-Engine - Operation Strategy and Power Density Potentials*. SAE Technical Paper 2004-01-2927.
Warrendale, PA: SAE International, Oct. 25, 2004. DOI: 10.4271/2004-01-2927.

[90] Y. Y. Kim, J. T. Lee, and G. H. Choi. “An Investigation on the Causes of Cycle Variation in Direct Injection Hydrogen Fueled Engines”.
In: *International Journal of Hydrogen Energy* 30.1 (Jan. 1, 2005), pp. 69–76.
ISSN: 0360-3199. DOI: 10.1016/j.ijhydene.2004.03.041.

[91] Y. Li et al. “Effects Study of Injection Strategies on Hydrogen-Air Formation and Performance of Hydrogen Direct Injection Internal Combustion Engine”.
In: *International Journal of Hydrogen Energy* 44.47 (Oct. 4, 2019), pp. 26000–26011.
ISSN: 0360-3199. DOI: 10.1016/j.ijhydene.2019.08.055.

[92] A. A. Boretti and H. C. Watson.
“The Lean Burn Direct Injection Jet Ignition Gas Engine”.
In: *International Journal of Hydrogen Energy* 34.18 (Sept. 1, 2009), pp. 7835–7841.
ISSN: 0360-3199. DOI: 10.1016/j.ijhydene.2009.07.022.

[93] A. B. Welch and J. S. Wallace.
Performance Characteristics of a Hydrogen-Fueled Diesel Engine with Ignition Assist.
SAE Technical Paper 902070. Warrendale, PA: SAE International, Oct. 1, 1990.
DOI: 10.4271/902070.

[94] H. S. Homan et al. "Hydrogen-Fueled Diesel Engine without Timed Ignition".
In: *International Journal of Hydrogen Energy* 4.4 (Jan. 1, 1979), pp. 315–325.
ISSN: 0360-3199. DOI: 10.1016/0360-3199(79)90006-5.

[95] S. Furuhama and Y. Kobayashi. "Development of a Hot-Surface-Ignition Hydrogen Injection Two-Stroke Engine".
In: *International Journal of Hydrogen Energy* 9.3 (Jan. 1, 1984), pp. 205–213.
ISSN: 0360-3199. DOI: 10.1016/0360-3199(84)90120-4.

[96] M. F. Rosati and P. G. Aleiferis.
"Hydrogen SI and HCCI Combustion in a Direct-Injection Optical Engine".
In: *SAE International Journal of Engines* 2.2009-01-1921 (1 June 15, 2009),
pp. 1710–1736. ISSN: 1946-3936, 1946-3944. DOI: 10.4271/2009-01-1921.

[97] P. G. Aleiferis and M. F. Rosati.
"Controlled Autoignition of Hydrogen in a Direct-Injection Optical Engine".
In: *Combustion and Flame* 159.7 (July 1, 2012), pp. 2500–2515. ISSN: 0010-2180.
DOI: 10.1016/j.combustflame.2012.02.021.

[98] J. M. Gomes Antunes, R. Mikalsen, and A. P. Roskilly. "An Investigation of Hydrogen-Fuelled HCCI Engine Performance and Operation".
In: *International Journal of Hydrogen Energy* 33.20 (Oct. 1, 2008), pp. 5823–5828.
ISSN: 0360-3199. DOI: 10.1016/j.ijhydene.2008.07.121.

[99] B. D. Gowda and T. Echekki.
"Complex Injection Strategies for Hydrogen-Fueled HCCI Engines".
In: *Fuel* 97 (July 1, 2012), pp. 418–427. ISSN: 0016-2361.
DOI: 10.1016/j.fuel.2012.01.060.

[100] H. Rottengruber et al. "Wasserstoff-Dieselmotor mit Direkteinspritzung, hoher Leistungsdichte und geringer Abgasemission".
In: *MTZ - Motortechnische Zeitschrift* 61.2 (Feb. 1, 2000), pp. 122–128.
ISSN: 2192-8843. DOI: 10.1007/BF03226557.

[101] J. M. Gomes Antunes, R. Mikalsen, and A. P. Roskilly. "An Experimental Study of a Direct Injection Compression Ignition Hydrogen Engine".
In: *International Journal of Hydrogen Energy* 34.15 (Aug. 1, 2009), pp. 6516–6522.
ISSN: 0360-3199. DOI: 10.1016/j.ijhydene.2009.05.142.

[102] G. P. McTaggart-Cowan et al. “The Effects of High-Pressure Injection on a Compression-Ignition, Direct Injection of Natural Gas Engine”. In: ASME 2005 Internal Combustion Engine Division Fall Technical Conference. American Society of Mechanical Engineers Digital Collection, Nov. 11, 2008, pp. 161–173. DOI: 10.1115/ICEF2005-1213.

[103] C. Barba et al. “Natural Gas-Diesel Dual Fuel for Commercial Vehicle Engines”. In: *Internationaler Motorenkongress 2017*. Ed. by J. Liebl and C. Beidl. Proceedings. Wiesbaden: Springer Fachmedien, 2017, pp. 391–407. ISBN: 978-3-658-17109-4. DOI: 10.1007/978-3-658-17109-4_23.

[104] L. Dai. “Study of the Injection and Mixture Process and the Combustion Simulation of Natural Gas/Diesel Dual-Fuel”. Masters Dissertation. Zhenjiang, China: Jiangsu University, 2016.

[105] C. W. J. Mabson. “Emissions Characterization of Paired Gaseous Jets in a Pilot-Ignited Natural-Gas Compression-Ignition Engine”. MSc. Vancouver: The University of British Columbia, 2015.

[106] P. Kheirkhah. “CFD Modelling of Injection Strategies in a High-Pressure Direct-Injection (HPDI) Natural Gas Engine”. MSc. Vancouver: The University of British Columbia, 2015.

[107] J. Rochussen, G. McTaggart-Cowan, and P. Kirchen. “Parametric Study of Pilot-Ignited Direct-Injection Natural Gas Combustion in an Optically Accessible Heavy-Duty Engine”. In: *International Journal of Engine Research* 21.3 (Mar. 1, 2020), pp. 497–513. ISSN: 1468-0874. DOI: 10.1177/1468087419836877.

[108] M. Jud et al. “Numerical Analysis of the Combustion Process in Dual-Fuel Engines With Direct Injection of Natural Gas”. In: ASME 2018 Internal Combustion Engine Division Fall Technical Conference. American Society of Mechanical Engineers Digital Collection, Jan. 3, 2019. DOI: 10.1115/ICEF2018-9579.

[109] E. Faghani. “Effect of Injection Strategies on Particulate Matter Emissions from HPDI Natural-Gas Engines”. PhD thesis. Vancouver: The University of British Columbia, 2015.

[110] G. K. Lilik et al. “Hydrogen Assisted Diesel Combustion”. In: *International Journal of Hydrogen Energy* 35.9 (May 1, 2010), pp. 4382–4398. ISSN: 0360-3199. DOI: 10.1016/j.ijhydene.2010.01.105.

[111] A. Maghbouli et al. “Modeling Knocking Combustion in Hydrogen Assisted Compression Ignition Diesel Engines”. In: *Energy* 76 (Nov. 1, 2014), pp. 768–779. ISSN: 0360-5442. DOI: 10.1016/j.energy.2014.08.074.

[112] L. Li, Y. Yu, and W. Lin.
"Numerical Investigation on the Effects of Load Conditions and Hydrogen-Air Ratio on the Combustion Processes of a HSDI Engine".
In: *International Journal of Hydrogen Energy*. AEM 2018 - Smart Materials for Hydrogen Energy 45.17 (Mar. 27, 2020), pp. 10602–10612. ISSN: 0360-3199. DOI: 10.1016/j.ijhydene.2019.08.207.

[113] V. Chintala and K. A. Subramanian. "CFD Analysis on Effect of Localized In-Cylinder Temperature on Nitric Oxide (NO) Emission in a Compression Ignition Engine under Hydrogen-Diesel Dual-Fuel Mode".
In: *Energy* 116 (Dec. 1, 2016), pp. 470–488. ISSN: 0360-5442. DOI: 10.1016/j.energy.2016.09.133.

[114] A. Yousefi et al. "Performance and Emissions of a Dual-Fuel Pilot Diesel Ignition Engine Operating on Various Premixed Fuels".
In: *Energy Conversion and Management* 106 (Dec. 1, 2015), pp. 322–336. ISSN: 0196-8904. DOI: 10.1016/j.enconman.2015.09.056.

[115] İ. Temizer and Ö. Cihan. "Analysis of Different Combustion Chamber Geometries Using Hydrogen / Diesel Fuel in a Diesel Engine".
In: *Energy Sources, Part A: Recovery, Utilization, and Environmental Effects* 43.1 (Jan. 2, 2021), pp. 17–34. ISSN: 1556-7036. DOI: 10.1080/15567036.2020.1811808.

[116] G. Tripathi et al. "Computational Investigation of Diesel Injection Strategies in Hydrogen-Diesel Dual Fuel Engine".
In: *Sustainable Energy Technologies and Assessments* 36 (Dec. 1, 2019), p. 100543. ISSN: 2213-1388. DOI: 10.1016/j.seta.2019.100543.

[117] A. I. Jabbr and U. O. Koylu.
"Influence of Operating Parameters on Performance and Emissions for a Compression-Ignition Engine Fueled by Hydrogen/Diesel Mixtures". In: *International Journal of Hydrogen Energy* 44.26 (May 21, 2019), pp. 13964–13973. ISSN: 0360-3199. DOI: 10.1016/j.ijhydene.2019.03.201.

[118] V. Knop et al. "Modelling of Combustion and Nitrogen Oxide Formation in Hydrogen-Fuelled Internal Combustion Engines within a 3D CFD Code".
In: *International Journal of Hydrogen Energy*. 2nd Asian Bio Hydrogen Symposium 33.19 (Oct. 1, 2008), pp. 5083–5097. ISSN: 0360-3199. DOI: 10.1016/j.ijhydene.2008.06.027.

[119] B. S. Soriano. "Theory and Modelling of Dual-Fuel Combustion".
PhD thesis. University of Southampton, July 2019. 220 pp.

[120] P. Nakod et al.
"A Comparative Computational Fluid Dynamics Study on Flamelet-Generated Manifold and Steady Laminar Flamelet Modeling for Turbulent Flames".
In: *Journal of Engineering for Gas Turbines and Power* 136.8 (Mar. 11, 2014).
ISSN: 0742-4795. DOI: 10.1115/1.4026806.

[121] R. Scarcelli et al. *Numerical and Optical Evolution of Gaseous Jets in Direct Injection Hydrogen Engines*. SAE Technical Paper 2011-01-0675.
Warrendale, PA: SAE International, Apr. 12, 2011. DOI: 10.4271/2011-01-0675.

[122] T.-H. Shih et al. "A New K-Epsilon Eddy Viscosity Model for High Reynolds Number Turbulent Flows".
In: *Computers & Fluids* 24.3 (Mar. 1, 1995), pp. 227–238. ISSN: 0045-7930.
DOI: 10.1016/0045-7930(94)00032-T.

[123] B. E. Launder and D. B. Spalding.
"The Numerical Computation of Turbulent Flows". In: *Computer Methods in Applied Mechanics and Engineering* 3.2 (Mar. 1, 1974), pp. 269–289.
ISSN: 0045-7825. DOI: 10.1016/0045-7825(74)90029-2.

[124] E. Pomraning, K. Richards, and P. K. Senecal. *Modeling Turbulent Combustion Using a RANS Model, Detailed Chemistry, and Adaptive Mesh Refinement*.
SAE Technical Paper 2014-01-1116.
Warrendale, PA: SAE International, Apr. 1, 2014. DOI: 10.4271/2014-01-1116.

[125] S. B. Pope. "Computationally Efficient Implementation of Combustion Chemistry Using in Situ Adaptive Tabulation".
In: *Combustion Theory and Modelling* 1.1 (Jan. 1, 1997), pp. 41–63.
ISSN: 1364-7830. DOI: 10.1080/713665229.

[126] B. MAGNUSSEN. "On the Structure of Turbulence and a Generalized Eddy Dissipation Concept for Chemical Reaction in Turbulent Flow".
In: *19th Aerospace Sciences Meeting*.
American Institute of Aeronautics and Astronautics. DOI: 10.2514/6.1981-42.

[127] H. Barths, C. Antoni, and N. Peters. *Three-Dimensional Simulation of Pollutant Formation in a DI Diesel Engine Using Multiple Interactive Flamelets*.
SAE Technical Paper 982459. Warrendale, PA: SAE International, Oct. 19, 1998.
DOI: 10.4271/982459.

[128] H. Pitsch, H. Barths, and N. Peters.
Three-Dimensional Modeling of NOx and Soot Formation in DI-Diesel Engines Using Detailed Chemistry Based on the Interactive Flamelet Approach.
SAE Technical Paper 962057. Warrendale, PA: SAE International, Oct. 1, 1996.
DOI: 10.4271/962057.

[129] N. Nordin. "Numerical Simulations of Non-Steady Spray Combustion Using a Detailed Chemistry Approach". Licentiate of Engineering. Dept. of Thermo and Fluid Dynamics: Chalmers University of Technology, 1998.

[130] F. Tao, R. Reitz, and D. Foster.
"Revisit of Diesel Reference Fuel (n-Heptane) Mechanism Applied to Multidimensional Diesel Ignition and Combustion Simulations".
In: (Jan. 1, 2007).

[131] S. Wijeyakulasuriya et al. "Multidimensional Modeling and Validation of Dual-Fuel Combustion in a Large Bore Medium Speed Diesel Engine". In: ASME 2015 Internal Combustion Engine Division Fall Technical Conference. American Society of Mechanical Engineers Digital Collection, Jan. 12, 2016. DOI: 10.1115/ICEF2015-1077.

[132] G. Smith et al. "GRI-Mech 3.0". In: *http://www.me.berkley.edu/gri_mech/* (1999).

[133] P. Zoldak et al. "Combustion Simulation of Dual Fuel CNG Engine Using Direct Injection of Natural Gas and Diesel".
In: *SAE International Journal of Engines* 8.2 (2015), pp. 846–858. ISSN: 1946-3936. JSTOR: 26277989.

[134] C. P. Fenimore. "Formation of Nitric Oxide in Premixed Hydrocarbon Flames". In: *Symposium (International) on Combustion*. Thirteenth Symposium (International) on Combustion 13.1 (Jan. 1, 1971), pp. 373–380. ISSN: 0082-0784. DOI: 10.1016/S0082-0784(71)80040-1.

[135] S. J. Brookes and J. B. Moss. "Predictions of Soot and Thermal Radiation Properties in Confined Turbulent Jet Diffusion Flames".
In: *Combustion and Flame* 116.4 (Mar. 1, 1999), pp. 486–503. ISSN: 0010-2180. DOI: 10.1016/S0010-2180(98)00056-X.

[136] B. M. Grimm and R. T. Johnson. *Review of Simple Heat Release Computations*. SAE Technical Paper 900445. Warrendale, PA: SAE International, Feb. 1, 1990. DOI: 10.4271/900445.

[137] M. F. J. Brunt and K. C. Platts.
Calculation of Heat Release in Direct Injection Diesel Engines.
SAE Technical Paper 1999-01-0187.
Warrendale, PA: SAE International, Mar. 1, 1999. DOI: 10.4271/1999-01-0187.

[138] H. L. Yip et al. "Visualization of Hydrogen Jet Evolution and Combustion under Simulated Direct-Injection Compression-Ignition Engine Conditions".
In: *International Journal of Hydrogen Energy* 45.56 (Nov. 13, 2020), pp. 32562–32578. ISSN: 0360-3199. DOI: 10.1016/j.ijhydene.2020.08.220.

[139] T. Tsujimura et al.
"A Study of Direct Injection Diesel Engine Fueled with Hydrogen".
In: *SAE Transactions* 112 (2003), pp. 390–405. ISSN: 0096-736X.
DOI: 10.4271/2003-01-0761.. JSTOR: 44742272.

[140] A. Hamzehloo and P. G. Aleiferis.
"LES and RANS Modelling of Under-Expanded Jets with Application to Gaseous Fuel Direct Injection for Advanced Propulsion Systems".
In: *International Journal of Heat and Fluid Flow* 76 (Apr. 1, 2019), pp. 309–334.
ISSN: 0142-727X. DOI: 10.1016/j.ijheatfluidflow.2019.01.017.

[141] V. Vuorinen et al. "Large-Eddy Simulation on the Effect of Injection Pressure and Density on Fuel Jet Mixing in Gas Engines".
In: *Fuel* 130 (Aug. 15, 2014), pp. 241–250. ISSN: 0016-2361.
DOI: 10.1016/j.fuel.2014.04.045.

[142] M. Banholzer et al. "Numerical Investigation of the Flow Characteristics of Underexpanded Methane Jets".
In: *Physics of Fluids* 31.5 (May 1, 2019), p. 056105. ISSN: 1070-6631.
DOI: 10.1063/1.5092776.

[143] C. Traxinger and M. Pfitzner. "Effect of Nonideal Fluid Behavior on the Jet Mixing Process under High-Pressure and Supersonic Flow Conditions".
In: *The Journal of Supercritical Fluids* 172 (June 1, 2021), p. 105195.
ISSN: 0896-8446. DOI: 10.1016/j.supflu.2021.105195.

[144] M. Thring and M. P. Newby.
"Combustion Length of Enclosed Turbulent Jet Flames". In: 1953.
DOI: 10.1016/S0082-0784(53)80103-7.

[145] E. Franquet et al.
"Free Underexpanded Jets in a Quiescent Medium: A Review".
In: *Progress in Aerospace Sciences* 77 (Aug. 1, 2015), pp. 25–53. ISSN: 0376-0421.
DOI: 10.1016/j.paerosci.2015.06.006.

[146] A. D. Birch et al.
"The Structure and Concentration Decay of High Pressure Jets of Natural Gas".
In: *Combustion Science and Technology* 36.5-6 (Apr. 1, 1984), pp. 249–261.
ISSN: 0010-2202. DOI: 10.1080/00102208408923739.

[147] A. D. Birch, D. J. Hughes, and F. Swaffield.
"Velocity Decay of High Pressure Jets".
In: *Combustion Science and Technology* 52.1-3 (Mar. 1, 1987), pp. 161–171.
ISSN: 0010-2202. DOI: 10.1080/00102208708952575.

[148] B. C. R. Ewan and K. Moodie.
"Structure and Velocity Measurements in Underexpanded Jets".
In: *Combustion Science and Technology* 45.5-6 (Mar. 1, 1986), pp. 275–288.
ISSN: 0010-2202. DOI: 10.1080/00102208608923857.

[149] K. Harstad and J. Bellan. "Global Analysis and Parametric Dependencies for Potential Unintended Hydrogen-Fuel Releases".
In: *Combustion and Flame* 144.1 (Jan. 1, 2006), pp. 89–102. ISSN: 0010-2180.
DOI: 10.1016/j.combustflame.2005.07.005.

[150] K. B. Yüceil and M. V. Ötügen.
"Scaling Parameters for Underexpanded Supersonic Jets".
In: *Physics of Fluids* 14.12 (Oct. 22, 2002), pp. 4206–4215. ISSN: 1070-6631.
DOI: 10.1063/1.1513796.

[151] G. Kleinstein. "Mixing in Turbulent Axially Symmetric Free Jets".
In: *Journal of Spacecraft and Rockets* 1 (July 1, 1964), pp. 403–408. ISSN: 0022-4650.
DOI: 10.2514/3.27669.

[152] P. Witze. "Centerline Velocity Decay of Compressible Free Jets".
In: *AIAA* 12.4 (1974).

[153] P. J. Kerney, G. M. Faeth, and D. R. Olson.
"Penetration Characteristics of a Submerged Steam Jet".
In: *AIChE Journal* 18.3 (1972), pp. 548–553. ISSN: 1547-5905.
DOI: 10.1002/aic.690180314.

[154] Y. Ra et al. *Multidimensional Modeling of Transient Gas Jet Injection Using Coarse Computational Grids*. SAE Technical Paper 2005-01-0208.
Warrendale, PA: SAE International, Apr. 11, 2005. DOI: 10.4271/2005-01-0208.

[155] L. Andreassi, A. L. Facci, and S. Ubertini. "Numerical Simulation of Gaseous Fuel Injection: A New Methodology for Multi-Dimensional Modelling".
In: *International Journal for Numerical Methods in Fluids* 64.6 (2010), pp. 609–626.
ISSN: 1097-0363. DOI: 10.1002/fld.2165.

[156] L. Andreassi et al. "Multidimensional Modelling of Gaseous Injection: Analysis of an Impinging Jet". In: *International Journal of Heat and Fluid Flow*. Sixth International Symposium on Turbulence, Heat and Mass Transfer, Rome, Italy, 14-18 September 2009 31.5 (Oct. 1, 2010), pp. 909–915. ISSN: 0142-727X.
DOI: 10.1016/j.ijheatfluidflow.2010.05.013.

[157] X. Li, E. S. Hecht, and D. M. Christopher. "Validation of a Reduced-Order Jet Model for Subsonic and Underexpanded Hydrogen Jets".
In: *International Journal of Hydrogen Energy* 41.2 (Jan. 12, 2016), pp. 1348–1358.
ISSN: 0360-3199. DOI: 10.1016/j.ijhydene.2015.10.071.

[158] X. Li et al.
"Validation of Two-Layer Model for Underexpanded Hydrogen Jets".
In: *International Journal of Hydrogen Energy*. ICHS 2019 Conference 46.23 (Mar. 31, 2021), pp. 12545–12554. ISSN: 0360-3199.
DOI: 10.1016/j.ijhydene.2020.08.204.

[159] K. Pan. "Computational Studies of Gas Injection, Ignition and Combustion Emissions in a Direct-Injection Natural Gas Engine".
PhD thesis. University of Toronto, 2019.

[160] A. Y. Deshmukh et al. "A Quasi-One-Dimensional Model for an Outwardly Opening Poppet-Type Direct Gas Injector for Internal Combustion Engines".
In: *International Journal of Engine Research* 21.8 (Oct. 1, 2020), pp. 1493–1519.
ISSN: 1468-0874. DOI: 10.1177/1468087419871117.

[161] R. P. Hessel et al.
Gaseous Fuel Injection Modeling Using a Gaseous Sphere Injection Methodology.
SAE Technical Paper 2006-01-3265.
Warrendale, PA: SAE International, Oct. 16, 2006. DOI: 10.4271/2006-01-3265.

[162] R. Whitesides et al. "Application of Gaseous Sphere Injection Method for Modeling Under-Expanded H2 Injection".
In: *Combustion Theory and Modelling* 15.3 (June 1, 2011), pp. 373–384.
ISSN: 1364-7830. DOI: 10.1080/13647830.2010.541286.

[163] M. Choi, S. Lee, and S. Park. "Numerical and Experimental Study of Gaseous Fuel Injection for CNG Direct Injection".
In: *Fuel* 140 (Jan. 15, 2015), pp. 693–700. ISSN: 0016-2361.
DOI: 10.1016/j.fuel.2014.10.018.

[164] M. Choi, J. Song, and S. Park. "Modeling of the Fuel Injection and Combustion Process in a CNG Direct Injection Engine".
In: *Fuel* 179 (Sept. 1, 2016), pp. 168–178. ISSN: 0016-2361.
DOI: 10.1016/j.fuel.2016.03.099.

[165] R. Yang. "Numerical Investigation of the Gas Injection Process in Large Marine DF Engines". In: *International Conference on Maritime Safety and Operations*. Glasgow, Sept. 13, 2016.

[166] J. Song et al. "Combustion Characteristics of Methane Direct Injection Engine Under Various Injection Timings and Injection Pressures".
In: *Journal of Engineering for Gas Turbines and Power* 139.082802 (Mar. 21, 2017).
ISSN: 0742-4795. DOI: 10.1115/1.4035817.

[167] T. Wang et al. "Numerical Analysis of the Influence of the Fuel Injection Timing and Ignition Position in a Direct-Injection Natural Gas Engine".
In: *Energy Conversion and Management* 149 (Oct. 1, 2017), pp. 748–759.
ISSN: 0196-8904. DOI: 10.1016/j.enconman.2017.03.004.

[168] J. Liu et al. "Optimization of the Injection Parameters of a Diesel/Natural Gas Dual Fuel Engine with Multi-Objective Evolutionary Algorithms".
In: *Applied Thermal Engineering* 150 (Mar. 5, 2019), pp. 70–79. ISSN: 1359-4311. DOI: 10.1016/j.applthermaleng.2018.12.171.

[169] C. duP Donaldson and R. S. Snedeker. "A Study of Free Jet Impingement. Part 1. Mean Properties of Free and Impinging Jets".
In: *Journal of Fluid Mechanics* 45.2 (Jan. 1971), pp. 281–319.
ISSN: 1469-7645, 0022-1120. DOI: 10.1017/S0022112071000053.

[170] B. S. Stratford.
"The Calculation of the Discharge Coefficient of Profiled Choked Nozzles and the Optimum Profile for Absolute Air Flow Measurement".
In: *The Aeronautical Journal* 68.640 (Apr. 1964), pp. 237–245.
ISSN: 0368-3931, 2398-4600. DOI: 10.1017/S0001924000060905.

[171] M. M. A. Alam et al.
"Nozzle Geometry Variations on the Discharge Coefficient".
In: *Propulsion and Power Research* 5.1 (Mar. 1, 2016), pp. 22–33. ISSN: 2212-540X. DOI: 10.1016/j.jppr.2016.01.002.

[172] T. Shudo and S. Oba. "Mixture Distribution Measurement Using Laser Induced Breakdown Spectroscopy in Hydrogen Direct Injection Stratified Charge".
In: *International Journal of Hydrogen Energy* 34.5 (Mar. 1, 2009), pp. 2488–2493.
ISSN: 0360-3199. DOI: 10.1016/j.ijhydene.2009.01.012.

[173] P. Ouellette. "Direct Injection of Natural Gas for Diesel Engine Fueling".
PhD thesis. The University of British Columbia, 1996.

[174] P. Ouellette and P. G. Hill. "Turbulent Transient Gas Injections".
In: *Journal of Fluids Engineering* 122.4 (July 13, 1999), pp. 743–752.
ISSN: 0098-2202. DOI: 10.1115/1.1319845.

[175] R. Ishibashi and D. Tsuru. "An Optical Investigation of Combustion Process of a Direct High-Pressure Injection of Natural Gas".
In: *Journal of Marine Science and Technology* 22.3 (Sept. 1, 2017), pp. 447–458.
ISSN: 1437-8213. DOI: 10.1007/s00773-016-0422-x.

[176] P. O. Witze. *Impulsively Started Incompressible Turbulent Jet*. SAND-80-8617. Sandia Labs., Livermore, CA (USA), Oct. 1, 1980. DOI: 10.2172/5017517.

[177] W. Warren. *An Analytical and Experimental Study of Compressible Free Jets*. 381. Aeronautical Engineering Laboratory: Princeton University, 1957.

[178] H. von Helldorff and G. Micklow.
"Gaseous and Liquid Jet Direct Injection Simulations Using KIVA-3V". In: *Journal of Multidisciplinary Engineering Science and Technology (JMEST)* 6.1 (2019).
ISSN: 2458-9403.

[179] D. R. Jonassen, G. S. Settles, and M. D. Tronosky.
"Schlieren "PIV" for Turbulent Flows".
In: *Optics and Lasers in Engineering*. Optical Methods in Heat Transfer and Fluid Flow 44.3 (Mar. 1, 2006), pp. 190–207. ISSN: 0143-8166.
DOI: 10.1016/j.optlaseng.2005.04.004.

[180] J. C. Lau. "Effects of Exit Mach Number and Temperature on Mean-Flow and Turbulence Characteristics in Round Jets".
In: *Journal of Fluid Mechanics* 105 (Apr. 1981), pp. 193–218.
ISSN: 1469-7645, 0022-1120. DOI: 10.1017/S0022112081003170.

[181] R. Baert, A. Klaassen, and E. Doosje. "Direct Injection of High Pressure Gas: Scaling Properties of Pulsed Turbulent Jets".
In: *SAE International Journal of Engines* 3.2 (2010), pp. 383–395. ISSN: 1946-3936.
JSTOR: 26275567.

[182] J. D. Gorhum. "Development of a Pneumatic Infrasound Generator".
MSc. University of Texas at Austin, May 2014.

[183] B. André, T. Castelain, and C. Bailly. "Investigation of the Mixing Layer of Underexpanded Supersonic Jets by Particle Image Velocimetry".
In: *International Journal of Heat and Fluid Flow* 50 (Dec. 1, 2014), pp. 188–200.
ISSN: 0142-727X. DOI: 10.1016/j.ijheatfluidflow.2014.08.004.

[184] X. Li et al. "A Comparative Study of Highly Underexpanded Nitrogen and Hydrogen Jets Using Large Eddy Simulation".
In: *International Journal of Hydrogen Energy* 41.9 (Mar. 9, 2016), pp. 5151–5161.
ISSN: 0360-3199. DOI: 10.1016/j.ijhydene.2016.01.120.

[185] F. Bonelli, A. Viggiano, and V. Magi.
"A Numerical Analysis of Hydrogen Underexpanded Jets". In:
ASME 2012 Internal Combustion Engine Division Spring Technical Conference.
American Society of Mechanical Engineers Digital Collection, July 18, 2013,
pp. 681–690. DOI: 10.1115/ICES2012-81068.

[186] H. Ashkenas and F. S. Sherman. "The Structure and Utilization of Supersonic Free Jets in Low Density Wind Tunnels". In: (1965), p. 84.

[187] S. Crist, D. R. Glass, and P. M. Sherman.
"Study of the Highly Underexpanded Sonic Jet."
In: *AIAA Journal* 4.1 (Jan. 1, 1966), pp. 68–71. ISSN: 0001-1452.
DOI: 10.2514/3.3386.

[188] V. S. Avduevskii et al. "Flow in Supersonic Viscous under Expanded Jet".
In: *Fluid Dynamics* 5 (1973), pp. 409–414. ISSN: 0015-4628.
DOI: 10.1007/BF01019275.

[189] J.-C. Lengrand, J. Allegre, and M. Raffin.
"Underexpanded Free Jets and Their Interaction with Adjacent Surfaces".
In: *AIAA Journal* 20.1 (1982), pp. 27–28. ISSN: 0001-1452. DOI: 10.2514/3.51040.

[190] A. L. Addy. "Effects of Axisymmetric Sonic Nozzle Geometry on Mach Disk Characteristics". In: *AIAA Journal* 19.1 (1981), pp. 121–122. ISSN: 0001-1452. DOI: 10.2514/3.7751.

[191] V. Vuorinen et al.
"Large-Eddy Simulation of Highly Underexpanded Transient Gas Jets".
In: *Physics of Fluids* 25.1 (Jan. 1, 2013), p. 016101. ISSN: 1070-6631. DOI: 10.1063/1.4772192.

[192] P. J. O'Rourke. *Collective Drop Effects on Vaporizing Liquid Sprays*. LA-9069-T. Los Alamos National Lab., NM (USA), Nov. 1, 1981.

[193] A. B. Liu, D. Mather, and R. D. Reitz.
"Modeling the Effects of Drop Drag and Breakup on Fuel Sprays".
In: *SAE Transactions* 102 (1993), pp. 83–95. ISSN: 0096-736X. JSTOR: 44611358.

[194] P. J. O'Rourke and A. A. Amsden.
"A Spray/Wall Interaction Submodel for the KIVA-3 Wall Film Model".
In: *SAE Transactions* 109 (2000), pp. 281–298. ISSN: 0096-736X. JSTOR: 44634219.

[195] D. W. Stanton and C. J. Rutland.
"Modeling Fuel Film Formation and Wall Interaction in Diesel Engines".
In: *SAE Transactions* 105 (1996), pp. 808–824. ISSN: 0096-736X. JSTOR: 44736319.

[196] A. D. Gosman and E. loannides.
"Aspects of Computer Simulation of Liquid-Fueled Combustors".
In: *Journal of Energy* 7.6 (1983), pp. 482–490. ISSN: 0146-0412. DOI: 10.2514/3.62687.

[197] C. M. Rhie and W. L. Chow. "Numerical Study of the Turbulent Flow Past an Airfoil with Trailing Edge Separation".
In: *AIAA Journal* 21.11 (1983), pp. 1525–1532. ISSN: 0001-1452. DOI: 10.2514/3.8284.

[198] R. I. Issa. "Solution of the Implicitly Discretised Fluid Flow Equations by Operator-Splitting".
In: *Journal of Computational Physics* 62.1 (Jan. 1, 1986), pp. 40–65. ISSN: 0021-9991. DOI: 10.1016/0021-9991(86)90099-9.

[199] J. D. Naber and J. E. Johnson.
"8 - Internal Combustion Engine Cycles and Concepts". In: *Alternative Fuels and Advanced Vehicle Technologies for Improved Environmental Performance*.
Ed. by R. Folkson. Woodhead Publishing, Jan. 1, 2014, pp. 197–224.
ISBN: 978-0-85709-522-0. DOI: 10.1533/9780857097422.2.197.

[200] R. Chen et al. *Quasi-Constant Volume (QCV) Spark Ignition Combustion*.
SAE Technical Paper 2009-01-0700.
Warrendale, PA: SAE International, Apr. 20, 2009. DOI: 10.4271/2009-01-0700.

[201] J. Ž. Dorić and I. J. Klinar. "Efficiency of a New Internal Combustion Engine Concept with Variable Piston Motion".
In: *Thermal Science* 18.1 (2014), pp. 113–127.

[202] A. Shaik, N. S. V. Moorthi, and R. Rudramoorthy. "Variable Compression Ratio Engine: A Future Power Plant for Automobiles - an Overview".
In: *Proceedings of the Institution of Mechanical Engineers, Part D: Journal of Automobile Engineering* 221.9 (Sept. 1, 2007), pp. 1159–1168. ISSN: 0954-4070.
DOI: 10.1243/09544070JAUTO573.

[203] C. Zhang and Z. Sun.
"Using Variable Piston Trajectory to Reduce Engine-out Emissions".
In: *Applied Energy* 170 (May 15, 2016), pp. 403–414. ISSN: 0306-2619.
DOI: 10.1016/j.apenergy.2016.02.104.

[204] C. Zhang, K. Li, and Z. Sun. "Modeling of Piston Trajectory-Based HCCI Combustion Enabled by a Free Piston Engine".
In: *Applied Energy* 139 (Feb. 1, 2015), pp. 313–326. ISSN: 0306-2619.
DOI: 10.1016/j.apenergy.2014.11.007.

[205] C. Zhang and Z. Sun. "Trajectory-Based Combustion Control for Renewable Fuels in Free Piston Engines". In: *Applied Energy* 187 (Feb. 1, 2017), pp. 72–83.
ISSN: 0306-2619. DOI: 10.1016/j.apenergy.2016.11.045.

[206] S. Rabl et al. "Understanding the Relationship between Ignition Delay and Burn Duration in a Constant Volume Vessel at Diesel Engine Conditions".
In: *Proceedings of the Combustion Institute* 35.3 (Jan. 1, 2015), pp. 2967–2974.
ISSN: 1540-7489. DOI: 10.1016/j.proci.2014.05.054.

[207] M. Lapuerta, J. Sanz-Argent, and R. R. Raine.
"Ignition Characteristics of Diesel Fuel in a Constant Volume Bomb under Diesel-Like Conditions. Effect of the Operation Parameters".
In: *Energy & Fuels* 28.8 (Aug. 21, 2014), pp. 5445–5454. ISSN: 0887-0624.
DOI: 10.1021/ef500535j.

[208] Covaxe Novel Engine Concept. June 19, 2018.
URL: https://www.covaxe.com/ (visited on 06/19/2018).

[209] M. P. B. Musculus et al. *End-of-Injection Over-Mixing and Unburned Hydrocarbon Emissions in Low-Temperature-Combustion Diesel Engines*.
SAE Technical Paper 2007-01-0907.
Warrendale, PA: SAE International, Apr. 16, 2007. DOI: 10.4271/2007-01-0907.

[210] H. Omidvarborna, A. Kumar, and D.-S. Kim.
"Recent Studies on Soot Modeling for Diesel Combustion".
In: *Renewable and Sustainable Energy Reviews* 48 (Aug. 1, 2015), pp. 635–647.
ISSN: 1364-0321. DOI: 10.1016/j.rser.2015.04.019.

[211] M. K. Bobba, C. L. Genzale, and M. P. B. Musculus.
"Effect of Ignition Delay on In-Cylinder Soot Characteristics of a Heavy Duty Diesel Engine Operating at Low Temperature Conditions".
In: *SAE International Journal of Engines* 2.1 (2009), pp. 911–924. ISSN: 1946-3936.
JSTOR: 26308440.

[212] J. H. Pollard. *A Handbook of Numerical and Statistical Techniques: With Examples Mainly from the Life Sciences*. CUP Archive, Nov. 29, 1979. 372 pp.
ISBN: 978-0-521-29750-9. Google Books: qs08AAAAIAAJ.

[213] J. Thangaraja and C. Kannan. "Effect of Exhaust Gas Recirculation on Advanced Diesel Combustion and Alternate Fuels - A Review".
In: *Applied Energy* 180 (Oct. 15, 2016), pp. 169–184. ISSN: 0306-2619.
DOI: 10.1016/j.apenergy.2016.07.096.

[214] *Engine Combustion Network Database*.
URL: https://ecn.sandia.gov/engines/hydrogen-engine/.

[215] R. Scarcelli et al. "CFD and Optical Investigations of Fluid Dynamics and Mixture Formation in a DI-H2ICE". In:
ASME 2010 Internal Combustion Engine Division Fall Technical Conference.
American Society of Mechanical Engineers Digital Collection, Jan. 10, 2011, pp. 175–188. DOI: 10.1115/ICEF2010-35084.

[216] T. Lucchini, G. D'Errico, and M. Fiocco. *Multi-Dimensional Modeling of Gas Exchange and Fuel-Air Mixing Processes in a Direct-Injection, Gas Fueled Engine*.
SAE Technical Paper 2011-24-0036.
Warrendale, PA: SAE International, Sept. 11, 2011.
DOI: 10.4271/2011-24-0036.

[217] Westport and P. Zloty. *Westport HPDI 2.0 in Daimler AG Engines*. 2015.
URL: https://cng-lng.pl/wiadomosci/Westport-HPDI-2.0-w-silnikach-Daimler-AG,wiadomosc,8751.html.

[218] P. K. Senecal et al. *A New Parallel Cut-Cell Cartesian CFD Code for Rapid Grid Generation Applied to In-Cylinder Diesel Engine Simulations*.
SAE Technical Paper 2007-01-0159.
Warrendale, PA: SAE International, Apr. 16, 2007. DOI: 10.4271/2007-01-0159.

[219] Z. Wang et al.
"A Computational Investigation of Diesel and Biodiesel Combustion and NOx Formation in a Light-Duty Compression Ignition Engine".
In: *Combustion Institute* GO8602569 (Apr. 24, 2012).
DOI: https://www.osti.gov/biblio/1079596.

[220] T. Hogg et al.
"A Benchmark Study on the Flow Metering Systems for the Characterisation of Fuel Injectors for Future Heavy Duty Commercial Vehicles".
In: *Measurement* 153 (Mar. 1, 2020), p. 107414. ISSN: 0263-2241.
DOI: 10.1016/j.measurement.2019.107414.

[221] ANSYS-Inc. *ANSYS Fluent UDF Manual*. 2013.

[222] C. A. Idicheria and L. M. Pickett.
"Ignition, Soot Formation, and End-of-Combustion Transients in Diesel Combustion under High-EGR Conditions".
In: *International Journal of Engine Research* 12.4 (Aug. 1, 2011), pp. 376–392.
ISSN: 1468-0874. DOI: 10.1177/1468087411399505.

[223] L. M. Pickett et al. "Relationship Between Diesel Fuel Spray Vapor Penetration/Dispersion and Local Fuel Mixture Fraction".
In: *SAE International Journal of Engines* 4.1 (2011), pp. 764–799. ISSN: 1946-3936.
JSTOR: 26278185.